Influence of the Nonlinear Behavior of Soft Soils on Strong Ground Motions

Florent de Martin

CENTRALE
PARIS

ÉCOLE CENTRALE DES ARTS ET MANUFACTURES « ÉCOLE CENTRALE PARIS »

THÈSE

présentée par

Florent DE MARTIN

pour l'obtention du

GRADE DE DOCTEUR

Spécialité	:	Dynamique des Sols, Modélisation numérique
Laboratoire d'accueil	:	Mécanique des Sols, Structures et Matériaux
Sujet	:	Influence of the Nonlinear Behavior of Soft Soils on Strong Ground Motions

Soutenue le: 7 juin 2010

devant un jury composé de:

M.	BARD Pierre-Yves	Président du jury
Mme.	MODARESSI Arézou	Directrice de Thèse
M.	KAWASE Hiroshi	Co-directeur de Thèse
M.	BONILLA Fabian	Rapporteurs
M.	PAROLAI Stefano	
M.	AOCHI Hideo	Examinateurs
M.	BARD Pierre-Yves	

2010ECAP0013

Acknowledgements

This manuscript is part of the research works performed at brgm, Orléans during March 2007 and March 2010 and includes a four-month stay at Kuyshu University, Japan in 2007 and a four-month stay at the Disaster Prevention Research Institute, Japan in 2008.
I gratefully acknowledges the financial assistance for my stays in Japan received from the CARNOT Institute and from the 21^{st} Century COE Program of Kyushu University (H-14).

I offer my sincerest gratitude to my supervisor, Dr. Arezou MODARESSI, who has supported me throughout my thesis whilst allowing me the room to work in my own way.

This thesis would not have been possible unless Dr. Hormoz MODARESSI, Director of the Natural Risks and CO_2 Storage Safety Division of brgm, provides me the freedom to work essentially on research projects during this period.

It was an honor for me to have Dr. Hiroshi KAWASE as a Co-supervisor of my thesis. He invited me several times in his Laboratory in Japan and gave me invaluable guidance on site effects evaluation techniques and on seismology in general.

I am grateful to Dr. Fabina BONILLA and Dr. Stephano PAROLAI for their valuable time spent proof reading this manuscript.

My Thanks also to Dr. Hideo AOCHI and Dr. Pierre-Yves BARD who have kindly accepted to examine my work.

Finally, I thank all my friends and colleagues from brgm and Japan with whom I spent three pleasant years during the preparation of my thesis.

Abstract

Nonlinear behavior of soft soils observed during strong ground motions is now well established and the deployment of vertical arrays (i.e., borehole stations) has contributed to detailed wave propagation analyses and the assessment for quantitative physical parameters such as shear-wave velocity, pressure-wave velocity and damping factors with respect to shear strain levels. Despite the growing number of studies on this phenomena, its knowledge is still recent and research on borehole station data remains an important step toward the understanding of the complex in-situ behavior of soft sediments subjected to strong ground motions.

The purpose of this work is threefold. First, an inversion code by genetic algorithm is developed in order to inverse borehole stations data via the Thomson-Haskell propagator matrix method. This technique allows us to validate the one-dimensional (1D) structure (e.g., shear-wave velocity, damping factors) of a borehole in the linear elastic domain and to show quantitative evidence of the nonlinear behavior of the soft sediments during the 2005 Fukuoka Prefecture western offshore earthquake, Japan. Second, the results of the inversion are used in order to test simple and advanced constitutive laws using the Finite Elements Method. The results clearly show that the bi-linear assumption of the simple constitutive law produces unrealistic velocity and acceleration time histories. The use of the advanced constitutive law leads to better results, however, the number of parameters to be tuned in order to obtain results consistent with the observation is an unavoidable obstacle. Third, in order to extend the study of site effects to higher dimensions, 2D and 3D codes of the very efficient Spectral Elements Method are developed and validated by comparing their results in the linear domain with those obtained theoretically or with other numerical methods.

Keywords: *site effects, inversion techniques, genetic algorithm, Thomson-Haskell propagator matrix, nonlinear soil behavior, equivalent linear method, Finite Elements Method, Spectral Elements Method, paraxial approximation*

Résumé

Le comportement nonlinéaire des sols observé lors des mouvements sismiques forts est maintenant bien admis et le déploiement des puits accélérométriques a permis des analyses détaillées de la propagation des ondes ainsi qu'une évaluation quantitative des paramètres physiques tels que la vitesse de cisaillement et de compression des ondes et les facteurs d' amortissements en fonction de la déformation. En dépit du nombre grandissant d'études sur ce phénomène, sa connaissance est encore récente et les recherches sur les données de puits accélérométriques restent une étape importante vers la compréhension du comportement complexe in-situ des sédiments soumis à des mouvements sismiques forts.

L'objectif de ces travaux est triple. Premièrement, un code d'inversion par algorithme génétique est développé afin d'inverser des données de puits accélérométriques via la théorie des matrices de propagation de Thomson-Haskell. Cette technique nous permet dans un premier temps de valider la structure en une dimension (1D) (e.g., vitesse des ondes de cisaillement, facteurs d' amortissements) d'un puits accélérométrique dans le domaine linéaire et dans un second temps de mettre en évidence de manière quantitative le comportement nonlinéaire des sédiments lors du séisme de Fukuoka, 2005, Japon. Deuxièmement, les résultats de l'inversion sont utilisés pour tester des lois de comportement simples et avancées en utilisant la Méthode des Éléments Finis. Les résultats montrent clairement que l'hypothèse bi-linéaire de la loi de comportement simple produit des séries temporelles non réalistes en vitesse et en accélération. L'utilisation d'une loi de comportement avancée mène à de meilleurs résultats, cependant, le nombre de paramètres ajustables pour obtenir des résultats consistants avec l'observation est un obstable inévitable. Troisièmement, afin d'étendre l'étude des effets de site à des dimensions supérieures, des codes 2D et 3D de la Méthode en Éléments Spectraux sont développés et validés en comparant leurs résultats dans le domaine linéaire avec ceux obtenus théoriquement ou via d'autres méthodes numériques.

Mots Clés: *effets de site, techniques d'inversion, algorithme génétique, matrice de propagation de Thomson-Haskell, comportement nonlinéaire des sols, méthode équivalent linéaire, Méthode des Éléments Finis, Méthode des Éléments Spectraux, approximation paraxiale*

Contents

Notations

We shall use boldface symbol (e.g., $\boldsymbol{u}, \boldsymbol{\tau}$) for vector and tensor fields, and subscripts (e.g. u_i, τ_{kl}) to designate vector and tensor components in a Cartesian coordinate system.
Overdots are used to indicate time derivatives (e.g., $\dot{\boldsymbol{u}} = \partial \boldsymbol{u}/\partial t, \ddot{\boldsymbol{u}} = \partial^2 \boldsymbol{u}/\partial t^2$) and a comma between subscripts is used for spatial derivatives (e.g., $u_{i,j} = \partial u_i/\partial x_j$). Moreover, we work in the infinitesimal strain framework.
The summation convention for repeated subscripts is followed throughout (e.g., $a_i b_i = a_1 b_1 + a_2 b_2 + a_3 b_3 = \boldsymbol{a} \cdot \boldsymbol{b}$) and frequent use is made of the Kronecker symbol δ_{ij}:

$$\delta_{ij} = 0 \text{ for } i \neq j \text{ and } \delta_{ij} = 1 \text{ for } i = j$$

Latin Alphabet

b	yield surface shape parameter of Cyberquake law
$\mathbf{c}$	fourth order tensor of the generalized Hooke's law
c_{ijkl}	$ijkl$th component of the fourth order tensor of the generalized Hooke's law
c_H	hysteresis scale factor
c	cohesion
$E(\mathbf{x})$	objective function
$\mathbf{F}$	layer matrix
$\mathbf{F}^{ext}$	External force vector
$\mathbf{f}$	motion-stress vector, in Section 1.2
$\mathbf{f}$	body forces vector, in Section 1.1
f_i	ith component of body forces vector
f	frequency
f_c	characteristic frequency of a source function
F_{bb}	backbone curve function
G	shear modulus
G_{sec}	secant shear modulus

G_{np}	Green tensor representing the nth component of a displacement generated by a unit impulse in the p-direction
H_{obs}	observed spectral ratio
H_{the}	theoretical spectral ratio
i	square root of minus one
i_ξ	takeoff angle
J_e	jacobian of a spectral element
$\mathbf{K}$	stiffness matrix
L_i	ith layer of a soil column
$\mathbf{M}$	mass matrix
$\boldsymbol{m}$	moment density tensor
M_0	seismic moment
N_i^{par}	number of bit of the inverted parameter par
N_{pop}^{MC}	number of Monte Carlo population
N_{ind}^{MC}	number of individuals in Monte Carlo population
N_{bes}^{MC}	number of best individuals found in Monte Carlo population
N_{pop}	number of genetic algorithm population
N_{ind}	number of individuals in a genetic algorithm population
n_i	ith component of the unit vector normal to a surface
$\mathbf{P}$	propagator matrix
p	ray parameter
Q	quality factor
S	surface of a solid
$\mathbf{T}$	traction vector
T_i	ith component of traction vector
t	time variable
$\mathbf{u}$	displacement vector
$\mathbf{U}$	discretized displacement vector
u_i	ith component of displacement vector
V	volume of a solid
$\mathbf{v}_\alpha$	eigen vector of a matrix
$\mathbf{v}$	arbitrary virtual displacement
$\mathbf{w}$	constant weighting vector for the Thomson-Haskell propagator matrix method, in Section 1.2
$\mathbf{w}$	shape function in the spectral elements method, in Chapter 4

w	weighting factor for numerical integration
w_i	ith component of the constant weighting vector
x	x component of a Cartesian coordinate system
$\mathbf{x}$	vector of unknown parameters to be inverted
y	y component of a Cartesian coordinate system
z	z component of a Cartesian coordinate system
z_{ref}	reference level for the exponential for the Thomson-Haskell propagator matrix method

Greek Alphabet

α	P-wave velocity
β	S-wave velocity
β^*	complex S-wave velocity
β	plastic compressibility parameter of Cyberquake law, in Table 3.1
β	Newmark integration parameter, in Equation 4.5 only
ϵ_{ij}	ijth component of strain tensor
η	vertical slowness for S waves, in Subsection 1.2.2
η	viscosity of a material, in Subsection 1.2.3
η	local coordinate of the reference square, in Chapter 4
δ	dip angle
Δt	time step
γ	shear strain
γ	Newmark integration parameter, in Equation 4.5 only
$\gamma^{ela,his,mob}$	domain of elasticity, hysteresis and mobilisation of Cyberquake law
λ_α	eigenvalue associated to the eigen vector $\mathbf{v}_\alpha$
λ	Lamé modulus
λ	rake angle, in Chapter 4
λ_{min}	Minimal wavelength to be accurately propagated in a numerical model
μ	Lamé modulus, i.e., shear modulus
μ^*	complex shear modulus
μ_{sec}	secant shear modulus
ν_j	jth component of the fault normal vector
ν	Poisson ratio
ω	angular frequency
φ	internal friction angle
φ_s	strike angle

ψ	dilatancy angle
π	mathematical constant whose value is the ratio of any circles circumference to its diameter in Euclidean space
θ	incidence angle of an incoming wave
ρ	density of a medium
σ_{c0}	critical initial stress of Cyberquake law
τ_{ij}	ijth component of stress tensor
τ_s	time shift of a source function
ξ	vertical slowness for P waves, in Subsection 1.2.2
ξ	damping ratio, in Subsection 1.2.3, Chapter 2 and 3
ξ	local coordinate of the reference square, in Chapter 4
$\boldsymbol{\xi}$	general position on a fault

Introduction

The world of seismology has experienced a remarkable evolution during the twentieth century. The pioneer works of Gutenberg, Lamb, Rayleigh or Richter followed by those of Aki, Bouchon, Kanamori, Richards and many others gave birth to strong fundamental basis used worldwide everyday to determine earthquakes' magnitude, source effects, path effects and site effects.

This thesis, grain of sand within the Earth created by those seismologists, mainly deals with the site effects generated by the shallow soil structure as shown in Figure 1 and with numerical methods used to tackle two or three-dimensional problems.

Site effects are of great importance in seismology and earthquake engineering because they modify the frequency content of the incident wave and lead to an amplification of the wave propagating inside the site (e.g., soft sedimentary bassin). As a results, the damage pattern of the engineering structures is often linked to the subsurface geology. For a long time, site effects during strong ground motions have been considered as linear elastic in term of the stress-strain relation by the seismologists. In the meantime, geotechnical earthquake scientists have demonstrated by laboratory tests that the stress-strain relation for soft soils could be nonlinear for large strain levels. Nowadays, both communities agree to say that during strong ground motions, nonlinear site effects are present (in order to fix mind, an overview of the domains of behavior for soft soils is shown in Figure 2 (e.g., Ishihara, 1996)).

With the deployment of vertical arrays, detailed wave propagation analyses and the assessment for quantitative physical parameters such as shear-wave velocity, pressure-wave velocity and damping factors with respect to shear strain levels are now possible through different inversion techniques.

The first part of this manuscript deals with inverse analysis methodology to determine one-dimensional (1D) soil structure at borehole stations. The second part deals with high performance numerical tools to simulate 1D/2D and 3D site effects.

Chapter 1 exposes the fundamental theorems used in dynamic elasticity; the mathematical model used to resolve the direct problem of plane waves propagating in a stack of homogeneous layers; and finally, the genetic

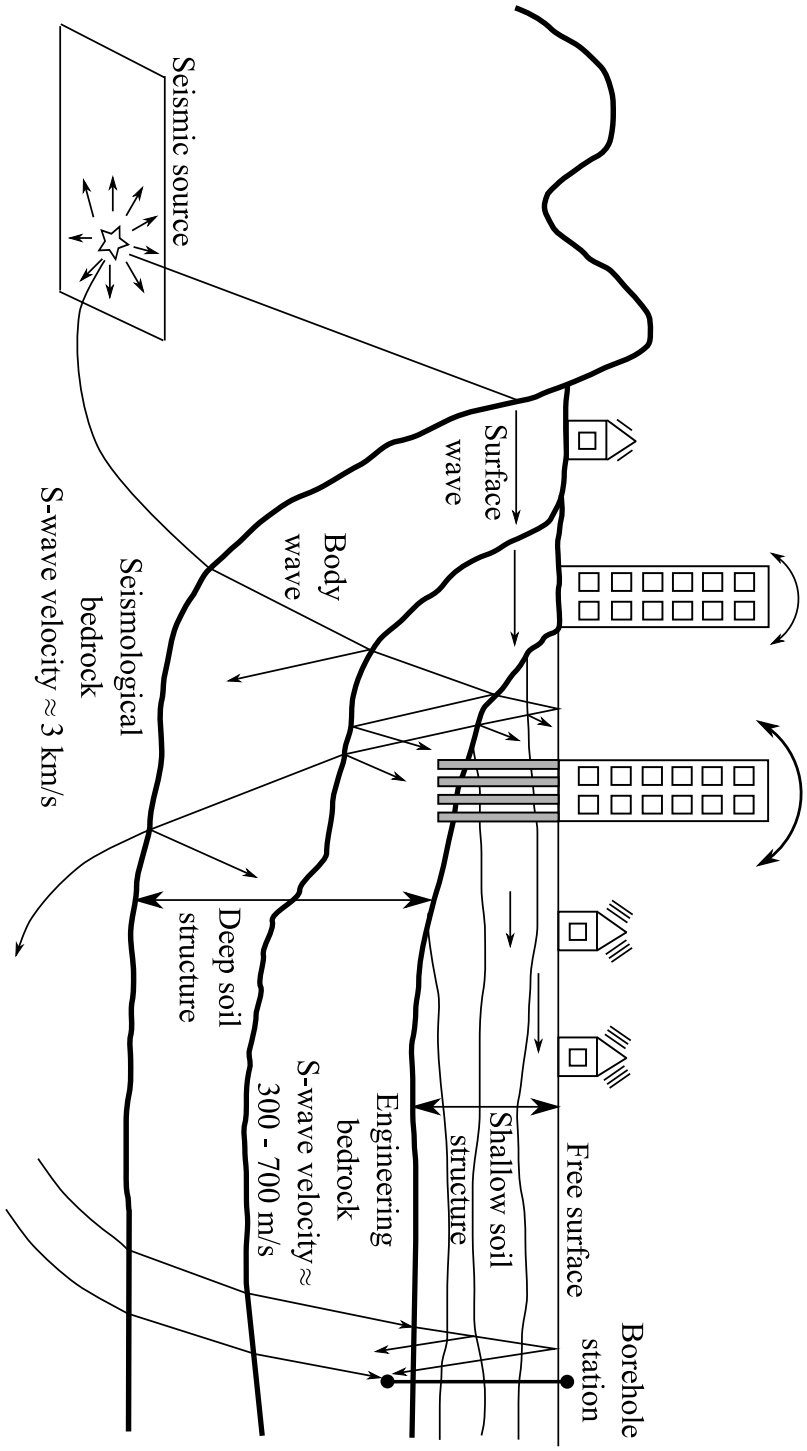

Figure 1: Shematization of seismic wave propagation from source to site.

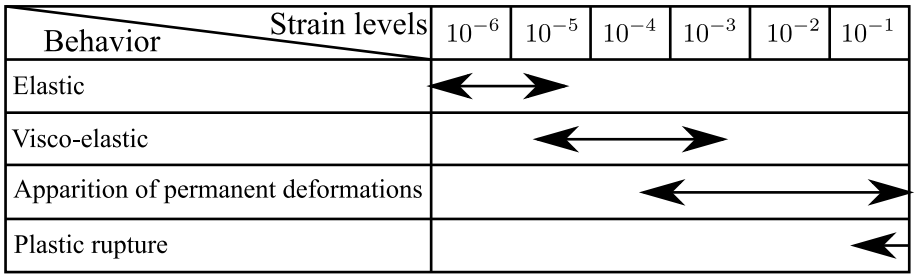

Figure 2: Domains of behavior of soft soils in function of the strain levels (e.g., Ishihara, 1996).

algorithm method used to inverse model parameters by using borehole data.

Chapter 2 applies the inversion method by genetic algorithm in order to quantify the nonlinear response (in term of observed equivalent linear parameters) of a borehole station based on a one-dimensional inversion during the 2005 West off Fukuoka Prefecture earthquake.

Chapter 3 summarizes the different mathematical models used to represent the stress-strain behavior of cyclically loaded soils and simulates the nonlinear response of the Fukuoka soil column by finite elements using a simple and an advanced constitutive nonlinear law.

Chapter 4 verifies the proper development of 1D, 2D and 3D spectral elements codes. The verification is done by comparing the numerical results with the theoretical ones or with other numerical methods.

Part I

Inverse Analysis Methodology to Determine Borehole Soil Structure

Chapter 1

Inversion of Borehole Soil Structure: Theory

Inverse problems often occur in many branches of science and mathematics where the values of some model parameters must be obtained from the observed data. By opposition to well-posed problems, inverse problems are often ill-posed. A well-posed problem as defined by Hadamard (1902) is a mathematical model of physical phenomenon which has the following properties:

1. a solution exists;
2. the solution is unique;
3. the solution depends continuously on the data, in some reasonable topology.

Even if inverse problems may break the above-mentionned properties 2 and 3, it is still useful to solve them either to consolidate or refine some model parameters obtained via in-situ or laboratory tests or to find mathematical solutions which can then be discussed on a physical point of view.

Among the different inverse problems which exist in seismology (e.g., inversions of Spectral Amplitude of Surface Wave (SASW), H/V inversions, source inversion, etc.), we tackle in this thesis the one used to quantify site effects via borehole station installed in sedimentary basin whose depth ranges from few meters to several hundreds of meters.

In the following, we present in Section 1.1 the fundamental theorems used in dynamic elasticity, then the Section 1.2 exposes the mathematical model used to solve the direct problem of plane waves propagating in a stack of homogeneous layers and finally we present in Section 1.3 the genetic algorithm method used to inverse model parameters by using borehole station data.

1.1 Fundamentals in Elastic Waves Propagation

Readers are referred to Aki and Richards (2002) to have a good grasp of basic theorems in dynamic elasticity and waves propagation in the Earth. We only remind without demonstration the fundamental equations which are the cornerstone of this thesis.

To analyze the distorsion of a medium, whether it be solid or fluid, elastic or inelastic, we use the *infinitesimal strain tensor* defined in a Cartesian coordinate system (x_1, x_2, x_3) as

$$\epsilon_{ij} = \frac{1}{2}(u_{i,j} + u_{j,i}), \tag{1.1}$$

with ϵ_{ij} the ijth component of strain tensor and u_i the ith component of displacement. A comman between subscripts is used for spatial derivatives (e.g., $u_{i,j} = \partial u_i / \partial x_j$).

To analyze the internal forces acting mutually between adjacent particles within a continuum, we use the concepts of *traction* and *stress tensor* related by

$$T_i = \tau_{ij} n_j, \tag{1.2}$$

with T_i the ith component of the traction vector acting on the plane of normal $\mathbf{n}$, τ_{ij} the ijth component of stress tensor and n_j the jth component of the unit vector normal to the surface where acts the traction $\mathbf{T}$. We note that in seismology, the stress tensor is often denoted by $\boldsymbol{\tau}$ whereas in geotechnical engineering or in mechanics of continuous media, it is denoted by $\boldsymbol{\sigma}$. We choose the seismological notation for this thesis.

To obtain the equation of motion of a general particle, we equate the rate of change of momentum of particles constituting a volume V with surface S to the forces acting on these particles as

$$\frac{\partial}{\partial t} \int\int\int_V \rho \frac{\partial \mathbf{u}}{\partial t} dV = \int\int\int_V \mathbf{f} + \int\int_S \mathbf{T} dS, \tag{1.3}$$

where ρ is the bulk density of the media.

By applying Gauss's divergence theorem which gives

$$\int\int_S T_i dS = \int\int_S \tau_{ij} n_j dS = \int\int\int_V \tau_{ij,j} dV, \tag{1.4}$$

we find for a general volume V that

$$\int\int\int_V (\rho \ddot{u}_i - f_i - \tau_{ij,j}) dV = 0. \tag{1.5}$$

This integrand must be zero wherever it is continuous, otherwise a volume V could be found that violates Equation (1.5), hence we obtain the equation of motion of a general particle

$$\rho \ddot{u}_i = f_i + \tau_{ij,j}. \tag{1.6}$$

The Equation (1.6) is the key equation for wave propagation. We note that the spatial derivative here should be carried out using an Eulerian approach because of the use of the Gauss's divergence theorem in Equation (1.4). However, as shown by Aki and Richards (2002, Chap. 2 Box 2.3), in seismology, the distinction between Lagrangian and Eulerian approaches rarely needs to be made since spatial fluctuations in the displacements, velocities, accelerations, strains and stresses have wavelengths much greater than their amplitude. Consequently, it makes no practical difference whether a spatial gradient is evaluated at a fixed positon (Euler) or for a particular particle (Lagrange), and differentation with respect to x_j will henceforth be assumed.

If the medium is linear elastic, then the generalization of Hooke's law can be used to express the stress tensor as a linear combination of all components of the strain tensor as

$$\tau_{ij} = c_{ijkl}\epsilon_{kl}. \tag{1.7}$$

Since both stress τ_{ij} and strain ϵ_{kl} are second-order tensors, it follows that c_{ijkl} is a fourth-order tensor which consists of $3^4 = 81$ material constants. Using the symmetries of the stress and strain tensors (i.e., $\tau_{ij} = \tau_{ji}$ and $\epsilon_{kl} = \epsilon_{lk}$), the number of 81 material constants is reduced to 36 under the symmetric condition of $c_{ijkl} = c_{jikl} = c_{ijlk} = c_{jilk}$. Using the thermodynamic argument (i.e., $c_{ijkl} = c_{klij}$) the number of independent components in $\mathbf{c}$ is reduced to 21. It can be shown (e.g., Jeffreys and Jeffreys, 1972; Chen and Mizuno, 1990) that the most general isotropic fourth-order tensor has the form

$$c_{ijkl} = \lambda\delta_{ij}\delta_{kl} + \mu(\delta_{ij}\delta_{jl} + \delta_{il}\delta_{jk}), \tag{1.8}$$

with λ and μ the Lamé moduli. The stress-strain relation becomes

$$\tau_{ij} = \lambda\delta_{ij}\epsilon_{kk} + 2\mu\epsilon_{ij}, \tag{1.9}$$

and the equation of motion presented in Equation (1.6) becomes

$$\rho\ddot{u}_i = f_i + (\lambda + \mu)u_{j,ji} + \mu u_{i,jj}. \tag{1.10}$$

The linear elastic stress-strain relation of Equation (1.9) is however an idealized behavior; the stresses and strains occuring within a propagating wave can lead to irreversible changes in the microscopic structures of the medium and dissipative work may also be done on grain boundaries. As a results, wave amplitude attenuates through a variety of processes that can be summarized macroscopically as "internal friction". The gross effect of this internal friction is often summarized by the dimensionless quantity Q in seismology or ξ in geotechnical engineering with the relation $\xi = \frac{1}{2Q}$. Details on wave propagating in an attenuating medium can be found in Aki and Richards (2002, Chap. 5). A panel of the different methods used to take into account this internal friction is exposed in Chapter 3 Section 3.1.

These phenomena (irreversible changes and dissipative work) have been clearly identified by laboratory tests (e.g., Seed and Idriss, 1970b; Seed et al., 1986); and it is now recognized in seismology that during strong ground motions, the stress-strain relation becomes nonlinear in soft soils (e.g., Chin and Aki, 1991; Darragh and Shakal, 1991; Aki, 1993; Field et al., 1997; Su et al., 1998; Cultrera et al., 1999; Frankel et al., 2002; Aki, 2003; Bonilla et al., 2005; De Martin et al., 2010). This assumption was for long time accepted by the geotechnical society and since the 90s, an atmosphere of cooperation between seismological and geotechnical communities is visible in order to better understand the complex soils behavior at the subsurface.

The different approaches developped in the geotechnical literature to tackle more complex stress-strain relationships are exposed in Section 3.1.

1.2 Plane Waves in a Stack of Homogeneous Layers

1.2.1 Model's assumptions

The mathematical model used in this thesis to solve the direct problem of waves propagation in a sedimentary basin is based on two fundamental assumptions.

- The first one is to consider the Earth (in our case, a sedimentary basin) as a stack of welded homogeneous horizontal layers as shown in Figure 1.1. This assumption is justified by two blind-prediction experiments conducted by the IASPEI/IAEE Joint Working Group on Effects of Surface Geology on Strong Motions showing that the geological structure is more important than the model dimension (e.g., Cramer and Real, 1992; Mirodikawa, 1992). This assumption is very acceptable for flat basins or in the middle of curved basins whereas it becomes debatable close to the edges of basins as shown by Bard and Gariel (1986).

- The second assumption is to avoid details of seismic source by considering only the case of a plane wave incident on the stack of homogeneous layers. This assumption may be quite good in practice for investigating waves at great distances from their source. In Chapter 2 where we study a strong ground motion ($M_w = 6.6$) using a borehole station, this assumption is justified because the borehole station is located 24 km away from the epicenter.

Moreover, for the resolution of the direct problem, we consider the medium as isotropic linear elastic governed by Equation (1.10).

The coordinate system associated with the mathematical model is shown in Figure 1.1. The plane (x, z) is associated with the component u_x and u_z

of the coupled P- and SV-waves. The y axis corresponds to the uncoupled SH-waves of component u_y.

For the steady-state plane waves solution of Equation (1.10) and the explanation of the different types of waves present in the Earth (e.g., P-wave, S-wave, Rayleigh wave, etc.), the reader is referred to Aki and Richards (2002). The following subsection describes the mathematical model used to solve the direct problem.

1.2.2 Thomson-Haskell propagator matrix method

The Thomson-Haskell propagator matrix method is a frequency domain method due to Thomson (1950) and corrected by Haskell (1953) which has been extensively used in surface-wave analysis. It is a special case of the propagator matrix method introduced to seismology by Gilbert and Backus (1966). The Thomson-Haskell method make use of motion-stress equations in order to relate the motion-stress vector at depth z to the one at depth z_0 via the propagator matrix computed using the layers properties between z and z_0 (see Figure 1.1 for notation). It is worth noticing that the Thomson-Haskell may suffer from numerical instabilities for anisotropic media or Rayleigh wave modes (e.g., Harvey, 1981; Castaings and Hosten, 1994); but these instabilities can be eliminated.

The motion-stress equation is obtained by combining the equations of motion with the constitutive relation in such a way that only first-order depth derivatives of stress and displacement are needed.

For example, the equation of motion for the SH-waves case (with $\tau_{yy,y} = 0$) which reduces to

$$\rho \ddot{u_y}(x,z,t) = \tau_{yz,z}(x,z,t) + \tau_{yx,x}(x,z,t) \tag{1.11}$$

can be combined with the constitutive relation which becomes for SH waves $\tau_{yz} = \mu \partial u_y/\partial z$, $\tau_{yx} = \mu \partial u_y/\partial x$ to give the system

$$\frac{d\mathbf{f}}{dz} = \mathbf{A}\mathbf{f}, \tag{1.12}$$

with

$$\mathbf{f} = \mathbf{f}(z) = \begin{pmatrix} u_y \\ \tau_{yz} \end{pmatrix} \tag{1.13}$$

and

$$\mathbf{A} = \begin{pmatrix} 0 & \mu^{-1} \\ \omega^2(\mu p^2 - \rho) & 0 \end{pmatrix} \tag{1.14}$$

where ω is the angular frequency, p the ray parameter, t the time and ρ the bulk density. The dependence in x and t of $u_y(x,z,t)$ is simply $\exp[i\omega(px-t)]$ where i is the square root of minus one.

Equations of type $d\mathbf{f}/dz = \mathbf{A}\mathbf{f}$ are coupled first-order differential equations whose solutions are well-known (e.g., Gantmatcher, 1959). If $\mathbf{v}^\alpha$ is the

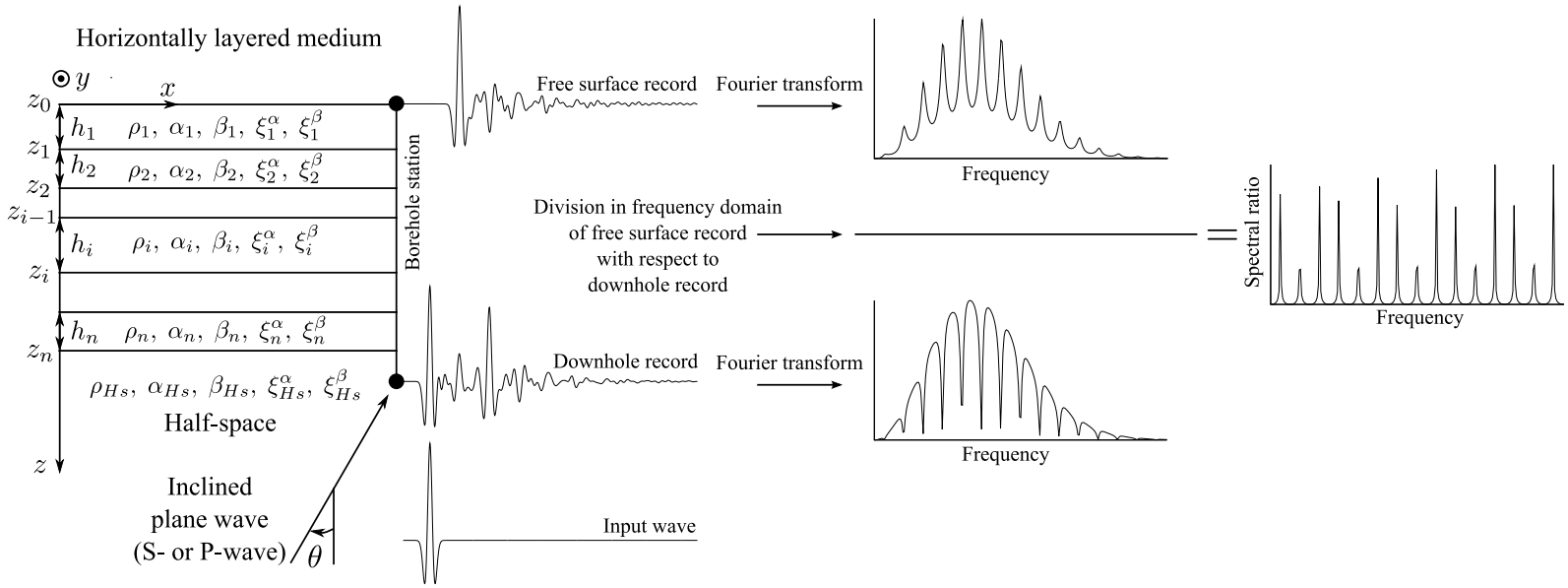

Figure 1.1: Horizontally layered medium used for computation of spectral ratio in inverse problems. Within each layer, parameters are constant. An example of propagation of a vertically incident SH wave is shown using a Ricker wavelet as input wave. The spectral ratio is the division in the frequency domain of the amplitude of the free surface record by the downhole record.

αth eigenvector of $\mathbf{A}$ and λ^α its associated eigenvalue (α =1, 2 for SH case); then a solution of Equation (1.12) can be written as

$$\mathbf{f} = \mathbf{v}^\alpha \exp[\lambda^\alpha (z - z_{ref})] \tag{1.15}$$

where z_{ref} is a reference level for the exponential. The most general solution $\mathbf{f}$ is a linear combination of the type

$$\mathbf{f} = \mathbf{F}\mathbf{w} \tag{1.16}$$

where $\mathbf{F}$ is a matrix whose columns consist in solutions of type (1.15) and $\mathbf{w}$ is a constant weighting vector.

The two eigenvalues of $\mathbf{A}$ are

$$\lambda^{1,2} = \pm i\omega\sqrt{1/\beta^2 - p^2} = \pm\eta, \tag{1.17}$$

where β is the S-wave velocity and η is the vertical slowness for S waves. The corresponding eigenvectors are

$$\begin{pmatrix} 1 \\ \pm i\omega\mu\eta \end{pmatrix}. \tag{1.18}$$

Hence, the general solution of Equation (1.12) for SH case is

$$\mathbf{f} = \mathbf{F}\mathbf{w} = \tag{1.19}$$

$$\begin{pmatrix} \exp[+i\omega\eta(z - z_{ref})] & \exp[-i\omega\eta(z - z_{ref})] \\ +i\omega\mu\eta \exp[+i\omega\eta(z - z_{ref})] & -i\omega\mu\eta \exp[-i\omega\eta(z - z_{ref})] \end{pmatrix} \begin{pmatrix} \mathrm{w}_1 \\ \mathrm{w}_2 \end{pmatrix} \tag{1.20}$$

where the $\exp[+i\omega\eta(z - z_{ref})]$ has the physical meaning of a downgoing SH-wave and $\exp[-i\omega\eta(z - z_{ref})]$ the meaning of an upgoing SH-wave (we remember that the z-axis points downward as shown in Figure 1.1). $\mathbf{F}$ is the well-known *layer matrix* in seismology.

The propagator matrix $\mathbf{P}(z, z_0)$ relates the motion-stress vector at depth z to the one at depth z_0 as

$$\mathbf{f}(z) = \mathbf{P}(z, z_0)\mathbf{f}(z_0). \tag{1.21}$$

Thus $\mathbf{P}(z, z_0)$ generates the motion-stress vector at z by operating on the vector at z_0. An interesting property of $\mathbf{P}(z, z_0)$ is that

$$\begin{aligned} \mathbf{f}(z_2) &= \mathbf{P}(z_2, z_1)\mathbf{f}(z_1) \\ &= \mathbf{P}(z_2, z_1)\mathbf{P}(z_1, z_0)\mathbf{f}(z_0). \end{aligned} \tag{1.22}$$

Hence, for a layered medium as shown in Figure 1.1, the propagator matrix $\mathbf{P}(z, z_0)$ for $z_{k-1} < z < z_k$ can be written as

$$\mathbf{f}(z) = \mathbf{P}(z, z_{k-1})\mathbf{P}(z_{k-1}, z_{k-2}) \cdots \mathbf{P}(z_1, z_0)\mathbf{f}(z_0) = \mathbf{P}(z, z_0)\mathbf{f}(z_0) \tag{1.23}$$

Providing the fact that z and z_0 are in the same homogeneous layer,

$$\mathbf{P}(z, z_0) = \mathbf{F}(z)\mathbf{F}^{-1}(z_0). \tag{1.24}$$

For SH case with $\mathbf{F}(z)$ given by Equation (1.20),

$$\mathbf{P}(z, z_0) = \begin{pmatrix} \cos[\omega\eta(z - z_0)] & \frac{1}{\omega\mu\eta}\sin[\omega\eta(z - z_0)] \\ -\omega\mu\eta\sin[\omega\eta(z - z_0)] & \cos[\omega\eta(z - z_0)] \end{pmatrix}. \tag{1.25}$$

For P-SV case, the layer matrix is given by

$$\mathbf{F} = \mathbf{E}\mathbf{\Lambda}, \tag{1.26}$$

with

$$\mathbf{E} = \begin{pmatrix} p & 1 & p & 1 \\ \xi & -p/\eta & -\xi & p/\eta \\ 2i\omega\rho\beta^2 p\xi & i\omega\rho(1 - 2\beta^2 p^2)/\eta & -2i\omega\rho\beta^2 p\xi & -i\omega\rho(1 - 2\beta^2 p^2)/\eta \\ i\omega\rho(1 - 2\beta^2 p^2) & -2i\omega\rho\beta^2 p & i\omega\rho(1 - 2\beta^2 p^2) & -2i\omega\rho\beta^2 p \end{pmatrix} \tag{1.27}$$

and

$$\mathbf{\Lambda} = \begin{pmatrix} \exp[+i\omega\xi\overline{z}] & 0 & 0 & 0 \\ 0 & \exp[+i\omega\eta\overline{z}] & 0 & 0 \\ 0 & 0 & \exp[-i\omega\xi\overline{z}] & 0 \\ 0 & 0 & 0 & \exp[-i\omega\eta\overline{z}] \end{pmatrix}, \tag{1.28}$$

where ξ is the vertical slowness for P waves equal to $\sqrt{1/\alpha^2 - p^2}$, α is the P-wave velocity, β is the S-wave velocity and $\overline{z}$ is equal to $(z - z_{ref})$. The propagator matrix for P-SV case is more complex than for the SH case and the reader is refered to Aki and Richards (2002, Chap. 9, Box 9.1) for its expression.

The Equation (1.21) is the key formula for 1-D wave propagation along borehole sensors since, knowing layers parameters, it allows theoretical computation of the free surface waveform knowing the downhole waveform or *vice-versa*. As for inverse problems, the objective will be to come back to the layers parameters knowing the free surface and downhole waveform.

The Thomson-Haskell theory also allows to deconvolve a wave recorded at a point in order to come back to the incident wave at the borehole station (i.e., the wave formed by the source and the path effects). Deconvolution formulae for SH and P-SV problem are given in Appendix A.

Finally, it is interesting to note that for the different types of incoming body waves on a horizontally layered medium, five spectral ratios can be of particular interest, namely:

- the spectral ratio in the y-direction for an incoming SH-wave;
- the spectral ratio in the x-direction for an incoming SV-wave;

- the spectral ratio in the z-direction for an incoming SV-wave;
- the spectral ratio in the x-direction for an incoming P-wave;
- and the spectral ratio in the z-direction for an incoming P-wave.

In practice, the incoming wave is often assumed to travel vertically so that the theoretical spectral ratio for an incoming SV-wave in the x-direction is equivalent to the spectral ratio for an incoming SH-wave in the y-direction. The use of several spectral ratios for inversion of soil structure and incidence angle of the incoming wave has been first performed by Satoh (2006).

1.2.3 Attenuation model for the Thomson-Haskell method

The above formulation was derived for a linear elastic stress-strain relationship without attenuation. The addition of attenuation in the Thomson-Haskell Method can be done by using the viscoelastic Kelvin-Voigt solid which allows the use of damping through a complex shear modulus. A Kelvin-Voigt solid (subjected to a one-dimensional vertically incident shear-wave) has a stress-strain relationship of the form (in the SH case)

$$\tau_{yz} = \mu\gamma_{yz} + \eta\frac{\partial\gamma_{yz}}{\partial t}. \tag{1.29}$$

where τ_{yz} is the shear stress, γ_{yz} the shear strain, and η the viscosity of the material. The viscous damping, by virtue of its mathematical convenience, is often used to represent the dissipation of elastic energy converted to heat but also to represent the hysteresis loop of soils under shear stress. For a harmonic shear strain loading of the form

$$\gamma_{yz} = \gamma_0 \sin\omega t, \tag{1.30}$$

the shear stress will be

$$\tau_{yz} = \mu\gamma_0 \sin\omega t + \omega\eta\gamma_0 \cos\omega t. \tag{1.31}$$

In the plane $\tau - \gamma$, these two equations form an ellipse. The elastic energy dissipated in a single cycle is given by the area of the ellipse as

$$A_{loop} = \int_{t_0}^{t_0+2\pi} \tau\frac{\partial\gamma}{\partial t}dt = \pi\eta\omega\gamma_0^2. \tag{1.32}$$

The damping ratio, ξ, is defined as the ratio of the elastic energy dissipated in a single cycle (A_{loop}) to the peak energy stored in one cycle ($W = \frac{1}{2}\mu\gamma_0^2$) via a factor $\frac{1}{4\pi}$. Thus

$$\xi = \frac{1}{4\pi}\frac{A_{loop}}{W} = \frac{1}{4\pi}\frac{\pi\eta\omega\gamma_0^2}{\frac{1}{2}\mu\gamma_0^2} = \frac{\eta\omega}{2\mu}. \tag{1.33}$$

In order to make the damping ratio frequency independent, the equivalent viscosity

$$\eta = \frac{2\mu}{\omega}\xi \tag{1.34}$$

can be used. We note that in geotechnical engineering, the damping ratio is noted ξ and is linked with the attenuation factor Q used in seismology by the relation

$$\xi = \frac{1}{2Q}. \tag{1.35}$$

For vertically incident SH-waves, the equation of motion simplifies to

$$\rho\ddot{u_y}(z,t) = \tau_{yz,z}(z,t). \tag{1.36}$$

Substituting Equation (1.29) into (1.36) with $\gamma_{yz} = \partial u_y/\partial z$ leads to the expression

$$\rho\ddot{u_y}(x,z,t) = \mu\frac{\partial^2 u_y}{\partial z^2} + \eta\frac{\partial^3 u_y}{\partial z^2 \partial t}. \tag{1.37}$$

For harmonic waves, the displacements can be written as

$$u_y(z,t) = U_y(z)\exp[i\omega t] \tag{1.38}$$

which, when substituted into the wave equation (1.37) yields the ordinary differential equation

$$(\mu + i\omega\eta)\frac{d^2U_y}{dz^2} = -\rho\omega^2 U_y \tag{1.39}$$

or

$$\mu^*\frac{d^2U_y}{dz^2} = -\rho\omega^2 U_y \tag{1.40}$$

where $\mu^* = \mu + i\omega\eta$ is the complex shear modulus. Using Equation (1.34) to eliminate the frequency dependence, the complex shear modulus can be written as

$$\mu^* = \mu + 2i\xi \tag{1.41}$$

and the complex shear-wave velocity as $\beta^* = \sqrt{\mu^*/\rho}$. An identical reasoning for complex primary-wave velocity can be done.

The use of complex wave velocities in the Thomson-Haskell propagator matrix method is a common way to take into account the damping in wave propagation. The influence of the damping on waves propagation in the frequency and time domain is shown in the Subsection 1.2.5.

1.2.4 Validation of the propagator code

The propagator code developped for inversion has been first validated with Kawase's code on direct problems (e.g., Kawase and Sato, 1992). Validation tests consist in propagating plane P, SV or SH waves with different incidence angles in the soil column presented in Table 1.1. Figure 1.2 to 1.7 compare

amplitude and phase of spectral ratio taken between free surface and 65 meters depth. The agreement between the two codes is excellent. The results are shown up to 20 Hz, however, the agreement is very good for higher frequencies as well.

Table 1.1: Soil column used to compare this study's propagator and Kawase's propagator. Damping factor (ξ_p or ξ_s) is frequency dependent of the type $\xi = \xi_0 f^{-a}$

No.	Depth (m)	P-wave velocity (m/s)	S-wave velocity (m/s)	ξ_0	a	Density (g/cm^3)
1	1	1195.3	150	0.05	0.4	1.80
2	2	1195.3	150	0.05	0.4	1.80
3	3	1195.3	150	0.05	0.4	1.80
4	4	1195.3	150	0.05	0.4	1.80
5	5	1203.2	151	0.05	0.4	1.80
6	6	1195.7	159	0.05	0.4	1.80
7	7	1210.7	161	0.05	0.4	1.80
8	9	1214.0	170	0.05	0.4	1.80
9	10	1676.5	197	0.05	0.4	1.80
10	11	1727.6	203	0.05	0.4	1.80
11	14	1699.5	226	0.05	0.4	1.80
12	15	1778.2	249	0.05	0.4	1.80
13	17	1798.1	361	0.05	0.4	1.80
14	19	1542.5	216	0.05	0.4	1.70
15	20	1635.3	229	0.05	0.4	1.70
16	21	1635.7	240	0.05	0.4	1.70
17	24	1574.4	231	0.05	0.4	1.70
18	25	1615.3	237	0.05	0.4	1.70
19	28	1729.9	331	0.05	0.4	1.90
20	30	1758.4	361	0.05	0.4	1.90
21	32	1719.5	368	0.05	0.4	1.90
22	34	1717.5	252	0.05	0.4	1.75
23	36	1729.9	331	0.05	0.4	1.75
24	37	1720.8	284	0.05	0.4	1.75
25	38	1775.6	331	0.05	0.4	1.90
26	39	1737.7	306	0.05	0.4	1.90
27	40	1729.9	331	0.05	0.4	1.90
28	42	1769.2	292	0.05	0.4	1.75
29	43	1711.3	262	0.05	0.4	1.75
30	45	1773.7	422	0.05	0.4	1.90
31	46	1789.2	405	0.05	0.4	1.90
32	47	1785.6	397	0.05	0.4	1.90

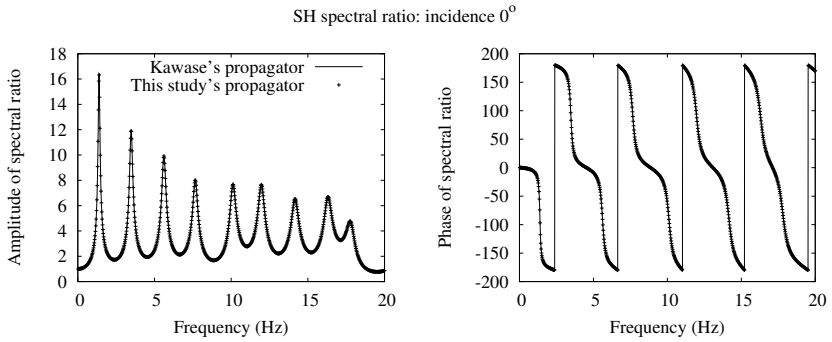

Figure 1.2: Comparison of this study's propagator and Kawase's propagator: y-component for a vertically incident SH-wave.

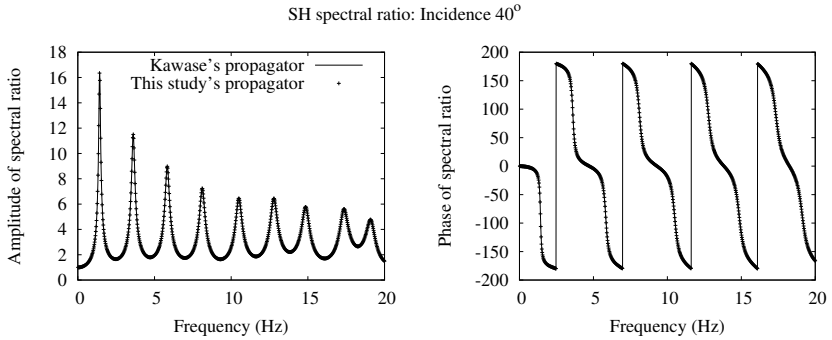

Figure 1.3: Comparison of this study's propagator and Kawase's propagator: y-component for a 40° incident SH-wave.

Table 1.1 – continued from previous page

No.	Depth (m)	P-wave velocity (m/s)	S-wave velocity (m/s)	ξ_0	a	Density (g/cm^3)
33	48	1710.9	292	0.05	0.4	1.80
34	50	1665.9	342	0.05	0.4	1.80
35	51	1718.1	382	0.05	0.4	1.80
36	54	1845.3	508	0.05	0.4	1.95
37	55	1851.4	521	0.05	0.4	1.95
38	56	1778.1	495	0.05	0.4	1.95
39	65	2335.0	650	0.05	0.4	2.00
40	∞	2335.0	650	0.05	0.4	2.00

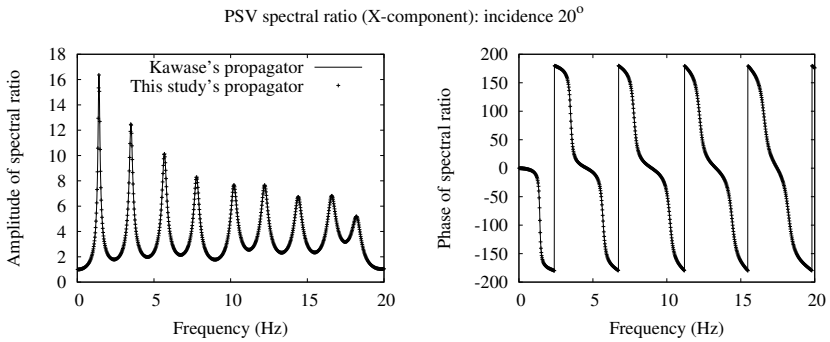

Figure 1.4: Comparison of this study's propagator and Kawase's propagator: x-component for a 20° incident SV-wave.

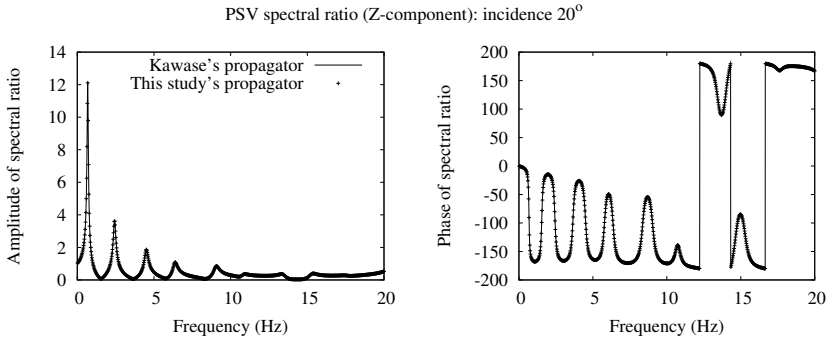

Figure 1.5: Comparison of this study's propagator and Kawase's propagator: z-component for a 20° incident SV-wave.

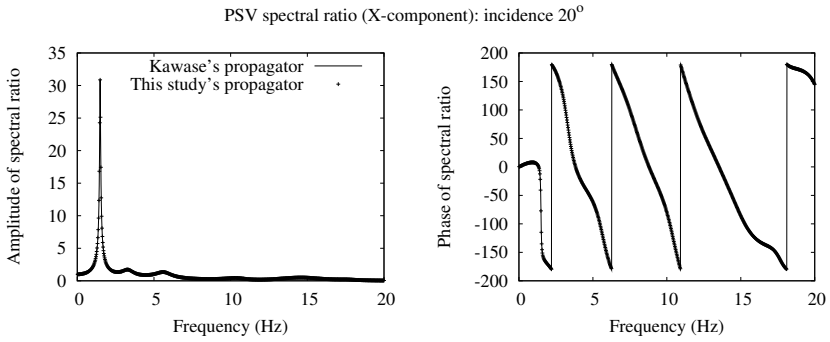

Figure 1.6: Comparison of this study's propagator and Kawase's propagator: x-component for a 20° incident P-wave.

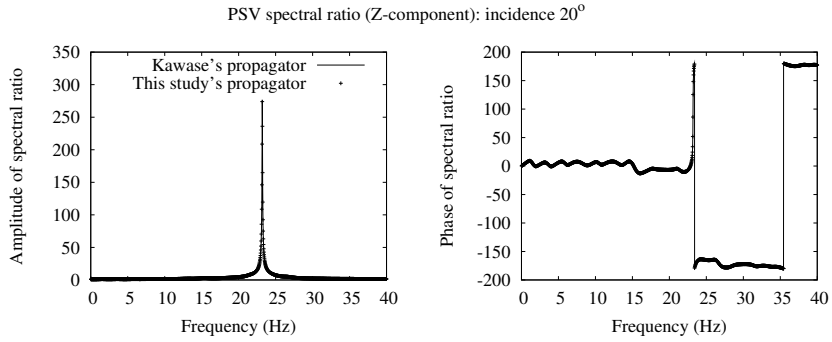

Figure 1.7: Comparison of this study's propagator and Kawase's propagator: z-component for a 20° incident P-wave.

1.2.5 Influence of wave velocity, damping and incidence angle on a spectral ratio

The influence on S-wave spectral ratios of the main parameters which govern the wave propagation in the Thomson-Haskell method (i.e., S-wave velocity, damping factors and incidence angle of the incoming wave) is investigated in this subsection. We note that the P-wave velocity has no influence on the S-wave spectral ratios. We also suppose that the thickness of the layers is fixed; it is justified for a borehole station since the well log allows to determine the thiknesses. This investigation will help

- to understand the discrepancy that could be seen between observed and theoretical spectral ratios;
- to better constrain the parameters to be inverted;
- to choose an appropriate objective function (i.e., cost function) during the inversion by genetic algorithm (cf. Section 1.3).

For this purpose, the soil column presented in Table 1.2 consists in five layers with increasing S-wave velocity overlying a half space. The influence of the S-wave velocity is investigated in the frequency and time domain by increasing or decreasing the S-wave velocity of one layer and keeping the other parameters to their reference value.

Table 1.2: Reference soil column used to investigate the influence of physical parameters on theoretical spectral ratios.

No.	Depth (m)	P-wave velocity (m/s)	S-wave velocity (m/s)	Damping factor (%)	Density (g/cm^3)
L01	10	173.2	100	1	1.8
L02	20	346.4	200	1	1.8
L03	30	519.6	300	1	1.8
L04	40	692.8	400	1	1.8
L05	50	866.0	500	1	1.8
L06	∞	1385.6	800	0	2.0

In the frequency domain, Figure 1.8 shows the influence of a decrease of 20 % of the S-wave velocity of the first layer on the SH spectral ratio taken between the free surface and the depth 50 m (a vertical incidence is assumed for the propagation). This figure exhibits three fundamental changes that the S-wave velocity can produce on a spectral ratio; the S-wave velocity has an influence on

- the location (along the frequency axis) of the resonant frequencies,

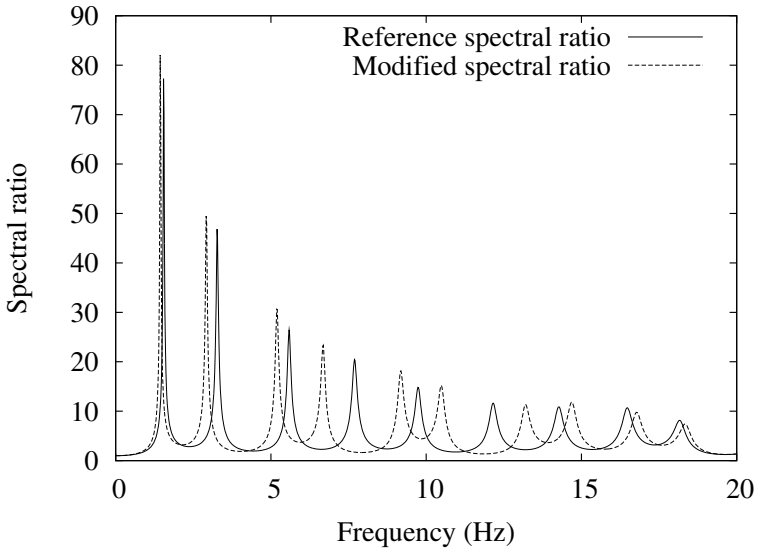

Figure 1.8: Influence of the decrease of the S-wave velocity of the first layer of Table 1.2 on the SH spectral ratio for a vertically incident wave.

- the amplitude of the resonant frequencies,
- the number of resonant frequencies in a given frequency range.

Moreover, when the S-wave velocity of a layer decreases, then, the location of resonant frequencies is shifted to lower frequencies or remains unchanged (i.e., a decrease of S-wave velocity cannot lead to an increase of the location of the resonant frequencies). On the contrary, an increase of the S-wave velocity of one or several layers leads to an increase of the location of the resonant frequencies. To have a full grasp of the influence of all the layers on each resonant frequency, a variation table that summarizes the amount of change in the location of resonant frequencies with respect to a change of S-wave velocity can be drawn as shown in Figure 1.9. Such a table allows to visualize how much a soil layer can influence the location of a resonant frequency. For example, we can see in Figure 1.9 that the layer L04 has low influence on the location of the resonant frequency F04. On the contrary, L01 influences quite much this frequency. An interesting property of a spectral ratio is also that the half space has no influence on the location of the resonant frequencies; in other words, only the soil paramaters in between the points used to compute the spectral ratio have an influence on it. This property can be seen mathematically from Equations (1.21) and (1.23) showing that the link between the motion-stress vector at depth z with the one at depth z_0 is the propagator matrix computed only with soil parameters

between depth z and z_0. The same kind of variation table can be computed to visualize the change in amplitude of the resonant frequencies.

In the time domain, the S-wave velocity has an influence on both the amplitude and the phase of the wave travelling through the soil layers. However, this influence also depends on the fundamental frequency of the input wave: if the fundamental frequency of the input wave is much lower than the fundamental frequency of the soil column, then a small variation of the S-wave velocity of a layer will not greatly affects the form of the output signal (this is not true when the fundamental frequency of the input wave is much larger than the fundamental frequency of the soil column since a small change in S-wave velocity can greatly affect the higher resonant frequencies of the soil column (cf. Figure 1.8)). As an example, Figure 1.10 shows an ouput waveform at the free surface when the incoming wave from the half space is a Ricker wavelet of order 2 with a pseudo-frequency of 5 Hz; Figure 1.11 represents the output of the same problem when the incoming wave from the half space is a Ricker wavelet of order 2 with a pseudo-frequency of 0.1 Hz.

The damping factors also have an influence on the shape of a spectral ratio. As shown in Figure 1.12, an increase of damping reduces the amplitude of the resonant frequencies. We note that small damping factors (i.e., smaller than 30% or 40%) have no influence on the location and the number of the resonant frequencies, however for very high damping factors, a small increase of the location of the resonant frequencies can be observed due to the fact that the damping factors contribute to the magnitude of the complex shear modulus in Equation (1.41). Besides, as shown for the influence of S-wave velocity, a variation table can be drawn to visualize how much the increase of the damping in one soil layer can affect a spectral ratio.

In the time domain, the damping factors have mainly an influence on the amplitude of the peaks of the time history if the damping is supposed to be small enough (cf. Figure 1.13). We can also note that since in the frequency domain, the damping factor ξ_i of the layer L_i could have or not an influence on the resonant frequency F_j, then the damping factor ξ_i of the layer L_i has a specific impact on the amplitude of the peak P_k of the time history: Figure 1.14 shows the impact of the increase to 5% of the damping factor of the layer L01 and L02.

Concerning the incidence angle of the incoming wave (cf. Figure 1.1 for definition), it also has an effect on the shape of a spectal ratio and consequently on the time history. Figure 1.15 shows spectral ratios for incidence angles of 0° (reference ratio), 30° and 60°. It can be observed that an increase of the incidence angle

- shifts the resonant frequencies to the high-frequency range (generally but not always, the higher the resonant frequency, the larger the shift toward the high frequencies);

	F01	F02	F03	F04	F05	F06
	1.54	3.27	5.59	7.69	9.74	12.16
L01	± 0.06	± 0.25	± 0.23	± 0.64	± 0.47	± 0.90
L02	± 0.06	± 0.02	± 0.29	± 0.12	± 0.39	± 0.29
L03	± 0.04	± 0.04	± 0.05	± 0.14	± 0.39	± 0.11
L04	± 0.04	± 0.08	± 0.06	± 0.02	± 0.08	± 0.08
L05	± 0.02	± 0.06	± 0.14	± 0.10	± 0.25	± 0.10
L06	± 0.00	± 0.00	± 0.00	± 0.00	± 0.00	± 0.00

Figure 1.9: Variation table of theoretical resonant frequencies with respect to S-wave velocity of a soil layer computed for a vertically incident S-wave using the velocity of Table 1.2. F followed by a number denoting a resonant frequency and L followed by a number denoting a layer (corresponding to Table 1.2). Float numbers indicate resonant frequencies' value. Vertical lines symbolically represent the original location of a resonant frequency Fi and horizontal lines located on the left-hand side and right-hand side of vertical lines quantitatively represent the amount of shift of the frequency Fi normalized by the height of the layer Lj with respect to the decrease or increase of the S-wave velocity of the soil layer Lj. Factors used to decrease or increase the S-wave velocity of a soil layer are 0.8 and 1.2, respectively. Float numbers quantitatively indicate the amount of shift.

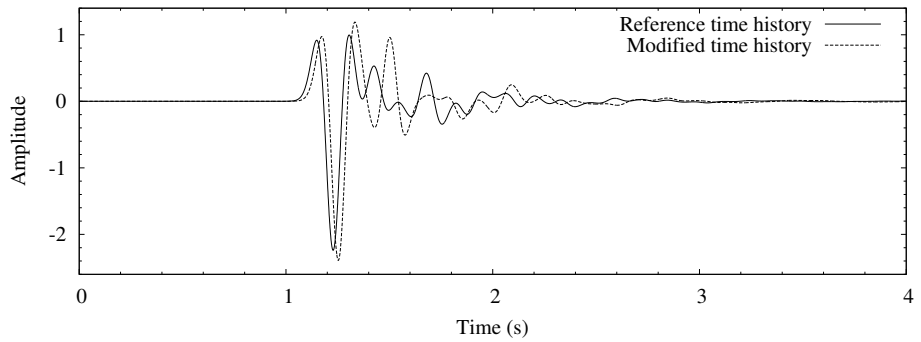

Figure 1.10: Influence of a 20% decrease of the S-wave velocity of the first layer of Table 1.2 on the SH time history for a vertically incident order 2 Ricker wavelet of pseudo-frequency 5.0 Hz. The free surface time history is shown.

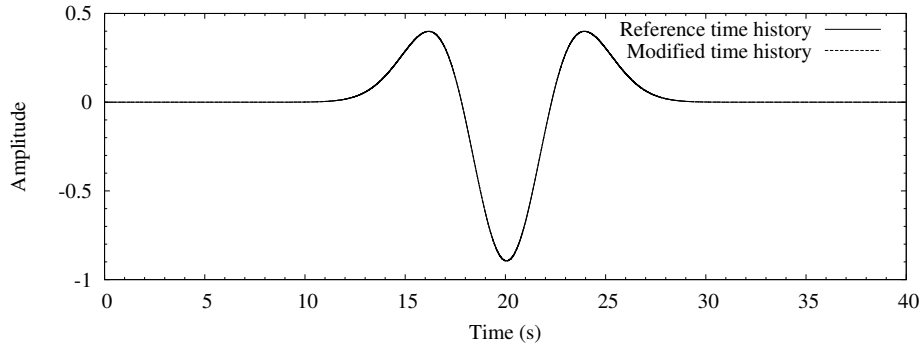

Figure 1.11: Influence of a 20% decrease of the S-wave velocity of the first layer of Table 1.2 on the SH time history for a vertically incident order 2 Ricker wavelet of pseudo-frequency 0.1 Hz. The free surface time history is shown.

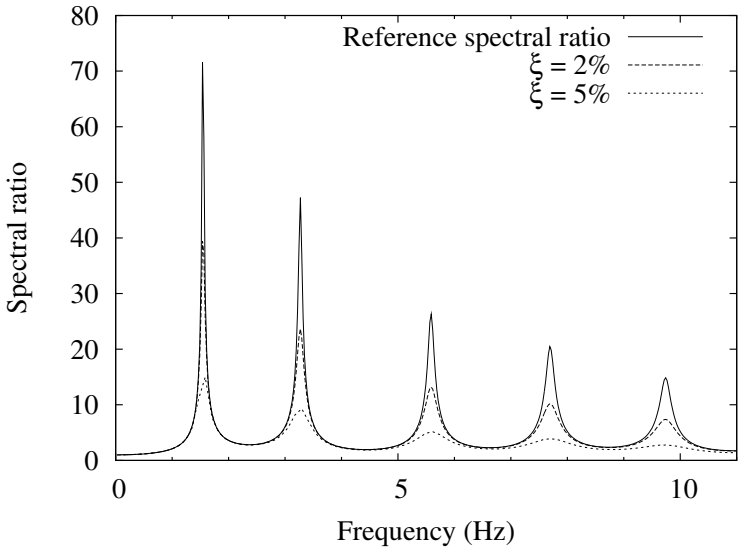

Figure 1.12: Influence of the increase of the damping factors of the layers L01 to L05 to 2% or 5% on the SH spectral ratio for a vertically incident wave.

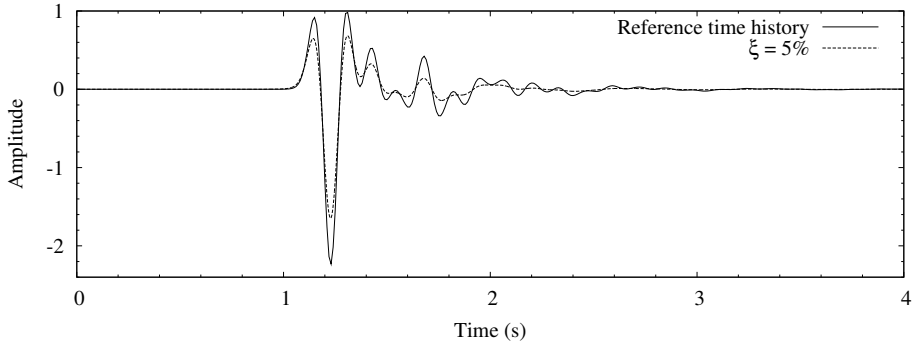

Figure 1.13: Influence of the increase of the damping factors of the layers L01 to L05 to 5% on the SH time history for a vertically incident wave. The free surface time history is shown.

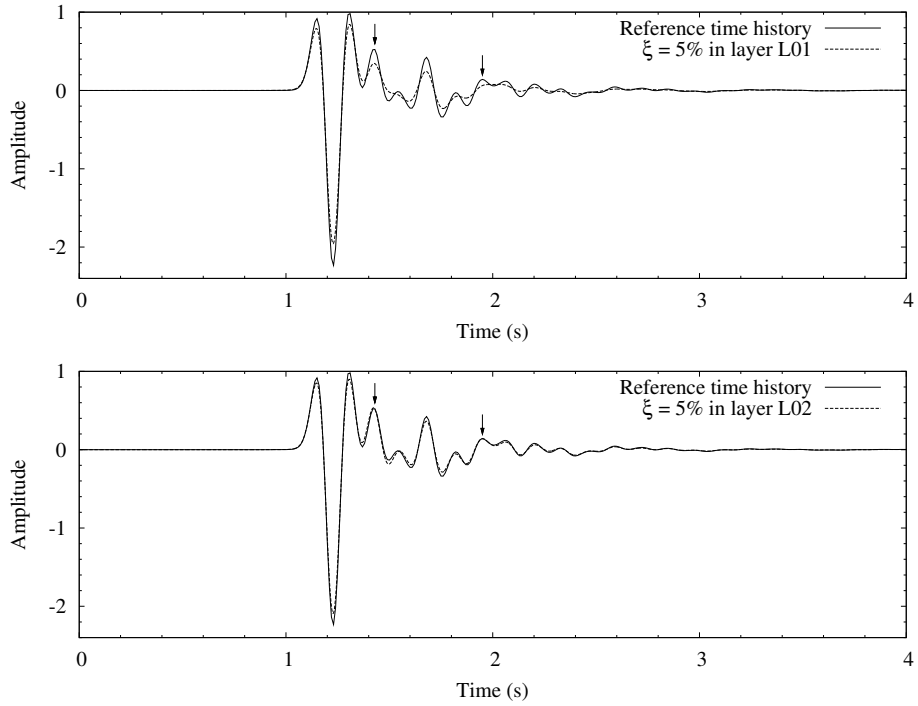

Figure 1.14: Influence of the increase of the damping factor of the layer L01 (top panel) or L02 (bottom panel) to 5% on the SH time history for a vertically incident wave. Arrows indicate some peaks of the time history where the damping factor of L01 and L02 have a different impact on their amplitude. The free surface time history is shown.

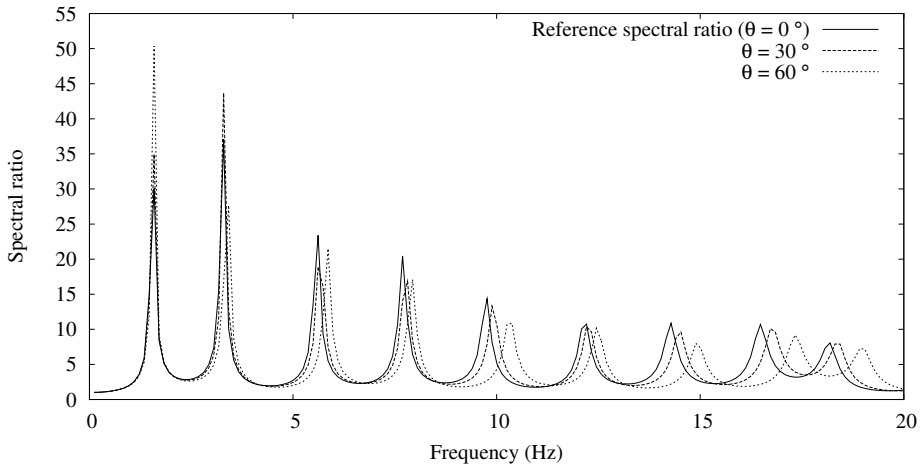

Figure 1.15: Influence of the increase of the incidence angle on SH spectral ratios.

- modifies the amplitude of the resonant frequencies.

These two observations are true for any soil column.

In the time domain, both phase and amplitude of the time history are modified as shown in Figure 1.16 (the phase shift could be deduced graphically: since the wave is plane, the larger the incidence angle, the smaller the arrival time at the free surface).

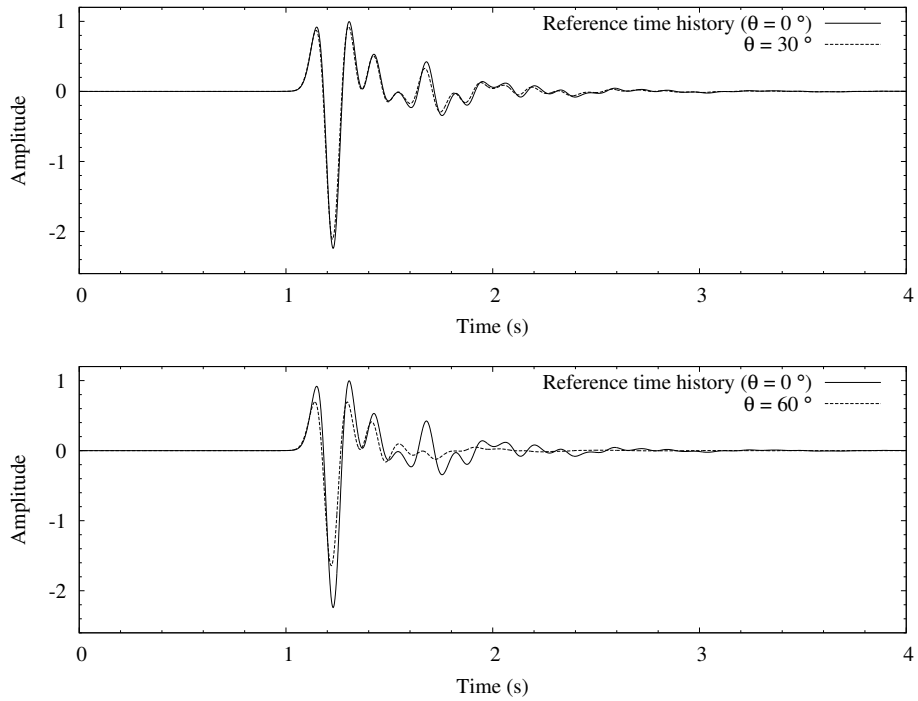

Figure 1.16: Influence of the increase of the incidence angle on SH time history. The free surface time history is shown.

1.3 Genetic Algorithm

A genetic algorithm (GA) is a search technique used in computing to find exact or approximate solutions to optimization and search problems. Genetic algorithms are categorized as global search heuristics. GA are a particular class of evolutionary algorithms that use techniques inspired by evolutionary biology such as inheritance, mutation, selection, and crossover (e.g., Goldberg, 1989; Fonseca and Fleming, 1993; Mitchell, 1998; Gen and Cheng, 1999). Genetic algorithms, despite their apparent simplicity, are highly dimensional, multi-faceted, nonlinear, stochastic complex systems that can interact with a large variety of problems.

This section presents the fundamentals of the so-called "simple genetic algorithm method" (the simple GA) that is used in the next chapter to invert the parameters of the soil structure of a borehole station. The inversion code has been developped for this thesis and is programmed in FORTRAN 90. Examples of the use of GA to invert soil parameters can be found in geotechnical engineering (e.g., Levasseur et al., 2007; Samarajiva et al., 2005) as well as in seismology (e.g., Zhou et al., 1995; Yamanaka and Ishida, 1996; Chang et al., 2004; Jimenez et al., 2005; Pezeshk and Zarrabi, 2005; Bhattacharyya et al., 1999).

1.3.1 Methodology

Genetic algorithms are implemented in a computer simulation in which a population of abstract representations (called chromosomes or the genotype of the genome) of candidate solutions (called individuals, creatures, or phenotypes) to an optimization problem evolves toward better solutions. Traditionally, solutions are represented in binary as strings of $0s$ and $1s$ (representation used in this thesis), but other encodings are also possible. The evolution usually starts from a population of randomly generated individuals and happens in generations. In each generation, the fitness of every individual in the population is evaluated, multiple individuals are stochastically selected from the current population (based on their fitness), and modified (recombined and possibly randomly mutated) to form a new population. The new population is then used in the next iteration of the algorithm. Commonly, the algorithm terminates when either a maximum number of generations has been produced, or a satisfactory fitness level has been reached for the population. If the algorithm has terminated due to a maximum number of generations, a satisfactory solution may or may not have been reached. The flowchart of the genetic algorithm used in this study is shown in Figure 1.17. We note that prior to the genetic algorithm optimization, a Monte Carlo method is used (i.e., generation of random solutions to investigate the problem) in order to better explore the search space. Then, the best individuals found during the Monte Carlo search are used to initialize the

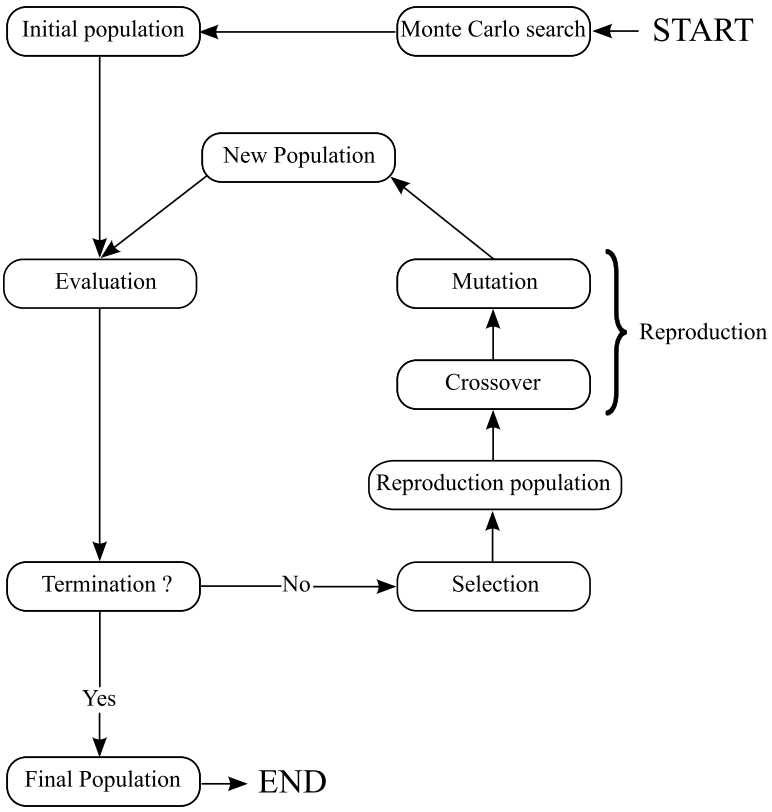

Figure 1.17: Flowchart of genetic algorithm inversion preceded by a Monte Carlo search.

first population of the GA optimization.

1.3.2 Problem discretization

A standard representation of the solution as an array of bits of 0s and 1s is used to discretize the search space. The process of discretization of a 1-D soil column is shown in Figure 1.18. Each inverted parameter of layers (e.g., β_i, ξ_i, etc.) is discretized within the search space using N_i^{par} bits where par represents the parameter (e.g., N_i^{β}, N_i^{ξ}, etc.) and i stands for the layer; this number of bit determines the accuracy of the discretization (the larger the number of bits, the better the accuracy). Once all the layers are discretized into binary individuals, they are put together to represent the entire soil column as a binary individual as shown in Figure 1.18. The total number of solutions is

$$N_{sol} = 2^{\sum_{i=1}^{n} \sum_{par=1}^{m} N_i^{par}}, \tag{1.42}$$

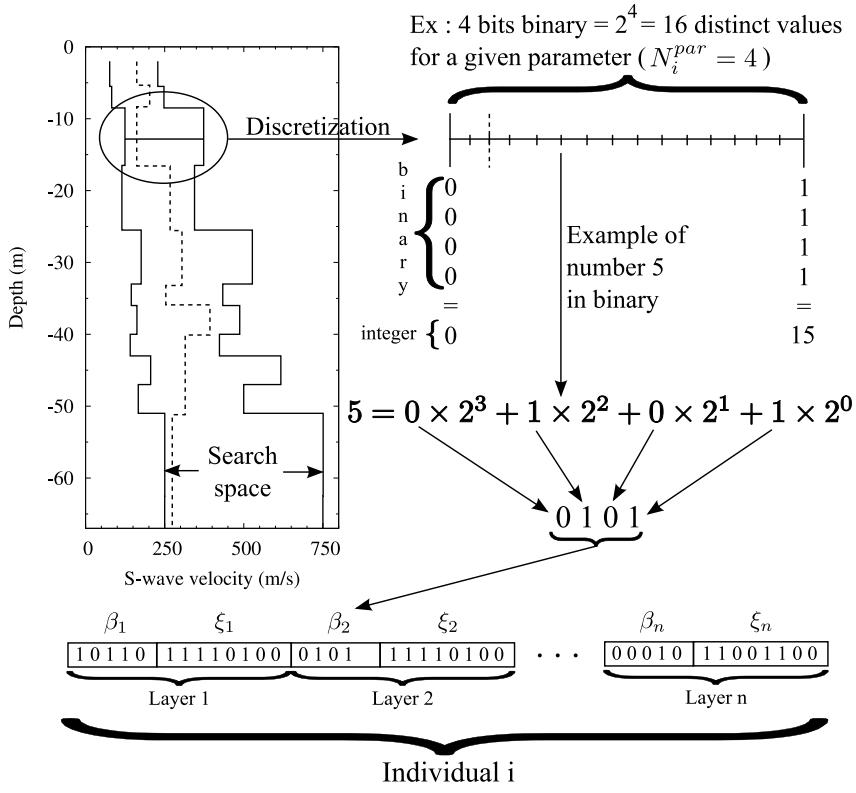

Figure 1.18: Discretization of the search space for the genetic algorithm optimization. In the left-hand side graphic, the search space of the S-wave velocity is shown in solid line and an example of soil column within the search space is shown in dashed line. The discretization process is emphasized on the right-hand side. An example of individual is shown at the bottom.

with n the number of layers and m the number of parameters to invert inside a layer.

1.3.3 Initialization

Prior to the genetic algorithm optimization, a Monte Carlo search is done on N_{pop}^{MC} populations of size N_{ind}^{MC} individuals (potential solutions for the soil column) in order to explore the search space. Then, the N_{bes}^{MC} best individuals found during the Monte Carlo search are used to initialize the first population of size N_{ind} of the GA optimization.

1.3.4 Evaluation and selection

During each successive generation, a proportion of the existing population is selected to breed a new generation. Individual solutions are selected through a fitness-based process, where fitter solutions (as measured by a fitness function (also called objective function), see below) are typically more likely to be selected. Certain selection methods rate the fitness of each solution and preferentially select the best solutions. Other methods rate only a random sample of the population, as this process may be very time-consuming (e.g., Srivinas and Patnaik, 1994). Most functions are stochastic and designed so that a small proportion of less fit solutions are selected. This helps keep the diversity of the population large, preventing premature convergence on poor solutions. Popular and well-studied selection methods include roulette wheel selection and tournament selection. The roulette wheel, also known as fitness proportionate selection, uses the fitness level to associate a probability of selection with each individual. If f_i is the fitness of an individual i, its probability of being selected is $p_i = \frac{f_i}{\sum_{j=1}^{N_{ind}} f_j}$. Tournament selection involves running several tournaments among few individuals chosen at random from the population. The winner (in terms of best fitness) of each tournament is selected for crossover. Selection pressure is easily adjusted by changing the tournament size.

As an exemple, Figure 1.19 shows the processus of evaluation of the fitness function of the individuals for a borehole inversion problem. The target is the observed spectral ratio and each theoretical spectral ratio is compared with the target in order to quantify its objective function. Figure 1.20 shows an example of tournament from which the population of reproduction is generated.

The traditional objective function (e.g., Satoh et al., 1995a), which depends on the unknown parameters to be inverted, evaluates the integrated residual between the observation and the theory as

$$E(\mathbf{x}) = \frac{\int_{f_s}^{f_e} |H_{obs}(f) - H_{the}(f, \mathbf{x})|^2 df}{\int_{f_s}^{f_e} |H_{obs}(f)|^2 df} \tag{1.43}$$

where E is the objective function, $\mathbf{x}$ is the vector of unknown parameters, f_s and f_e are the start and end frequencies of integration, H_o is the observed spectral ratio and H_t is the theoretical spectral ratio. This objective function has for advantage to try to minimize the integrated residual in the frequency range f_s to f_e. However, if effects other than 1-D effects (e.g., shift of a frequency peak due to a 2-D effects) are present in the integration range of the observed spectral ratio, then, they are also inverted by using the 1-D theory and could lead to false inverted parameters. In order to compensate this shortcoming, the integration could be done piecewisely in order to avoid the range containing an unwanted effect or another objective function (less

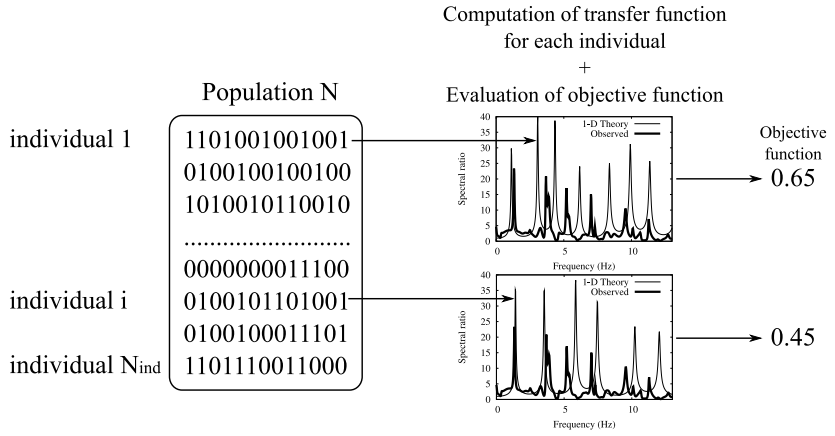

Figure 1.19: Evaluation of the fitness function of the individuals of a population N for a borehole inversion problem in which the observed spectral ratio is the target to be reached.

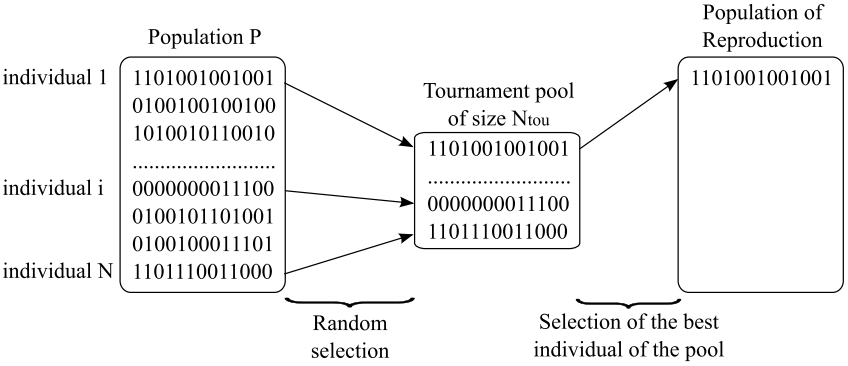

Figure 1.20: Example of a tournament pool. The individuals who participate to the tournament are randomly selected in the population P. The winner of the tournament (i.e., the individual with the best fitness function) is injected in the population of reproduction.

dependent of the integration range) could be used as shown hereafter.

In order to avoid effects other than 1-D effects embedded in the observed spectral ratio, we present an objective function which focuses on the location of the peaks along the frequency axis and on the amplitude of the peaks as:

$$E(\mathbf{x}) = \frac{\sum_{i=1}^{n_{PF}} \frac{|PF_i^{obs} - PF_i^{the}(\mathbf{x})|}{PF_i^{obs}}}{\sum_{j=1}^{n_{PF}} PF_j^{obs}} + \frac{\sum_{i=1}^{n_{PA}} \frac{|PA_i^{obs} - PA_i^{the}(\mathbf{x})|}{PF_i^{obs}}}{\sum_{j=1}^{n_{PA}} PA_j^{obs}} \tag{1.44}$$

where $|.|$ denotes the absolute value and with $\mathbf{x}$ the vector containing parameters to invert, PF_i^{obs} the i-th observed peak frequency, PF_i^{the} the i-th theoretical peak frequency, PA_i^{obs} the i-th observed peak amplitude, PA_i^{the} the i-th theoretical peak amplitude, n_{PF} the number of peak frequencies to use and n_{PA} the number of peak amplitudes to use. In order to give more weight to low-frequency peaks, each member is divided by PF_i^{obs}. Normalization by $\sum_{j=1}^{n_{PF}} PF_j^{obs}$ and $\sum_{j=1}^{n_{PA}} PA_j^{obs}$ is done to avoid overweighting the frequency or amplitude portions.

This objective function focuses on the location of peaks along the frequency axis and on the amplitude of peaks. Peaks used in an inversion can be chosen at will to calculate the objective function. We note that this objective function has the virtue of being the summation of linear functions of the form $|X_i^{obs} - X_i^{the}(\mathbf{x})|$, which makes its shape simple for inversion techniques in an n-dimensional space. Its disadvantage resides in the fact that one has to know *a priori* which peaks have to be inverted.

1.3.5 Reproduction

The next step is to generate a second generation population of solutions from those selected through genetic operators: crossover (also called recombination), and/or mutation.

For each new solution to be produced, a pair of "parent" solutions is selected at random for breeding from the pool selected previously. By producing a "child" solution using the above methods of crossover and mutation, a new solution is created which typically shares many of the characteristics of its parents. New parents are selected for each new child, and the process continues until a new population of solutions of appropriate size is generated. An example of crossover and mutation is shown in Figure 1.21.

These processes ultimately result in the next generation population of chromosomes that is different from the initial generation. Generally the average fitness will have increased by this procedure for the population, since only the best individuals from the first generation are selected for breeding, along with a small proportion of less fit solutions (in order to keep the diversity of the solutions).

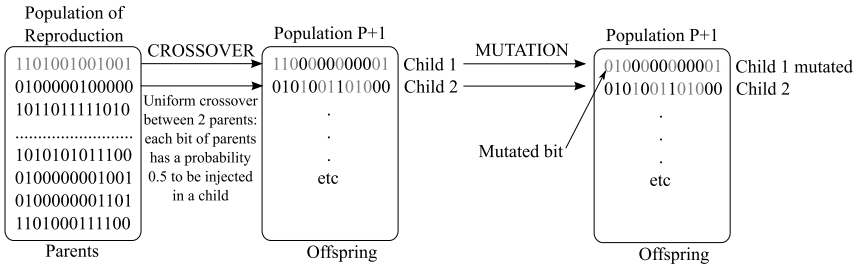

Figure 1.21: Example of a crossover and a mutation. In the population of reproduction, the first two parents are representated by a gray and a black binary. The children are generated by a uniform crossover from these parents. A mutation is the change of a bit from 0 to 1 or *vice-versa*.

1.3.6 Termination

This generational process is repeated until a termination condition has been reached. Common terminating conditions are:

- a solution is found that satisfies minimum criteria for the objective function;
- a fixed number of generations (i.e., populations) is reached;
- an allocated budget (e.g., computation time) is reached;
- the highest ranking solution's fitness is reaching or has reached a plateau such that successive iterations no longer produce better results;
- a manual inspection;
- combinations of the above.

1.3.7 Validation

In order to validate the inversion code developed in this thesis, we set up a simple problem with two unknown parameters and first perform a grid search in the entire search space (i.e., all objective functions of the possible couple (x_1, x_2) are computed) so that the surface to be obtimized is viewable as shown in Figure 1.22. Here x_1 and x_2 represent the factor applied on the S-wave velocity of two layers of the soil column presented in Table 1.2. We note that the global minimum has been explicitly located around the couple $(x_1 = 0.6, x_2 = 1.4)$.

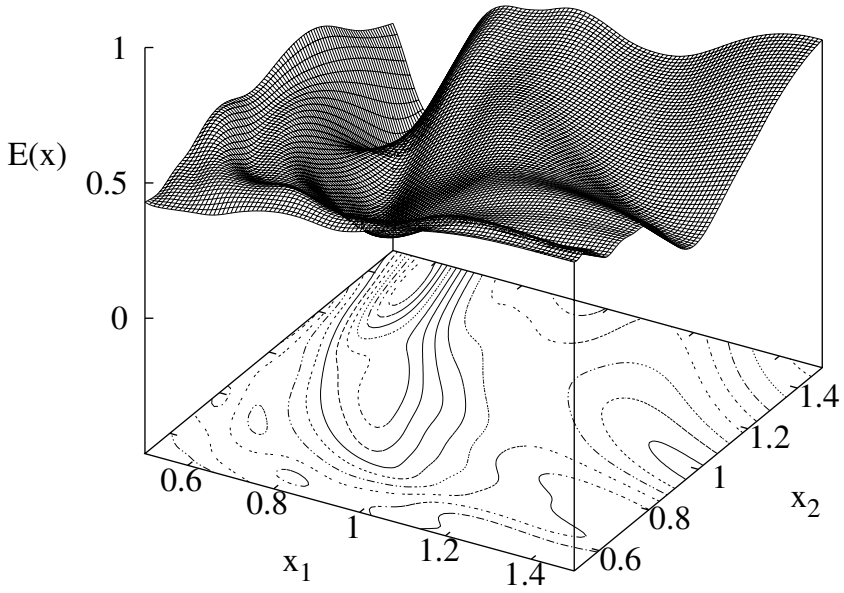

Figure 1.22: Representation of the surface of an objective function in the space $x_1 \in [0.5, 1.5] \times x_2 \in [0.5, 1.5]$ (x_1 and x_2 represent the factor applied on the S-wave velocity of two layers of the soil column presented in Table 1.2). At the bottom of the figure, the 3-D surface is mapped in the horizontal plane by using contour lines.

Figure 1.23 shows the evolution of a genetic algorithm inversion of the parameters x_1 and x_2 from the population 1 to 15 (we note that no Monte Carlo search is performed for this inversion). For the initial population (i.e., population 1), the individuals are generated at random over the entire search space. After five populations, we see that the global minimum is found. In order to keep the diversity of the solutions and to better explore the entire search space, some individuals are still present far from the global optimum. We also note that the inversion has not been locked in a local minimum (in order to check the robustness of the inversion, several independent inversions have been performed and the global minimum has always been found).

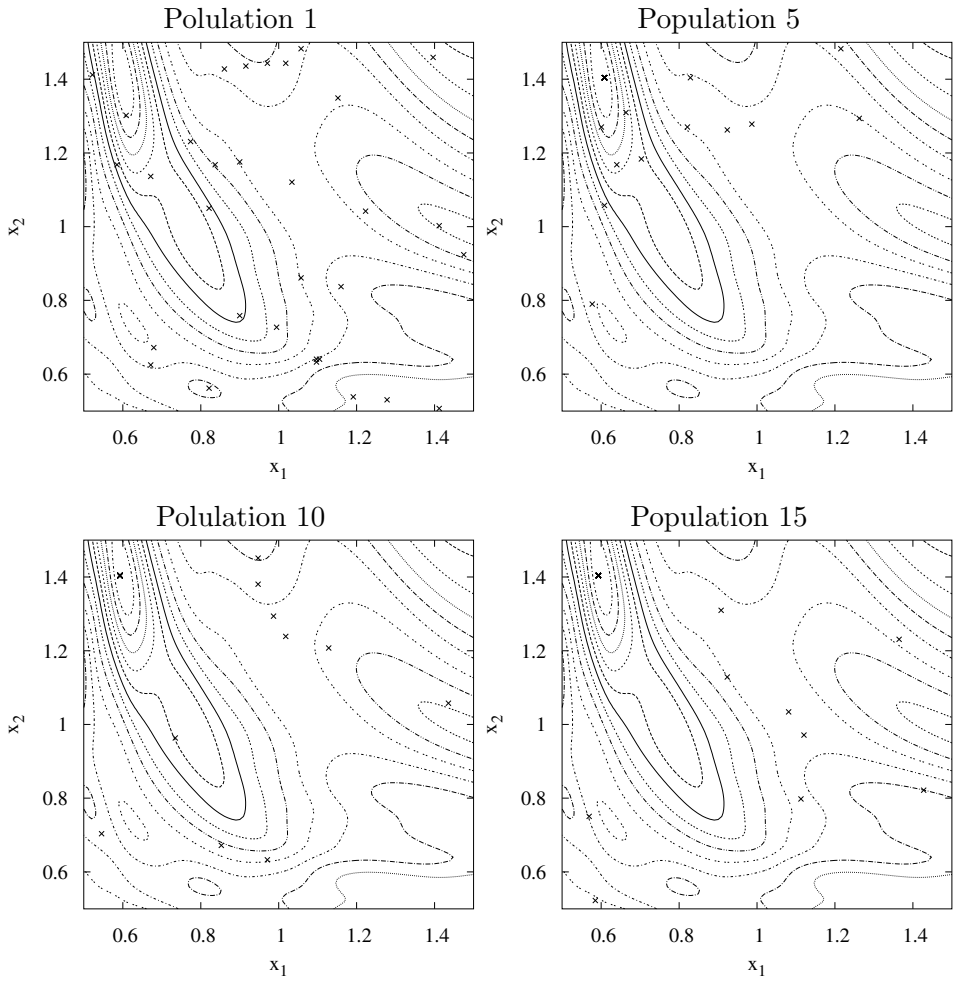

Figure 1.23: Evolution of a genetic algorithm inversion from the population 1 to 15. The crosses represent the individuals of a population. The contour lines represent the 3-D surface of Figure 1.22.

1.4 Conclusion

Based on the Thomson-Haskell propagator matrix method (i.e., specific case of the linear elastic wave propagation in a one-dimensional welded homogeneous stack of layers), we have developed a genetic algorithm inversion code in order to inverse in the frequency domain the soil parameters of a soil column by matching the theoretical spectral ratios on an observed spectral ratio. The advantage of the use of 1-D theory is that the spectral ratio depends only on the soil parameters between the sensors of the borehole station. The code is developped to invert:

- the S-wave velocity α;
- the P-wave velocity β;
- the compressional damping factor ξ_α;
- the shear damping factor ξ_β;
- and the incidence angle of the incoming wave.

In the following chapter, the code is used to invert the equivalent linear soil properties of the CTI borehole station, Fukuoka, Japan, during the 2005 Fukuoka prefecture werstern offshore earthquake.

Chapter 2

Inversion of Borehole Soil Structure: Applications

This chapter has been published as:

- De Martin, F., H. Kawase, and A. Modaressi (2010). Nonlinear Soil Response of a Borehole Station Based on One-Dimensional Inversion during the 2005 Fukuoka Prefecture Western Offshore Earthquake. Bull. Seism. Soc. Am..

2.1 Inversion During the 2005 West Off Fukuoka Earthquake

Nonlinear behavior of soft soil observed during strong ground motions is now well established (e.g., Chin and Aki, 1991; Darragh and Shakal, 1991; Aki, 1993; Field et al., 1997; Su et al., 1998; Cultrera et al., 1999; Frankel et al., 2002; Aki, 2003; Bonilla et al., 2005) and the deployment of vertical arrays has contributed to detailed wave propagation analyses and the assessment for quantitative physical parameters such as shear-wave (S-wave) velocity, pressure-wave (P-wave) velocity and damping factors with respect to shear strain levels (e.g., Seed and Idriss, 1970a; Chang et al., 1991; Archuleta et al., 1992, 1993; Wen, 1994; Beresnev et al., 1995; Satoh et al., 1995a; Zeghal et al., 1995; Ghayamghamain and Kawakami, 1996; Kawase et al., 1996; Aguirre and Irikura, 1997; Satoh et al., 1997, 2001; Bonilla et al., 2002; Pavlenko and Irikura, 2003; Kokusho, 2004; Pavlenko and Irikura, 2005, 2006; Assimaki and Steidl, 2007; Chávez-García and Raptakis, 2008; Kwok et al., 2008).

A natural approach to study borehole data is one-dimensional (1-D) modeling, which has been proved to be a good approximation for many cases (e.g., some of the aforementioned studies). Moreover, it has been shown during two blind-prediction experiments conducted by the IASPEI/IAEE

Joint Working Group on Effects of Surface Geology on Strong Motions that the geological structure is more important than the model dimension (e.g., Cramer and Real, 1992; Mirodikawa, 1992). However, in recent years, 2-D or 3-D effects of basins have been found to be relevant for some strong ground motions (e.g., Bard et al., 1988; Kawase and Aki, 1989; Kawase and Sato, 1992; Graves, 1993; Frankel, 1994; Kawase and Matsushima, 1998). Those geometrical effects were observed essentially in the low-frequency range and would disappear in the high-frequency range because the shorter the wavelength, the more local the phenomenon. Unfortunately, short wavelengths are thought to be vulnerable to mutual interference of multiple reflection/refraction and to intrinsic or scattering attenuation, and consequently, clear disappearance of 2-D or 3-D geometrical effects in the high-frequency range has not been reported yet.

In this study, we first confirm the major and minor axes of several stations surrounding the epicenter and then corroborate, at the borehole station, the 1-D velocity structure in the linear elastic domain by computing time-dependent spectral ratios on the S-wave portion of small aftershocks. Possible geometrical effects, soil heterogeneity and/or soil-structure interaction embedded within 1-D spectral ratios are detecting using 360° spectral ratios.

Finally, conspicuous evidence of nonlinearity during the S-wave portion of the main shock is shown by computing spectral ratios whose several resonant frequencies are shifted toward low frequencies. In order to quantify the degree of nonlinearity, we invert by a genetic algorithm (e.g., Goldberg, 1989; Yamanaka and Ishida, 1996) the observed equivalent linear parameters (i.e., shear-wave velocity structure and damping factors) via the Thomson-Haskell propagator matrix method (e.g., Thomson, 1950; Haskell, 1953). Because of a directional effect present only in the major axis clearly visible on 360° spectral ratios around 8 Hz, the conventional objective function, which minimizes the integrated residuals between observed and theoretical ratios cannot be used. We therefore introduce a simple objective function that depends only on the peaks' frequency and amplitude. To show the efficiency of the objective function and the robustness of the inversion, we perform eight independent inversions, which converge to very close solutions.

2.1.1 Overview of strong ground motions

Fukuoka City is located on the northern part of Kyushu Island, southwestern Japan (Figure 2.1, inset on the top left-hand side). A topographic map around the city is shown in Figure 2.1 (main panel). The 2005 West off Fukuoka Prefecture earthquake with a JMA (Japanese Meteorological Agency) magnitude M_J of 7.0 (M_w = 6.6) and focal depth of 9.2 km occurred on March 20 2005 off the northern coast of Kyushu Island along an unmapped fault at the northern extension of the well-known active fault,

the Kego fault (e.g., Shibuya et al., 2009). Figure 2.2 shows the Kego fault and accelerograms at some stations surrounding the epicenter. Here we use K-NET (indicated by three letters + three digits) and KiK-net stations (indicated by three letters + 'H' + two digits), as well as Fukuoka Prefecture's seismic intensity meter network (indicated by three letters + 'S' + two digits). A rapid comparison between accelerograms at the K-NET station FKO006 and the other ones clearly shows that longer-period components are present at FKO006; suggesting the site effects due to the existence of soft sediments within Fukuoka City.

In order to confirm the major and minor axes according to the source mechanism, we calculate the directional energy distribution given by Equation 2.1 (e.g., Takizawa, 1982), which was successfully used to confirm the major axis of strong motion by Kawase and Aki (1990). First, the total power and cross spectra of the two orthogonal components n (referring to north) and e (referring to east) is calculated in the frequency range of interest:

$$[E] = \int_{\omega_1}^{\omega_2} \Re \begin{pmatrix} S_{nn}(\omega) & S_{ne}(\omega) \\ S_{en}(\omega) & S_{ee}(\omega) \end{pmatrix} d\omega,$$

where $[E]$ is the matrix of energy of velocity power spectra, ω_1 and ω_2 are the lower and upper bounds of integration in the frequency domain, $\Re$ indicates the real part of a complex number, $S_{nn}(\omega)$ is a velocity power spectrum of the n direction and $S_{ne}(\omega)$ is a velocity cross power spectrum between the n and e direction, and so on. The cross power spectrum S_{ij} is computed as:

$$S_{ij}(\omega) = \int_{-\infty}^{\infty} C[v_i v_j](\tau) e^{-i\omega\tau} d\tau,$$

where $C[v_i v_j](\tau)$ denotes the cross correlation fucntion of the velocity in the direction i, v_i, and the velocity in the direction j, v_j. Then, the energy in the direction ϕ measured in a clockwise direction from the n-axis can be obtained as:

$$E_\phi = \{\cos\phi, \sin\phi\}[E] \begin{Bmatrix} \cos\phi \\ \sin\phi \end{Bmatrix}. \tag{2.1}$$

This energy distribution will be two elliptic lobes in line with the major axis if the ground motion is perfectly unidirectional, while it will become a single circle if the ground motion is not directional at all. Fukuoka earthquake being a strike-slip crustal earthquake with a strike direction equal to N122°E, a dip angle of 89° and a rake angle of -11° (e.g., Asano and Iwata, 2006), we can first plot theoretical far-field radiation pattern of the now familiar double-couple mechanism in an infinite homogeneous medium to have in mind the predominant direction of motion. Figure 2.3 shows the S-wave radiation pattern and its SH and SV components. The fault plane (i.e., radial component) and the auxiliary plane (i.e., transverse component) are predominant planes for the S-wave. By decomposition of S-wave into SH

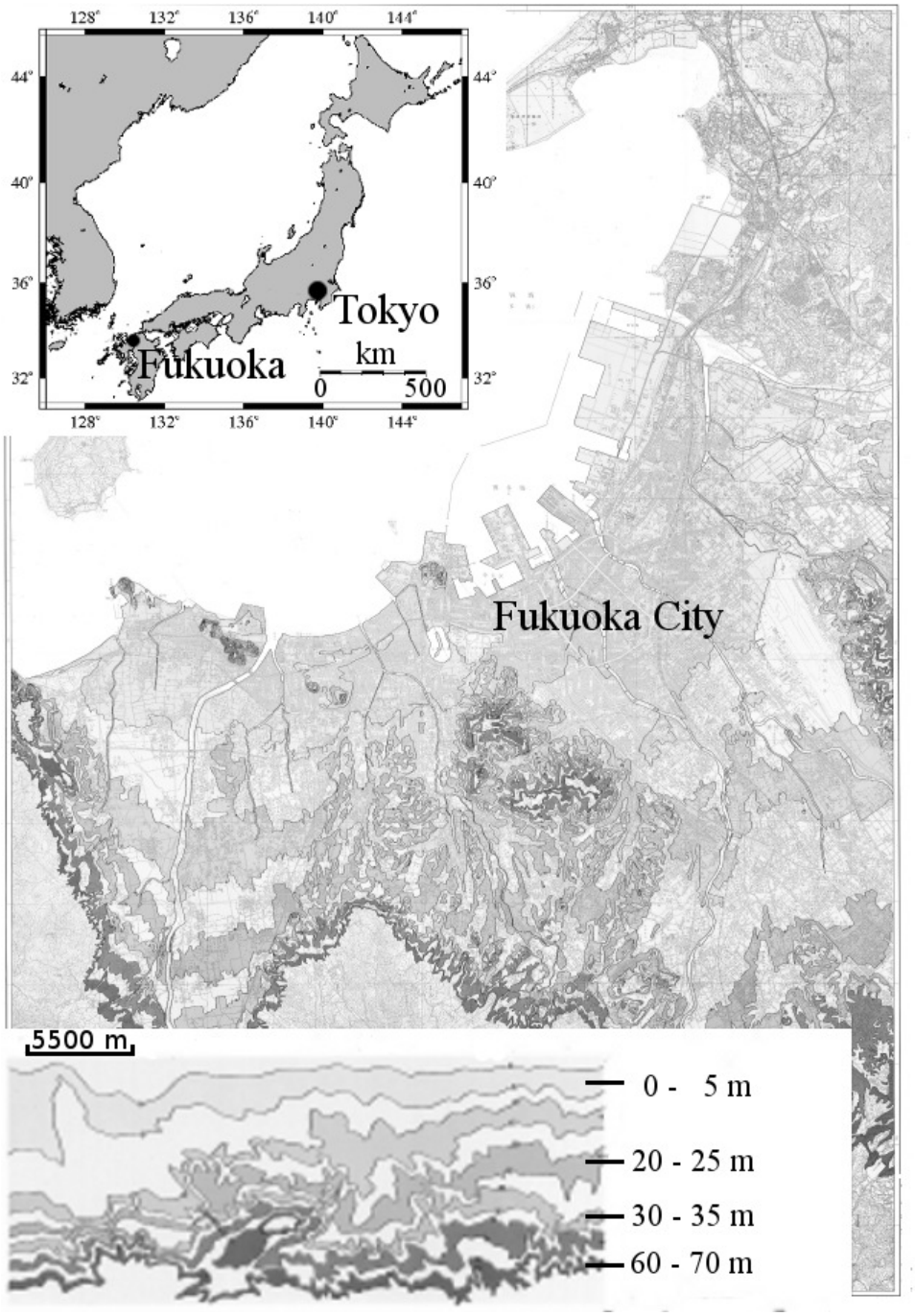

Figure 2.1: Inset on the top left-hand side: Localization of Fukuoka City, northern Kyushu Island, Japan. Main panel: Topographic map of Fukuoka City.

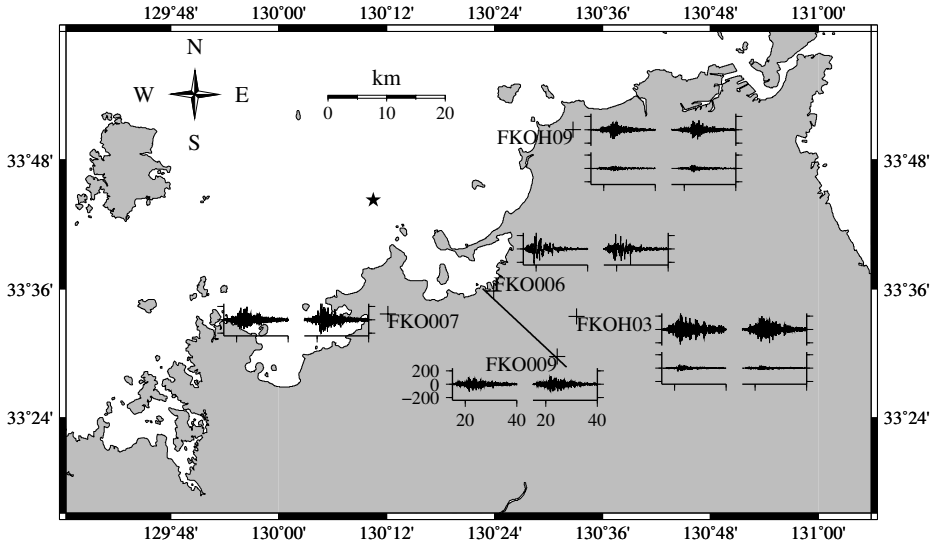

Figure 2.2: Location of the Kego fault (solid line at the south-western side of the station FKO006) and accelerograms recorded at stations surrounding the epicenter (pointed out by a star) of the Fukuoka earthquake. Stations $FKOxxx$ are stations from Kyoshin Network (K-NET) and stations $FKOHxx$ are stations from Kiban Kyoshin Network (KiK-Net). For both K-Net and KiK-Net stations, accelerograms on the left-hand side represent the north-south ground motion and accelerograms on the right-hand side represent east-west ground motion. For KiK-Net stations, accelerograms at the bottom are downhole records.

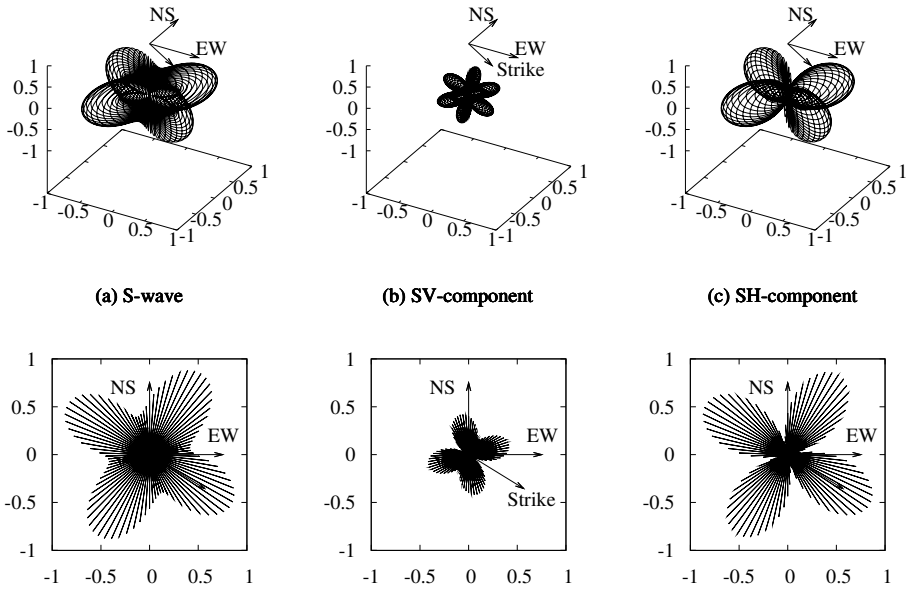

Figure 2.3: Theoretical far-field S-wave radiation pattern for a double couple point source model in an infinite homogeneous medium oriented as followed: strike = 122°, dip = 89° and rake = -11°. North-south (NS), east-west (EW) and strike direction are indicated by arrows. Panels (a) shows S-wave radiation pattern and panels (b) and (c) expose SV and SH component of the S-wave, respectively. Top panels show a 3-D view of the radiation patterns and bottom panels show them mapped into the horizontal plane.

and SV component, we see that SH component is predominant in the fault plane and in the auxiliary plane whereas these planes are nodal lines for the SV component.

Figures 2.4 and 2.5 show the energy distribution calculated in the horizontal plane for records observed at 22 stations (it should be noted that, if necessary, these energy distributions have been corrected for the sensors' rotation for K-NET and KiK-net stations based on the information published by NIED, www.bosai.go.jp/e/). Depending on the station, observations show more or less a good agreement with the solution of the double-couple point source model. The energy distribution in the fault plane at the stations FKOS02, FKOS05, FKOS06 and FKO009 shows a good coherence since it exhibits a major axis perpendicular to the fault plane (i.e., predominance of the SH-component). The same agreement can be seen for the auxiliary plane, where stations SAG001, SAGH01 and FKOH09 exhibit the same predominance. However, within Fukuoka City, we can notice that

the energy distribution of FKO006, FKOS01 and CTI are slightly rotated toward the north. This rotation could be due to basin geometrical effects and/or to trapped waves propagating along the fault gouge. The possible presence of trapped wave is exposed in Appendix B.

In the following, we will describe the configuration of the borehole station and the data available at the borehole site.

2.1.2 The borehole station: configuration and data

The borehole station is CTI Engineering Co., Ltd borehole station (http:// www.ctie.co.jp /earthquake /eq_20050320.html) located within Fukuoka's basin in a zone where sediments' thickness is the largest ($\approx$ 62 m). North-south and east-west geologic cross-sections realized 100 meters from the borehole are shown in Figure 2.6. On the western and southern side of the borehole, the abrupt variation of the sediments-bedrock interface is due to the activity of the Kego fault indicated by crosses. The bedrock's depth increases from 10 m to 60 m in approximately 300 m.

The borehole station is composed of two sensors, with a sample frequency of 100 Hz, located below CTI Engineering's seven-story base-isolated building, as shown in the schematic view of Figure 2.7. One sensor is placed in the basement of the building and the other one is located 67 meters below the free surface embedded inside the bedrock. Hereafter, we call these sensors: basement sensor and downhole sensor, respectively. Since the fundamental frequency of such a base-isolated building is around 0.3-0.4 Hz, and since the fundamental frequency of the CTI soil column is 1.4 Hz (see Subsection 2.1.3), we neglect soil-structure interaction and the basement sensor is considered as a free surface sensor. A third sensor located at the seventh story of the building has not been used for this study. Previous studies related to CTI Engineering site are the following: Mazda et al. (2005); Satoh and Kawase (2005); Kawase et al. (2006).

The geology of the 1-D soil column consists of an alternation of sand and clay overlying a thick layer of gravel and bedrock. The top 15 meters mainly consists of sand whose S-wave velocity increases from 150 m/s to 250 m/s and whose Standard Penetration Test (SPT) N-values range between 2 and 34. Then follows an alternation of clay and sand whose S-wave velocity ranges between 282 m/s and 411 m/s and STP N-values between 10 and the upper limit of 50. Below, a thick layer of 11 meters of gravel whose S-wave velocity is approximately 500 m/s overlays the engineering bedrock made of mudstone dating from the pre-Tertiary period of Cenozoic era and whose S-wave velocity is approximately 500m/s.

Characteristics of records of the main shock and aftershocks provided by CTI Engineering are shown in Table 2.1. EQ01 refers to the main shock and EQ02 to EQ25 refers to aftershocks. Figure 2.8 displays the location of their epicenters around the CTI station. A clear alignment of the events with the

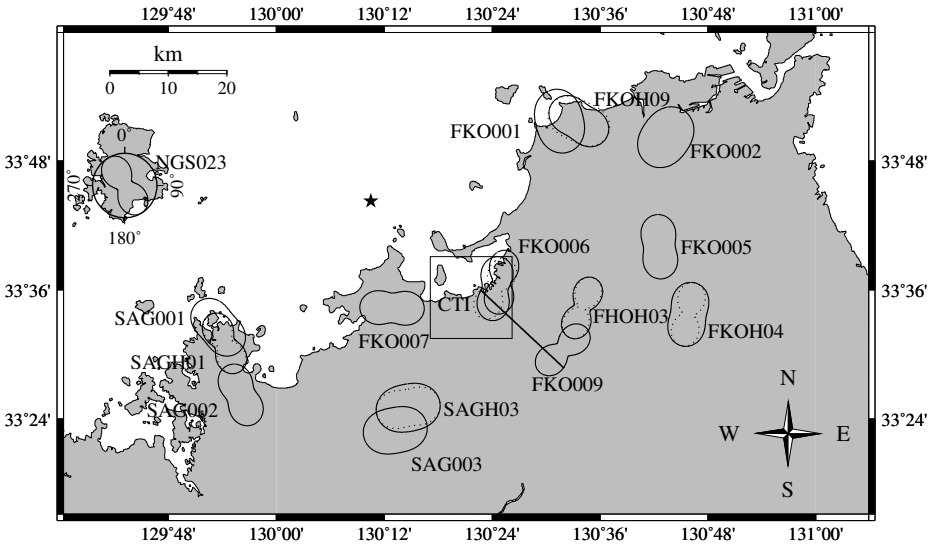

Figure 2.4: Energy distribution in the horizontal plane (NS-EW) for the records observed at stations within 60 km from the epicenter. The principal axis measured clockwise from the north (see station NGS023) has +/- 180° ambiguity. The energy distribution is calculated from velocity power spectra which are derived from NS and EW components of velocity seismograms (the entire record has been used to compute the power spectra). The frequency range used to integrate a power spectrum is 0.1 to 10 Hz. Solid lines represent the energy distribution calculated at the free surface sensor and dashed lines that of the downhole sensor. The approximate location of the Kego fault is represented by a solid straight line and the epicenter of the earthquake by a star. The rectangle denotes the area shown in Figure 2.5.

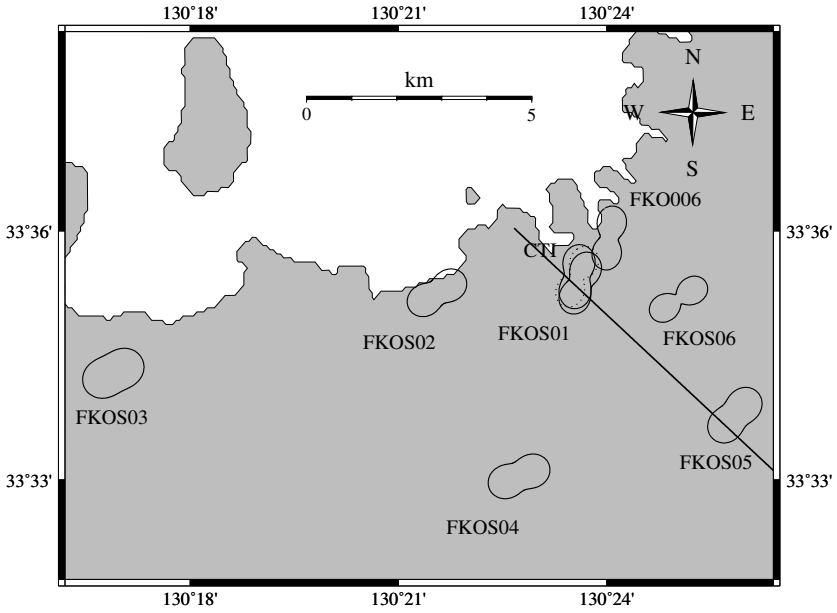

Figure 2.5: Zoom of the rectangle in Figure 2.4. Explanation are given in caption of Figure 2.4. Stations $FKOSxx$ are stations from Fukuoka Prefecture's seismic intensity meter network.

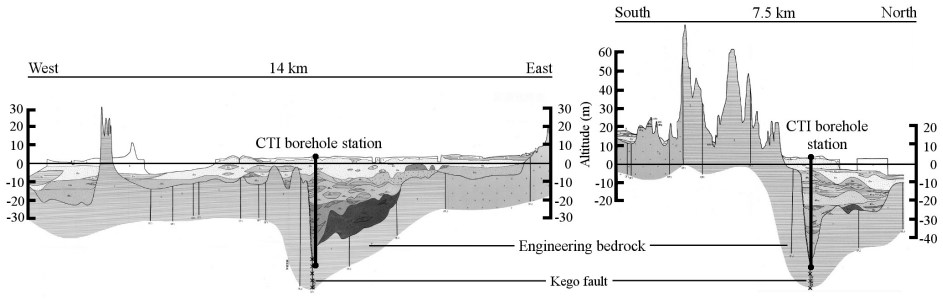

Figure 2.6: North-south and east-west geologic cross-section located some hundred meters from CTI borehole station. The vertical axis has been exaggerated 50 times. The borehole station is indicated by a solid line and the sensors are represented by two points along this line. The Kego fault is indicated by crosses.

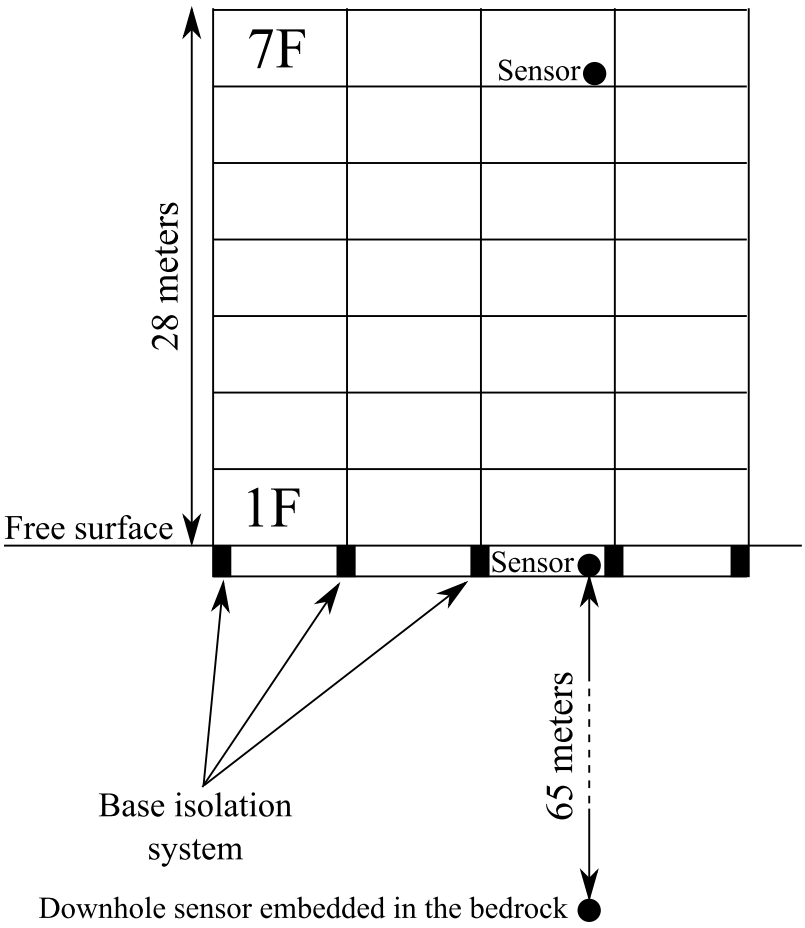

Figure 2.7: Schematic representation of the system {base-isolated building + borehole station} at the CTI Engineering site. Sensors are represented by circles.

Table 2.1: List of earthquakes whose parameters are determined by Japan Meteorological Agency. M_J means Japan Meteorological Agency Magnitude. The symbol - indicates that values are unknown.

No.	Date/Time	Lat./Lon.	Focal depth (km)	M_J	Hypocentral distance from CTI (km)
EQ01	2005.03.20/10h53	33.74/130.18	9	7.0	27.5
EQ02	2005.04.20/06h11	33.68/130.29	14	5.8	23.6
EQ03	2005.04.21/07h32	33.77/130.11	12	3.8	35.1
EQ04	2005.04.24/11h25	33.65/130.32	11	3.1	14.2
EQ05	2005.04.25/04h37	-	-	-	-
EQ06	2005.04.28/03h43	33.67/130.30	13	3.8	17.7
EQ07	2005.05.02/01h24	33.67/130.32	11	5.0	15.5
EQ08	2005.05.03/01h29	33.61/130.41	8	3.1	8.5
EQ09	2005.05.10/11h53	-	-	-	-
EQ10	2005.05.13/18h52	33.75/130.12	13	3.9	33.6
EQ11	2005.05.29/00h58	-	-	-	-
EQ12	2005.05.30/08h52	33.67/130.38	8	3.0	12.0
EQ13	2005.06.03/04h23	33.77/130.09	15	4.1	37.2
EQ14	2005.06.26/19h55	33.70/130.25	10	3.4	20.6
EQ15	2005.07.05/05h10	33.74/130.12	15	4.2	33.5
EQ16	2005.05.30/14h55	-	-	-	-
EQ17	2005.08.03/12h45	33.70/130.24	6	3.5	19.9
EQ18	2005.08.09/04h13	33.69/130.29	12	3.3	19.2
EQ19	2005.09.12/20h19	33.78/130.10	12	4.1	36.0
EQ20	2005.09.13/17h01	33.70/130.27	15	3.5	22.7
EQ21	2005.11.12/05h41	33.74/130.18	15	3.7	30.0
EQ22	2005.12.09/02h15	33.68/130.31	15	3.6	19.8
EQ23	2006.01.31/00h19	33.77/130.12	14	3.8	34.9
EQ24	2006.04.28/00h19	33.77/130.11	13	3.8	35.5
EQ25	2006.08.25/15h09	-	-	-	-

Kego fault can be seen. Table 2.2 shows the PGA of the main shock and aftershocks in major and minor axes.

In the following, we will describe surface-to-downhole spectral ratios performed in the major and in minor axes associated to transverse and radial components, respectively.

2.1.3 Surface-to-downhole spectral ratios during aftershocks

The original PS logging being very detailed (i.e., 12 layers with 39 measurements of S-wave and P-wave velocity), we have simplified the soil column by taking the average of velocities within each layer in order to facilitate the inversion. The simplified linear elastic soil properties and SPT N-values are presented in Table 2.3. The original and simplified velocity profile for S-wave and P-wave are shown in Figure 2.9 (a) and (b), respectively. Their one-dimensional spectral ratio computed for a vertically incident S-wave are

Table 2.2: PGA in major and minor axes recorded during the main shock and the aftershocks.

	PGA (gal)			
	Major axis		Minor axis	
No.	Free surface	Downhole	Free surface	Downhole
EQ01	362.0	164.3	419.7	151.7
EQ02	278.8	97.6	267.3	108.9
EQ03	3.1	1.1	4.9	1.4
EQ04	3.5	1.3	4.6	1.8
EQ05	6.0	1.9	8.5	2.3
EQ06	8.1	2.4	11.2	3.2
EQ07	83.9	23.8	152.2	37.8
EQ08	15.0	4.4	28.0	9.8
EQ09	4.6	1.9	8.3	2.8
EQ10	4.8	1.6	7.7	2.1
EQ11	3.7	1.2	5.2	1.3
EQ12	5.6	2.1	10.6	2.7
EQ13	6.0	2.4	10.4	2.6
EQ14	3.0	0.8	3.3	1.2
EQ15	21.7	8.9	35.7	8.1
EQ16	3.9	1.8	5.9	2.0
EQ17	6.1	1.8	9.7	3.2
EQ18	4.4	1.4	7.7	2.2
EQ19	7.5	2.2	10.4	3.1
EQ20	5.8	2.1	7.8	2.8
EQ21	3.7	1.5	6.2	1.3
EQ22	10.6	2.0	8.9	3.2
EQ23	9.0	3.4	17.0	4.1
EQ24	4.7	1.8	7.0	3.2
EQ25	4.7	1.6	7.2	1.9

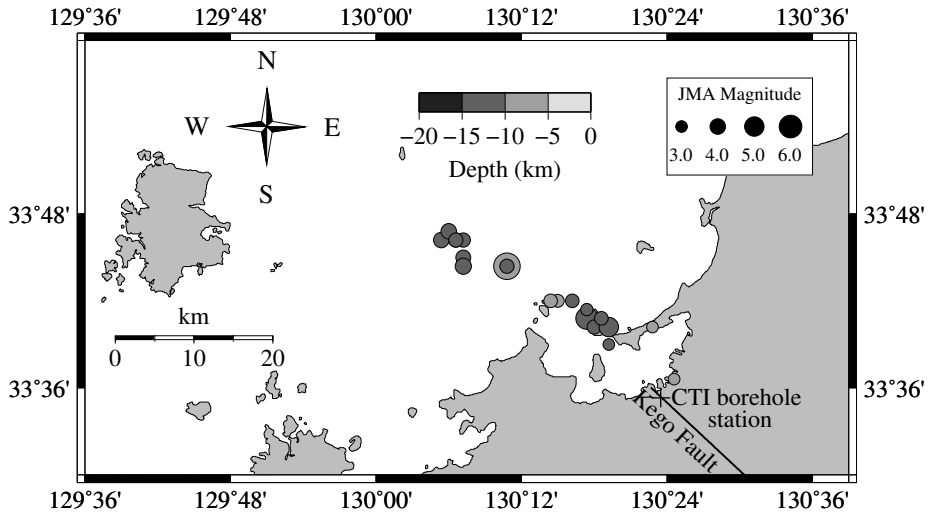

Figure 2.8: Epicenter of the events used in this study.

shown in Figure 2.9 (c). Figure 2.9 (c) shows that the simplification has no influence on the first six resonant frequencies and has only a small influence on higher frequencies. The fundamental frequency of the soil column is found to be 1.4 Hz.

In order to detect resonant frequencies of the soil column in the linear elastic domain, we use aftershocks whose PGA at the basement sensor does not exceed 40 Gal and perform spectral ratios analyses either by choosing a fixed S-wave portion selected by eye or by using a time-dependent (moving window) spectral ratios around the S-wave portion.

Figure 2.10 shows spectral ratios whose S-wave portion has been chosen by eye. The length of the S-wave has been tuned for each earthquake and is generally larger than 1 second and smaller than 5 seconds. A cosine shape of 25% at both ends of the S-wave has been used to smoothly set the data to zero at the boundaries of the window. We can see that observed and theoretical fundamental frequencies in the transverse direction show a good agreement whereas the theory tends to underestimate the fundamental frequency in the radial direction. In order to have a full vision of the directional dependence of spectral ratios, we compute 360° spectral ratios using the aftershocks. 360° spectral ratios are spectral ratios computed by rotating simultaneously in the horizontal plane basement and downhole records from the North and plotting them as a mapped view with respect to their azimuth by using a color code to represent their amplitude. By computing

Table 2.3: Simplified soil profile based on the density and PS logging provided by CTI Engineering.

No.	Depth (m)	Thickness (m)	S-wave velocity (m/s)	P-wave velocity (m/s)	Density (g/cm^3)	Mean of N-values	Soil classification
1	5.5	3.5	152.1	1194.3	1.80	10.25	sand
2	8.5	3.0	165.2	1209.7	1.80	2.67	sand with clay
3	16.5	8.0	248.7	1706.8	1.80	23.12	sand
4	25.5	9.0	229.6	1587.6	1.70	11.56	clay
5	33.0	7.5	351.3	1730.0	1.90	30.00	sand
6	36.0	3.0	289.0	1712.0	1.75	25.00	clay
7	40.0	4.0	324.7	1744.9	1.90	49.00	sand
8	43.0	3.0	282.0	1765.2	1.75	17.00	clay
9	47.0	4.0	411.5	1785.2	1.90	49.50	sand with gravel
10	51.0	4.0	333.2	1689.9	1.80	23.75	clay
11	62.5	11.5	500.6	1808.8	1.95	49.17	gravel
12	∞	∞	500.0	1808.8	2.00	46.00	mudstone

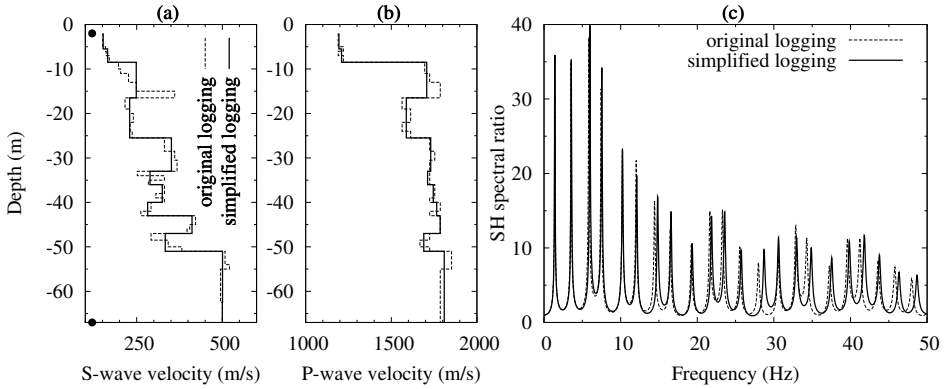

Figure 2.9: Panels (a) and (b) : original and simplified PS logging. Upper and lower sensors (indicated by dots) are located at 2 meters and 67 meters below the free surface, respectively. Panel (c): SH spectral ratio of original and simplified soil column. Few damping has been purposely used to better see the shift of resonant frequencies due to S-wave simplification.

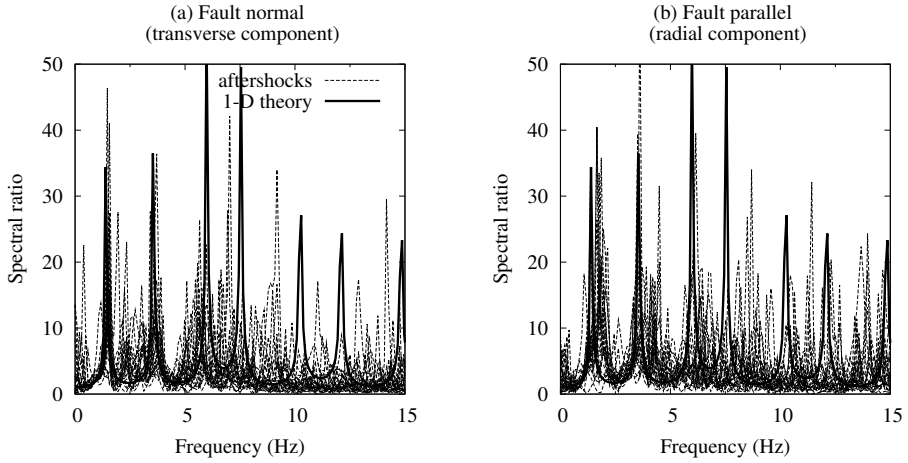

Figure 2.10: Spectral ratios performed on the S-wave portion chosen by sight of aftershocks (dashed lines). The theoretical one-dimensional spectral ratio for a vertically incident S-wave using the velocity logging is plotted as a bold solid line. The left-hand side panel (a) and right-hand side panel (b) show fault normal and fault parallel spectral ratios, respectively. The frequency discretization of spectral ratios is 1/40.96 Hz. A Parzen spectral window (Parzen, 1962) of bandwidth 0.1 Hz has been used to slightly smooth observed and theoretical ratios.

360° spectral ratios on all aftershocks, we find for several spectral ratios that the fundamental frequency forms a spiral instead of forming a circle in accordance with 1-D theory as shown in Figure 2.11. Because of the particular location of the borehole station, this phenomenon could be due either to soil heterogeneity, geometrical effects and/or soil-structure interaction. As for the second resonant frequency, even if its position fluctuates in the observations for both direction, the theoretical peak seems correspond well to the observed ones. The precise position of higher frequencies are hardly seen in the observations.

In order to find the best location of spectral ratios' time windows to observe resonant frequencies, we also perform time-dependent spectral ratios analyses around the S-wave portion of aftershocks. A time-dependent spectral ratio is the ratio of the short-time Fourier transform of the basement record with respect to the downhole record; the short-time Fourier transform being defined as:

$$STFT\left\{x(t)\right\} \equiv x(\tau,\omega) = \int_{-\infty}^{\infty} x(t)w(t-\tau)e^{+i\omega t}\,dt,$$

where $w(t)$ is a window function and $x(t)$ is the signal to be transformed. $x(\tau,\omega)$ is essentially the Fourier transform of $x(t)w(t-\tau)$, a complex function

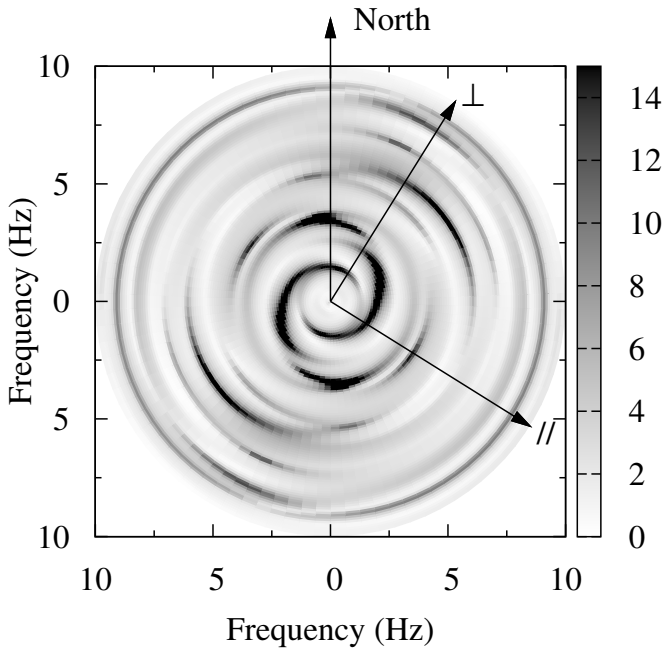

Figure 2.11: 360 degrees spectral ratios of EQ06 in the frequency range 0 to 10 Hz. Spectral ratios are computed by rotating simultaneously basement and downhole records from the North (represented by a vertical arrow). The coordinate (0,0) is the frequency 0 while the radius' end represents the frequency 10 Hz. Plots are symmetric with respect to the center (0,0) due to the equality of Fourier spectra in two opposite directions. Axes denoted by $\perp$ and // indicate fault normal direction (i.e., transverse component) and fault parallel direction (i.e., radial component), respectively.

representing the phase and magnitude of the signal over time and frequency. Time and frequency being conjugate variables, given a signal containing some event, one cannot assign simultaneously an exact time and frequency response scale to that event and consequently, the more precisely one variable is known, the less precisely the other is known. Since we focus in this study on the fundamental frequency of the soil column and its higher modes, the sliding window used to isolate a portion of the waveform is a Tukey window (often called cosine-tapered) of ratio 1 (i.e., no flat portion is present in the Tukey window) and length 2.56 seconds, that is to say, 85% of its length contains approximately three fundamental periods. Sliding windows are overlapped by 96% which corresponds to 0.1 second. Moreover, we do not apply a time shift between basement and downhole sensors to account for the travel time.

We must, however, note that great care has to be taken when analyzing results of such a time-dependent analysis. When the waveform is simple, like a Ricker function, applying the window with smooth tapers at both ends in order to make the waveform causal has few effects on the time-dependent analysis as shown in Figure 2.12. When the smoothing window of length 2.56 s enters into the S-wave portion, resonant frequencies start appearing (e.g., time window 2.4 s), and when the window encloses the main part of the signal, resonant frequencies become clearly visible (e.g., time window 3.0 s). However, when the waveform becomes complex (for instance a summation of random Ricker functions or a natural wave), then time-dependent analysis is influenced by the smoothing window as shown in Figure 2.13. Both amplitude and resonant frequency location can be affected by the window shape. Moreover, the use of Tukey windows with ratios 1.0, 0.5 or 0.25 can give quite different results.

Figure 2.14 presents observed spectral ratio showing a good agreement with theory for the transverse component. We note that time windows for which resonant frequencies are visible in both transverse and radial components are rare. Hence, the transverse component has been chosen since it seems less influenced by soil heterogeneity, geometrical effects and/or soil-structure interaction (we note that soil heterogeneity should affect more higher harmonic frequencies than those corresponding to the fundamental resonant frequency). Spectral ratios' time window shown in this figure have been chosen when the amplitude of the fundamental frequency was the largest; except for EQ03 which shows a better overall agreement with theory for the shown time windows, for EQ04 time window [10.50 - 13.06] s, which is used to show the quick change in the time of peaks' amplitudes, and for EQ17, which shows a better overall agreement with theory for the shown time window. The following comments can be made on Figure 2.14.

- Generally speaking, 1-D theory reproduces well the location of the observed fundamental frequency; however, fluctuations of the location

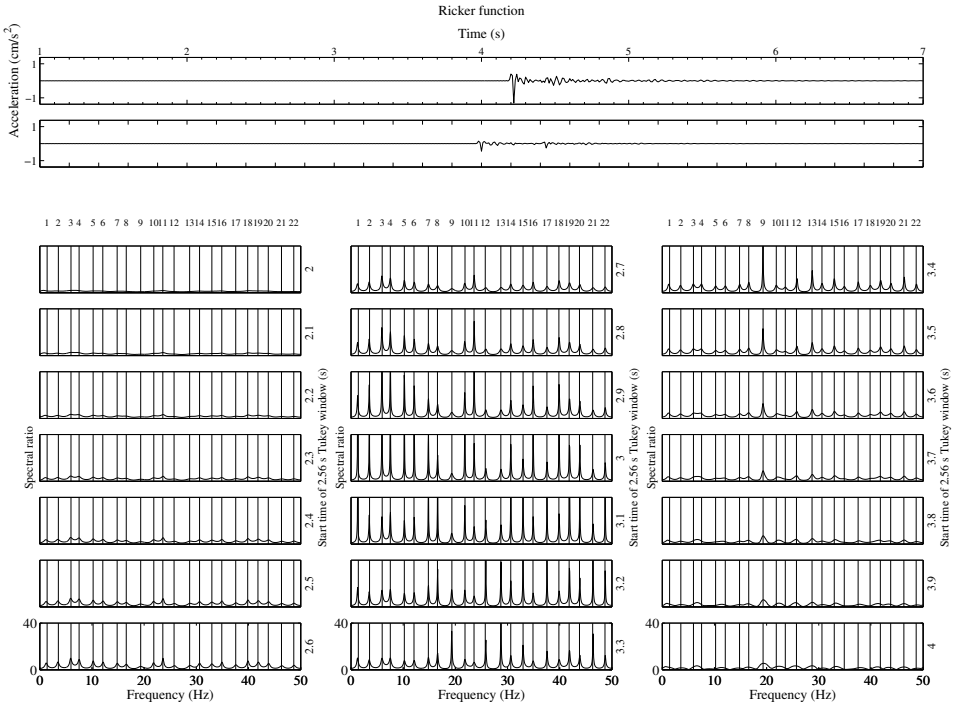

Figure 2.12: Time-dependent spectral ratios analysis performed between downhole and basement waveform when the input wave is a Ricker function of pseudo-frequency 25 Hz. Basement and downhole waveforms are shown on top of the Figure. Ratios are computed using 2.56 s Tukey windows with ratio 1 and translated by 0.1 s (i.e., 96% of overlapping). Numbers on the right-hand side of each panel indicate start time of Tukey windows. X and Y-axes boundaries of spectral ratios are indicated on bottom-most panels. No smoothing window is applied. Vertical lines on spectral ratios panels indicate theoretical resonant frequencies of the velocity logging and theoretical resonant frequencies are numbered by integers above the top-most panel of spectral ratio.

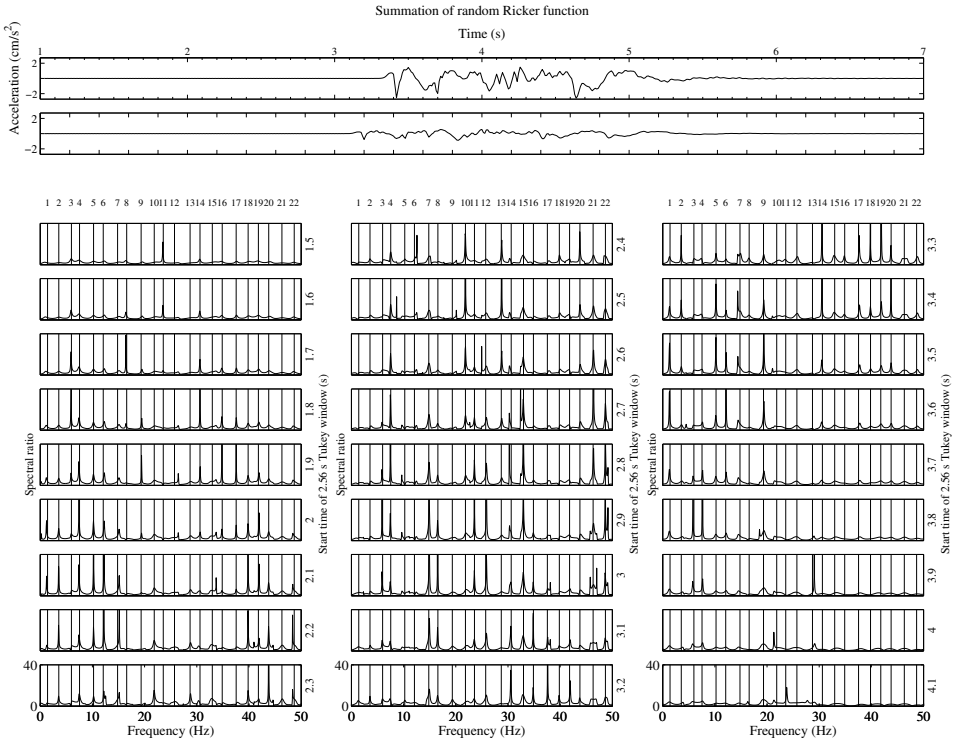

Figure 2.13: Time-dependent spectral ratios analysis performed between downhole and basement waveform when the input wave is a summation of ten Ricker functions whose pseudo-frequency is randomly chosen within the interval 0.5-25 Hz.

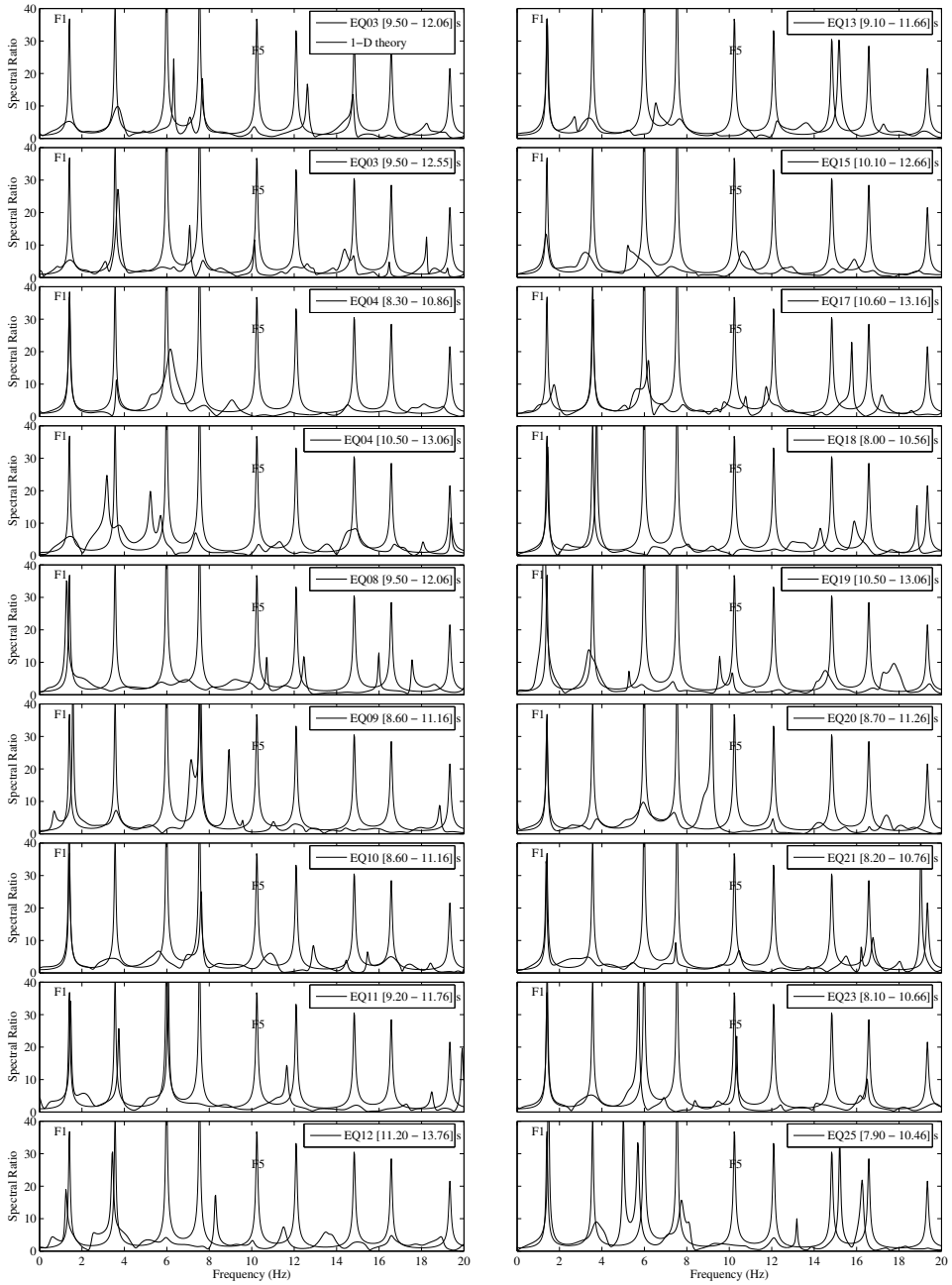

Figure 2.14: Observed spectral ratios computed within S-wave portion of small aftershocks using time-dependent analyses (bold lines) plotted together with 1-D theory (thin lines) in the transverse direction. Theoretical spectral ratios are plotted using a constant damping of the form $\xi = \xi_0 f^{-\alpha}$ with $\xi_0 = 0.01$ and $\alpha = 0.6$. Both observed and theoretical ratios are smoothed using a Parzen window of bandwidth 0.1 Hz. EQ03 and EQ04 are plotted two times with different time window to emphasis the rapid variation in time of the shape of the ratio (especially, the amplitude of the peak). Theoretical resonant frequencies F1, F5 are annotated to facilitate the reading of the Figure.

are seen on observations.

- By comparing the location of the peak along the frequency axis (i.e., without comparing the amplitude of the peak), EQ03 time window [9.50-12.06] s shows, despite small frequency shifts, a good agreement from the fundamental frequency (also called F1 hereafter, F2 being the second theoretical resonant frequency, F3 the third theoretical resonant frequency and so on) to the seventh frequency. The two different time windows for EQ03 and EQ4 exhibit the possible quick change in the time of peaks' amplitudes.

- No spectral ratio shows all the resonant frequencies for a unique time window. For instance, for EQ11, F1, F2 and F3 are visible while F4 and F5 are not; however, F4 is visible on EQ10 while F2 and F3 are absent. This could mean that 1-D wave propagation is not sufficient to thoroughly explain observations or that the smoothing window influences the shape of the ratios.

- For the aftershocks, inversion of damping factors in the frequency domain is not possible due to the above comment.

- EQ09 and EQ20 clearly show a peak between F4 and F5, which would not be a shift of F5 since F5 can be seen on EQ21 or EQ23. Note that the amplitude of input waves for these earthquakes are too low to assume soil nonlinearity.

- Expect for the resonant frequency F5 of EQ09 and EQ20, the locations of the resonant frequencies are well reproduced up to 12 Hz by the 1-D theory.

By considering all the spectral ratios of Figure 2.14 and the possible influence on peaks' location of soil heterogeneity, geometrical effects, soil-structure interaction, incidence angle of the incoming wave, and/or smoothing window effects, we conclude that the S-wave velocity logging is accurate in the linear domain for the transverse direction and does not need to be inverted (if the spectral ratios had shown a better stability, then an inversion on the mean of several spectral ratios would have been possible). The explanation of the shift of the fundamental frequency in the radial direction would need further research, consequently, the following is based on the conclusions drawn up for the transverse direction.

As for the damping factors of each layer used to take into account intrinsic absorption by anelasticity and scattering by heterogeneity, we assume it to be of the form $h = h_0 f^{-\alpha}$ (e.g., Satoh et al., 2001) and constant along the soil column. Since for this study inversion of damping factors in the frequency domain could be influenced by other phenomenon, we adjust it manually by comparing simulations and observations in the time domain

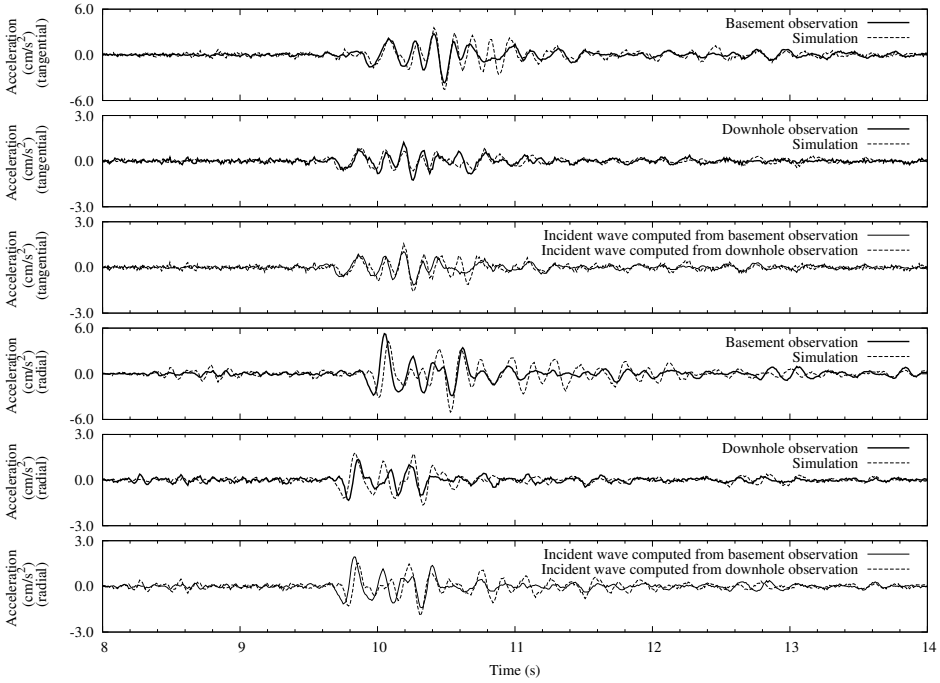

Figure 2.15: Simulations and deconvolutions of EQ11 in transverse and radial direction using S-wave velocity logging and constant damping factor along the soil column of the form $\xi = \xi_0 f^{-\alpha}$ with f the frequency, $\xi_0 = 0.13$ and $\alpha = 0.6$.

and find that $h_0 = 0.13$ and $\alpha = 0.6$ fit well the data. Figure 2.15 shows simulations of basement and downhole acceleration as well as deconvolution from basement and downhole waveform. Reproduction of waveforms in transverse and radial direction is acceptable during the S-wave portion for a 1-D model. Phase shift for the radial component is consistent with the fact that S-wave logging underestimates the observed fundamental frequency, which is shifted to high frequencies (as seen in Figure 2.11). We note that other simulations of aftershocks show a good agreement as well using the same damping factors. This good agreement justifies one more time that the S-wave velocity logging is accurate in the linear domain.

In the following, we will compute spectral ratios on the main shock records and describe the inversion by a genetic algorithm of the S-wave velocity structure and damping factors.

2.1.4 Inversion of the soil structure during the main shock

In order to detect possible nonlinear behavior of the CTI borehole soil column during the 2005 West off Fukuoka earthquake, we perform a time-

dependent spectral ratios analysis in the major and minor axes. For this time-dependent analysis, the beginning of the window is fixed to three seconds (i.e., before the onset of the S-wave portion) and the end of the window is extended incrementally. Spectral ratios in the transverse and radial directions are shown in Figure 2.16 (two top panels) when the amplitude of the fundamental mode is the highest in the transverse direction. At that time, the length of the smoothing window is 5.9 s (i.e., it mainly covers the S-wave portion of the signal). The fundamental frequency originally at 1.41 Hz is shifted to 1.15 Hz in the transverse direction and to 1.32 Hz in the radial direction (the fact that the radial mode has a higher frequency than the transverse one is consistent with observations made on aftershocks). In both directions, the shift toward low frequencies of observed peaks F1, F3, F5 and F6 is typical of nonlinear behavior of soft sediments (i.e., decrease of the shear modulus). However, an inconsistency remains for F4. It is shifted toward low frequencies in the radial direction while it is shifted toward high frequencies in the transverse direction. According to 1-D theory, the decrease of S-wave velocity of some layers can shift certain resonant frequencies toward low frequencies and leave others unchanged; however, it is impossible that this decrease shifts resonant frequencies toward high frequencies as seen for F4 in the transverse direction. A 360° spectral ratios shown in Figure 2.17 reveals that F4 is present for almost all azimuths but disappears in the vicinity of the fault-normal direction (i.e., transverse component) and appears to be shifted to higher frequencies. This shift could, therefore, be due to geometrical effects and/or soil-structure interaction. We note that this peak appears approximately at the location of the additional peak seen for EQ09, EQ12 and EQ20 of Figure 2.14. We also note that F2 and F3 form a clear circle in accordance with 1-D theory while F1 exhibits the same spiral pattern as observed on some aftershocks (e.g., Figure 2.11). As a result, F4 in the transverse direction will be ignored in the 1-D inversion.

In order to quantify S-wave velocity reduction that causes shift of resonant modes toward low frequencies, we invert by a genetic algorithm observed spectral ratios presented in Figure 2.16 using the Thomson-Haskell propagator matrix method. As the S-wave logging transfer function is accurate for simulations of aftershocks, the search space of S-wave velocity is limited to values smaller than or equal to S-wave logging's velocity. However, because of the shift toward high frequencies of F4 in the transverse direction which is inconsistent with the 1-D assumption, the common objective function, which tends to minimize the integrated residuals between observed and theoretical spectral ratios (e.g., Satoh et al., 1995a) cannot be used for this study. Therefore, we introduce a simple objective function that is independent of the global shape of spectral ratios of the form:

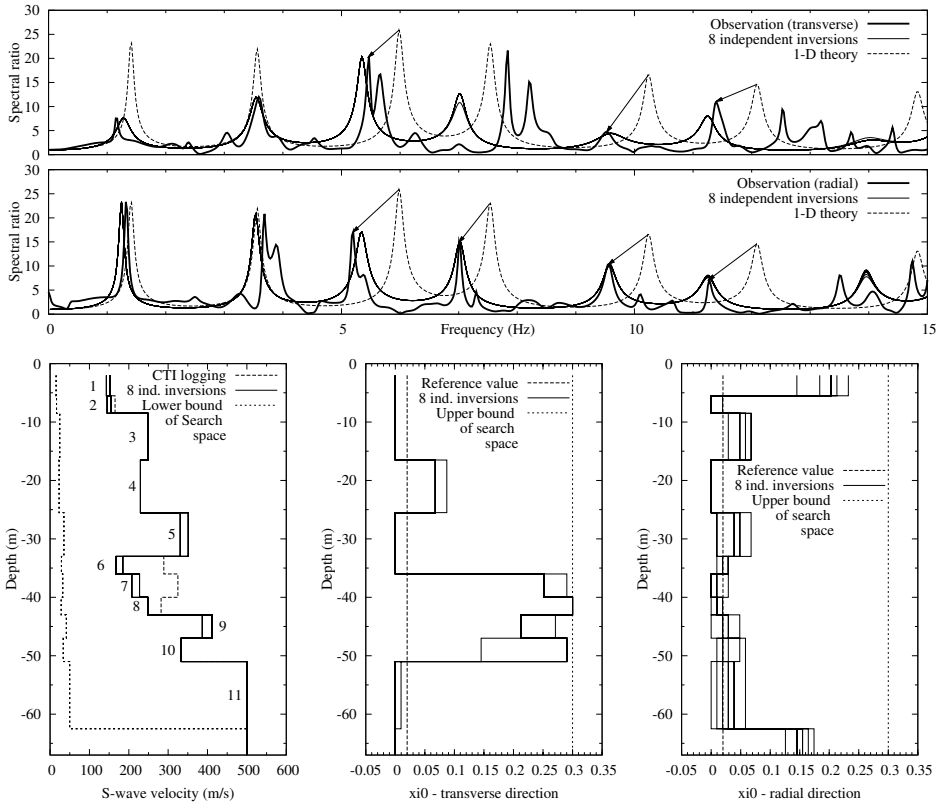

Figure 2.16: First two top panels: spectral ratios observed in transverse and radial direction (bold solid line) plotted together with S-wave logging 1-D theory transfer function (dashed-line) and inverted spectral ratios (thin solid lines) from 8 independent inversions. Logging transfer function has been computed using a constant damping of the form $\xi = \xi_0 f^{-\alpha}$ with $\xi_0 = 0.02$ and $\alpha = 0.6$. Bottom left panel: 8 inverted S-wave velocity structures (thin solid lines) plotted with logging structure (dashed line). A dashed line represents the lower bound of the search space, the upper bound being the logging's structure. Numbers indicate layers of Table 2.3. Bottom middle and right panels: 8 inverted damping factors in transverse and radial direction (thin solid lines). The reference value (bold solid line) is the one used to compute theoretical ratios of the top panels. A dashed line represents the upper bound of the inversion.

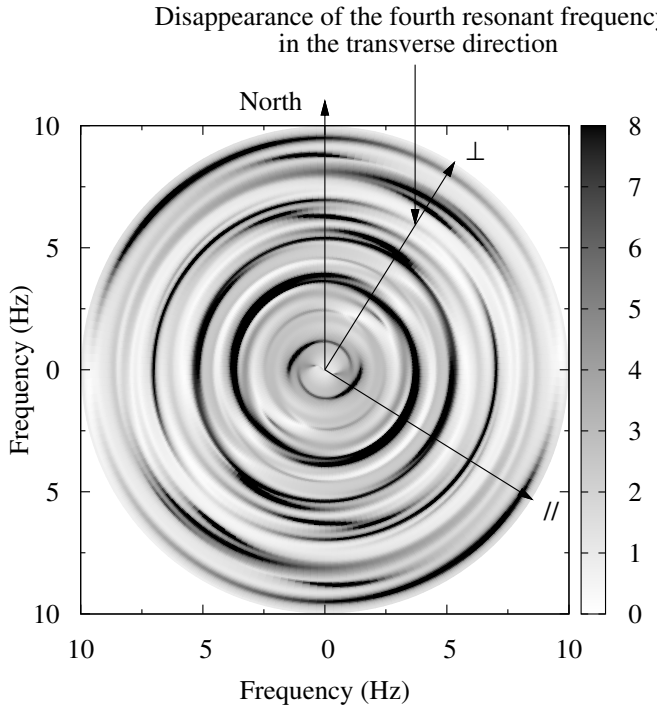

Figure 2.17: 360 degrees spectral ratios computed during EQ01. Axes denoted by $\perp$ and // indicate the fault normal direction (i.e., transverse component) and the fault parallel direction (i.e., radial component), respectively.

$$E(\mathbf{x}) = \frac{\sum_{i=1}^{n_{PF}} \frac{|PF_i^{obs} - PF_i^{the}(\mathbf{x})|}{PF_i^{obs}}}{\sum_{j=1}^{n_{PF}} PF_j^{obs}} + \frac{\sum_{i=1}^{n_{PA}} \frac{|PA_i^{obs} - PA_i^{the}(\mathbf{x})|}{PF_i^{obs}}}{\sum_{j=1}^{n_{PA}} PA_j^{obs}}$$

with $\mathbf{x}$ the vector containing parameters to invert, PF_i^{obs} the i-th observed peak frequency, PF_i^{the} the i-th theoretical peak frequency, PA_i^{obs} the i-th observed peak amplitude, PA_i^{the} the i-th theoretical peak amplitude, n_{PF} the number of peak frequency to use and n_{PA} the number of peak amplitude to use. In order to give more weight to low-frequency peaks, each member is divided by PF_i^{obs}. Normalization by $\sum_{j=1}^{n_{PF}} PF_j^{obs}$ and $\sum_{j=1}^{n_{PA}} PA_j^{obs}$ is done to avoid overweight the frequency or amplitude portions.

This objective function focuses on the location of peaks along the frequency axis and on the amplitude of peaks. Peaks used in an inversion can be chosen at will to calculate the objective function. We note that this objective function has the virtue of being the summation of linear functions of the form $|X_i^{obs} - X_i^{the}(\mathbf{x})|$, which makes its shape simple for inversion techniques in an n-dimensional space. Its disadvantage resides in the fact that one has to know *a priori* which peaks have to be inverted.

Neglecting the fact that large damping factors can increase S-wave velocities due to their contribution in the complex shear modulus (i.e., $G^* = G(1+2i\xi)$, with G the shear modulus and ξ the damping value), we perform two independent inversions by first inverting S-wave velocities to shift theoretical peaks to low frequencies and then damping factors to adjust peak amplitudes (i.e., first and second member of residual $E(\mathbf{x})$ are used independently and normalization by $\sum_{j=1}^{n_{PF}} PF_j^{obs}$ and $\sum_{j=1}^{n_{PA}} PA_j^{obs}$ is omitted). Since the transverse and radial observed resonant frequencies are close and considering the fact that fluctuancy of peaks' location is possible due to phenomena other than the 1-D assumption, we use the mean of observed resonant frequencies between transverse and radial components for PF_i^{obs} except for F4 for which the value of the radial component has been chosen. For peaks' amplitude, we perform independent inversions for transverse and radial components due to the strong discrepancy of amplitudes in the fundamental mode. Table 2.4 summarizes frequencies and amplitudes of peaks targeted for the inversion.

The flowchart of the inversion is presented in Figure 1.17. Prior to the genetic algorithm optimization, a Monte Carlo search is perfomed on five populations of size 2048 binary individuals in order to explore the search space. Each individual represents the S-wave velocity of 11 layers (S-wave velocity of the bedrock has not been inverted since it is assumed to be linear elastic). The minimum bound for the S-wave velocity of each layer is fixed to 0.1 times the S-wave velocity of the logging. The maximum bound is the S-wave velocity from the logging itself since it has been corroborated using small aftershocks. A total of 4 bytes per layer has been used so that the interval [0.1-1.0] is divided into 16 values (called inversion factors hereafter).

Table 2.4: Peak frequency and amplitude before inversion (B) (i.e., using S-wave logging), targeted for the inversion (T) (i.e., selected from observed ones) and inverted (I). Inverted values of peak frequency correspond to resukts of S-wave inversions.

	Peak frequency			Peak amplitude					
				Transverse			Radial		
Frequency	B	T	I	B	T	I	B	T	I
F1	1.41	1.24	1.24	25.32	7.58	7.58	25.32	23.30	23.28
F2	3.56	3.56	3.54	28.27	11.97	11.92	28.27	20.82	20.71
F3	5.86	5.34	5.35	32.57	20.32	20.30	32.57	17.04	16.97
F4	7.74	7.00	6.98	25.05	-	10.81	25.05	15.00	14.97
F5	10.22	9.56	9.59	19.93	4.73	4.51	19.93	10.31	10.25
F6	12.08	11.33	11.32	17.55	10.86	8.09	17.55	7.13	7.69

The total number of possible solutions is therefore $2^{4\times11} = 1.759\times10^{13}$. Coefficient h_0 of the damping factors are inverted for each soil layer and the bedrock within the interval [0.0-0.3] is discretized into 32 inversion factors (i.e., 5 bytes per layer). The total number of possible solutions is $2^{5\times12} = 1.153\times10^{18}$. The exponent α of the damping factors are not inverted and they are fixed to 0.6.

Individuals' transfer functions are computed using the Thomson-Haskell propagator matrix method and are smoothed with the same Parzen window's bandwidth used to smooth observed ratios (i.e., 0.1 Hz). Their objective function is evaluated by $E(\mathbf{x})$. Once the Monte Carlo search is terminated, the best 1024 individuals found are used to generate the initial genetic algorithm population of 1024 individuals. If the termination criterion is not reached (i.e., a small residual or a large number of population), a selection by tournament is performed with a pool of 10 individuals in order to generate the reproduction population of size 1024. Elitism is activated so that if the best 10 individuals are not present in the reproduction population, they are automatically added. The new population is generated with a crossover probability of 85% and a mutation probability of 0.1%. If crossover does not occur, random individuals are generated in the new population to maintain the genetic diversity.

In order to avoid convergence to local minima, the summation of the distance between inversion factors of individuals (i.e., $N(N+1)/2$ additions with N the number of individuals in a population) is monitored and if this summation drops below a threshold, then a new population is generated at random. An example for an inversion of the evolution of the global minimum residual, the minimum residual of new populations and the summation of distance between individuals is shown in Figure 2.18. From population number 20, the objective function does not evolve anymore and the summation

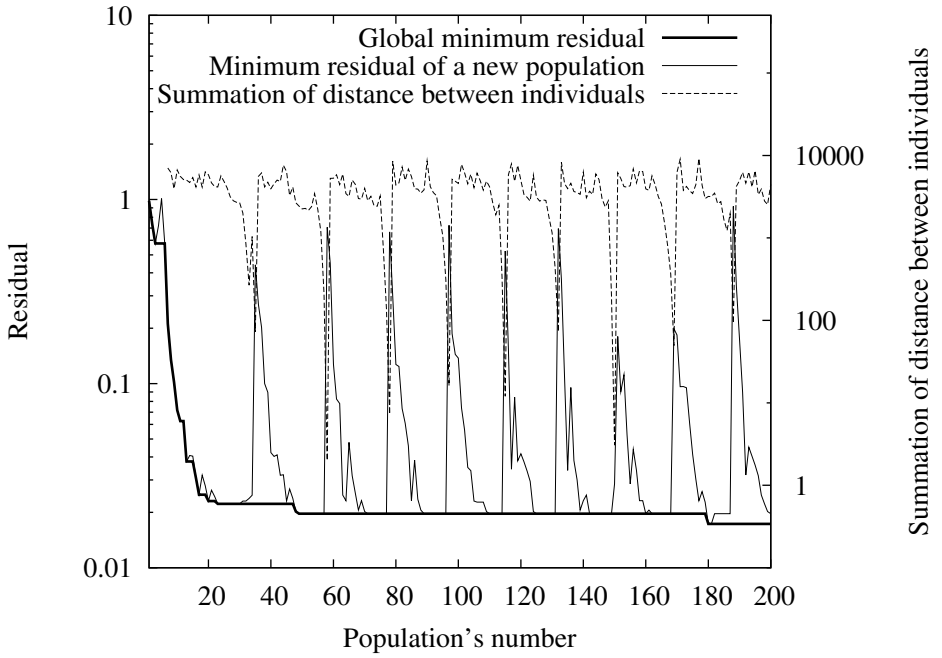

Figure 2.18: Example for an inversion of the evolution of the global minimum residual (bold line), the minimum residual of a new population (thin line) and the summation of distance between individual (dashed line).

of distances between individuals starts decreasing rapidly around population 30. This means that a possible local minimum has been found and that populations start stagnating (i.e., all individuals in a population become identical and offsprings are identical to their parents). In order to avoid such a possible local minimum, a random population is generated when the summation of distance between individuals goes below a threshold fixed to 100 in term of summation of inversion factors. This has almost the effect of starting the inversion from a totally new population; however, the best individuals found so far are still injected inside the reproduction population and can either be improved or participate to build new best individuals in another region of the search space. As a result, better individuals are found around population number 50 and 180 as shown in Figure 2.18.

In order to guarantee the robustness of the solution, eight independent inversions are made to invert either S-wave velocity in the first step or damping factors in the second step. Evolution of the global minimum residual for eight independent inversions of S-wave velocity is shown in Figure 2.19. The first five population correspond to a Monte Carlo search, then genetic algorithm optimization is activated and a fast convergence is visible. After 200 populations, even if a unique minimum is not found, the three distinct

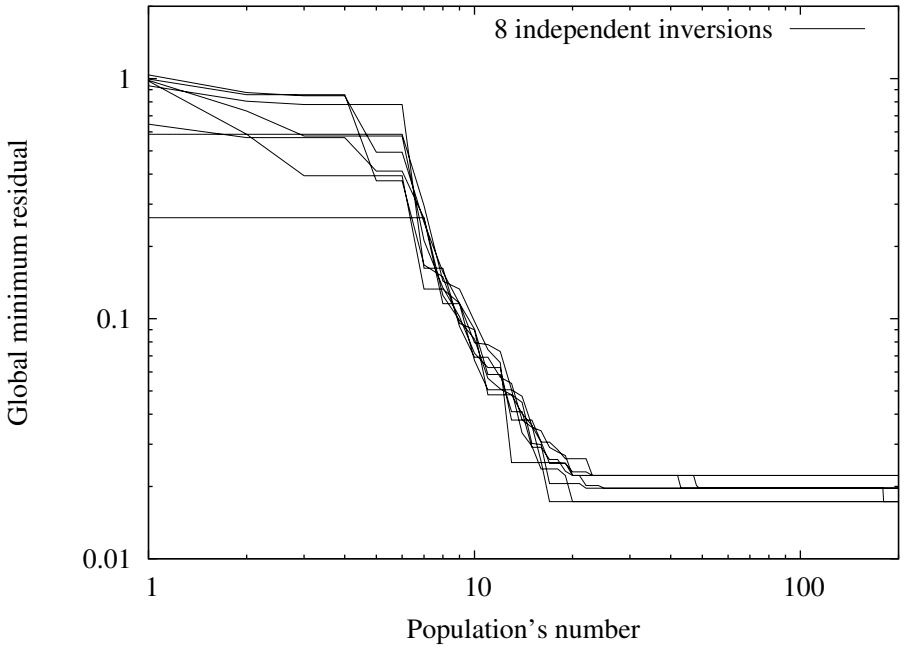

Figure 2.19: Evolution of global minimum residual $E(\mathbf{x})$ of 8 independent inversions with respect to population number.

minima lead to close velocity profiles shown on the bottom left panel of Figure 2.16 and hence this guarantees the robustness of the solution. Inverted damping factors are shown on bottom middle and right panels of Figure 2.16. Even if several minima are found (especially in the radial direction), they are close to each other and this guarantees the quality of the convergence. Corresponding spectral ratios are shown in the first two top panels of Figure 2.16; for some modes, we note that small shifts between inverted resonant frequencies and observed ones are due to the fact that the mean of resonant frequencies between transverse and radial component has been inverted. Accuracy of the inversion is shown in Table 2.4, which compares peaks' frequency and amplitude targeted and inverted. We also note that by inverting only F1, F2, F3, F5 and F6 in the transverse direction, a similar velocity profile is found and F4 goes naturally to 7.0 Hz; hence confirming that the shift toward high frequency of F4 is not consistent with a 1-D assumption.

Moreover, in order to reinforce the inversion obtained by using the objective function $E(\mathbf{x})$ presented above, we perform a separate inversion in the transverse direction by using the traditional objective function which tends to minimize the integrated residuals between observed and theoretical spectral ratios (e.g., Satoh et al., 1995a). Parameters of the search space

and the discretization are identical but S-wave velocity and damping factors are inverted at the same time. To avoid the directional effect on F4 as shown above, the integration is performed from 0.1 to 7.0 Hz and from 9.0 to 12 Hz. Results are shown in Figure 2.20. The localization of the significant decrease of the S-wave velocity is consistent with the previous results and is found to appear in the layers 6 to 9. As for the damping, the order of magnitude is globally the same along the soil column but discrepancies are found for the layers 1 and 5. We note that an inversion performed by integrating the residual from 0.1 to 12 Hz includes the directional effect and leads to different results.

Spectral ratios used for the inversion being taken over the entire S-wave portion, the inverted profile can be used to perform time history simulations of this S-wave portion. Acceleration simulations of the basement are shown in Figure 2.21. The agreement with observations is acceptable in both directions. Nevertheless, observed radial accelerations are often underestimated by the simulation, denoting an overestimation of inverted damping factors in this direction. This can be due to the fact that spectral ratios in both transverse and radial directions have been selected when the amplitude of the spectral ratio in the transverse direction was the highest whereas the amplitude of the spectral ratio in the radial direction was not at its highest point. In order to clearly see the effect of the decrease of the S-wave velocity on the S-wave portion of the basement acceleration, Figure 2.22 shows the simulation of the acceleration in the transverse direction using the elastic linear soil properties and a 1% constant damping along the soil column. The amplitude and the duration of the signal are clearly overestimated. However, a simulation using the elastic linear soil properties and a commonly used 5% damping reproduced quite well the observation as shown in Figure 2.23.

With regards the localization of nonlinearity with depth, the reduction of the S-wave velocity around 35 meters depth is consistent with the variation table of peak frequency of the soil column presented in Figure 2.24. The fact that the observed second resonant frequency did not shift under loading as seen on Figure 2.16 means that significant nonlinear behavior could take place only within layers 6 and 7 that have no influence on the second mode. We also note that in the transverse direction, the increase of damping factors is not always consistent with the decrease of S-wave velocity. The ratio of the length of the decrease of S-wave velocity to the length of the increase of damping is approximately 93%. This can be due to the fact that the inversed solution is not the best one or that other phenomena which influence the shape of the ratio as soil-structure interaction or geometrical effects are included in the inversion. This discrepancy is even more obvious in the radial direction. This suggests that for this site, independent inversions should be carried out in the transverse and radial directions.

We also note that damping factors adjusted during the aftershocks seem

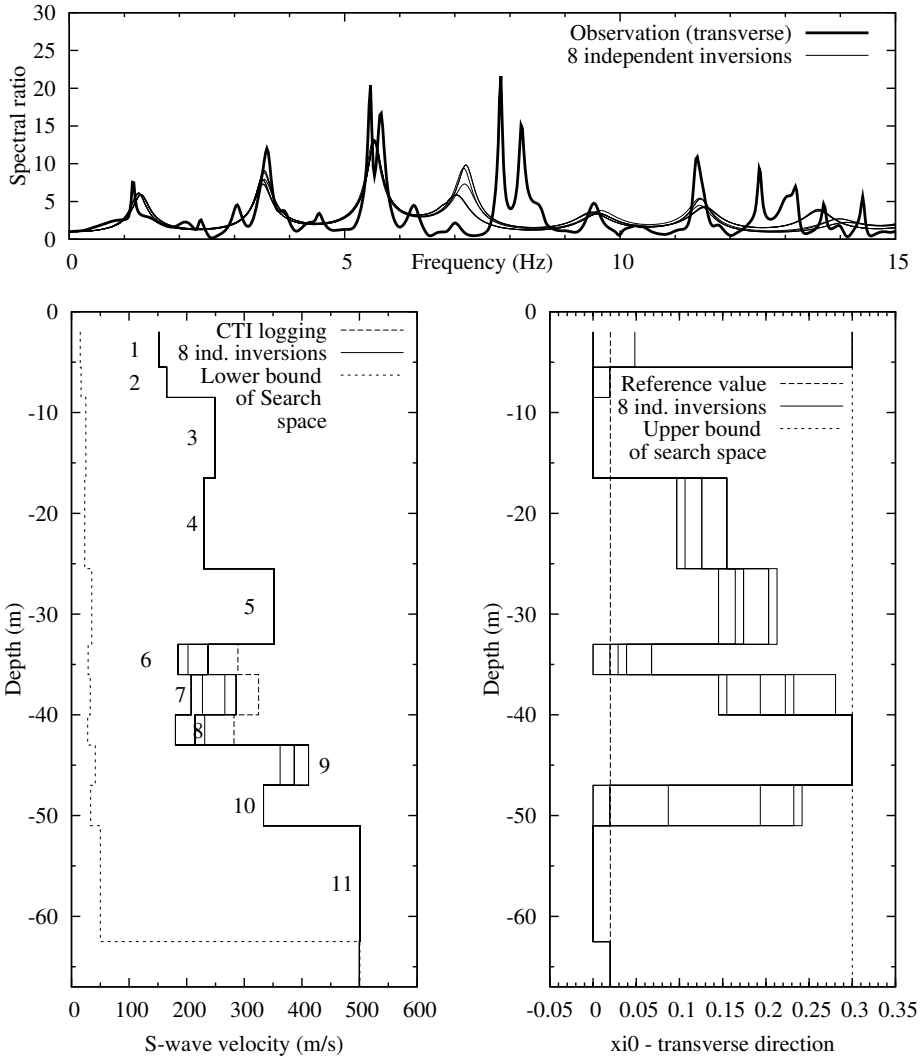

Figure 2.20: Results of 8 independent inversions obtained by using the conventional objective function (e.g., Satoh et al., 1995a). Top panel: spectral ratios observed in transverse direction (bold solid line) plotted together with inverted spectral ratios (thin solid lines) from 8 independent inversions. Bottom left panel: 8 inverted S-wave velocity structures (thin solid lines) plotted with logging structure (dashed line). Bottom right panel: 8 inverted damping factors in transverse direction (thin solid lines).

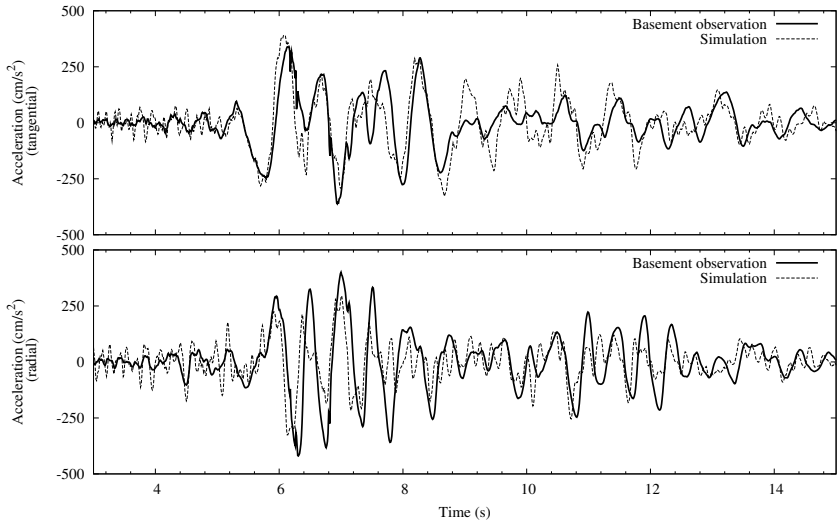

Figure 2.21: Comparison between observed (solid line) and simulated (dashed line) acceleration at the basement in transverse and radial directions for the main shock.

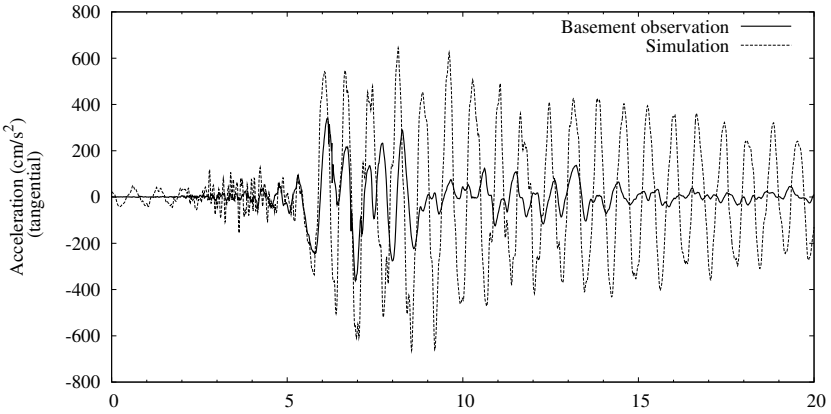

Figure 2.22: Comparison between observed (solid line) and simulated (dashed line) acceleration at the basement in the transverse directions using the elastic linear soil properties and a constant 1% damping along the soil column.

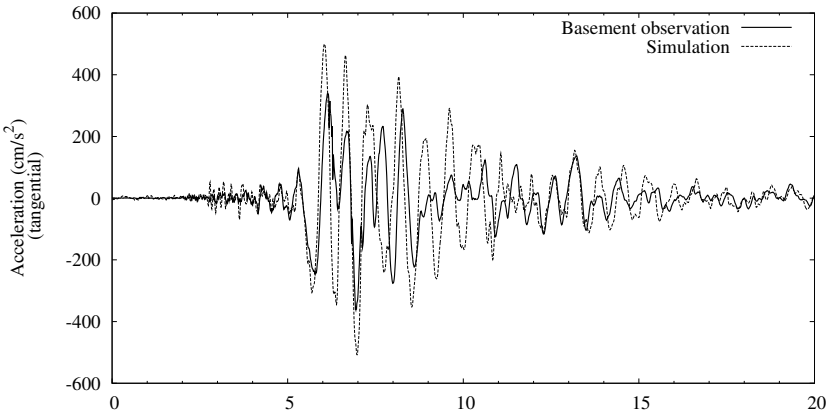

Figure 2.23: Comparison between observed (solid line) and simulated (dashed line) acceleration at the basement in the transverse directions using the elastic linear soil properties and a constant 5% damping along the soil column.

too high compared to those inverted during the main shock. This can be due to the fact that the damping found for aftershocks is an equivalent damping manually adjusted in the time domain (because the amplitude of the resonant peaks in the frequency domain were not constant), consequently, this equivalent damping is mainly controlled by scattering around the fundamental frequency and is not comparable with damping factors inverted in the frequency domain for the main shock. Besides, as noted by Satoh et al. (2001), the reason why the strain dependence of damping factors is not as significant as that of shear modulus ratios may be because scattering attenuation is dominant in the low-strain range.

Shear modulus ratios versus shear strain are compared in Figure 2.25 with laboratory test results from Seed and Idriss (1970b) for sand and gravel and from Vucetic and Dobry (1991) for clay (due to the fact that peaks' amplitude is more sensible than peaks' frequency when doing spectral ratios as shown before, only shear modulus reduction is compared with standardized curves). Shear strain levels of layers are calculated using the S-wave velocity logging and a constant damping along the soil column adjusted to 5% to best reproduce the basement and downhole acceleration time histories (this technique to compute the strain level is used because the Thomson-Haskell propagator code developped here does not compute the strain level at the middle of each layer). As for sand and gravel layers, it is clear that results of the inversion are situated above standardized curves. This result can be explained by the following facts:

- for layers below 40 m depth, the effective vertical stress (overburden

	F01		F02		F03		F04		F05		F06	
	1.42		3.56		5.98		7.54		10.23		12.08	
L01		0.00		0.06		0.22		0.39		0.50		0.61
L02		0.00		0.20		0.78		0.78		0.46		0.33
L03		0.02		0.20		0.24		0.12		0.37		0.42
L04		0.07		0.24		0.09		0.30		0.43		0.41
L05		0.05		0.03		0.18		0.05		0.42		0.13
L06		0.13		0.00		0.39		0.26		0.33		0.78
L07		0.10		0.00		0.20		0.29		0.05		0.29
L08		0.13		0.07		0.13		0.46		0.39		0.07
L09		0.05		0.05		0.00		0.10		0.34		0.24
L10		0.10		0.15		0.05		0.05		0.49		0.73
L11		0.05		0.10		0.14		0.10		0.08		0.12
L12		0.13		0.13		0.26		0.26		0.26		0.26
L13		0.07		0.13		0.26		0.33		0.39		0.39

Figure 2.24: Variation table of theoretical resonant frequencies with respect to S-wave velocity of a soil layer computed for a vertically incident S-wave using the velocity logging. F followed by a number denotes a resonant frequency and L followed by a number denotes a layer (corresponding to Table 2.3). Float numbers indicate resonant frequencies' value. Vertical lines symbolically represent the original location of a resonant frequency Fi and horizontal lines located on the left-hand side and right-hand side of vertical lines quantitatively represent the amount of shift of the frequency Fi normalized by the height of the layer Lj with respect to the decrease or increase of the S-wave velocity of the soil layer Lj. Factors used to decrease or increase the S-wave velocity of a soil layer are 0.8 and 1.2, respectively. Float numbers quantitatively indicate the amount of shift.

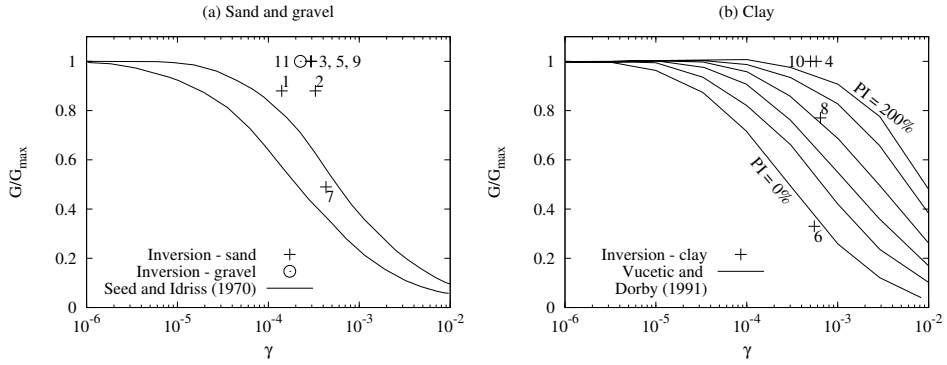

Figure 2.25: (a) Comparison of the strain-dependent characteristics inverted for sand and gravel layers with laboratory test results for sand (Seed and Idriss, 1970b) whose effective vertical stress ranges from 0.05 to 0.5 MPa. (b) Comparison of the strain-dependent characteristics inverted for clay layers with laboratory test results for clay (Vucetic and Dobry, 1991) whose plasticity index (PI) ranges from 0% to 200%. For both panel, numbers indicate layers of Table 2.3.

pressure) is larger than the one used to draw the upper bound of the standardized curves and since the higher the effective vertical stress the lower the shear modulus reduction with respect to shear strain, shear modulus ratios for layers 9 or 11 are consistent with standardized curves since they are located above them. A better agreement should be obtained by using depth-dependent shear modulus reduction curves.

- for layers between the free surface and 40 m depth, strain levels calculated by using the S-wave velocity logging and a constant damping of 5% might be higher than the reality due to the dissipation of energy that took place in layers 6, 7 and 8; consequently, shear moduli found by inversion are consistent with the shift of resonant modes but shear strain levels might be overestimated by the 1-D linear assumption.

As for clay, standardized curves show a clear dependence of shear modulus ratios with respect to plasticity index, especially for large shear strain levels. Since the plasticity indexes for the soil column of this study are unknown, an accurate comparison is not possible.

2.2 Conclusion

In order to detect nonlinear behavior of soft soil during the 2005 West off Fukuoka earthquake, we have first corroborated the S-wave velocity logging in the linear elastic domain by using time-dependent spectral ratios analyses.

Despite a good agreement between observation and theory in the transverse direction for several resonant modes, the observed fundamental mode in the radial direction exhibits a higher resonant frequency. We found by using 360° spectral ratios that a clear drift of the fundamental mode was visible in the radial direction might be due to either soil heterogeneity, geometrical effects and/or soil-structure interaction. Moreover, because of a large inhomogeneity of peak amplitudes amongst aftershocks, frequency-dependent damping factors have been adjusted in the time domain.

Then to show qualitative evidence of nonlinearity during the main shock we have performed a time-dependent spectral ratios analysis, which showed that several resonant modes were shifted toward low frequencies; thus pointing out shear moduli reduction for high shear strain levels.

Finally, in order to evaluate the degree of nonlinearity, we have inverted by a genetic algorithm the equivalent linear S-wave velocity and damping factors on the S-wave portion via the Thomson-Haskell propagator matrix method. Because of effects inconsistent with the 1-D assumption in the transverse direction, common objective functions which minimize integrated residuals between observed and theoretical spectral ratios could not be used. We have, therefore, introduced an objective function depending only on peak frequency and peak amplitude in order to choose which modes to invert. We note that in cases where soil heterogeneity, geometrical effects and/or soil-structure interaction affect the 1-D assumption, transverse and radial directions could be inverted separately. The robustness of the inversion on S-wave velocity was shown by performing eight independent inversions that lead to minima associated with close velocity profiles; thus guaranteeing a convergence toward a probable global minimum. However, for inversion results in general, it can be useful to show the 10% best solutions near the best individual found in order to see the dispersion around this individual.

In the following Part, we present high-performance numerical tools to deals with 1D/2D and 3D site effects. In Chapter 3, we first summarize the main nonlinear methods exposed in the literature. Then, a simple nonlinear constitutive law (a pertectly-plastic law using the Mohr-Coulomb criteria) and an advanced nonlinear constitutive law (Aubry et al., 1982) implemented in the GEFDyn code are tested on the soil column of Fukuoka (cf. Chapter 2). In Chapter 4, we develop and verify 1-D, 2-D and 3-D spectral elements codes (EFISPEC1D, EFISPEC2D and EFISPEC3D) based on the detailed explanations given by Komatitsch (1997).

Part II

High-Performance Numerical Tools to Simulate 1D/2D/3D Site Effects

Chapter 3

Nonlinear Finite Elements Simulations

3.1 Stress-Strain Behavior of Cyclically Loaded Soils

The constitutive relationship which relates the stress τ_{ij} to the strain ϵ_{ij} is an important characteristic of the medium; it has a direct effect on the acceleration as shown in the equation of motion and consequently, influences particles motion in wave propagation. Numerous models have been developped and are still being developped because the behavior of soil is very complex. Therefore, any attempt to incorporate various features of soils properties in a single mathematical model is not likely to be successful. Even if such a model could be constructed, it would be far too complex to serve as the basis for the solution of pratical seismological or geotechnical engineering problems. Simplifications and idealizations are essential in order to produce models that can represent the main properties of the soils related to a given application. The point at which the conflicting requirements of simplicity and accuracy are balanced depends on many factors, and many combinations have been proposed. The evaluation of these models is in general based on the following three considerations:

- Theoretical evaluation of the models with respect to the basic principles of continuum mechanics to ascertain their consistency with the theoretical requirements of continuity, stability and uniqueness.

- Experimental evaluation of the models with respect to their suitability to fit experimental data and the ease of the determination of the material parameters from standard test data.

- Numerical and computational evaluation of the models with respect to the facility with which they can be implemented in computer calculations.

For the purpose of this thesis, three broad classes of soil models will be briefly exposed in order to choose the most appropriates to compute the nonlinear responses of soils based on the three above-mentioned considerations. These models are

- the equivalent linear models;
- the cyclic nonlinear models;
- simple and advanced constitutive models (also called perfectly-plastic constitutive models and hardening-plastic constitutive models, respectively).

Detailed mathematical descriptions of these models can be found in Chen and Mizuno (1990); Kramer (1996); Potts and Zdravkovic (1999).

3.1.1 Equivalent linear model

The equivalent linear approach is most commonly used in practice in geotechnical engineering. It assumes that a multi-layered soil subjected to a symmetric cyclic shear loading exhibits a hysteresis loop (see Figure 3.1), which relates the shear stresses τ to the cyclic distortion γ. This hysteresis loop is first characterized by the secant shear modulus G_{sec}, which represents the loop inclination:

$$G_{sec} = \mu_{sec} = \frac{\tau_c}{\gamma_c}$$

where τ_c and γ_c are the shear stress and shear strain amplitudes, respectively. The loop area A_{loop} represents the energy dissipation and is conveniently described by the damping ratio ξ, given by:

$$\xi = \frac{1}{2\pi} \frac{A_{loop}}{G_{sec}\gamma_c^2}.$$

The parameters G_{sec} and ξ are often referred to as *equivalent linear* material parameters. The equivalent linear procedure then consists in providing $G - \gamma$ and $\xi - \gamma$ curves, expressing the evolution of both parameters with respect to the cyclic distortion. These curves can be constructed by laboratory tests as shown in Figure 3.2 (e.g., Seed and Idriss, 1970b; Kokusho, 1980; Seed et al., 1986) and then used for numerical computations. Such a linear procedure is hence not capable of predicting permanent strains or failure, for high seismic distortion levels. Moreover, the past experience in the use of the equivalent linear method leads to the conclusion that for problems where strain levels remain low (stiff soil profiles and/or relatively weak input motions), this method provides reasonable results, however, for problems involving high strain levels, this method tends to overestimate the shear modulus reduction and the increase of damping (Joyner and Chen,

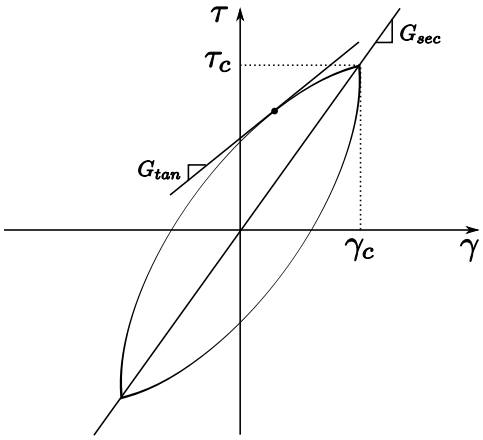

Figure 3.1: Definition of parameters of an equivalent linear model.

1975; Martin and Seed, 1978; Dikmen and Ghaboussi, 1984). Nevertheless, it is still widely used in practice because it allows a very efficient class of computational models to be used for earthquake and geotechnical engineering.

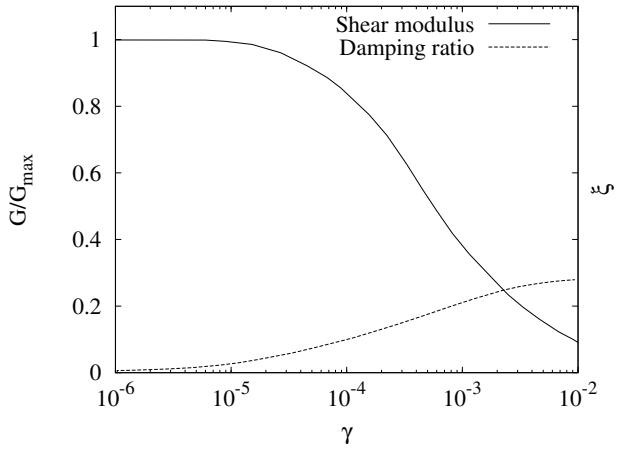

Figure 3.2: Shear modulus (solid line) and damping ratio (dashed line) versus shear distorsion from Seed and Idriss (1970b).

3.1.2 Cyclic nonlinear models

The nonlinear stress-strain can be represented more accurately by cyclic nonlinear models that follow the actual stress-strain path during cyclic load-

ing. Such models are able to represent the shear strength of the soil, and with an appropriate pore pressure model, changes in effective stress during undrained cyclic loading (e.g., Finn et al., 1977; Bonilla, 2000). A variety of cyclic nonlinear models has been developed; all are characterized by

- a backbone curve
- and a series of "rules" that govern unloading-reloading behavior, stiffness degradation and other effects.

The reader is referred to Bonilla (2000) for a view of the history and evolution of the different series of rules that govern unloading-reloading behavior.

To summarize briefely, the concept and the first rules were initially exposed by Masing (1926). Then, several models have followed and improved these rules (e.g., Iwan, 1967; Finn et al., 1977; Pyke, 1979; Vucetic, 1990). The performance of cyclic nonlinear models can be illustrated by a very simple example in which the shape of the backbone curve is described by $\tau = F_{bb}(\gamma)$. The shape of any backbone curve is tied to two parameters, the initial (low-strain) stiffness and the (high-strain) shear strength of the soil. For the simple example, the backbone function, $F_{bb}(\gamma)$, can be described by a hyperbola

$$F_{bb}(\gamma) = \frac{\mu_{max}\gamma}{1 + (\mu_{max}/\tau_{max})|\gamma|}.$$

The shape of the hyperbolic backbone curve is illustrated in Figure 3.3. Other expressions (e.g., Ramberg and Osgood, 1943) can also be used. The response of the soil to cyclic loading is governed by the first two rules given by Masing (1926):

1. for initial loading, the stress-strain curve follows the backbone curve;
2. if a stress reversal occurs at a point defined by (γ_r, τ_r), the stress-strain curve follows a path given by

$$\frac{\tau - \tau_r}{c_H} = F_{bb}\left(\frac{\gamma - \gamma_r}{c_H}\right),$$

where c_H, the hysteresis scale factor, acts on the slope of the reversal curve. Initially, Masing used $c_H = 2$ and the first work for controlling the hysteresis scale factor has been done by Pyke (1979). He suggested that this factor could be stress depend as

$$c_H = \left|\pm 1 - \frac{\tau_r}{\tau_{max}}\right|$$

where the sign is chosen positive for loading and negative for unloading. This operation is known as the Cundall-Pyke hypothesis because they both reached the same formulation independently (Pyke, 1979).

These two rules are however not sufficient to describe the soil response under a general cyclic loading since the maximum stress τ_{max} can be exceeded. As a results, additional rules have been expressed:

3. if the unloading or reloading curve exceeds the maximum past strain and intersects the backbone curve, it follows the backbone curve until the next stress reversal;

4. if an unloading or reloading curve crosses an unloading or reloading curve from the previous cycle, the stress-strain follows that of the previous cycle.

Models that follow these four rules are often called *extended Masing models*. These rules mimic (without mathematical formulations) the yield stress conditions and the progressive mobilization of plasticity through strain hardening mechanisms of the advanced constitutive models that are exposed in the following of this section.

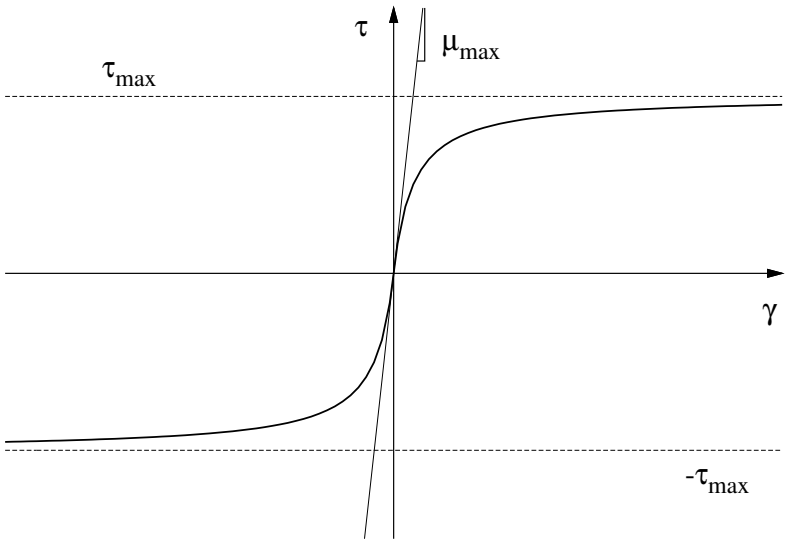

Figure 3.3: Hyperbolic backbone curve asymptotic to $\tau = \mu_{max}\gamma$ and to $\tau = \tau_{max}$ and $\tau = -\tau_{max}$.

An interesting point of the cyclic nonlinear models is that the backbone curves can be constructed directly from the shear modulus reduction curves (data that tend to be more and more available on a site as the elastic parameters ρ, α and β). As an example, Figure 3.4 shows a laboratory tests curves from Seed et al. (1986) as a backbone curve. On the contrary of the equivalent linear method, the damping curve provided by laboratory tests

cannot be used directly. However, the amount of damping can be controlled by tunning the value of c_H. In Figure 3.4, two reversals at (γ_r, τ_r) are shown with $c_H = 1$ and $c_H = 2$. A modulus reduction curve presented by Seed et al. (1986) and the associated damping curves for $c_H = 1.0$, $c_H = 1.5$ and $c_H = 2.0$ are shown in Figure 3.5. As we can see, an increase of the parameter c_H increases the damping with respect to the strain level.

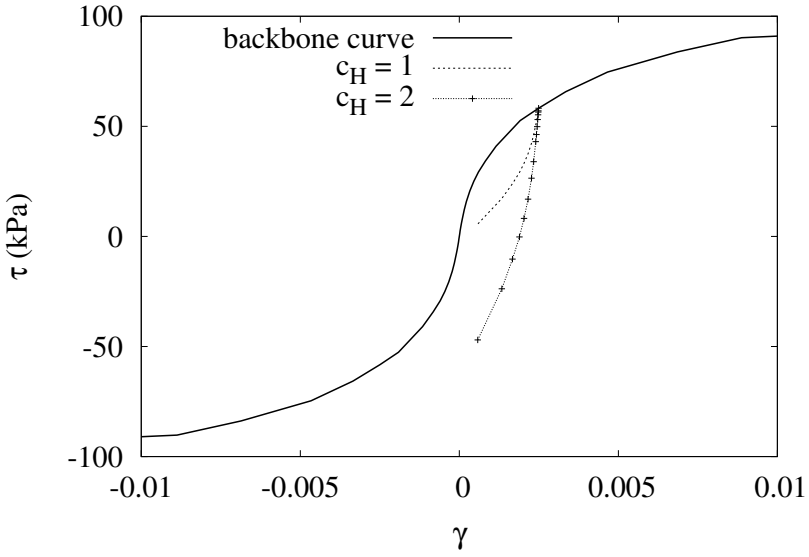

Figure 3.4: Backbone curve (bold line) using a laboratory curve from Seed et al. (1986). Two reversals are shown with $c_H = 1$ and $c_H = 2$.

Note that the cyclic nonlinear model does not require the shear strain to be zero when the shear stress is zero. The ability to represent the development of permanent strains is one of the most important advantages of the cyclic nonlinear models over the equivalent linear models. However, cyclic nonlinear models do not allow for the determination of shear-induced volmetric strains that can lead to hardening under drained conditions or to pore pressure development with attendant stiffness degradation under undrained conditions.

3.1.3 Simple and advanced constitutive models

The perfectly-plastic or hardening-plastic constitutive models (i.e., simple and advanced constitutive models, respectively), mainly considering an elastoplastic constitutive behavior for soil deposits, are able to reproduce the intrinsic complex features of soil behavior under seismic loading in a wide range of shear strains, namely from 10^{-6} to 10^{-2}. Hardening-plastic constitutive models can reproduce stiffness degradation, irrecoverable displace-

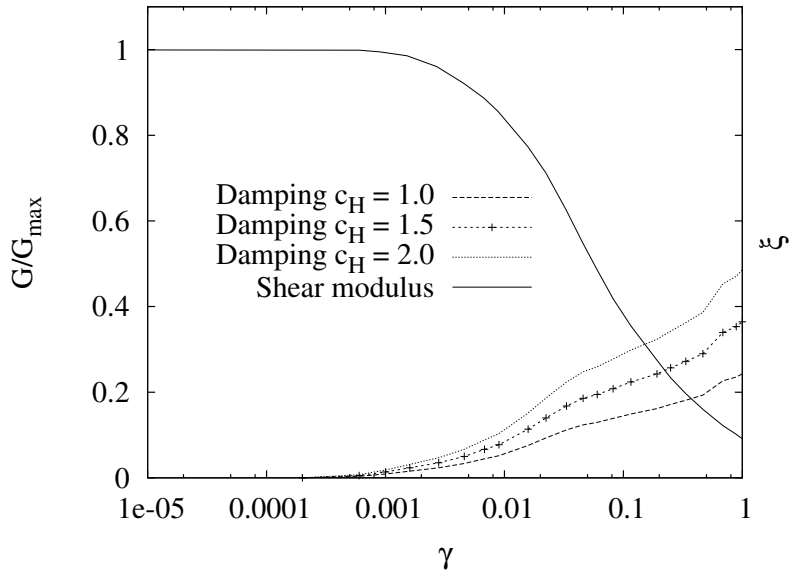

Figure 3.5: Modulus reduction curve from laboratory tests (Seed et al., 1986) plotted together with damping curves for $c_H = 1.0$, $c_H = 1.5$ and $c_H = 2.0$.

ment, volumetric strain generation, etc. The use of models based on the elastoplasticity theory is more suitable than equivalent-linear approach as they represent a rational mechanical process.

"Plastic" behavior of solids is characterized by a non-unique stress-strain relationship (as opposed to that of nonlinear elasticity). Indeed, one definition of plasticity may be the presence of irrecoverable strains on load removal. If uniaxial behavior of a material is considered, as shown in Figure 3.6-(a), a nonlinear relationship on loading alone does not determine whether nonlinear elastic or plastic behavior is exhibited. Unloading will immediately discover the difference, with the elastic material following the same path and the plastic material showing a history-dependent, different, path.

Materials that have a perfectly-plastic behavior (i.e., a simple constitutive model), as shown in Figure 3.6-(b), have a limiting yield stress, σ_y, at which the strains are indeterminate. For all stresses below such a yield, a linear (or nonlinear) elasticity relationship is assumed. The yield surface (i.e., surface in the stress space which delimits the linear and plastic behavior) is often determined by a Tresca, von Mises, Mohr-Coulomb or Drucker-Prager criteria. Figure 3.7 (left-hand side) shows the yield surface in the Mohr plane, characterized by the cohesion c and the internal friction angle φ. Figure 3.7 (right-hand side) describes the shape of a hysteresis loop in the plane γ - τ. By using a Mohr-Coulomb yield surface for instance, only two

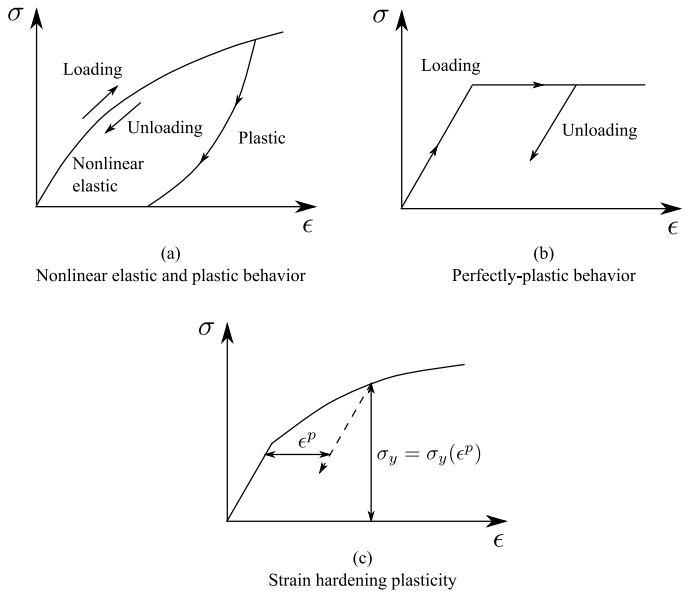

Figure 3.6: Example of uniaxial behavior of real materials.

new parameters (i.e., c and φ) are needed in addition to the elastic parameters to fully describe the simple constitutive model. From the parameters that describe the hysteresis loop shown in Figure 3.8, the ratio between the maximum shear modulus and the secant shear modulus as a function of the deformation γ_a can be derived in a close mathematical form as

$$\frac{G_{sec}}{G_{max}} = \frac{\gamma_{lim}}{\gamma_a}. \tag{3.1}$$

The same reasoning leads to a damping ratio of the form

$$\xi = \frac{2}{\pi}\left(1 - \frac{\gamma_{lim}}{\gamma_a}\right) = \frac{2}{\pi}\left(1 - \frac{G_{sec}}{G_{max}}\right). \tag{3.2}$$

The shortcoming of the perfectly-plastic behavior is that the shear modulus reduction curves and damping factor curves given by Equations (3.1) and (3.2) are far to represent a smooth shape as exhibited by the laboratory tests. Figure 3.9 plots these equations together with the laboratory tests from Seed et al. (1986): we can see that once the plasicity domain is reached, the decrease of the shear modulus is too sharp and the increase of damping as well. Moreover, the damping is highly overestimated.

Some other advanced constitutive models use the critical state concept, with one or more yield stress conditions depending on the loading type (monotonous or cyclic), represented as yield surfaces in the stress space,

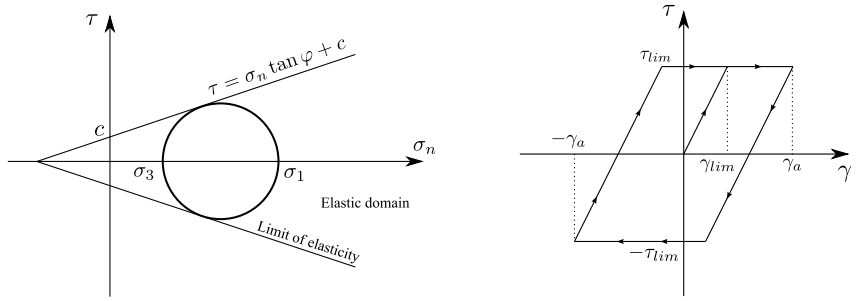

Figure 3.7: Left panel: Schematic representation of Mohr-Coulomb criterion in the plane $\sigma_n - \tau$ (i.e., normal stress - shear stress). The cohesion is defined by the letter c and the limit of elasticity is defined by the straight line $\tau = \sigma_n tan\varphi + c$. σ_1 and σ_3 are major and minor principal stress defining the Mohr circle. Right panel: Schematic representation of the nonlinear stress-strain constitutive law. Arrows indicate the stress-strain path of a full hysterisis under sinusoidal cyclic loading. Plasticity arises when the stress state reaches the limit of elasticity of Mohr-Coulomb criterion.

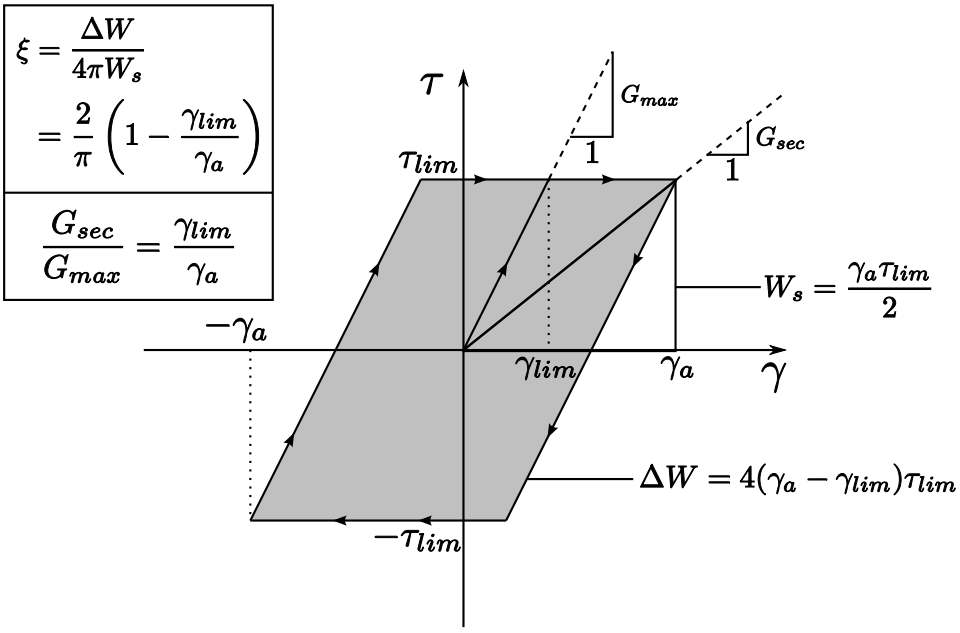

Figure 3.8: Hysteresis loop for a perfectly-plastic behavior and definition of the variables used to express the ratio $\frac{G_{sec}}{G_{max}}$ and the damping factor ξ.

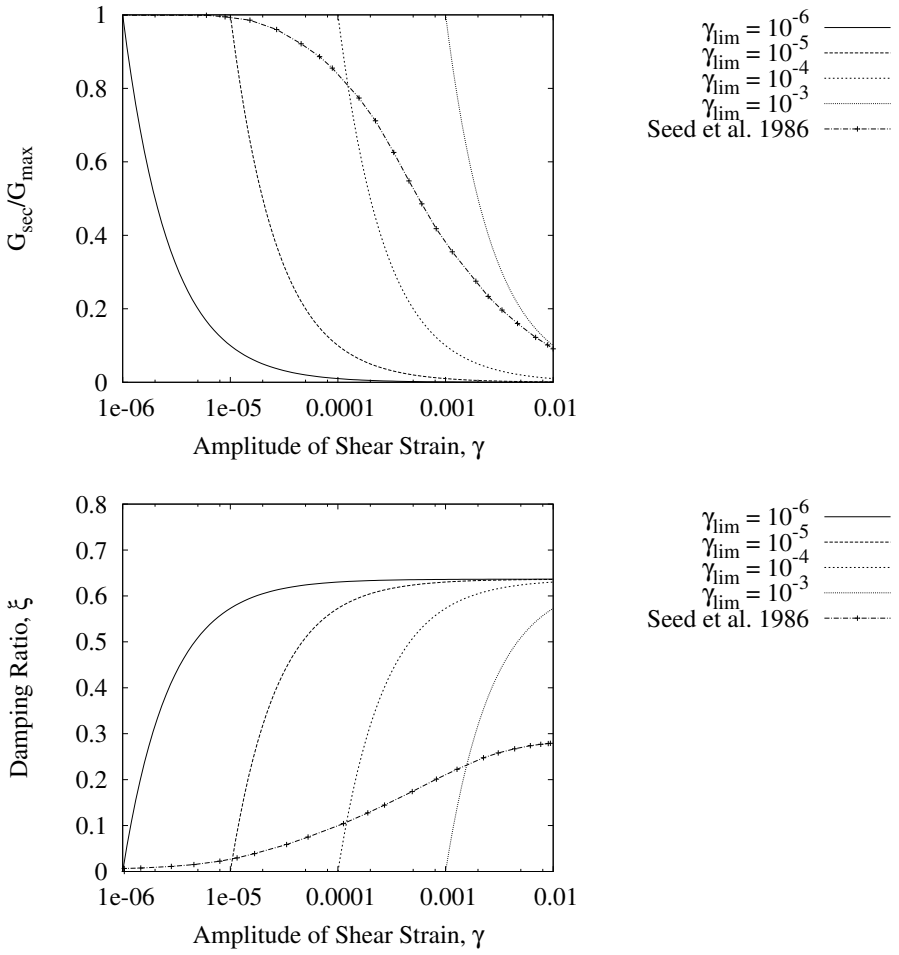

Figure 3.9: Top panel: shear modulus reduction curves obtained by Equation (3.1) plotted together with the laboratory tests results from Seed et al. (1986). Bottom panel: Damping factor obtained by Equation (3.2) plotted together with the laboratory tests results from Seed et al. (1986).

in order to describe the limit between elastic and inelastic domain behavior. Some models also propose progressive mobilization of plasticity through strain hardening mechanisms (schematically represented in Figure 3.6-(c)) and specific flow rules that relates the plastic volumetric and shear strain rates to the stress state through plastic multipliers (e.g., Mroz, 1967; Prevost, 1977; Hujeux, 1979; Aubry et al., 1982; Hujeux, 1985; Prevost, 1985).

In such advanced models, parameters should be chosen such that they are closely related to the rheology that describes the material properties at various strain levels. In some cases, these rheological models do not necessarily have physical parameters. Sometimes there are mathematical parameters that cannot be measured in the laboratory. Besides, the lack of knowledge of soil properties is common in seismic studies and a complete geotechnical description of a site is very rare. Thus, one of the obstacles in using such models is the difficulty in identifying their parameters. However, some correlations can be made between laboratory tests and mathematical parameters as shown by Lopez-Caballero et al. (2003, 2007).

3.1.4 Conclusion

After a brief vision of the different mathematical models used to mimic the real nonlinear behavior of soil in geomechanics, one of the most attractive in terms of simplicity of formulation, efficiency is the cyclic nonlinear model.

In term of additional parameters to the elastic ones, the cyclic nonlinear model is approximately equivalent to the simple constitutive models, however, the realisticness of the shear modulus reduction curves is much better than the one derived from the simple constitutive models, especially when laboratory tests curves are directly used.

Advanced constitutive models may be the closest from the real behavior of soil, however, numerous additional parameters are requiered for their mathematical formulation (parameters that are sometimes not available on a site or that have no physical meaning). It would be far too complex to use these laws as the basis for the solution of pratical seismological or geotechnical engineering problems. In addition, such advance models are more complex to implement in numerical methods.

In the following section, we used the GEFDyn code and Cyberquake to simulate the nonlinear wave propagation along the soil column of the CTI borehole station. As for GEFDyn, a simple constitutive law is used, whereas for Cyberquake, an advanced constitutive law is used.

3.2 Nonlinear Simulations at the CTI Borehole Station

3.2.1 Presentation of the problem

In order to test a simple constitutive model, we use the GEFDyn code with an elastic perfectly-plastic law using the Mohr-Coulomb yield criterion presented above. We note that as a first approximation, no distinction is made between sand and clay layer and both are modeled by a perfectly-plastic law using the Mohr-Coulomb yield criterion. Besides, despite the clear shortcomings of this simple constitutive model (i.e., quick reduction of the shear modulus and rapid increase of the damping), we investigate its use to have in mind its influence on the soil response. Both associated (i.e., $\varphi = \psi$) and non-associated (i.e., $\varphi \neq \psi$) flow rules are used for the simulations. A common modified Newton-Raphson method is used to resolve the finite element nonlinear problem (e.g., Zienkiewicz and Taylor, 1989b). In order not to have numerical dispersion, the recommendations exposed in the previous chapter have been applied up to 40 Hz (i.e., 30 nodes per minimal wavelength).

The soil column used for the simulations is the one presented in Table 2.3. Only the layers for which a nonlinear behavior has been detected by the inversion are modeled by a nonlinear law. As shown in Chapter 2, mainly the transverse direction at the CTI borehole station suffered from strong nonlinearity; consequently, only this direction is investigated. The incoming wave used for the FEM simulations of the free surface waveform is the one deconvolved by using the Thomson-Haskell propagator matrix method using the downhole waveform and the initial linear elastic parameters with a 5% damping. We note that for performing a rigourous deconvolution, the soil column inverted in Chapter 2 should be used since it is the closest from the reality and consequently, the most adapted to recover the incoming wave. However, in practice, an inversion is not always possible and the common technique using the linear elastic parameters with a 5% damping is used here. We note that simulations using an incident wave deconvolved via the inversion results or via the 5% damping technique lead to close results in our case.

3.2.2 Results of the nonlinear simulations

We first test the effect of an associated law on the response of the CTI soil column. The elastic properties of the soil column are given in Table 2.3.

For this purpose, the cohesion is fixed to a small value (i.e., $c = 1$ kPa) and the friction angle φ and dilatancy angle ψ are tuned together with a same value (the dilatancy angle has a role on the nature of the sand: contractant or dilatant and on the mathematical flow rule: associated

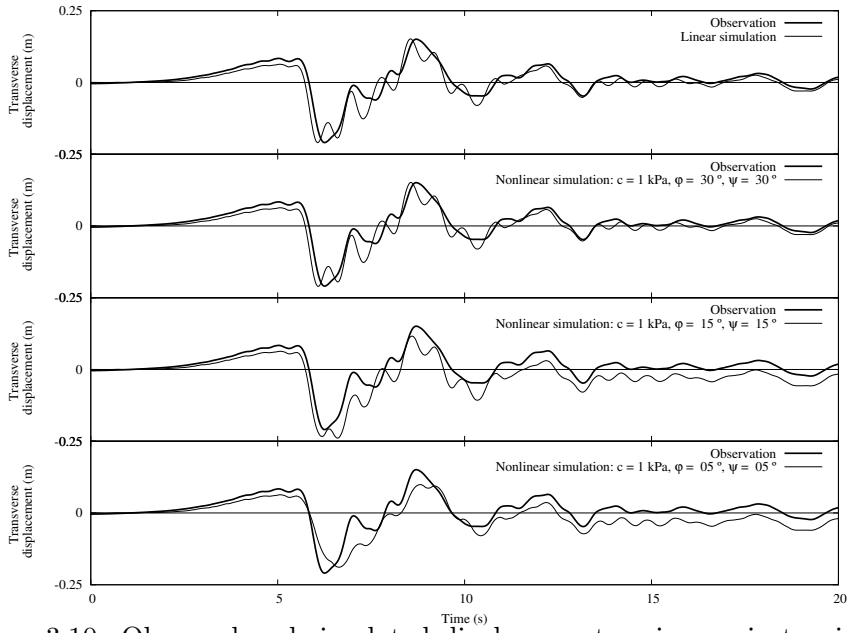

Figure 3.10: Observed and simulated displacements using an isotropic linear elastic law and an elastic associated perfectly-plastic law with a Mohr-Coulomb criterion with $\varphi = 30°$, $15°$ and $5°$.

or non-associated). Figures 3.10 to 3.12 show the simulated displacement, velocity and acceleration for different values of the internal friction angle (the dilatancy angle is fixed equal to the friction angle). As for the displacement, we can see that the decrease of the friction angle (which makes appear the nonlinear behavior for smaller stress as shown in Figure 3.7) has an effect on the amplitude of the oscillations, on their periods and on the permanent displacement. For the simulation using $\varphi = 5°$, we observe that the overall oscillation becomes smoother (i.e., decrease of the short periods oscillations present between 5 s and 10 s) as in the observation. However, a simple look at the velocity and acceleration time histories clearly shows that the simple constitutive law is too rough: the shape of the velocity time history has a triangle shape and the acceleration has more or less a square shape. The positive point is that the amplitude of the velocity and acceleration that are overestimated by the linear simulation decreases as the nonlinearity increases (i.e., decrease of the friction angle).

In order to check if a non-associated law (i.e., a flow rule not associated with the yield function) could lead to smoother velocity and acceleration time histories, we perform simulations with a friction angle fixed to $-15°$ and tune the dilatancy angle. Figures 3.13 to 3.15 show the displacement, velocity and acceleration time histories. As we can see, the use of a non-associatied law has very small effects on the results. The main phenomenon

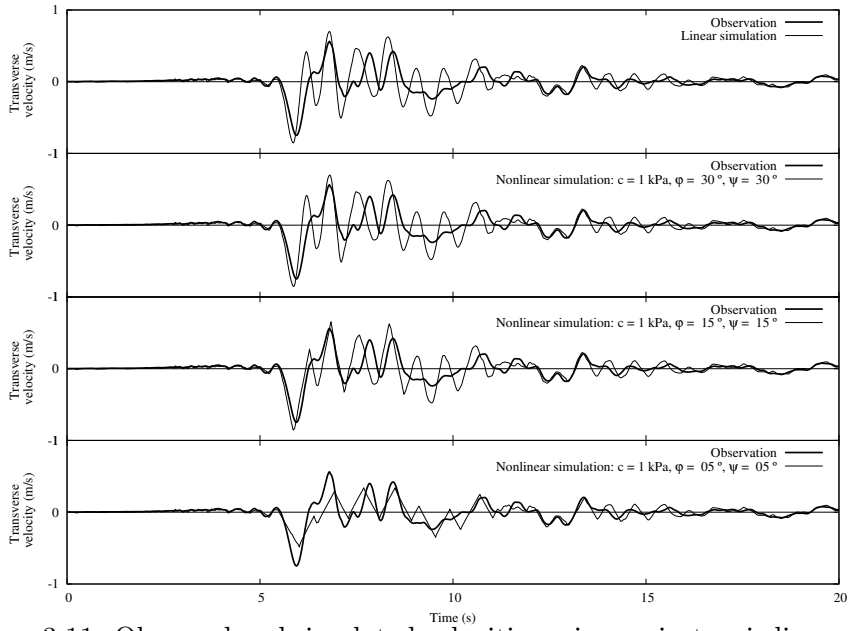

Figure 3.11: Observed and simulated velocities using an isotropic linear elastic law and an elastic associated perfectly-plastic law with a Mohr-Coulomb criterion with $\varphi = 30°$, $15°$ and $5°$.

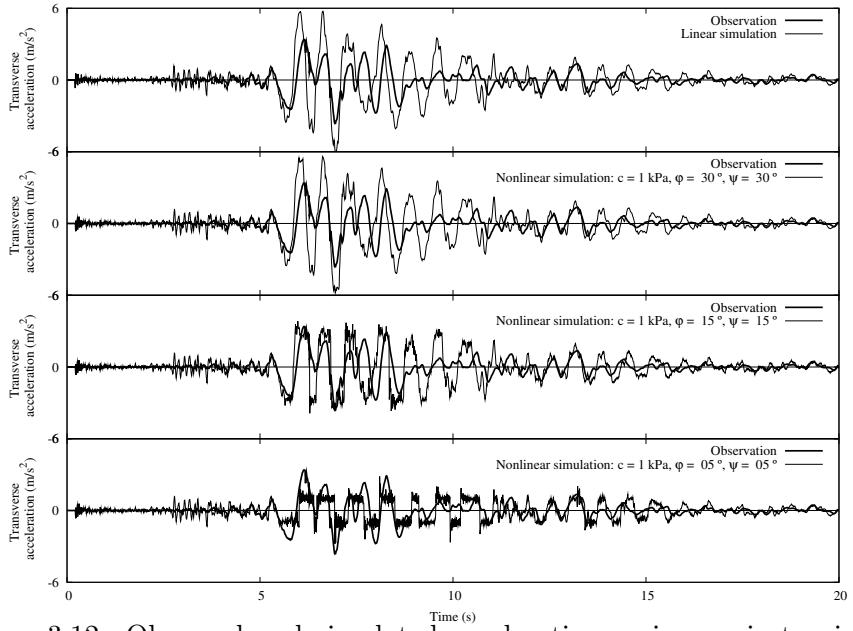

Figure 3.12: Observed and simulated accelerations using an isotropic linear elastic law and an elastic associated perfectly-plastic law with a Mohr-Coulomb criterion with $\varphi = 30°$, $15°$ and $5°$.

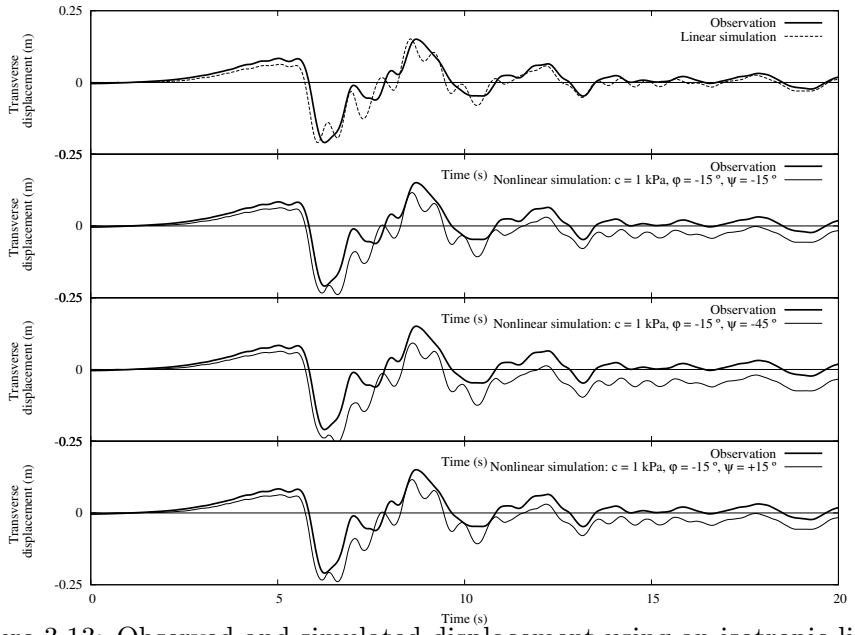

Figure 3.13: Observed and simulated displacement using an isotropic linear elastic law and an elastic non-associated perfectly-plastic law with a Mohr-Coulomb criterion with $\psi = -45°$ and $+15°$.

Table 3.1: Default parameters of the Cyberquake model for sand and clay.

	Elasticity	Yield surface	Hardening	Behavior domains	Initial state
	V_s, V_p	ϕ', β, b	E_p, ψ, α_ψ, n_r	γ^{ela}, γ^{his}, γ^{mob}	σ_{co}/σ'
Sand	cf. Table 2.3	30, 40, 0.1	20, 30, 1, 0.5	10^{-08}, 0.1, 0.5	1
Clay	cf. Table 2.3	15, 10, 1	5, 15, 1, 0.5	10^{-09}, 10^{-06}, 10^{-05}	2

which governs the shape of the velocity and acceleration time histories is the smoothness of the stress-strain curve.

As a result, we perform in the following nonlinear simulations using the software Cyberquake with an advanced constitutive law (Hujeux, 1985; Lopez-Caballero et al., 2007) that allows a smooth relation between the stress and the strain. The default parameters of the nonlinear law for sand and clay are used for the layers for which the inversion of Chapter 2 has shown a nonlinear behavior (i.e., the layers 6 to 9 of Table 2.3). The default parameters are summarized in Table 3.1. A detailed explanation of the meaning of these parameters is given by Lopez-Caballero et al. (2007).

Figure 3.16 shows the observed and simulated displacements, velocities and accelerations using the cyberquake model with the parameters of Table 3.1. We note that this simulation use the same incident wave as used previously. Consequently, if the simulation was linear elastic, the match between observation and simulation would be perfect. The stress-strain relation in

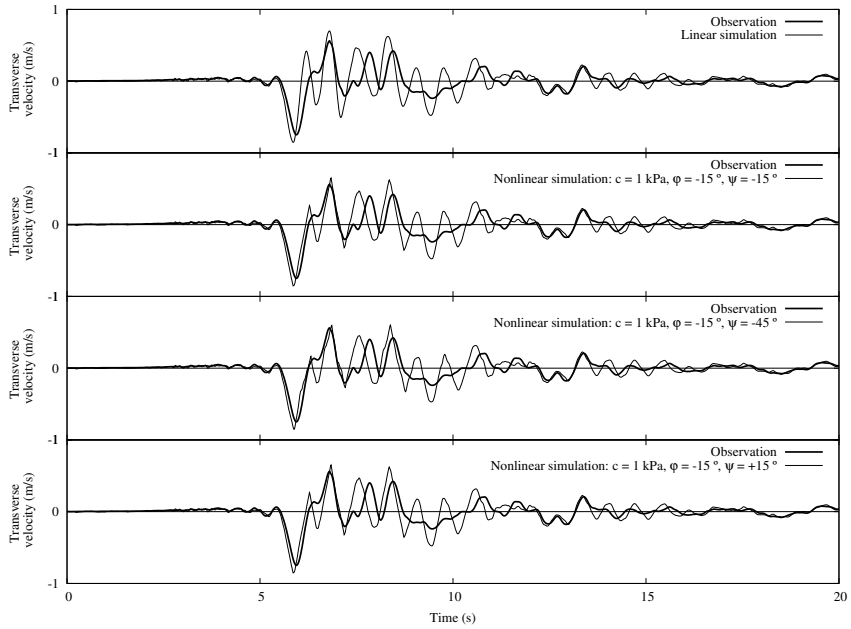

Figure 3.14: Observed and simulated velocity using a linear elastic law and an elastic non-associated perfectly-plastic law with a Mohr-Coulomb criterion with $\psi = -45°$ and $+15°$.

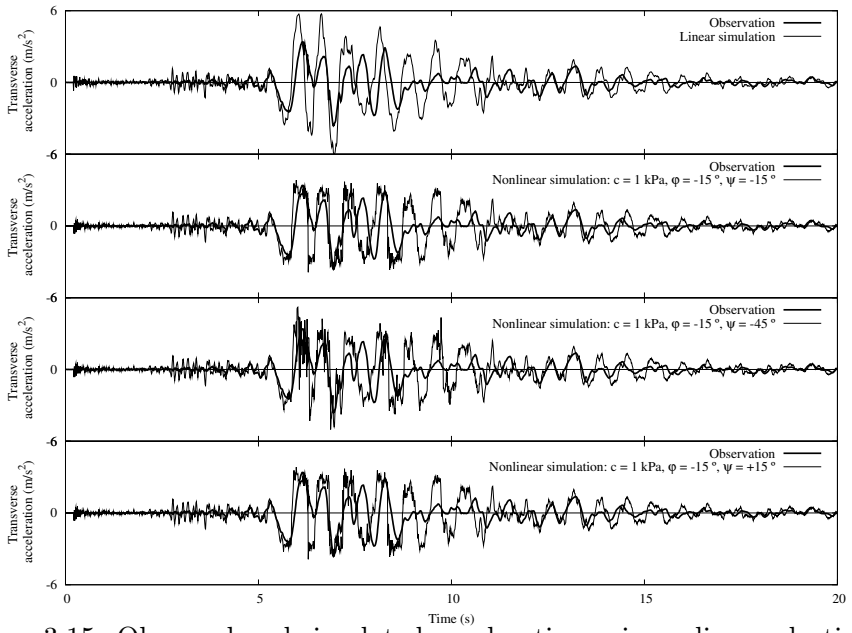

Figure 3.15: Observed and simulated acceleration using a linear elastic law and an elastic non-associated perfectly-plastic law with a Mohr-Coulomb criterion with $\psi = -45°$ and $+15°$.

the middle of the layers 6 to 9 are shown in Figure 3.17. This figure clearly shows the smooth nonlinear relation between the stress and the strain (by opposition to the bi-linear stress-strain relation shown in Figure 3.7 (right panel)). As a results, the velocity and acceleration shown in Figure 3.16 are slightly more realistic. However, the damping seems too high and a tune of the parameter of the Cyberquake law would be necessary (at least to adjust the peak ground acceleration). We can also note that the stress-strain curves for the clay layers (layers 6 and 8) exhibit too high maximum strain levels that would need some calibrations to obtain better results.

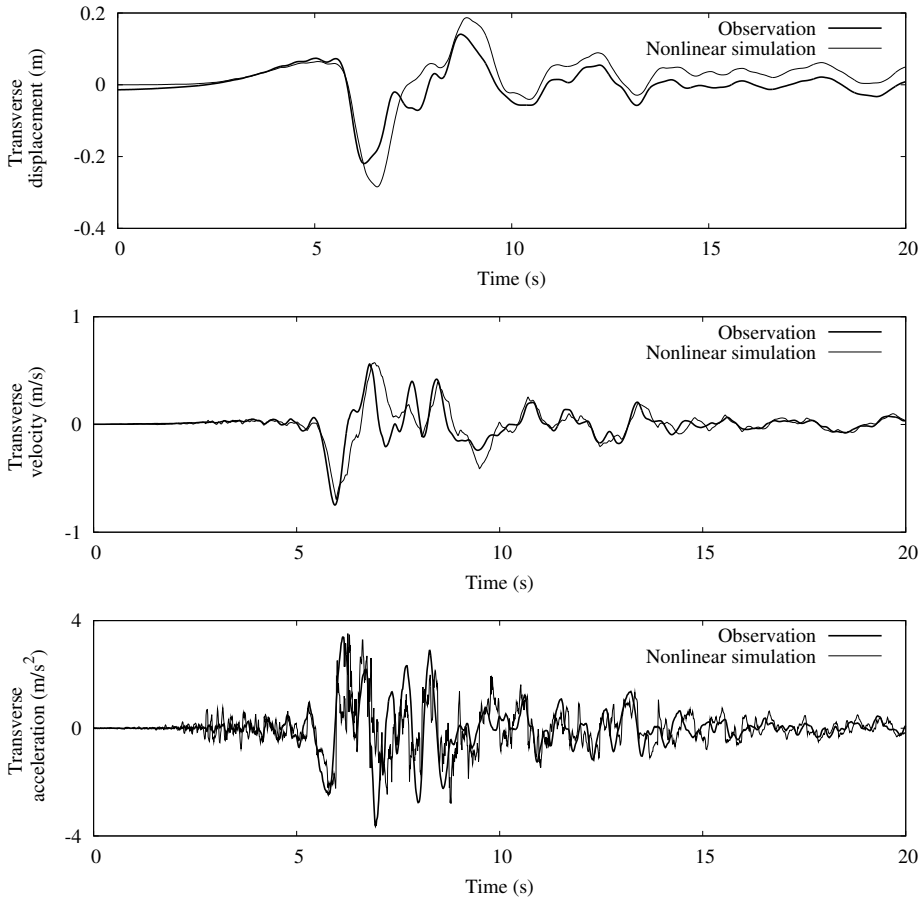

Figure 3.16: Observed and simulated displacements, velocities and accelerations using the advanced constitutive law of the Cyberquake software.

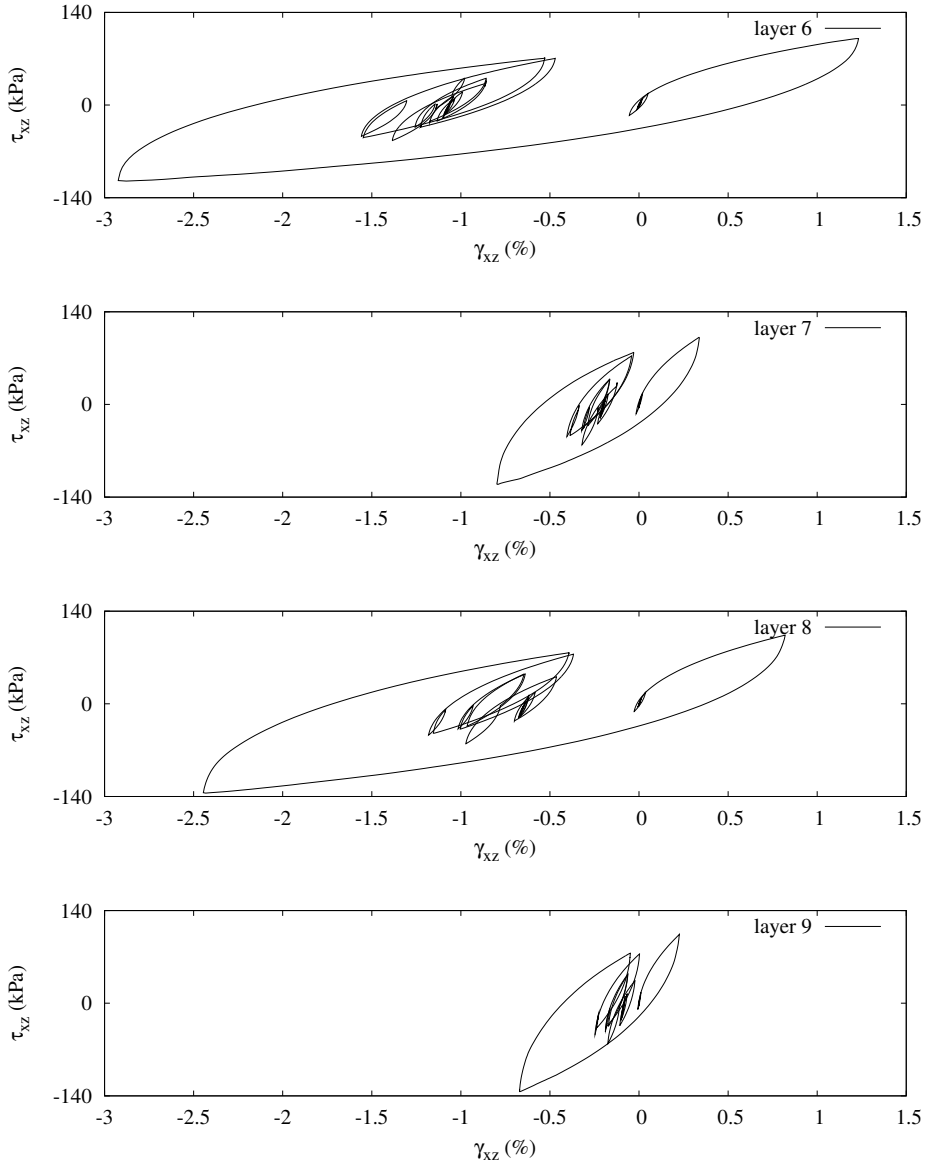

Figure 3.17: Stress-strain relation in the middle of the layers 6 to 9 using the advanced constitutive law of the Cyberquake sotfware.

3.3 Conclusion

We have performed in this chapter nonlinear simulations based on the results of the inversions in Chapter 2. Two nonlinear laws have been tested: a simple constitutive law and an advanced one from Cyberquake software. The results clearly show that the bi-linear assumption of the simple elasto-plastic law with a Mohr-Coulomb criterion produces unrealistic velocity and acceleration time histories. In order to obtain a smoother stress-strain relationship, we have also used an advanced constitutive law that lead to better results, however, the number of parameters to be tuned in order to obtain results consistent with the observation is an unavoidable obstacle. Even if smoother results have been found in the stress-strain plane, the simulated acceleration remained far from the observation and far from the results presented in Chapter 2 Figure 2.21 obtained using the observed equivalent linear parameters from the inversion. Moreover, we note that for the simulations, only the layers where nonlinear behavior have been found during the inversion were allowed to behave nonlinearly. Simulations for which all layers are allowed to behave nonlinearly overestimate the appearance of nonlinearity.

Chapter 4

The Finite Elements Method and Spectral Elements Method in Seismology

As shown in the previous Chapter, the one-dimensional (1D) and plane waves assumptions are often appropriate to study the local site effects. However, the rapid development of strong-motion seismology in the past decades has generated much interest in 2D or 3D solutions of seismic problems. The analytical or semi-analytical solutions of the elastic wave equations can be found for simplified problems including seismic sources (e.g., Lamb, 1904; Garvin, 1956; Niazy, 1973; Aki and Richards, 2002), however, with the current mathematical theories, such exact solutions are not available for complex realistic structures.

In order to overcome the difficulty to find exact solutions, considerable efforts have been devoted for developing accurate numerical techniques for the solution of elastic wave equations. For more than three decades the most widely used approaches have been:

- The methods based on the discrete wavenumber method (Bouchon and Aki, 1977) using boundary integral equations or boundary elements (e.g., Sanchez-Sesma and Esquivel, 1979; Dravinski, 1983; Bouchon, 1985; Campillo and Bouchon, 1985; Campillo, 1987; Bravo et al., 1988; Kawase, 1988; Coutant, 1989; Kawase and Aki, 1989; Gaffet and Bouchon, 1989, 1991; Papageorgiou and Kim, 1991; Sanchez-Sesma and Campillo, 1991; Mossessian and Dravinski, 1992; Clouteau and Aubry, 2003). The main advantages of these methods are that the solution is sought over a domain one dimension lower than the physical domain, and that the radiation condition is a priori satisfied. Such methods require piecewise homogeneous domains and linear constitutive laws. The linear system to be solved is non-symmetric and can be cumbersome to resolve. A solution to this shortcoming has been

proposed by Bouchon et al. (1995) who use a boundary integral equation (BIE) /conjugate gradient formulation to study the propagation of seismic waves through complex geological structures. The method is aimed at extending the range of applications of boundary integral equations or boundary element methods (BEM) to geological models of relatively large size or complexity. The authors show that the system of equations that expresses the boundary conditions at the medium interfaces and that is inherent to the BIEM or BEM approach can be drastically reduced in size and that only 10 to 20% of the terms of this system contribute significantly to the solution.

- The finite difference method (e.g., Virieux, 1986; Graves, 1996; Oprsal and Zahradnk, 2002). This is a very popular method because of its ease of implementation, but it suffers from numerical dispersion and from difficulties related to the implementation of boundary conditions. Recent advances for absorbing properly waves impiging on the boundaries is the implemetation of an unsplit convolutional perfectly matched layer (e.g., Komatitsch and Martin, 2007).

- The global pseudo-spectral method (e.g., Carcione and Wang, 1993; Tessmer and Kosloff, 1994). Pseudo-spectral methods exhibit very weak numerical dispersion, but instabilites arise in the treatment of boundary conditions and induce difficulties in the time integration scheme (e.g., Komatitsch et al., 1996). Moreover, due to the use of a global polynomial basis, numerical oscillations appear in the presence of strong heterogeneities or sharp boundaries within the model.

- The finite elements methods (e.g., Zienkiewicz, 2005) and the spectral elements method (SEM) (e.g., Priolo et al., 1994; Komatitsch, 1997; Faccioli et al., 1997; Komatitsch and Vilotte, 1998; Stupazzini and Paolucci, 2009). Classical finite element methods (FEM) circumvent most of these problems, but are based upon low-order approximations and come with high numerical overhead because of the large linear systems involved in its implicit formulation, particularly in the 3-D case (Bao et al., 1998; Dupros et al., 2008). Because of the low-order approximations, a significant numerical dispersion can arise when few nodes per minimal wavelength are present.

  The spectral elements method has appeared more than 20 years ago in computational fluid mechanics (e.g., Patera, 1984; Maday and Patera, 1989; Fischer and Rønquist, 1994) and is an elegant formulation of the finite elements method with a high degree of piecewise polynomial basis. The method has been used to accurately model wave propagation on local, regional and very large scales, both in 2-D and 3-D cases (e.g., Komatitsch, 1997; Chaljub et al., 2003). Because of the use of high degree of piecewise polynomial basis, the numerical dispersion is

significantly reduced compared with the FEM for the same number of nodes per minimal wavelength.

- The meshless methods. At the end of the 70s, Lucy (1977) introduced the SPH (Smoothed Particle Hydrodynamics) to simulate the interaction of celest particles. Then, the method has been theorized by Gingold and Monaghan (1977); Monaghan (1982). In these methods, the classical notion of mesh is replaced by unconnected nodal data. A method can be considered as meshless when the approximation basis is constructed from supports associated with arbitrary scattered nodes without the need of a domain partition as for the FEM of the FDM. These methods have been then widely studied in mechanics and geomechanics (e.g., Randles and Libersky, 1996; Swegle et al., 1995; Belytschko et al., 1996; Aubert, 1997; Modaressi and Aubert, 1998; Foerster, 2003).

Each one of the above-mentionned methods has its advantages and shortcomings, however, having as objective to study nonlinear site effects, we first lean towards time domain methods because the implementation of the nonlinear soil behavior is much easier than in the frequency domain methods. Among time domain methods, one of the most promising is the spectral elements method which combines the flexibility of the finite elements method with the rapid convergence of spectral methods.

Consequently, we present in the following the verification in the linear elastic domain of the 1D spectral elements code (EFISPEC, i.e., Elements FInis SPECtraux) developed in this thesis. The verification is done by comparing 1D wave propogation with the Thomson-Haskell propagator matrix code exposed in Chapter 1 and with the finite elements code Cyberquake (e.g., Foerster and Modaressi, 2007). The development of a 1D spectral element code allowed us to grasp the fundamentals of the method. A future implementation of nonlinear law will be also easier starting by a 1D assumption. The verification of the 2D spectral elements code developed in this thesis is done by comparing 2D wave propagation with the finite elements code GEFDyn (e.g., Aubry et al., 1985; Modaressi, 1987; Aubry and Modaressi, 1996) and the verification of the 3D spectral elements code with the theoretical double couple point source model in an infinite homegeneous media. The perspective of this thesis being then to implement known nonlinears law in the spectral element method.

Since this thesis does not aim to detail the spectral elements method, the following sections briefly describe the basics step of the method. For a detailed introduction to finite elements and spectral elements methods, the reader is referred to Zienkiewicz (2005); Komatitsch (1997); Faccioli et al. (1997); Komatitsch and Vilotte (1998).

4.1 Virtual Work as the Weak Form of the Equations of Motion

In a finite or spectral elements approach, the strong form of the equations of motion (1.6) is first rewritten in a weak formulation. This is accomplished by dotting it with an arbitrary virtual displacement $\mathbf{v}$ and integrating by parts over the region of interest (e.g., Zienkiewicz and Taylor, 1989a) which gives

$$\int_{\Omega} \boldsymbol{\epsilon}(\mathbf{v})^T : \boldsymbol{\tau}\, d\Omega - \int_{\Omega} \mathbf{v}^T \cdot \mathbf{f}\, d\Omega - \int_{\Gamma} \mathbf{v}^T \cdot \mathbf{T}\, d\Gamma = \int_{V} \rho \mathbf{v}^T \cdot \ddot{\mathbf{u}}\, dV \qquad (4.1)$$

where Ω and Γ are the volume and the surface area of the domain under study, respectively. $\boldsymbol{\epsilon}$ is the virtual strain tensor related to the virtual displacement vector $\mathbf{v}$. $\mathbf{f}$ is the body force vector and $\mathbf{T}$ is the traction vector acting on Γ. ^{T} denotes the transposed symbol and a colon denotes the contracted tensor product. Equation (4.1) is valid for linear as well as nonlinear stress-strain (or stress-rate of strain) relationships. Using a Galerkin formulation, we consider that the test function $\mathbf{v}$ is equal to $\mathbf{w}$, the shape functions used for the displacement field discretization.

4.2 Spatial Discretization

The notations on the spectral elements method follow those presented by Komatitsch (1997); Komatitsch et al. (2001).

As in any finite elements method, a first crucial step is the design of a mesh: the volume Ω needs to be subdivided into a number of non-overlapping elements Ω_e, $e = 1, \ldots, n_e$, such that $\Omega = \cup_{e=1}^{n_e} \Omega_e$.

We note that for two-dimensional spectral elements, the discretization has first been performed by using the classical Legendre discretization based upon quadrilaterals and the Gauss-Lobatto-Legendre quadrature. In order to solve more general problems with a complex geometry, the use of triangle is also feasible (e.g., Komatitsch et al., 2001).

In two dimensions, the classical Legendre spectral element discretization of problem based on quadrilaterals proceeds as follows: a conforming mesh of n_e non-overlapping quadrilaterals is defined on the domain Ω. These elements are subsequently mapped individually to a reference square $\Lambda = [-1, 1] \times [-1, 1]$ using an invertible local mapping $F_e : \Lambda \rightarrow \Omega_e$, which

enables to go from the reference domain to the physical domain as

$$\begin{aligned} x(\xi,\eta) &= \sum_{a=1}^{n_g} N_a(\xi,\eta) x_a^e \\ y(\xi,\eta) &= \sum_{a=1}^{n_g} N_a(\xi,\eta) y_a^e. \end{aligned} \tag{4.2}$$

where n_g denotes the total number of nodes used to define the geometry of a quadrilateral. The shape functions $N_a(\xi,\eta)$ can be Lagrange polynomial of first or second order for a linear or parabolic description of the edge of the element, respectively. The value x_a^e and y_a^e are the coordinates of the geometrical nodes of the element in the physical domain. ξ and η are local axes as shown in Figure 4.1.

In the reference square Λ, a set of local basis functions consisting of polynomials of degree N is introduced. On each element Ω_e, mapped to the reference square Λ, a set of nodes is defined and the polynomial approximations u_x^e and u_z^e of u_x and u_z are chosen as the Lagrange interpolants on this set of nodes. These nodes, $\xi_p \in [-1,1], p \in 0,\ldots,N$, are the Gauss-Lobatto-Legendre (GLL) points, which are the $N+1$ roots of $(1-\xi^2)P'_N(\xi) = 0$, where $P'_N(\xi)$ is the derivative of the Legendre polynomial of degree N. They can be computed numerically (Canuto et al., 1987). In the reference square Λ, the restriction of a given function u^e to the element Ω_e can be expressed using a product of 1-D Lagrange interpolants, a property that is often referred to as the tensorisation of the basis:

$$u^e(\xi,\eta,t) = \sum_{i=1}^{N+1}\sum_{j=1}^{N+1} u_a^e(\xi_j,\eta_i,t) h_j(\xi) h_i(\eta). \tag{4.3}$$

Here $h_j(\xi)$ denotes the j-th 1-D Lagrange interpolant, which is by definition the unique polynomial of degree N that is equal to one at $\xi = \xi_j$ and to zero at all other points $\xi = \xi_i$ for which $i \neq j$. It is of the form:

$$h_j(\xi) = \prod_{l=1, l\neq j}^{N_{gll}} \frac{\xi - \xi_l}{\xi_j - \xi_l} = \frac{(\xi-\xi_1)}{(\xi_j-\xi_1)} \cdots \frac{(\xi-\xi_{l-1})}{(\xi_j-\xi_{l-1})} \frac{(\xi-\xi_{l+1})}{(\xi_j-\xi_{l+1})} \cdots \frac{(\xi-\xi_{N_{gll}})}{(\xi_j-\xi_{N_{gll}})},$$

with $N_{gll} = N+1$. From this definition we obtain the fundamental property:

$$h_i(\xi_j) = \delta_{ij}. \tag{4.4}$$

Once the piecewise polynomial approximation (4.3) is injected in Equation (4.1), the integrals can be approximated at the elemental level using the GLL integration rule to obtain a system of the form

$$\mathbf{M}\ddot{\mathbf{U}} + \mathbf{K}\mathbf{U} = \mathbf{F}^{\mathbf{ext}}.$$

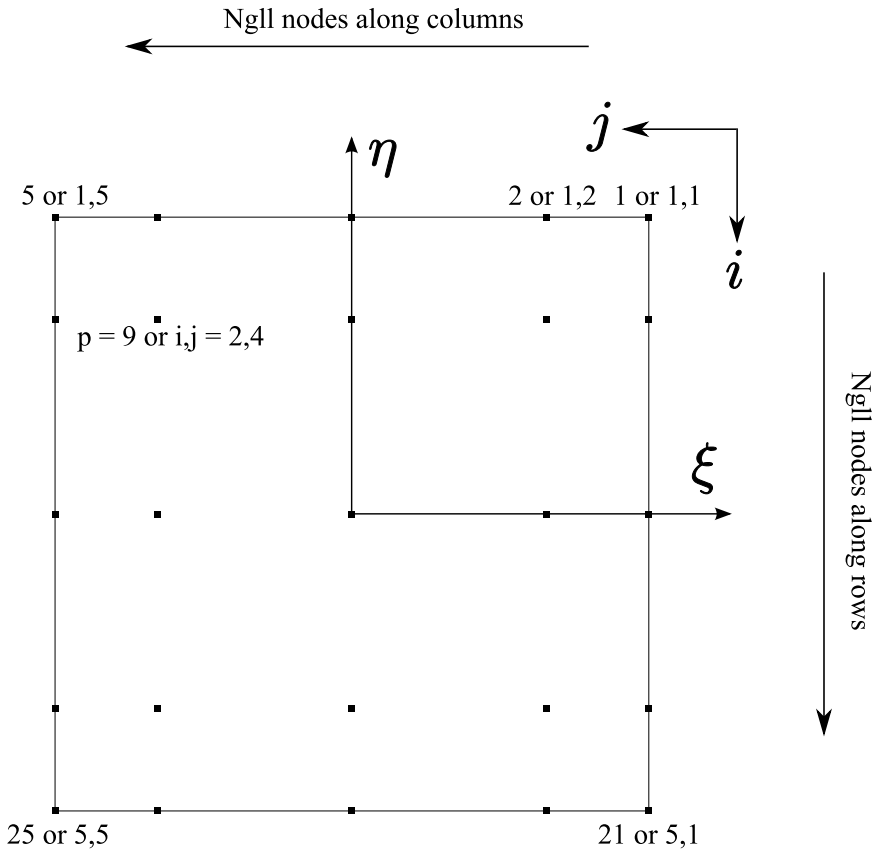

Figure 4.1: Local numbering of a spectral element with 25 Gauss-Lobatto-Legendre points. GLL points are represented by dots. Two numbering are presented, a row-column numbering with two digits separated by a comma and a full numbering from 1 to 25.

In the case where viscosity is present, the term $\mathbf{C}\dot{\mathbf{U}}$ arises in the left-hand side of the above equation.

Because of the property of Equation (4.4), the cost for computing integral is reduced and the mass matrix is naturally diagonal. This property is specific to the spectral element method (i.e., they are not present in the classical finite element method). As an example, the natural diagonallity of the mass matrix is exposed hereafter. The elemental mass matrix is expressed as

$$\mathbf{m^e} = \int_{\Omega e} \mathbf{w}^{\mathrm{T}} \rho \mathbf{w} \, d\Omega_e$$

with

$$\mathbf{w} = \begin{pmatrix} \mathrm{w}_1 & 0 & \mathrm{w}_2 & 0 & \cdots & \mathrm{w}_n & 0 \\ 0 & \mathrm{w}_1 & 0 & \mathrm{w}_2 & \cdots & 0 & \mathrm{w}_n. \end{pmatrix}$$

where

$$\mathrm{w}_p = h_j(\xi) h_i(\eta)$$

The indice p (with $p = mod(i-1, N_{gll}) * N_{gll} + j$) corresponds to the full numbering presented in Figure 4.1 and the indices i and j correspond to the row-column numbering of the same figure, j being associated with a column and i to a row. Thus,

$$\mathbf{w}^{\mathrm{T}}\mathbf{w} = \begin{pmatrix} \mathrm{w}_1^2 & 0 & \mathrm{w}_1\mathrm{w}_2 & 0 & \cdots & \mathrm{w}_1\mathrm{w}_n & 0 \\ 0 & \mathrm{w}_1^2 & 0 & \mathrm{w}_1\mathrm{w}_2 & \cdots & 0 & \mathrm{w}_1\mathrm{w}_n \\ \mathrm{w}_1\mathrm{w}_2 & 0 & \mathrm{w}_2^2 & 0 & \cdots & \mathrm{w}_2\mathrm{w}_n & 0 \\ \vdots & \vdots & \vdots & \ddots & \vdots & \vdots & \vdots \\ \mathrm{w}_1\mathrm{w}_n & 0 & \mathrm{w}_2\mathrm{w}_n & 0 & \ddots & \vdots & \vdots \\ 0 & \mathrm{w}_1\mathrm{w}_n & 0 & \mathrm{w}_2\mathrm{w}_n & \cdots & 0 & \mathrm{w}_n^2 \end{pmatrix}$$

and for $k \neq l$

$$\int_{\Omega_e} \mathrm{w}_k \mathrm{w}_l \, d\Omega_e = \sum_i \sum_j J_e w_i w_j h_k(\eta_i) h_k(\xi_j) h_l(\eta_i) h_l(\xi_j) = 0$$

since

$$h_k(\xi_j) \; or \; h_k(\eta_i) = \delta_{kj} \; or \; \delta_{ki}$$

4.3 Time Integration

Because of the natural diagonality of the mass matrix in the spectral element method, an explicit time scheme is often used for the resolution of the numerical problem. The equations of motion being second-order equations, the classical Newmark method (Newmark, 1959) for second-order equations is generally used (higher order could be used as well). The most general

quadratic expension of the Newmark algorithm derived from the truncated Taylor series expension is defined as

$$\begin{aligned} \mathbf{U}_{n+1} &= \mathbf{U}_n + \Delta t \dot{\mathbf{U}}_n + \frac{\Delta t^2}{2}(1-\beta)\ddot{\mathbf{U}}_n + \frac{\Delta t^2}{2}\beta\ddot{\mathbf{U}}_{n+1} \\ \dot{\mathbf{U}}_{n+1} &= \dot{\mathbf{U}}_n + \Delta t(1-\gamma)\ddot{\mathbf{U}}_n + \Delta t\gamma\ddot{\mathbf{U}}_{n+1}. \end{aligned} \tag{4.5}$$

This, together with the dynamic equation

$$\mathbf{M}\ddot{\mathbf{U}}_{n+1} + \mathbf{K}\mathbf{U}_{n+1} = \mathbf{F}^{ext}_{n+1} \tag{4.6}$$

allow the three unknowns $\ddot{\mathbf{U}}_{n+1}$, $\dot{\mathbf{U}}_{n+1}$ and $\mathbf{U}_{n+1}$ to be determined. For an explicit time scheme, the parameter β is set to zero.

4.4 Absorbing Boundary Condition

In the FEM or SEM, boundaries of the domain behave as free boundaries (i.e., vanishing of stress) and waves reflexions occurs. In order to avoid these reflexions and to mimic an unbounded media, different types of absorbing boundary conditions have been developped as the paraxial approximation (e.g., Claerbout, 1976; Engquist and Majda, 1977), Perfectly Matched Layer (PML) or unsplit Convolutional Perfectly Matched Layer (CPML) (e.g., Komatitsch and Martin, 2007).

The most simple to implement (but also the less efficient) is the paraxial approximation. The paraxial or parabolic approximation (or 15° approximation) was presented for the first time by Claerbout (1976) for scalar waves, then completed and studied in detail for elastic waves (e.g., Engquist and Majda, 1977; Clayton and Engquist, 1977). This approximation is useful for the computation in the transient domain and permits to build dynamic impedance, locally in space and in time, on the boundary for which wave absorption is needed. Cohen and Jennings (1983) and then Modaressi (1987) proposed a numerical procedure of this approximation in the finite element methods.

A detailed derivation of the paraxial approximation to different order for the elastic wave equation is presented in Appendix C. In summary, the first approximation (i.e., order 0) is such that the stress applied by a wave impiging on a boundary is approximated by

$$\tau(x_1, x_2, x_3, t) = \begin{pmatrix} -\rho\beta\partial_t u_1 \\ -\rho\beta\partial_t u_2 \\ -\rho\alpha\partial_t u_3 \end{pmatrix}.$$

where (x_1, x_2, x_3) forms the local coordinate of a paraxial element and α and β are P and S-wave velocity, respectively. For this first approximation, the elastodynamic dispersion relation is well approximated when the direction of propagation of the wave is perpendicular to a paraxial element or at high frequency (e.g., Clayton and Engquist, 1977; Modaressi, 1987).

4.5 Validation of 1-D Wave Propagation

4.5.1 Mesh design for the spectral element method

In practice, a spatial sampling of the order of 4 or 5 points per minimum wavelength has been found very accurate when working with a polynomial degree between $N = 5$ and $N = 8$ (e.g., Seriani and Priolo, 1994; Komatitsch et al., 1999). If higher-order polynomials are used, because of the densification of the GLL points close to the edges of the element, there is no important gain in precision whereas the computational time increases significantly at the elemental level. On the other hand, if a low-order polynomial is chosen, the spectral elements method tends to the classical low-order finite element method and numerical dispersion and diffusion arises.

4.5.2 Comparison of the propagator method, the SEM and the FEM

In order to test the accuracy of the spectral elements method to propagate a wave in one dimension, we compare the numerical computation with the Thomson-Haskell propagator matrix method (THPMM) which is the semi-analytical reference. For this purpose, we use the soil column presented in Table 4.1. The incoming wave is a vertically incident order two Ricker with a pseudo frequency of $f_0 = 10$ Hz and a time shift of 0.5 second (the maximal energy to account for in the simulation will be approximately $f_{max} \approx 2.5 f_0$ for a Ricker wavelet). For the spectral element method, the incoming wave is input with an implicit paraxial elements positionned at the depth of 51 m.

Table 4.1: Soil column used to compare the 1-D solution between the Thomson-Haskell method, the SEM and the FEM.

No.	Depth (m)	P-wave velocity (m/s)	S-wave velocity (m/s)	Damping factor (%)	Density (g/cm^3)
1	50.0	663.325	200.0	0.00	1.80
3	∞	1658.312	500.0	0.00	2.00

For the SEM simulation, polynomial of order 8 are used with approximately 5 GLL points per minimum wavelength ($\lambda_{min} \approx 200/25 = 8$ m) and the time step is fixed to $\Delta t = 1e^{-4}$ s. The comparison between the results obtained by using the THPMM and the SEM is shown in Figure 4.2. The agreement is excellent even for the reflexions present after 4.5 s.

On the other hand, the classical finite elements method (in our case, 3 node elements with shape functions using polynomials of order two and a

time step Δt of $8e^{-4}$) is soiled by numerical dispersion and/or diffusion as shown in Figure 4.3. The common rule of thumb of 10 nodes per minimum wavelength is far to be accurate and the results start to be acceptable for 30 nodes per minimum wavelength. However, even with 40 nodes per minimum wavelength, the reflexions present after 4.5 s are not well reproduced by the classical FEM as shown in Figure 4.4. An increase of the number of nodes per minimum wavelength up to 120 leads to spurious oscillations as shown in Figure 4.5. We note that these spurious oscillations do not occur when increasing to 120 the number of GLL nodes per minimum wavelength for the SEM as shown in Figure 4.6.

We note that by increasing the number of layers in the soil column in order to increase the multiple reflections, the results of the SEM remain excellent.

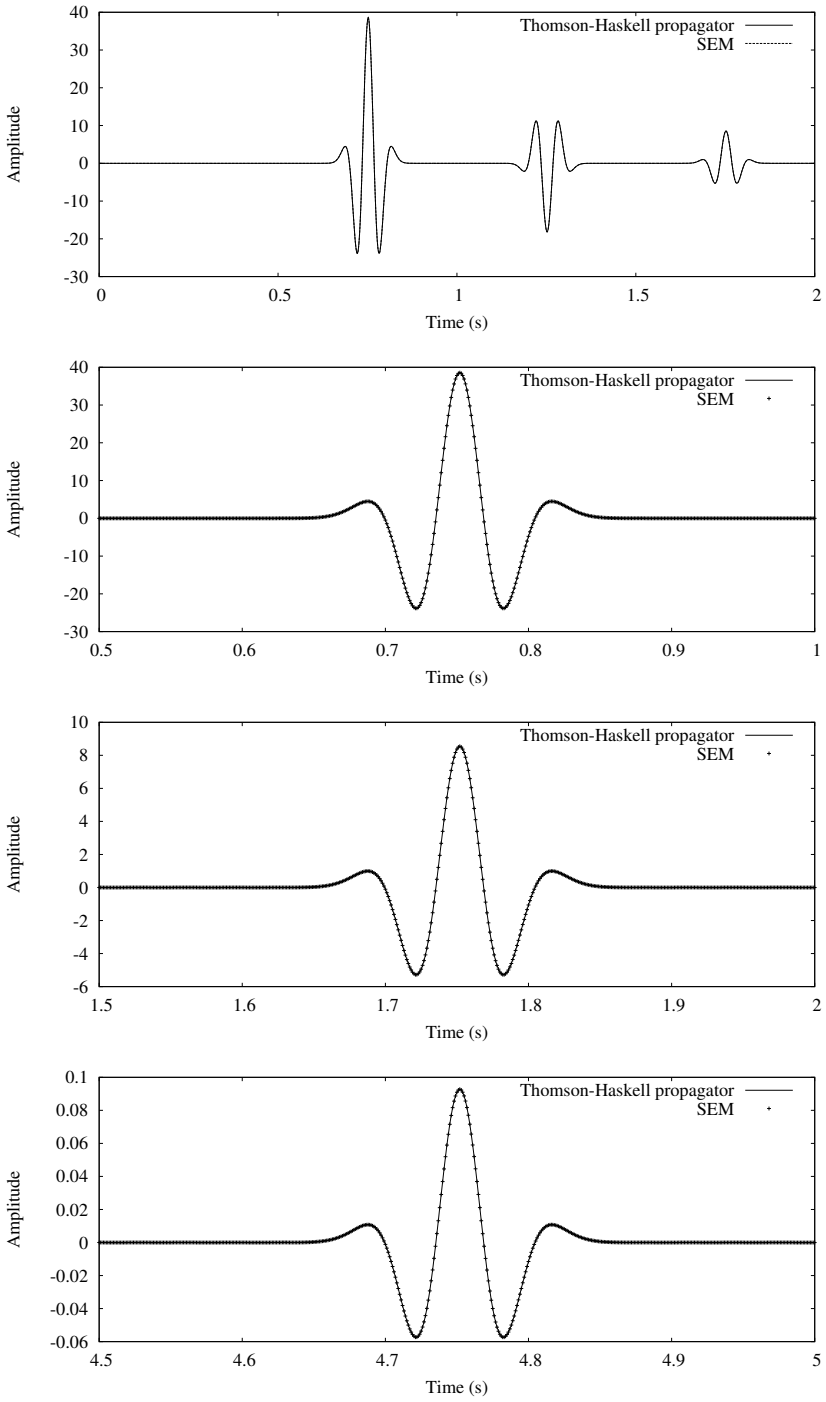

Figure 4.2: Comparison between the Thomson-Haskell propagator matrix method and the spectral elements method at the free surface of the soil column presented in Table 4.1. The top panel shows the results from 0.0 s to 2.0 s. The other panels show zoom from 0.5 s to 1.0 s, 1.5 s to 2.0 s and 4.5 s to 5.0 s

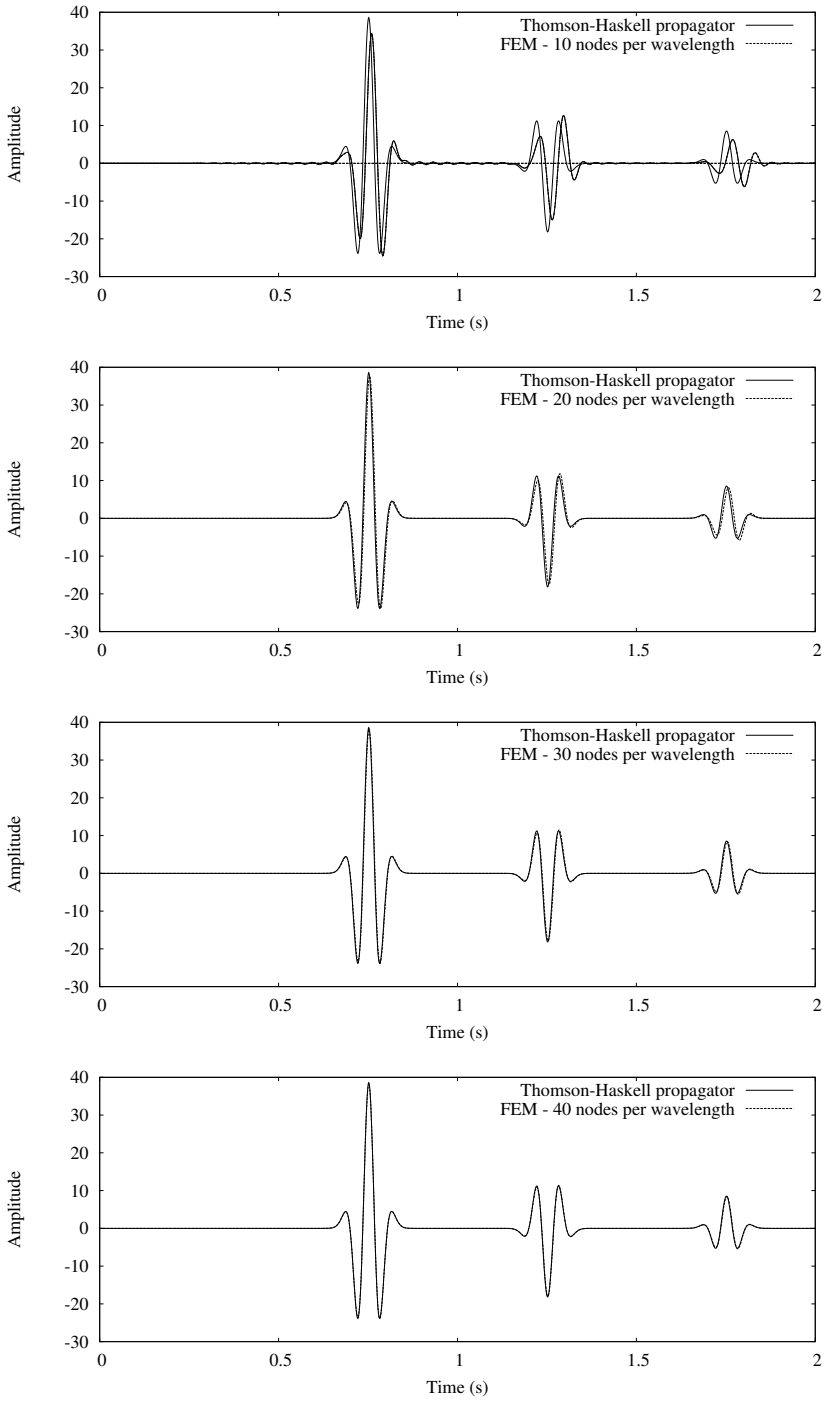

Figure 4.3: Comparison between the Thomson-Haskell propagator matrix method and the classical finite elements method at the free surface of the soil column presented in Table 4.1. Panels from top to bottom show simulations using 10 nodes, 20 nodes, 30 nodes and 40 nodes per minimum wavelength, respectively.

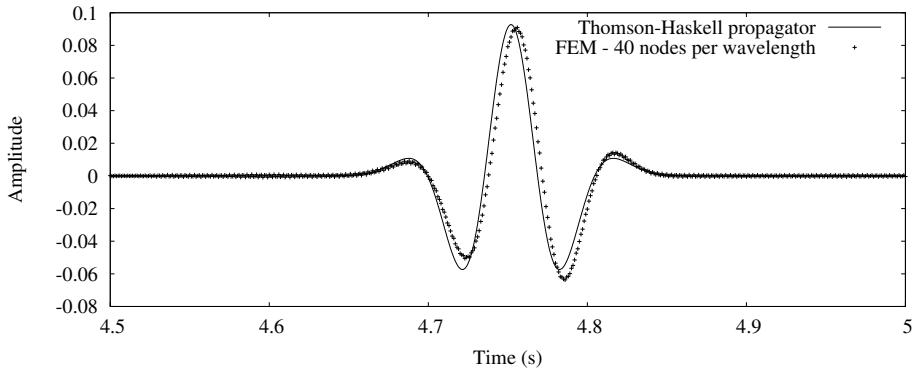

Figure 4.4: Comparison between the Thomson-Haskell propagator matrix method and the classical finite elements method with 40 nodes per minimum wavelength at the free surface of the soil column presented in Table 4.1. The figure shows a reflection from 4.5 s to 5.0 s.

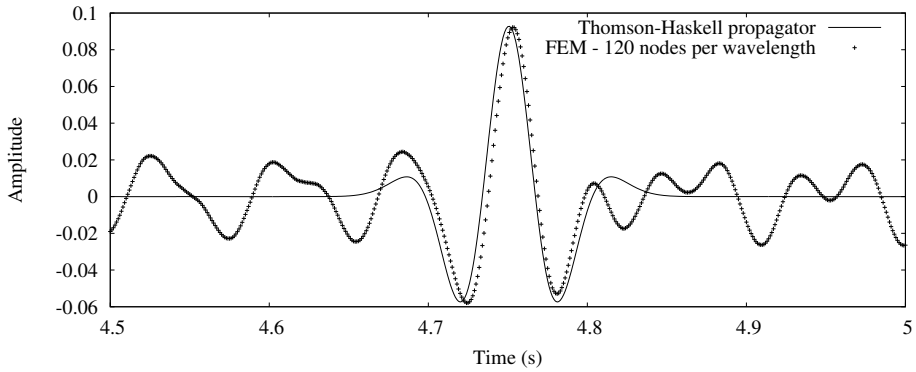

Figure 4.5: Comparison between the Thomson-Haskell propagator matrix method and the classical finite elements method with 120 nodes per minimum wavelength at the free surface of the soil column presented in Table 4.1. The figure shows a reflection from 4.5 s to 5.0 s.

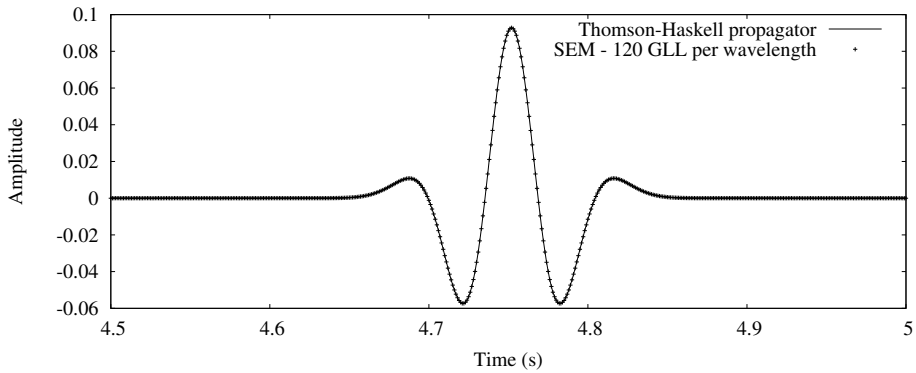

Figure 4.6: Comparison between the Thomson-Haskell propagator matrix method and the SEM with 120 nodes per minimum wavelength at the free surface of the soil column presented in Table 4.1. The figure shows a reflection from 4.5 s to 5.0 s.

4.6 Validation of 2-D Wave Propagation in the P-SV plane

The verification of the accuracy of the SEM in 2D has been already demonstrated by Komatitsch (1997); Komatitsch et al. (2001). The verification consisted in comparing the semi-analytical solution with the one obtained by the SEM for different types of problems with point source. The results have shown an excellent accuracy of the SEM.

4.6.1 Burried point source problem

In order to validate the code developed in this thesis, we compare the results obtained by the SEM with the ones from the classical FEM (by taking into account the remarks made in the previous section about the number of nodes requiered per minimum wavelength). The problem is a burried point source problem. The lower-left corner is taken as the coordinate $(x = 0, z = 0)$. The domain is a homogeneous square of size 20000 m x 20000 m presented in Figure 4.7. The linear elastic properties of the medium are presented in Table 4.2. The source is a point force acting vertically (i.e., z-direction) located at the coordinate $(x = 10000, z = 10000)$ and its shape is a Ricker wavelet of order 2 with a center frequency of 0.25 Hz (i.e., the maximum frequency to take into account for the numerical computation is equal to $2.5 \times 0.25 = 0.625$ Hz). The location of the receivers are exposed in Table 4.3. The four edges of the domain act as a free surface.

The mesh for the SEM is presented in Figure 4.7. It is composed of quadrilaterals of size 1000 m x 1000 m. The order of the Lagrange polynomial is 8 so that the number of GLL points for a minimum wavelength

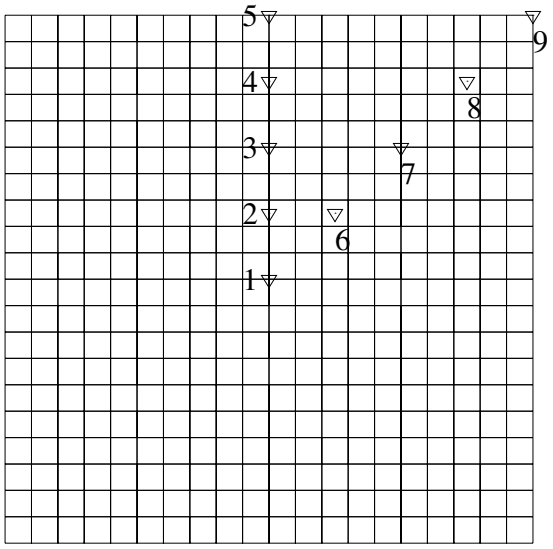

Figure 4.7: Domain used to compare the results of a point source problem in the P-SV plane between the SEM and the classical FEM. The domain is a square of size 20 km x 20 km. The mesh represents the one used in the SEM computation. The receivers are indicated by triangles. The source is located at receiver 1.

$\lambda_{min} = 2000/0.625 = 3200$ m is fully accomplished (i.e., ≈ 20 GLL points at λ_{min}. We remember that the SEM is accurate from 4 or 5 GLL points at λ_{min}). As for the computation using the FEM, the domain is meshed with quadrilaterals of size 125 m x 125 m and polynomials of order 1 are used for the interpolation of the solution so that approximately 30 nodes are present at λ_{min}. For both methods, an explicit time scheme is used with a time step of 0.25 ms. In order to make the FEM mass matrix diagonal, a conventional lumped mass matrix is used with $\alpha = 0.5$ and $\beta = 0$.

The comparison of the results is shown in Figures 4.8 and 4.9. The agreement between the two methods is excellent: both amplitude and phase of the signal are idendical at each receiver. We note that for the receivers 2 to 5 (Figure 4.7), no x-component is present because the point force acts vertically so that the z-axis passing through the source is a nodal line (a zoom on these results show that the amplitude along this line is of the order of magnitude of the numerical noise: $\approx 10^{-17}$).

Table 4.2: Characteristics of the linear elastic medium.

P-wave velocity (m/s)	S-wave velocity (m/s)	Damping factor (%)	Density (g/cm^3)
4000	2300	0.0	1.80

Table 4.3: Coordinates of the receivers shown in Figure 4.7 used to compare the SEM and the classical FEM.

No.	x (m)	z (m)
1	10000	10000
2	10000	12500
3	10000	15000
4	10000	17500
5	10000	20000
6	12500	12500
7	15000	15000
8	17500	17500
9	20000	20000

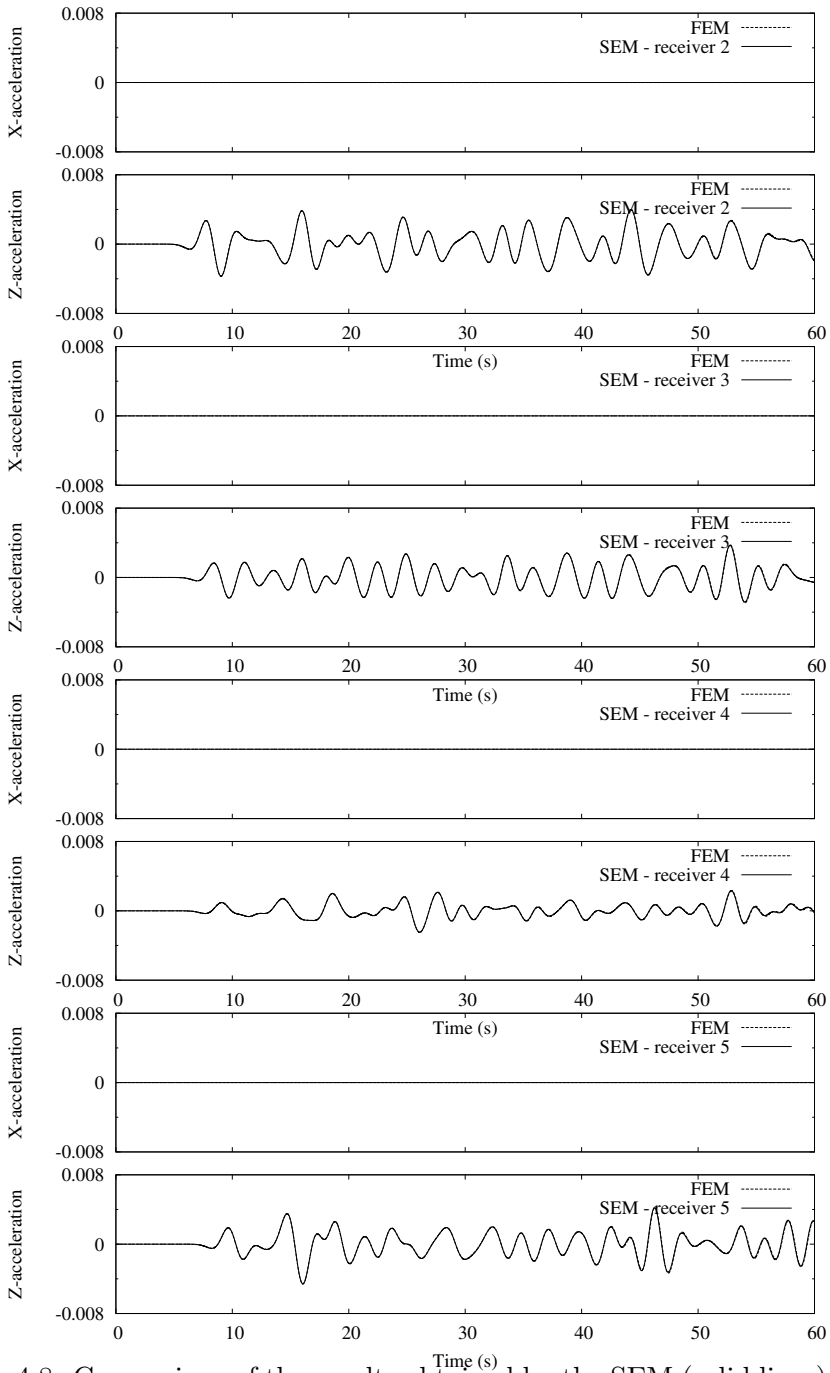

Figure 4.8: Comparison of the results obtained by the SEM (solid lines) and by the classical FEM (dashed lines) for the receivers 2 to 5. The source function has a center frequency of 0.25 Hz.

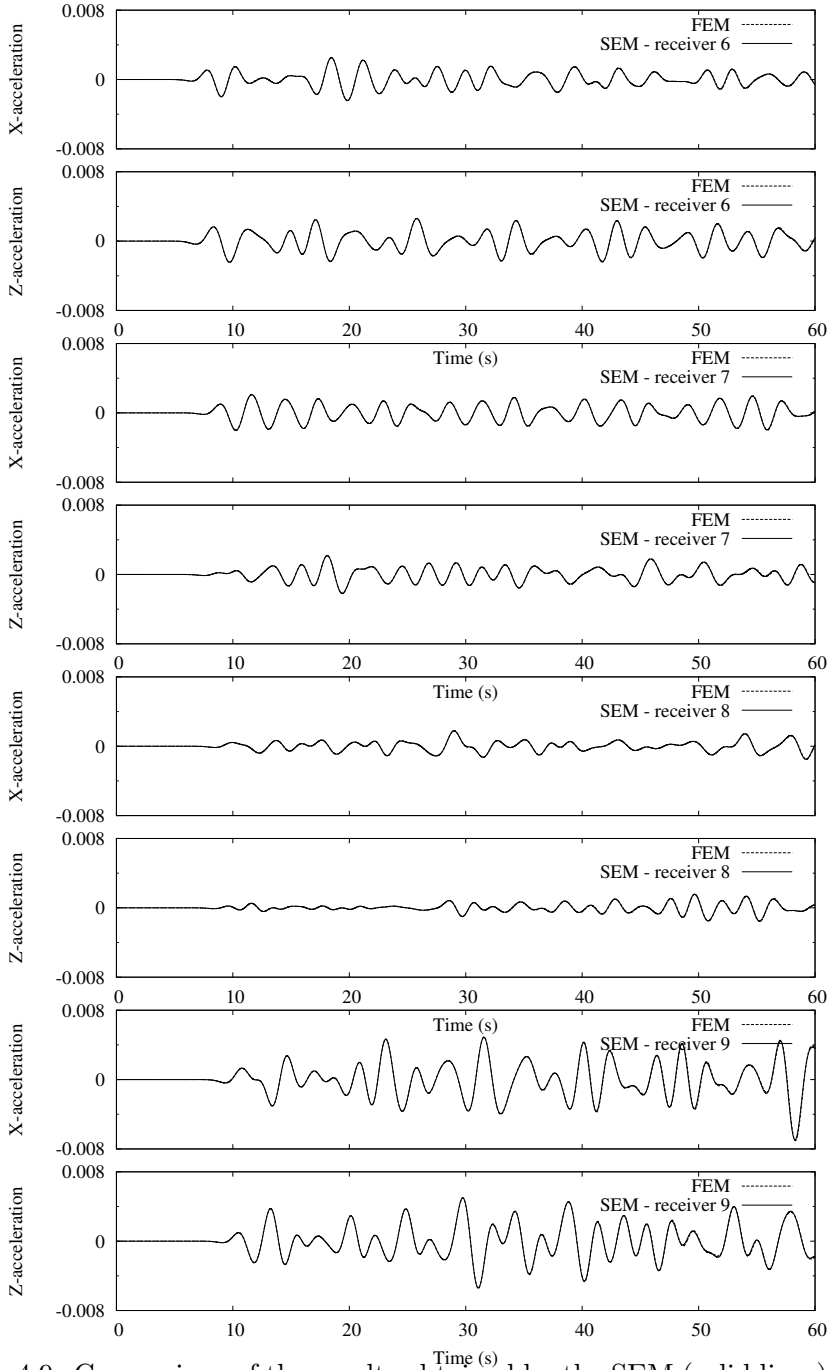

Figure 4.9: Comparison of the results obtained by the SEM (solid lines) and by the classical FEM (dashed lines) for the receivers 6 to 9. The source function has a center frequency of 0.25 Hz.

4.6.2 Ridge subjectted to plane wave

The second test of the 2-D spectral elements code consists in reproducing a well-known topographic effect: a ridge subjectted to a plane SV-wave. The results will be compared to those obtained by Gaffet and Bouchon (1989) and Komatitsch (1997). The topography is represented by a mathematical function given by Sills (1978) as:

$$s(x) = h(1-a)\exp(-3a), \quad with\ a = (x/l)^2$$

where h and l denote the height and the half-width of the hill, respectively. We choose to reproduce the case with $h/l = 0.375$ and $\eta_h = h/(\beta t_p) = 1.0$, where β denotes the S-wave velocity and t_p the period of the Ricker pulse. η_h is thus an adimensional number that represents the ratio between the height of the hill to the wavelength of the incoming wave. The domain is shown in Figure 4.10.

The incoming Ricker wavelet is introduced directly in the domain of the SEM by computing analytically the initial conditions $u(x, z, t_0)$, $\dot{u}(x, z, t_0)$ and $\ddot{u}(x, z, t_0)$ with $u(x, z, t_0)$ being a Ricker wavelet of order two in the space domain. Periodic conditions are present along the vertical edges of the domain (i.e., for a SEM or a FEM, the equation numbers of the nodes located on the left edge of the domain are identical to those of the nodes located on the right edge, or *vice-versa*). Snapshots of the computation results are shown in Figure 4.10 and the synthetics along the free surface are shown in Figure 4.11. The domain of computation is set in an adimensional way with a S-wave velocity $\beta = 1$. The size of the domain is 60×30. The discretization is done using 556×166 spectral elements with polynomials of order 8 (i.e., $9 \times 9 = 81$ GLL nodes per spectral element). The time step Δt is equal to $1e^{-3}$.

Quantitatively, we find the same waves-patterns as those found by Gaffet and Bouchon (1989) and Komatitsch (1997): the ridge gives birth to a Rayleigh wave and to a surface P-wave. The quantitative comparison, which consists in taking the amplitude ratio between the signal recorded at the top of the ridge to the signal recorded in the free field, leads to the same results. The ratio found by Komatitsch (1997) for this ridge's geometry is 2.2; we find in this study a ratio of 2.2 as well. On the other hand, Gaffet and Bouchon (1989) found a larger ratio equal to 2.7. The difference found by the two different methods has not been investigated.

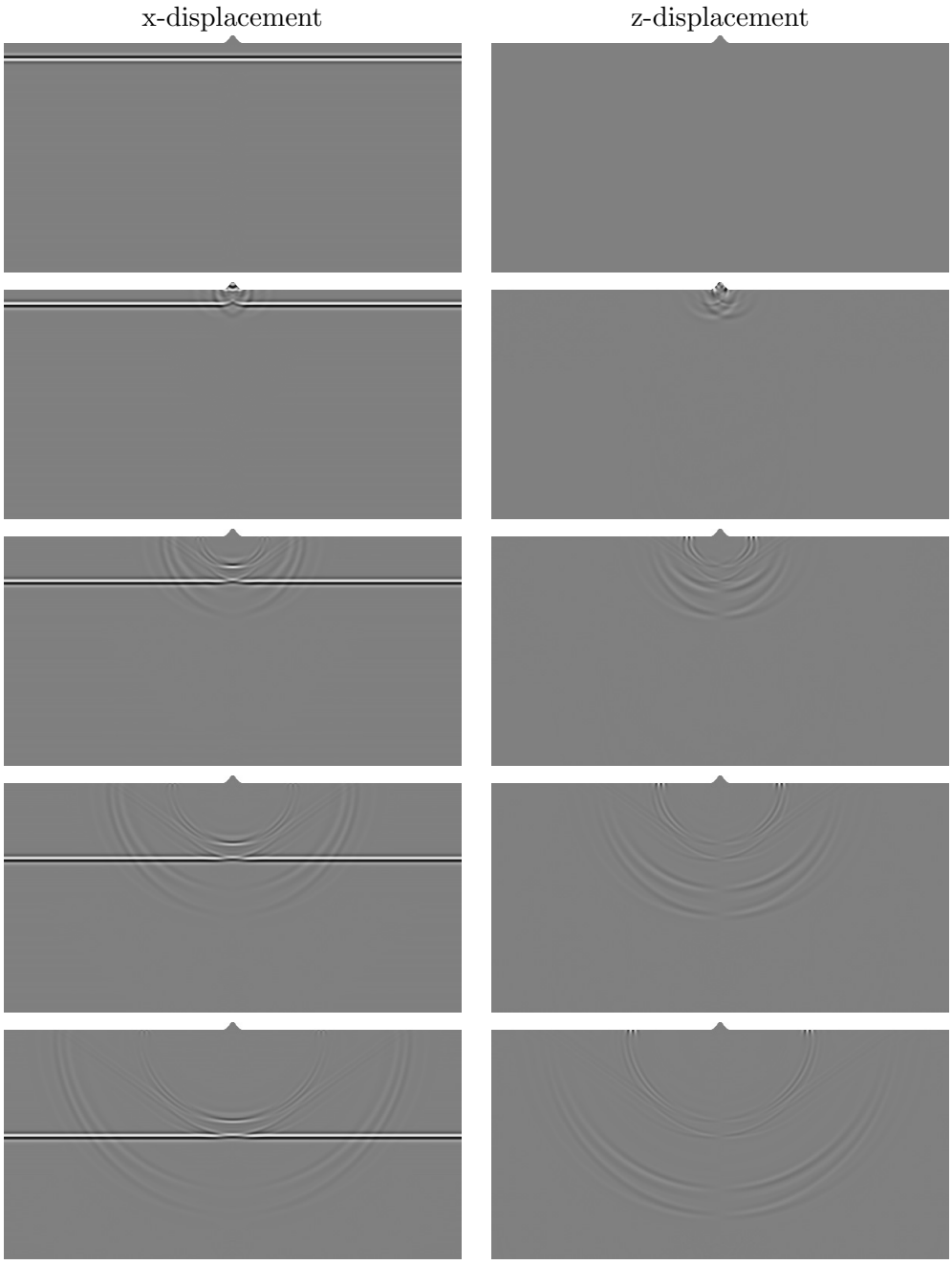

Figure 4.10: Snapshots of a SV-wave propagating toward a ridge. The left-hand side panels represent the x-displacement and the right-hand side panels the z-displacement. From top to bottom, the time of the snapshot is t = 0 s, 4 s, 8 s, 12 s and 16 s. We note that the SV-wave is injected directly at the time t = 0 s by providing the analytical solution to the SEM.

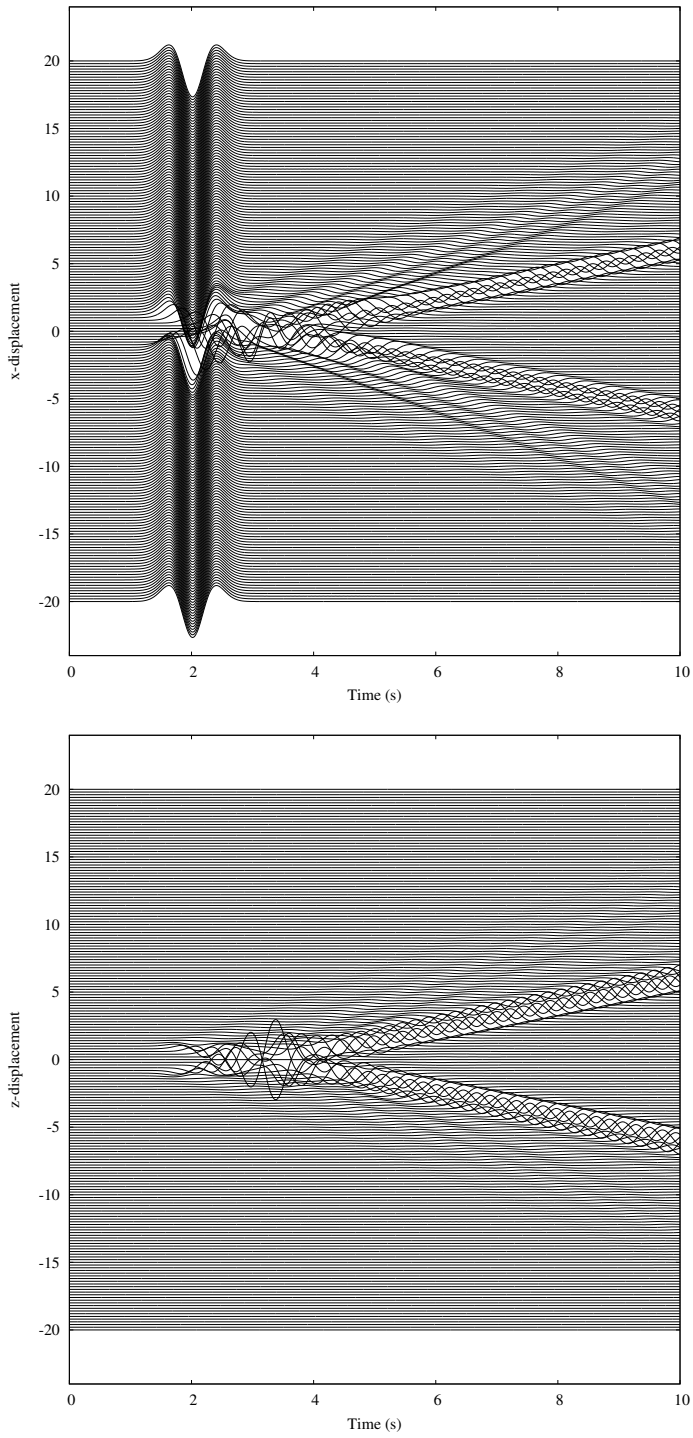

Figure 4.11: Top panel: synthetics of the x-displacement along the free surface of the domain shown in Figure 4.10. Bottom panel: synthetics of the z-displacement along the free surface.

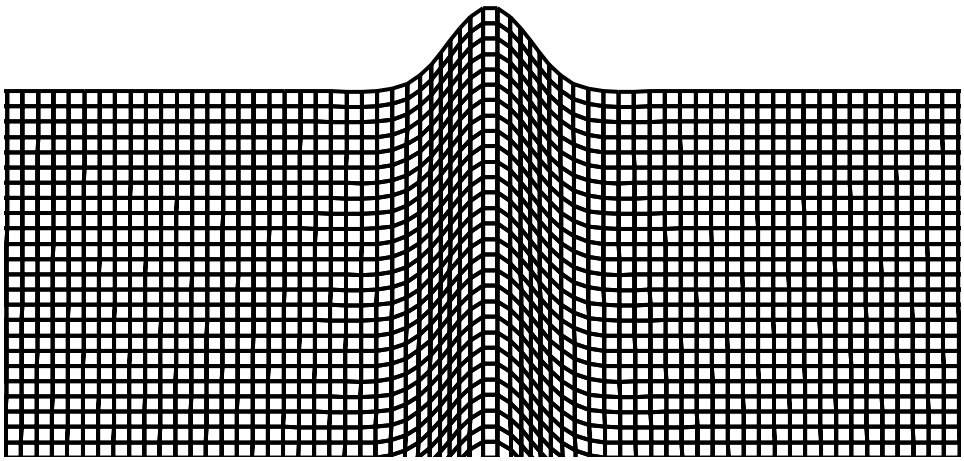

Figure 4.12: Zoom on the mesh of the ridge $h/l = 0.375$.

4.7 Arising of numerical dispersion in the numerical methods

In order to test the numerical dispersion in 2-D that could arise in the classical FEM or SEM, we increase the center frequency of the source function in order to decrease the number of nodes per wavelength. A computation using a source function with a center frequency of 1.0 Hz is performed. For the SEM using the mesh shown in Figure 4.7 and polynomial of order 8, the number of GLL points at 2.5 Hz is approximately 7 or 8 (a fix number of GLL points per wavelength in the SEM is difficult to calculate because the GLL points are not evenly spaced). For the FEM, the mesh is designed to have 7.36 nodes per wavelength at 2.5 Hz (i.e., 18.40 nodes per wavelength at 1.0 Hz).

Figures 4.13 and 4.14 show the results obtained by SEM and FEM. A clear difference is visible. In order to show that the solution obtained by the SEM is accurate, we perform two other simulations using polynomial of order 4 and 20 so that approximately 3 and 16 GLL points are present for wavelengths around 2.5 Hz, respectively. Figure 4.15 exposes the computation done with polynomial of order 4, 8 and 20. We can see that the results obtained by using polynomial of order 8 and 20 are identical, consequently, the simulation using poynomial of order 8 (i.e, $\approx$ 7 or 8 GLL points per wavelength for this problem) is accurate. On the other hand, the simulation using 3 GLL points per wavelength slightly deviates from the simulation using 16 GLL points per wavelength; this means that numerical dispersion/diffusion start to be present in the SEM when only 3 GLL points per minimum wavelength are present.

As a result, the computation performed by the FEM presented in Fig-

ures 4.13 and 4.14 is soiled by numerical dispersion/diffusion as well. We note that for all the receivers, the first wave train is more or less well reproduced by the FEM and that the strong numerical dispersion/diffusion starts appearing after multiple reflexions of the initial wave against the four free surface of the domain.

In order to shown if the degradation of the solution comes from the fact that a lumped mass matrix is used in the FEM, we also perfom a simulation using a consistent mass matrix and an implicit time scheme. The results are identical to the ones found with a lumped mass matrix and consequently, the lumped process is not the cause of the numerical dispersion.

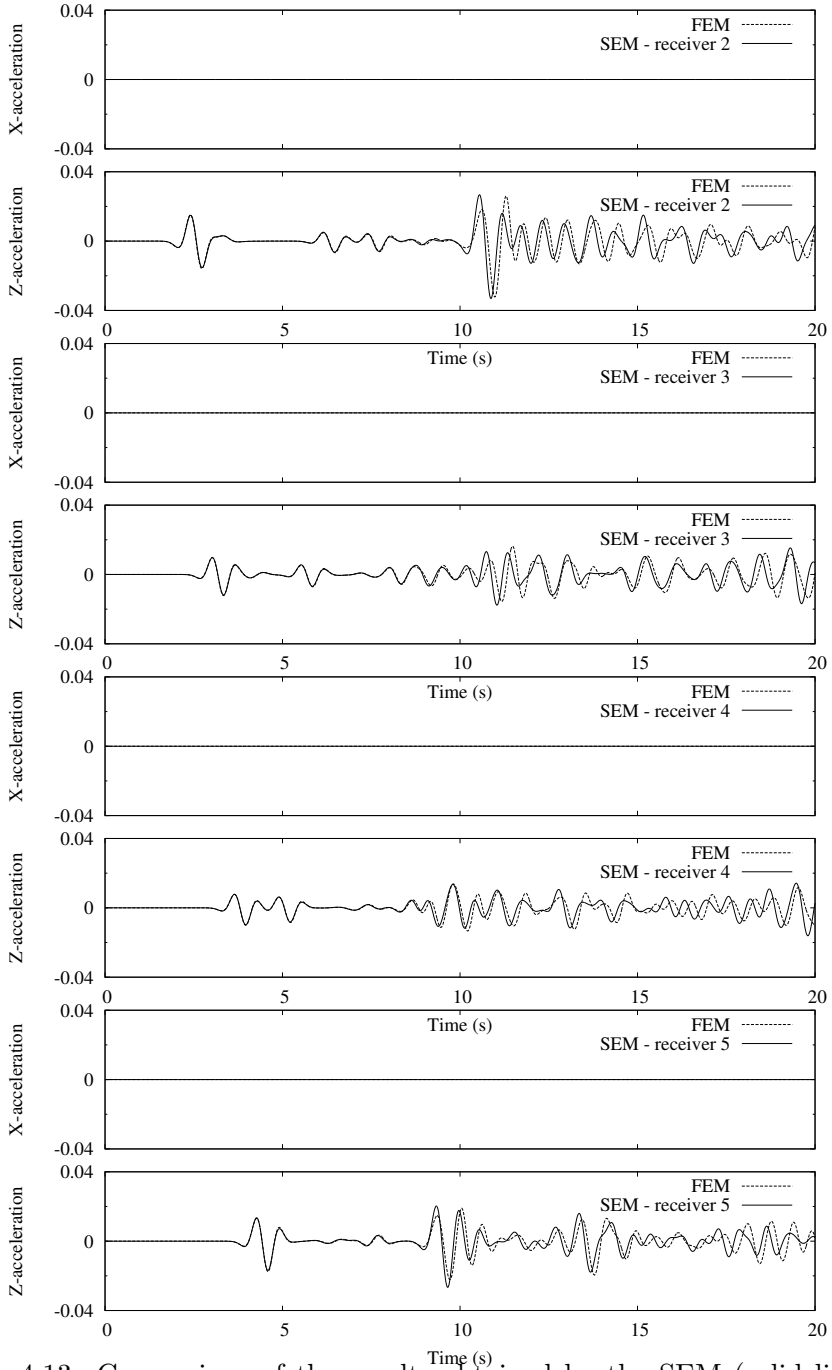

Figure 4.13: Comparison of the results obtained by the SEM (solid lines) and by the classical FEM (dashed lines) for the receivers 2 to 5. The source function has a center frequency of 1.00 Hz.

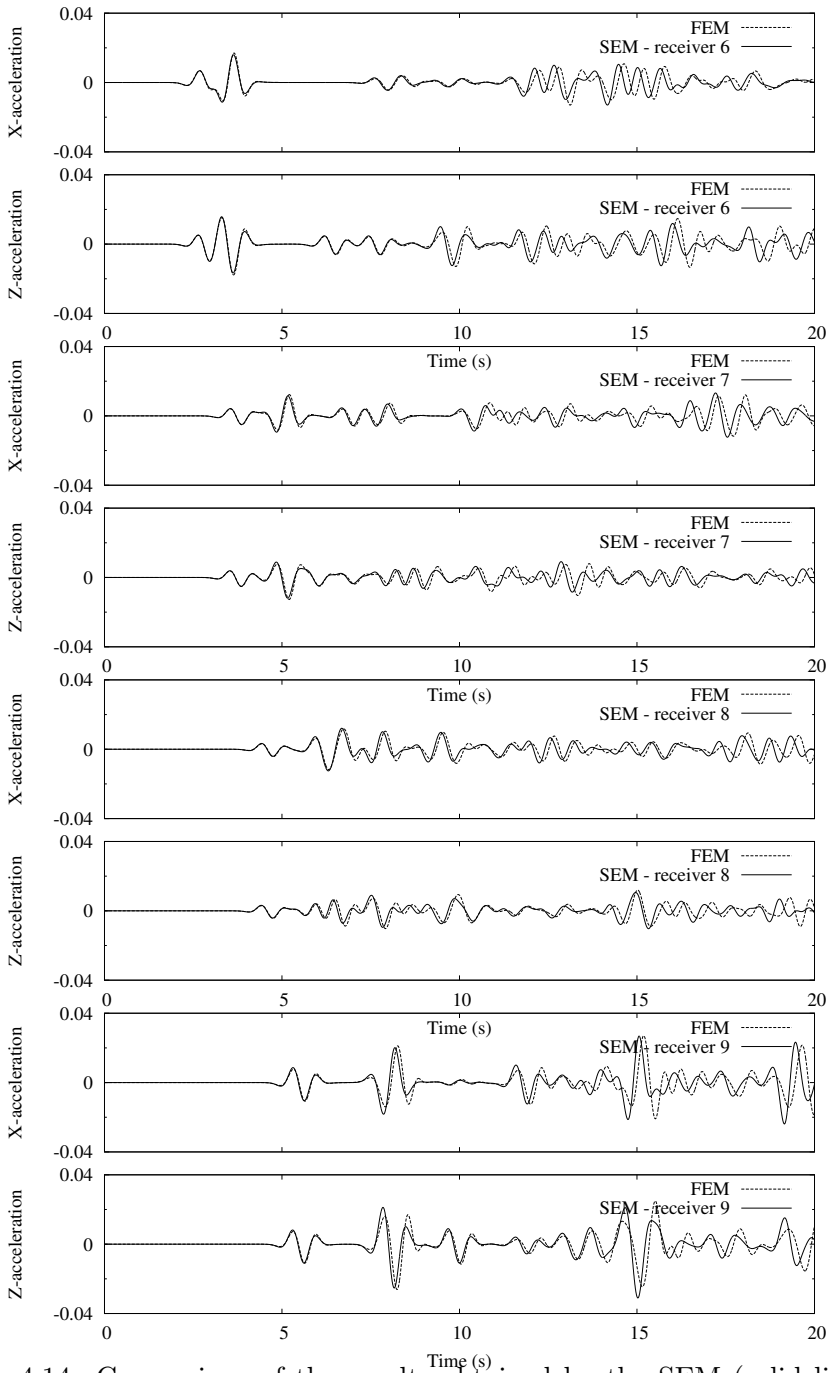

Figure 4.14: Comparison of the results obtained by the SEM (solid lines) and by the classical FEM (dashed lines) for the receivers 6 to 9. The source function has a center frequency of 1.00 Hz.

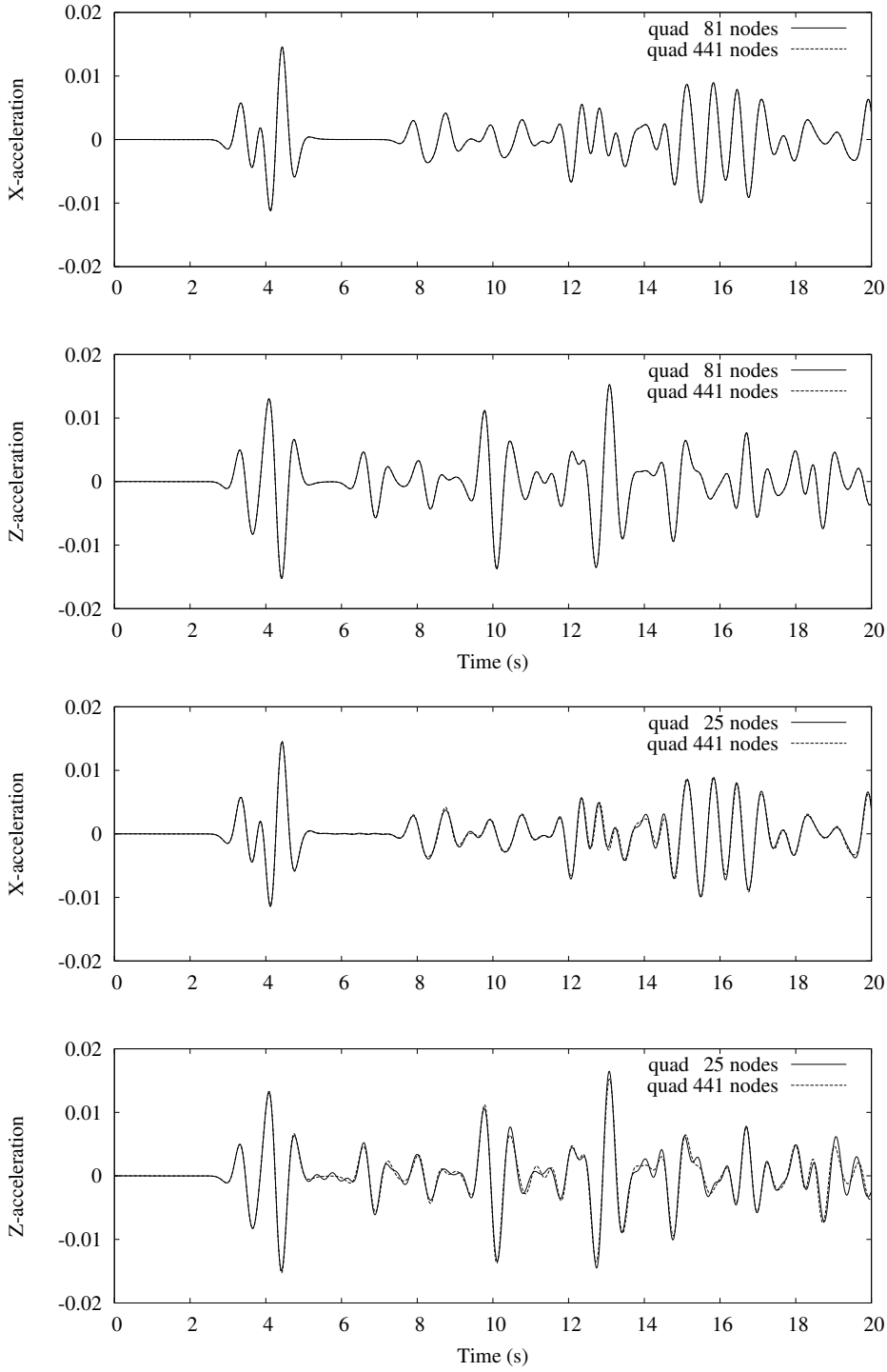

Figure 4.15: Two top panels: comparison between results obtained by the SEM using approximately 7 GLL points per wavelength (i.e., quad 81 nodes) and using approximately 16 GLL points per wavelength (i.e., quad 441 nodes). Two bottom panels: comparison between results obtained by the SEM using approximately 3 GLL points per wavelength (i.e., quad 25 nodes) and using approximately 16 GLL points per wavelength (i.e., quad 441 nodes).

4.8 Testing the Point Source Double-Couple in GEFDyn and EFISPEC

The objective of the present section is to test the accuracy of the Finite Elements Program GEFDyn and of the 3-D spectral elements code programmed for this thesis to generate and propagate seismic wave from a double-couple point source model. For this purpose, we intend to compare theoretical and numerical wave propagation in a 3-D infinite homogeneous medium. The following steps are followed:

1. Representation of the seismic sources and calculus of theoretical seismograms generated from a double-couple point source model in a three-dimensional infinite homogeneous medium;
2. Generation of numerical seismograms using a system of equivalent body forces or imposed displacements in GEFDyn or equivalent body forces in the SEM code;
3. Comparison of theoretical and numerical wave propagation for two-dimensional and three-dimensional tests.

4.8.1 Overview of the double-couple theory

Two different kinds of source can produce seismic waves: sources external to the solid Earth (winds, ocean waves, meteorite impacts, rocket launching, etc.) and sources internal to the solid Earth (earthquakes, underground explosions, etc.). This chapter is about internal sources and more specifically, faulting sources (by opposition to volume sources).

Following Aki and Richards (2002), the easiest Green function to compute general displacements in a volume V from an internal surface Σ (Figure 4.16) is given by

$$u_n(\mathbf{x},t) = \int_{-\infty}^{\infty} d\tau \int\int_{\Sigma} [u_i(\boldsymbol{\xi},\tau)] c_{ijpq} \nu_j \frac{\partial}{\partial \xi_q} G_{np}(\mathbf{x}, t-\tau; \xi, 0) d\Sigma, \qquad (4.7)$$

where u_n is the nth component of displacement, $\mathbf{x}$ is the general position of a point in the volume V, t is the time, τ is the temporal convolution, $[u_i]$ is the ith component of displacement discontinuity on the fault, $\boldsymbol{\xi}$ is the general position on the fault, c_{ijpq} are components of a fourth-order tensor, ν_j is the jth component of the fault normal vector and G_{np} is a Green tensor representing the nth component of a displacement generated by a unit impulse in the p-direction. Using the convolution symbol $*$, the general displacement can be written as:

$$u_n(\mathbf{x},t) = \int\int_{\Sigma} [u_i] \nu_j c_{ijpq} * \frac{\partial}{\partial \xi_q} G_{np} d\Sigma, \qquad (4.8)$$

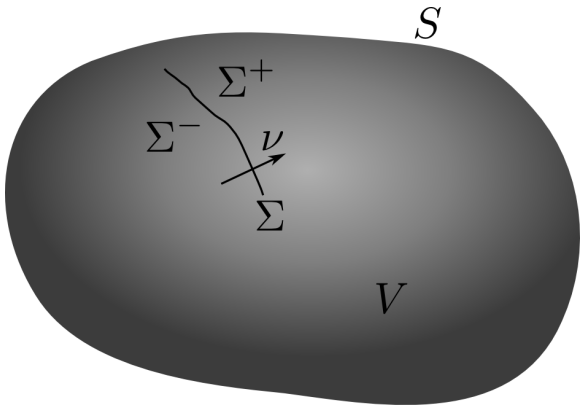

Figure 4.16: A finite elastic body, with volume V and external surface S. The buried fault is represented by the surface Σ across which discontinuities may arise. That is, displacements on the Σ^- side of Σ may differ from displacements on the Σ^+ side of Σ. The normal to Σ is ν, pointing from Σ^- to Σ^+ and the displacement discontinuity is denoted by $[\boldsymbol{u}(\boldsymbol{\xi},\tau)]$ ($\boldsymbol{\xi}$ is a general position on Σ and square brackets referred to the difference $\boldsymbol{u}(\boldsymbol{\xi},\tau)|_{\Sigma^+} - \boldsymbol{u}(\boldsymbol{\xi},\tau)|_{\Sigma^-}$). This figure has been reproduced from Aki and Richards (2002).

with $f * g = \int_0^t f(\tau)g(t-\tau)d\tau = \int_0^t f(t-\tau)g(\tau)d\tau$. The seismic *moment density tensor* $\boldsymbol{m}$ (quantity which depends on source strength and fault orientation; and which characterizes all the information about the source that can be learned from observing waves whose wavelengths are much longer than the linear dimension of Σ) is defined as

$$m_{pq} = [u_i]\nu_j c_{ijpq} \tag{4.9}$$

and consequently,

$$u_n(\mathbf{x},t) = \int\int_\Sigma m_{pq} * G_{np,q} d\Sigma. \tag{4.10}$$

For an isotropic body and for a displacement discontinuity (or slip) parallel to Σ at ξ, then

$$m_{pq} = \mu(\nu_p[u_q] + \nu_q[u_p]), \tag{4.11}$$

with μ one of the Lamé Moduli. In order to visualize the well-known double-couple, we take the case where

- Σ is lying in the plane $\xi_3 = 0$ (horizontal fault)
- and the slip is in the ξ_1-direction,

then

$$\boldsymbol{m} = \begin{pmatrix} 0 & 0 & \mu[u_1(\boldsymbol{\xi},\tau)] \\ 0 & 0 & 0 \\ \mu[u_1(\boldsymbol{\xi},\tau)] & 0 & 0 \end{pmatrix} \tag{4.12}$$

Remembering that our objective is to calculate theoretical seismograms generated from a double-couple Point Source Model and then compare theoretical and numerical seismograms, let us expose the double-couple solution of the elastodynamics equation in an infinite homogeneous medium. The demonstation is presented by Aki and Richards (2002, p.76). Supposing the average displacement discontinuity, $\overline{\boldsymbol{u}} = \frac{\int\int_\Sigma [\boldsymbol{u}] d\Sigma}{A}$ (where $A = \int\int_\Sigma d\Sigma$), parallel to the fault ($\overline{\boldsymbol{u}} \cdot \boldsymbol{\nu} = 0$), we can write the displacement as,

$$\begin{aligned} u_n(\mathbf{x},t) &= \mu(\nu_p\,[u_q] + [\nu_q]\,u_p) A * G_{np,q} \\ &= \left(\frac{30\gamma_n\gamma_p\gamma_q\nu_q - 6\nu_n\gamma_p - 6\delta_{np}\gamma_q\nu_q}{4\pi\rho r^4}\right)\mu A \int_{r/\alpha}^{r/\beta} \tau\overline{u}_p(t-\tau)d\tau \\ &+ \left(\frac{12\gamma_n\gamma_p\gamma_q\nu_q - 2\nu_n\gamma_p - 2\delta_{np}\gamma_q\nu_q}{4\pi\rho\alpha^2 r^2}\right)\mu A\overline{u}_p(t-r/\alpha) \\ &- \left(\frac{12\gamma_n\gamma_p\gamma_q\nu_q - 3\nu_n\gamma_p - 3\delta_{np}\gamma_q\nu_q}{4\pi\rho\beta^2 r^2}\right)\mu A\overline{u}_p(t-r/\beta) \\ &+ \frac{2\gamma_n\gamma_p\gamma_q\nu_q}{4\pi\rho\alpha^3 r}\mu A\dot{\overline{u}}_p(t-r/\alpha) \\ &- \left(\frac{2\gamma_n\gamma_p\gamma_q\nu_q - \nu_n\gamma_p - \delta_{np}\gamma_q\nu_q}{4\pi\rho\beta^3 r}\right)\mu A\dot{\overline{u}}_p(t-r/\beta) \end{aligned} \tag{4.13}$$

where $\boldsymbol{\gamma}$ is the P-wave direction, ρ is the density of the medium, α is the P-wave velocity, β is the S-wave velocity and r is the distance $|\mathbf{x} - \boldsymbol{\xi}|$.

This is the formula that we use in the present section to compute theoretical seismograms generated by a double-couple Point Source. We can see that the total field $u_n(\mathbf{x},t)$ is composed of three types of field.

The so-called *near-field* term is:

$$u_n^N(\mathbf{x},t) = \left(\frac{30\gamma_n\gamma_p\gamma_q\nu_q - 6\nu_n\gamma_p - 6\delta_{np}\gamma_q\nu_q}{4\pi\rho r^4}\right)\mu A \int_{r/\alpha}^{r/\beta} \tau\overline{u}_p(t-\tau)d\tau. \tag{4.14}$$

$\boldsymbol{u}^N$ is composed of both P- and S-wave motions. It is neither irrotational (i.e., having zero curl), nor solenoidal (i.e., having zero divergence), and this indicates that it is not always fruitful to decompose an elastic displacement field into its P- and S-wave components. The *near-field* attenuates as r^{-4}.

The so-called *intermediate-field* terms are:

$$u_n^{IP}(\mathbf{x},t) = \left(\frac{12\gamma_n\gamma_p\gamma_q\nu_q - 2\nu_n\gamma_p - 2\delta_{np}\gamma_q\nu_q}{4\pi\rho\alpha^2 r^2}\right)\mu A\overline{u}_p(t-r/\alpha) \tag{4.15}$$

and

$$u_n^{IS}(\mathbf{x},t) = \left(\frac{12\gamma_n\gamma_p\gamma_q\nu_q - 3\nu_n\gamma_p - 3\delta_{np}\gamma_q\nu_q}{4\pi\rho\beta^2 r^2}\right)\mu A\overline{u}_p(t-r/\beta). \tag{4.16}$$

$\boldsymbol{u}^{IP}$ is the P-wave component and $\boldsymbol{u}^{IS}$ is the S-wave component. Both components attenuate as r^{-2}.

The so-called *far-field* terms are:

$$u_n^{FP}(\mathbf{x},t) = \frac{2\gamma_n\gamma_p\gamma_q\nu_q}{4\pi\rho\alpha^3 r}\mu A\dot{\overline{u}}_p(t-r/\alpha) \tag{4.17}$$

and

$$u_n^{FS}(\mathbf{x},t) = \left(\frac{2\gamma_n\gamma_p\gamma_q\nu_q - \nu_n\gamma_p - \delta_{np}\gamma_q\nu_q}{4\pi\rho\beta^3 r}\right)\mu A\dot{\overline{u}}_p(t-r/\beta) \tag{4.18}$$

$\boldsymbol{u}^{FP}$ is the P-wave component and $\boldsymbol{u}^{FS}$ is the S-wave component. Both components attenuate as r^{-1}.

4.8.2 Calculus of theoretical seismograms in a three-dimensional infinite homogeneous medium

Before exposing the source function $\overline{\boldsymbol{u}}$, let us turn the Equation (4.13) into its vectorial form which is easier to manipulate if we want to program the solution. This gives:

$$\begin{aligned}\boldsymbol{u}(\mathbf{x},t) = {} & \frac{[30(\boldsymbol{\gamma}\cdot\boldsymbol{\nu})(\boldsymbol{\gamma}\cdot\int_{r/\alpha}^{r/\beta}\tau\overline{\boldsymbol{u}}d\tau)\boldsymbol{\gamma} - 6(\boldsymbol{\gamma}\cdot\int_{r/\alpha}^{r/\beta}\tau\overline{\boldsymbol{u}}d\tau)\boldsymbol{\nu} - 6(\boldsymbol{\gamma}\cdot\boldsymbol{\nu})\int_{r/\alpha}^{r/\beta}\tau\overline{\boldsymbol{u}}d\tau]\mu A}{4\pi\rho r^4} \\ & + \frac{[12(\boldsymbol{\gamma}\cdot\boldsymbol{\nu})(\boldsymbol{\gamma}\cdot\overline{\boldsymbol{u}})\boldsymbol{\gamma} - 2(\boldsymbol{\gamma}\cdot\overline{\boldsymbol{u}})\boldsymbol{\nu} - 2(\boldsymbol{\gamma}\cdot\boldsymbol{\nu})\overline{\boldsymbol{u}}]\mu A}{4\pi\rho\alpha^2 r^2} \\ & - \frac{[12(\boldsymbol{\gamma}\cdot\boldsymbol{\nu})(\boldsymbol{\gamma}\cdot\overline{\boldsymbol{u}})\boldsymbol{\gamma} - 3(\boldsymbol{\gamma}\cdot\overline{\boldsymbol{u}})\boldsymbol{\nu} - 3(\boldsymbol{\gamma}\cdot\boldsymbol{\nu})\overline{\boldsymbol{u}}]\mu A}{4\pi\rho\beta^2 r^2} \\ & + \frac{2(\boldsymbol{\gamma}\cdot\boldsymbol{\nu})(\boldsymbol{\gamma}\cdot\dot{\overline{\boldsymbol{u}}})\mu A\boldsymbol{\gamma}}{4\pi\rho\alpha^3 r} - \frac{[2(\boldsymbol{\gamma}\cdot\boldsymbol{\nu})(\boldsymbol{\gamma}\cdot\dot{\overline{\boldsymbol{u}}})\boldsymbol{\gamma} - (\boldsymbol{\gamma}\cdot\dot{\overline{\boldsymbol{u}}})\boldsymbol{\nu} - (\boldsymbol{\gamma}\cdot\boldsymbol{\nu})\dot{\overline{\boldsymbol{u}}}]\mu A}{4\pi\rho\beta^3 r}\end{aligned} \tag{4.19}$$

Defining Cartesian coordinates as exposed in Figure 4.17, we can express $\overline{\boldsymbol{u}}$, $\boldsymbol{\gamma}$ and $\boldsymbol{\nu}$ as a function of the strike angle φ_s, the dip angle δ, the rake angle λ, the take-off angle i_ξ and the azimuth angle φ.

$$
\begin{aligned}
\text{slip } \overline{\boldsymbol{u}} = \quad & \overline{u}(\cos\lambda\cos\varphi_s + \cos\delta\sin\lambda\sin\varphi_s)\mathbf{x} \\
& +\overline{u}(\cos\lambda\sin\varphi_s - \cos\delta\sin\lambda\cos\varphi_s)\mathbf{y} \\
& -\overline{u}\sin\lambda\sin\delta\mathbf{z},
\end{aligned}
$$

$$
\text{fault normal } \boldsymbol{\nu} = \quad -\sin\delta\sin\varphi_s\mathbf{x} + \sin\delta\cos\varphi_s\mathbf{y} - \cos\delta\mathbf{z},
$$

$$
\text{P-wave direction } \boldsymbol{l} = \boldsymbol{\gamma} = \quad \sin i_\xi\cos\varphi\mathbf{x} + \sin i_\xi\sin\varphi\mathbf{y} + \cos i_\xi\mathbf{z},
$$

$$
\text{SV-wave direction } \boldsymbol{p} = \quad \cos i_\xi\cos\varphi\mathbf{x} + \cos i_\xi\sin\varphi\mathbf{y} - \sin i_\xi\mathbf{z},
$$

$$
\text{SH-wave direction } \boldsymbol{\phi} = \quad -\sin\varphi\mathbf{x} + \cos\varphi\mathbf{y}.
$$

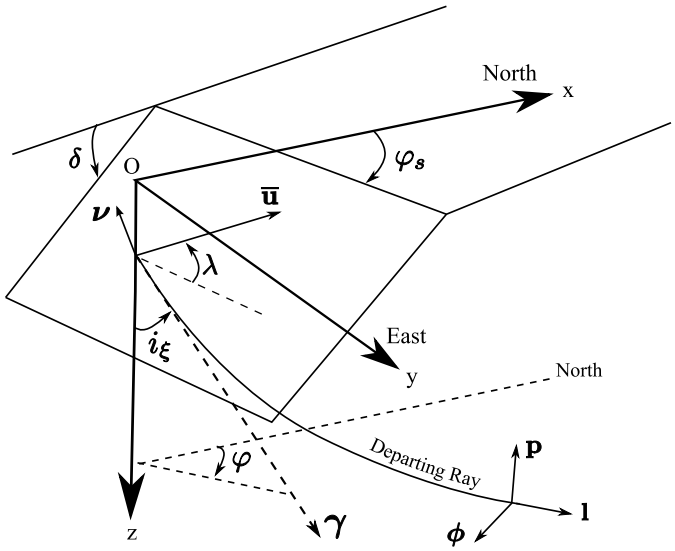

Figure 4.17: Definition of Cartesian coordinates ($\mathbf{x}$, $\mathbf{y}$, $\mathbf{z}$) used to obtain the explicit dependence of $\overline{\boldsymbol{u}}$, $\boldsymbol{\gamma}$, $\boldsymbol{\nu}$, $\boldsymbol{p}$ and $\boldsymbol{\phi}$ on (φ_s, δ, λ, i_ξ, φ). This figure has been reproduced from Aki and Richards (2002).

The last function to express in order to derive theoretical seismograms is the source function $\overline{\boldsymbol{u}}$. For this purpose, let choose the smoothed ramp function whose mathematical expression is easy to manipulate and whose form can be seen as displacement discontinuity along a fault. The smoothed ramp function is of the form (e.g., Bouchon and Coutant, 1994)

$$
\overline{u}(t) = \frac{B[1 + tanh(4f_c(t - \tau_s))]}{2}, \tag{4.20}
$$

with B the amplitude of the final displacement, tanh the hyperbolic tangent, f_c the characteristic frequency, t the time and τ_s the time where the function

is centered (i.e. time shift). Figure 4.18 shows the function with $B = 1$, $\tau_s = 2$ and f_c as a parameter. The first, second and third derivatives are

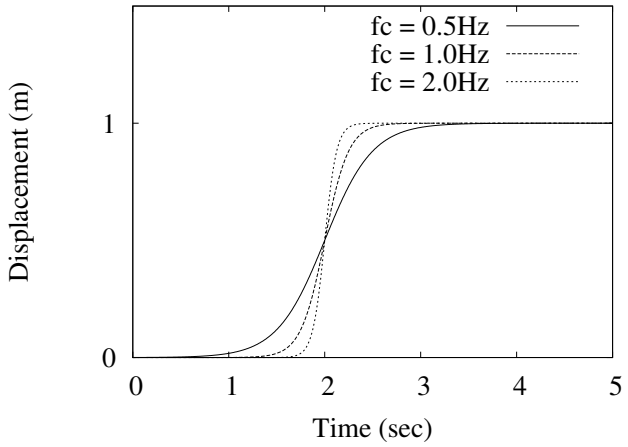

Figure 4.18: Displacement source function of the form $\overline{u} = \frac{B(1+tanh(4f_c(t-\tau_s)))}{2}$. The characteristic frequency is determined by f_c.

obtained by using the chain rule (i.e., $(f \circ g)' = f'(g(x))g'(x)$) and are of the

$$\dot{\overline{u}}(t) = 2Bf_c[1 - tanh^2(4f_c(t-\tau_s))]$$

form: $$\ddot{\overline{u}}(t) = -16Bf_c^2 tanh(4f_c(t-\tau_s))[1 - tanh^2(4f_c(t-\tau_s))]$$

$$\dddot{\overline{u}}(t) = -64Bf_c^3[1 - 3tanh^2(4f_c(t-\tau_s))][1 - tanh^2(4f_c(t-\tau_s))]$$

The third derivative of the source function $\overline{u}$ is necessary if we want to compute the general acceleration $\ddot{\boldsymbol{u}}(\mathbf{x}, t)$ since the general displacement $\boldsymbol{u}(\mathbf{x}, t)$ depends on $\dot{\overline{u}}$. Figure 4.19 shows the first, second and third derivative of the source function with respect to time. We can notice that the third derivative is of the form of the well-known Ricker of order 2 function, widely used in the literature, whose principal advantage is not to create high frequencies due to its smoothed cut-off frequency (e.g., Bard and Bouchon, 1980; Bard, 1983; Modaressi, 1987).

The characteristics of the theoretical example that will be used to verify the validity of the FEM and SEM to propagate elastic waves are given in Table 4.4, Table 4.5 and Table 4.6.

Figure 4.20 shows displacement, velocity and acceleration seismograms for the above-mentionned characteristics. Two receivers are located above the source at $i_\xi = 180°$, $\varphi = 0°$ and $r = [10, 20]km$. The far field radiation pattern for P- and S-wave associated to this fault parameters are shown in

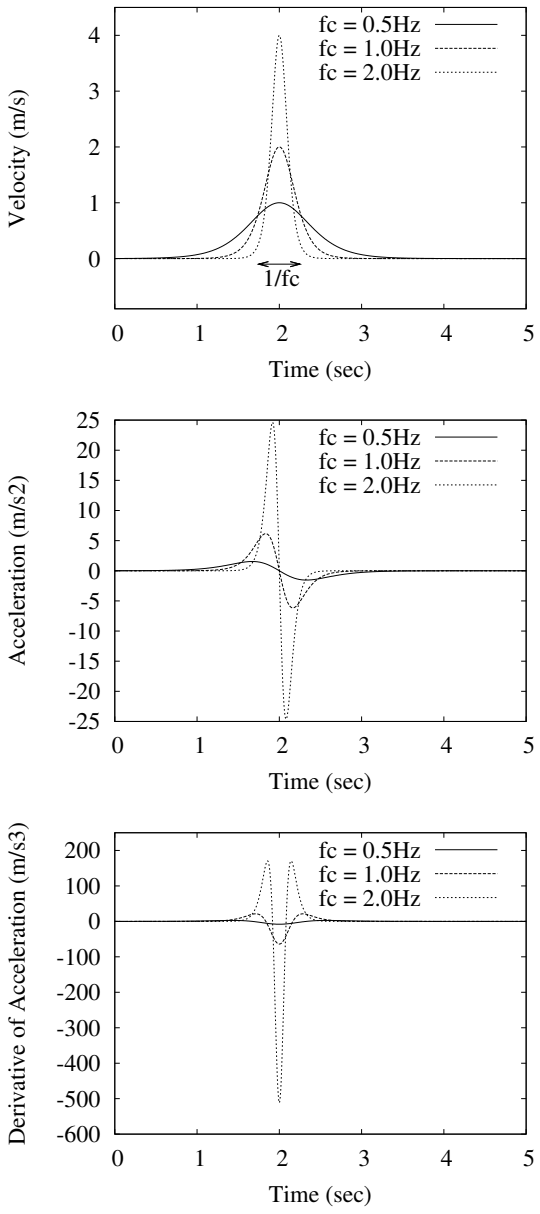

Figure 4.19: Top panel: Velocity source function. For $f_c = 2.0$, 1.0 and 0.5 Hz, the characteristic period is shown by a horizontal arrow and is equal to $1/f_c = 1/2 = 0.5$ s. Middle panel: Acceleration source function. Bottom panel: Derivative of the acceleration source function with respect to time.

Table 4.4: Fault's Parameters (horizontal fault)

Strike	Dip	Rake
$\varphi_s = 0°$	$\delta = 0°$	$\lambda = 0°$

Table 4.5: Source's Parameters

Seismic Moment M_0 $(N.m)$	Characteristic Frequency f_c (Hz)	Time Shift τ_s (sec)
10^{16}	1	2

Figure 4.21.

4.8.3 Comparison of theoretical and numerical waves propagation in a linear elastic infinite homogeneous medium

In this section, two-dimensional and three-dimensional tests of wave propagation generated from a double-couple Point Source in a linear elastic medium are presented. The two-dimensional test can not be compared quantitatively with wave propagation theory exposed above since this theory holds for 3-D medium. Hence, only a qualitative comparison of radiation pattern has been done. On contrary, the three-dimensional tests compare quantitatively theoretical and numerical wave propagation.

Description of the two-dimensional test

The geometry we chose to test the validity of the double-couple Point Source Model in GEFDyn is a square whose edge is 20 km. The 2-D plane used for the simulation is the plane **xz** of the Figure 4.17. The mesh is composed of quadrangle whose size is $\Delta_x = 125m$ and $\Delta_z = 125m$. The point source is located at the center of the domain and the double-couple has been modeled by equivalent body forces as exposed in Figure 4.22. The fault and the source function are those exposed in Section 4.8.2. Moreover, paraxial elements have been attached to the boundaries in order to avoid reflected waves (e.g., Engquist and Majda (1977); Clayton and Engquist (1977); Modaressi

Table 4.6: Characteristics of the infinite homogeneous medium

$\rho(kg/m^3)$	$\alpha(m/s)$	$\beta(m/s)$
1800	4000	2300

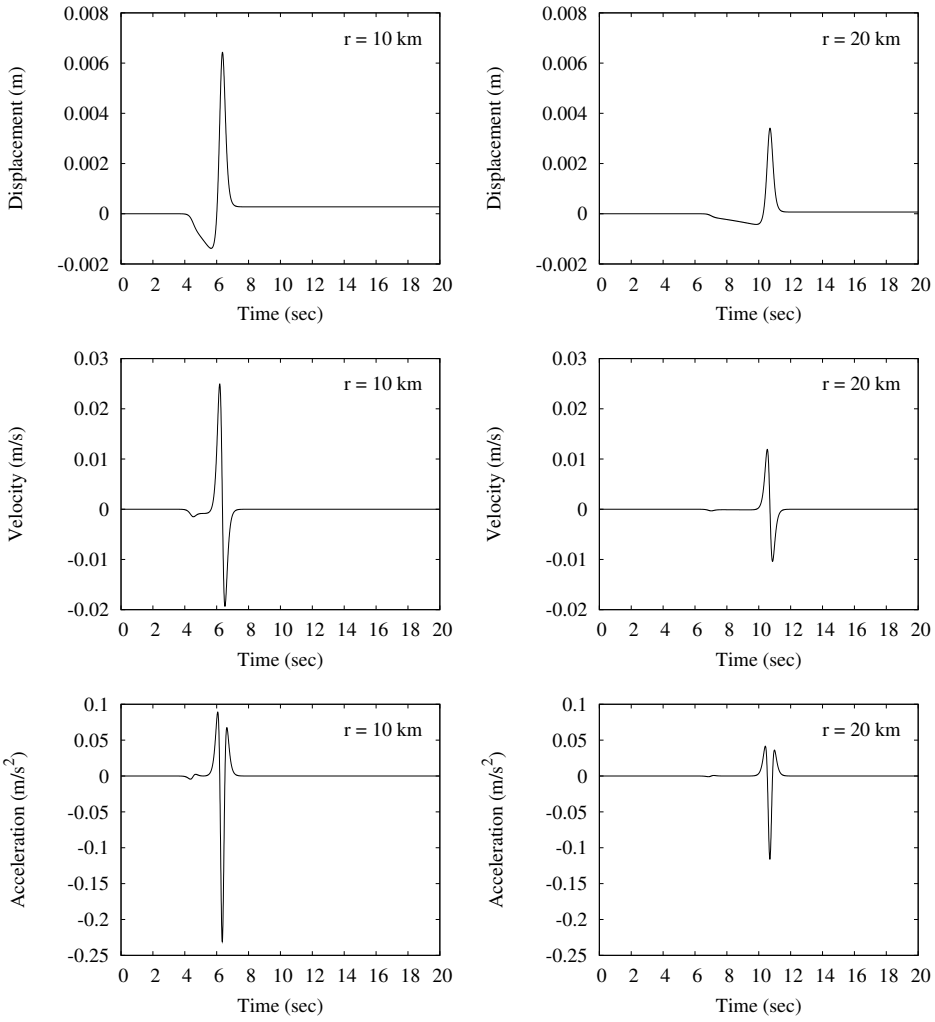

Figure 4.20: Total x-displacement (u_x, top panel), total x-velocity ($\dot{u}_x$, middle panel) and total x-acceleration ($\ddot{u}_x$, bottom panel) for receivers at $i_\xi = 180°$, $\varphi = 0°$ and $r = [10, 20]km$.

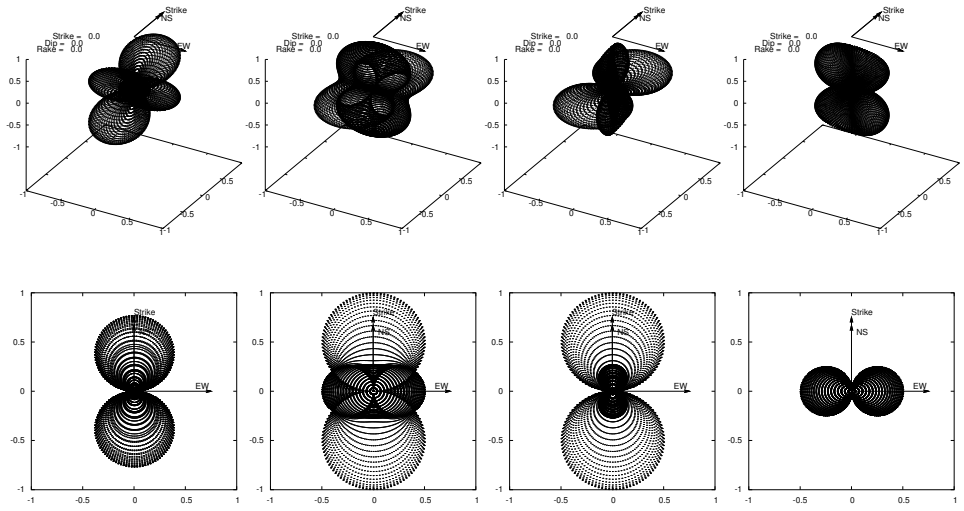

(a) P-wave (b) S-wave (c) SV-component (d) SH-component

Figure 4.21: Theoretical radiation pattern of far-field wave for a double-couple Point Source Model in an homogeneous medium oriented as followed: $\varphi_s = 0°$, $\delta = 0°$ and $\lambda = 0°$. Panels (a) and (b) show P- and S-wave radiation pattern, respectively. Panels (c) and (d) expose SV- and SH-component of the S-wave, respectively. Top panels show a 3-D view of the radiation patterns and bottom panels show them mapped into the horizontal plane.

(1987)).

The Finite Element simulation has been performed with a lumped mass matrix and the Newmark-Beta Method using $\Delta t = 0.01s$, $\gamma = 1/2$ and $\beta = 1/4$. For these algorithm parameters, the dispersion relation for harmonic waves is given by Bamberger et al. (1980) and Modaressi (1987) as

$$\alpha \frac{\Delta t}{\Delta x} \leq 0.5. \tag{4.21}$$

Medium's characteristics are exposed in Table 4.6. Characteristics are those of a seismological bedrock and it should be noted that we chose approximately 20 nodes per wavelength for this 2-D test so that the dispersion relation of Equation (4.21) was fully satisfied.

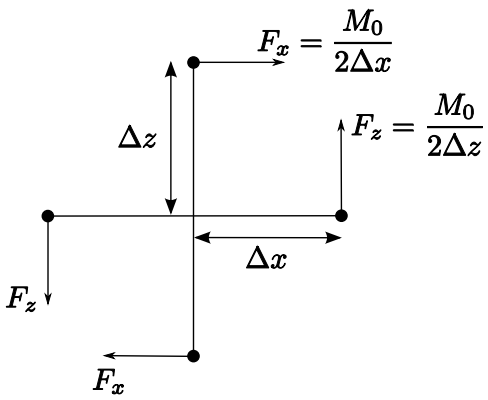

Figure 4.22: Configuration of the equivalent body force modelling the double-couple Point Source. The solid points indicate nodes of the Finite Element spatial discretization.

Results of the two-dimensional test

Figure 4.23 shows the modulus of acceleration that can be assimilated to the 2-D numerical radiation pattern of P- and S-wave from the double-couple point source. Hence, this Figure can be compared with Figure 4.21 which exposes 3-D theoretical radiation pattern. Qualitatively, we can observe a good agreement between theoretical and numerical radiation pattern (we remind that the 2-D simulation has been performed in the plane **xz** of Figure 4.17). As for P-waves, we find they are predominant for take-off angles $i_\xi = \pi/4$ *modulo* $\pi/2$ and nonexistent for $i_\xi = 0$ *modulo* $\pi/2$. On the contrary, S-waves are predominant for take-off angles $i_\xi = 0$ *modulo* $\pi/2$ and nonexistent for $i_\xi = \pi/4$ *modulo* $\pi/2$. This is what exhibits the theoretical radiation pattern of Figure 4.21. Moreover, we have also verified that the inward and outward motions were respected. Thus, qualitatively speaking, the Finite Elements Method reproduce quite well the theoretical radiation pattern.

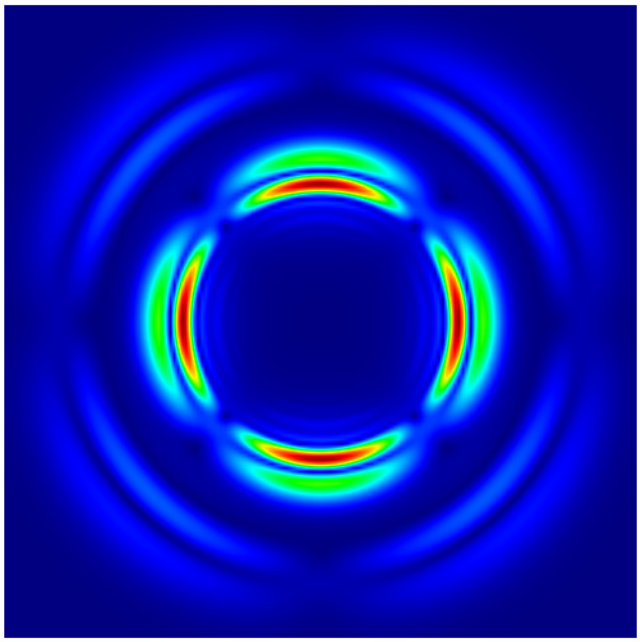

Figure 4.23: Visualization of the numerical radiation pattern of P-wave and S-wave in the **xz**-plane of Figure 4.17 (the modulus of the acceleration is represented on the Figure).

Description of the three-dimensional test

As for the 3-D numerical test performed using GEFDyn, the geometry is a cube whose edge is 6.9 km. Receivers are positionned so that the superposition of the so-called *Near Field*, *Intermediate Field* and *Far Field* is present. The medium and source's characteristics (i.e., central frequency = 1 Hz) are the same as those used for the 2-D test. The source is located at the center of the geometry (i.e., $x = 0$, $y = 0$ and $z = 0$). The spatial discretization is made of regular hexahedron whose edge is 230 meters. The associated polynomials are of order one so that four nodes per wavelength are present at 2.5 Hz (i.e., maximum frequency where energy is still present using a tanh of central frequency of 1 Hz as source function). Paraxial elements are attached at the six boundaries of the cube to mimic an infinite medium. Moreover, GEFDyn offers the possibility to impose forces or displacements at a node; consequently, we have tested both methods to represent the double-couple. The forces or displacements are imposed as shown in Figure 4.22.

As for the 3-D numerical test using the spectral elements code EFISPEC, two dimensions of domain are considered. The first domain is large enough (cube of 28 km edge) so that the receivers are not infected by the reflected waves at the boundaries. The second domain is smaller (cube of 10 km edge) and paraxial elements are attached at the boundaries to mimic an infinite medium. In both cases, the domain is discretized so that approximately six nodes per wavelength are present at 2.5 Hz (polynomials of order four are used for the simualtions). In EFISPEC, the source is implemented in a more elegant way as:

$$\mathbf{f}(\mathbf{x}, t) = -div(\boldsymbol{m}(\mathbf{x}, t)),$$

with $\mathbf{f}$ the equivalent body force, $\boldsymbol{m}$ the moment density tensor presented above and div the divergence operator.

Results of the three-dimensional tests

This section exposes the results for the cube whose edge is 6.9 km. First, we have compared the theoretical source function with the simulated one using GEFDyn. Figure 4.24 exposes the normalized displacement and velocity at a source node where an equivalent body force or an equivalent imposed displacement is applied. We can see that both methods reproduce well the theory, however, the method using equivalent body forces generates some spurious oscillations once the ramp has been reached.

Figures 4.25, 4.26 and 4.27 show raw results of $u_x(\mathbf{x}, t)$, $\dot{u}_x(\mathbf{x}, t)$ and $\ddot{u}_x(\mathbf{x}, t)$ for receivers located above the source along the $\mathbf{z}$-axis using equivalent body forces to represent the double-couple (It should be noted that x-component along the $\mathbf{z}$-axis represents SV-wave). Figures 4.28, 4.29 and 4.30 show the same results using equivalent imposed displacements to represent the double-couple.

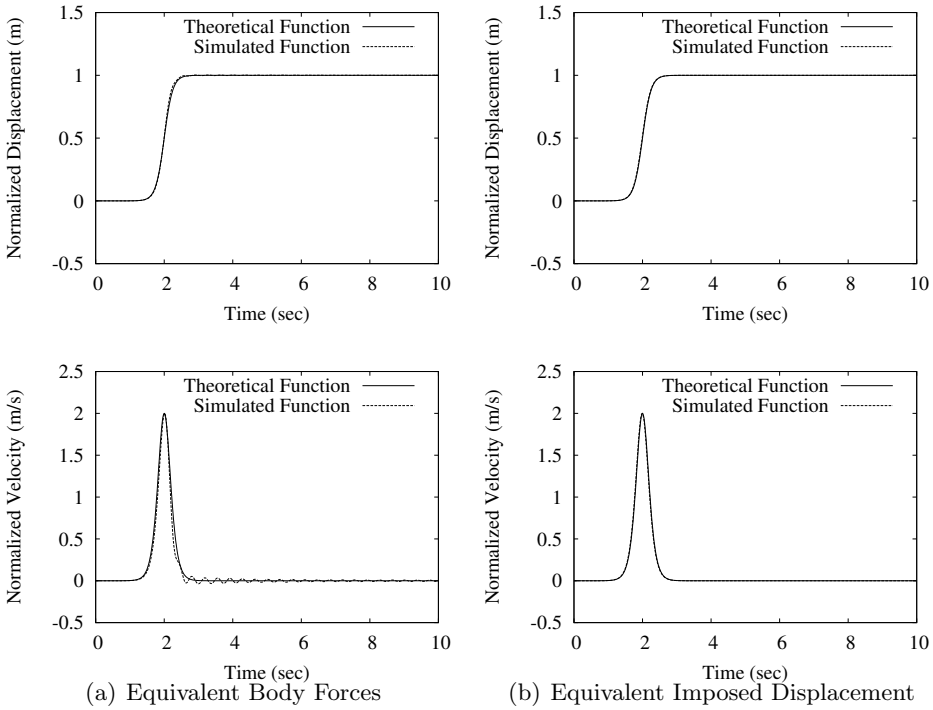

(a) Equivalent Body Forces (b) Equivalent Imposed Displacement

Figure 4.24: Normalized displacement and velocity at a source node where an equivalent body force (left panels) or an equivalent imposed displacement (right panels) is applied.

Observing displacements, we can see that both methods used to represent the double-couple tend to overestimate final displacement. Nevertheless, time of arrival and maximum amplitude are fairly reproduced by simulations. We note that using equivalent body forces generates spurious oscillations once the shear dislocation reaches its maximum.

Velocities and accelerations being first and second derivative of displacement, these spurious oscillations become more pronounced on velocity seismogram and accelerogram when using equivalent body forces to represent the double-couple.

In conclusion, even if both methods used to represent the double-couple fairly reproduce theoretical wave propagation, we can see at a glance that using equivalent imposed displacements generates few oscillations once the source function reaches its maximum. Moreover, simulation of amplitude of physical quantities is much sharper. For both cases, the numerical dispersion is the cause of the spurious oscillations.

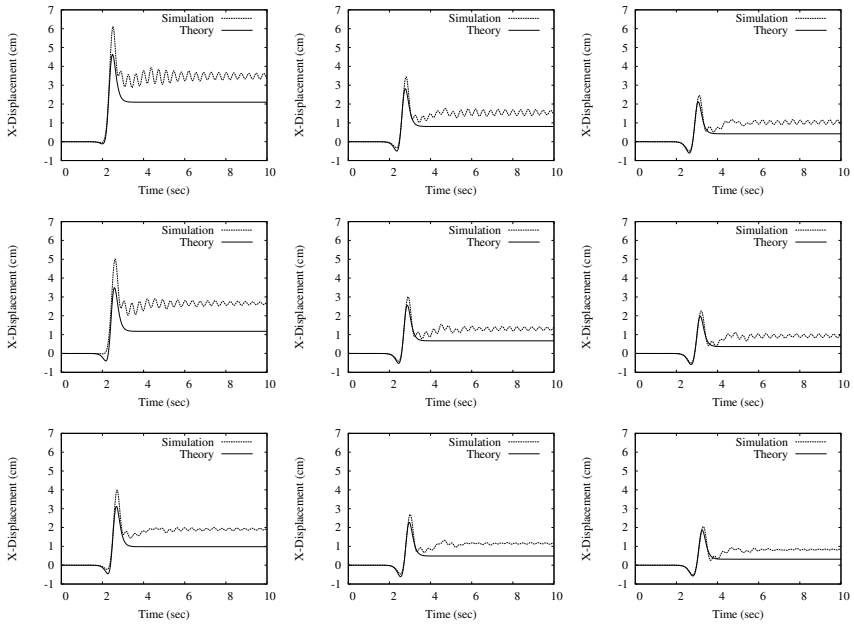

Figure 4.25: Comparison between theoretical and numerical x-displacement ($u_x(\mathbf{x}, t)$) using GEFDyn with equivalent body forces. Receivers are located along the **z**-axis ($\varphi = 0°$, $i_\xi = 180°$) at distance $r = [920, 1150, 1380]m$ (left column from top to bottom), $r = [1610, 1840, 2070]m$ (middle column from top to bottom) and $r = [2300, 2530, 2760]m$ (right column from top to bottom).

The following of this section exposes the results using the spectral elements code EFISPEC (for these simulations, the strike (φ_s), dip (δ) and rake

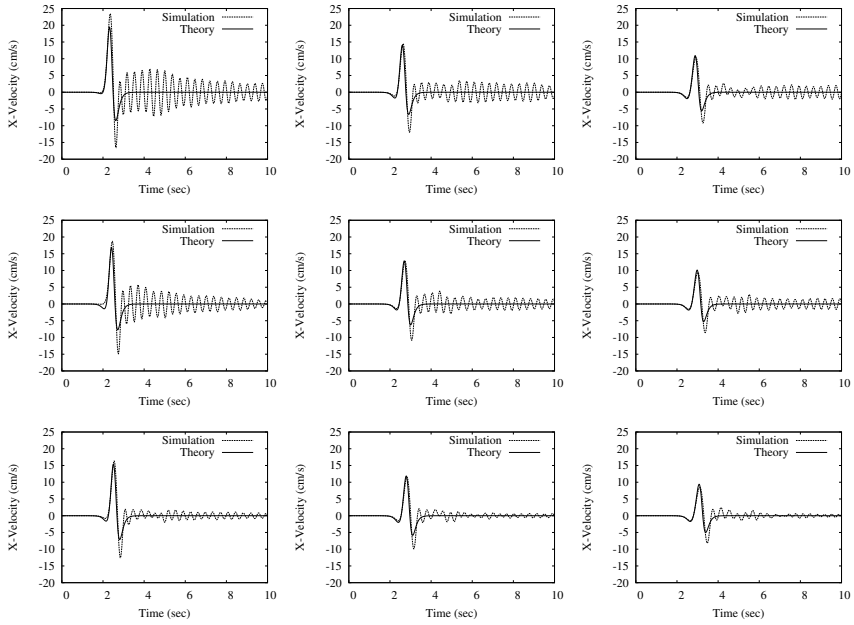

Figure 4.26: Comparison between theoretical and numerical x-velocity ($\dot{u}_x(\mathbf{x}, t)$) using GEFDyn with equivalent body forces. Receivers are those described in Figure 4.25.

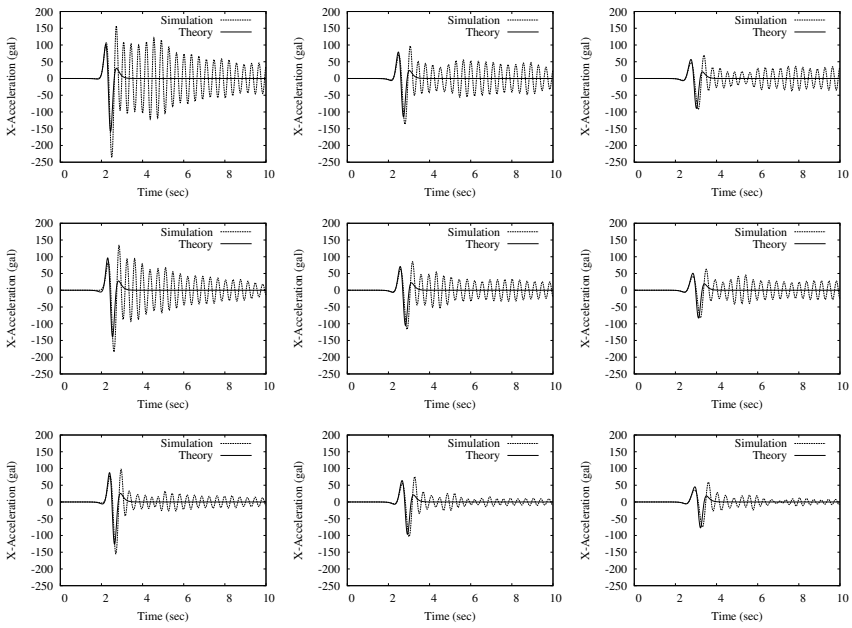

Figure 4.27: Comparison between theoretical and numerical x-acceleration ($\ddot{u}_x(\mathbf{x}, t)$) using GEFDyn with equivalent body forces. Receivers are those described in Figure 4.25.

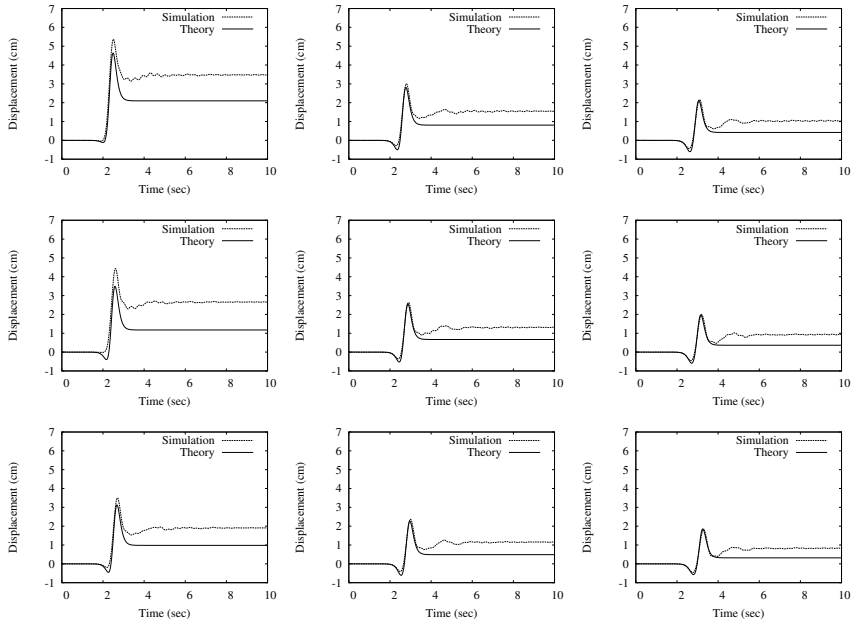

Figure 4.28: Comparison between theoretical and numerical x-displacement ($u_x(\mathbf{x}, t)$) using GEFDyn with equivalent imposed displacements. Receivers are those described in Figure 4.25.

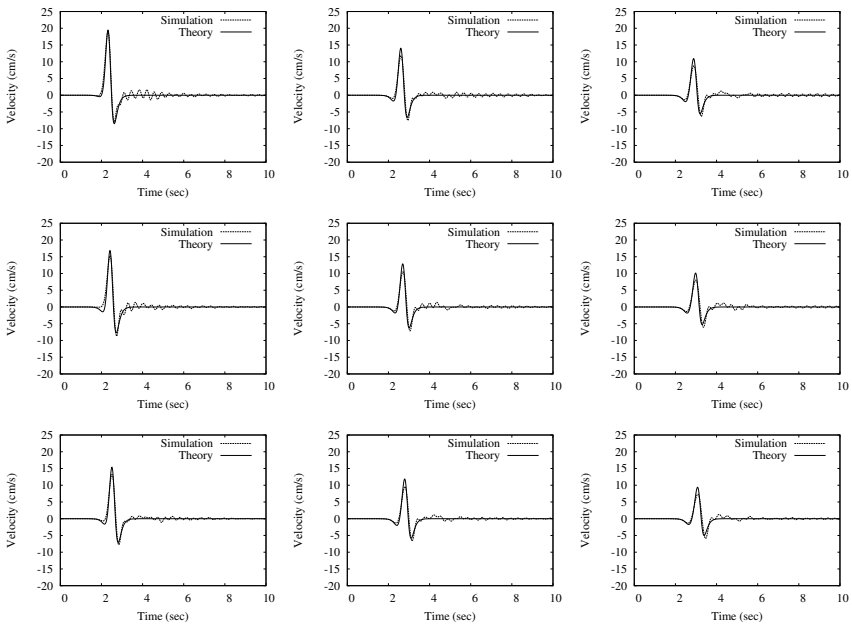

Figure 4.29: Comparison between theoretical and numerical x-velocity ($\dot{u}_x(\mathbf{x}, t)$) using GEFDyn with equivalent imposed displacements. Receivers are those described in Figure 4.25.

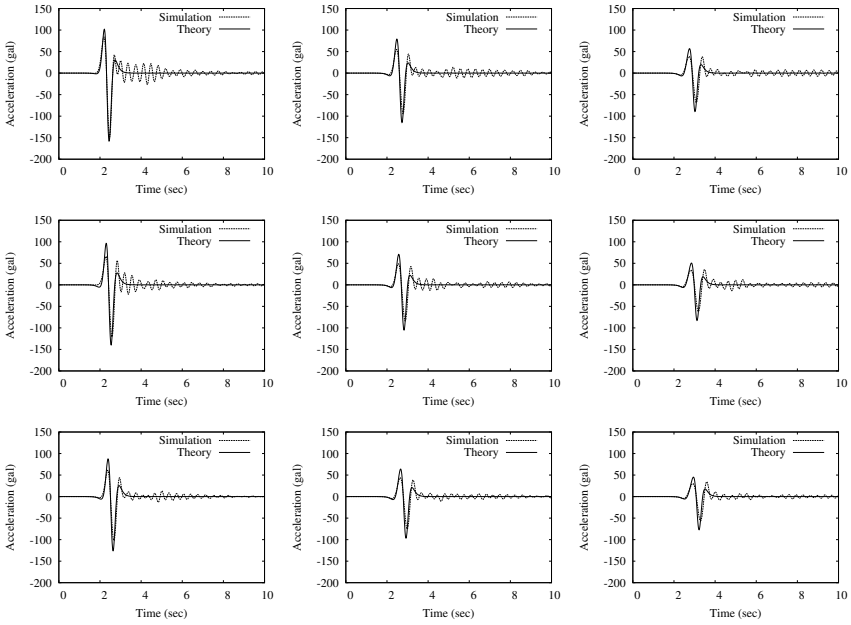

Figure 4.30: Comparison between theoretical and numerical x-acceleration ($\ddot{u}_x(\mathbf{x}, t)$) using GEFDyn with equivalent imposed displacements. Receivers are those described in Figure 4.25.

angle (λ) of the source are arbitrary (i.e., $\varphi_s = 30°$, $\delta = 15°$ and $\lambda = \text{-}100°$)). Figures 4.31 to 4.33 show the results for the large domain (i.e., no need of absorbing conditions) at the receivers located at $(x, y, z) = (0{,}2000{,}0)$, $(x, y, z) = (0{,}3000{,}0)$ and $(x, y, z) = (0{,}4000{,}0)$. The SEM nicely reproduces the theoretical results. Only small oscillations are visible on the acceleration between 4 and 5 s (certainly due to a light numerical dispersion).

We note that close from the point source, the theory shows that the physical quantities (e.g., displacement, velocity, etc.) tend to infinity due to their dependency in $1/r$. The numerical simulation is not able to reproduce such a phenomenon as shown for a receiver located at $(x, y, z) = (0{,}1000{,}0)$ in Figure 4.34.

Figure 4.35 shows the same receiver than Figure 4.32 but for the domain using paraxial approximation as boundary conditions to mimic an infinite medium. We can see that the results are influenced by the presence of the paraxial elements and that the wave is not absorbed totally (as already shown by previous studies (e.g., Ma and Liu, 2006)).

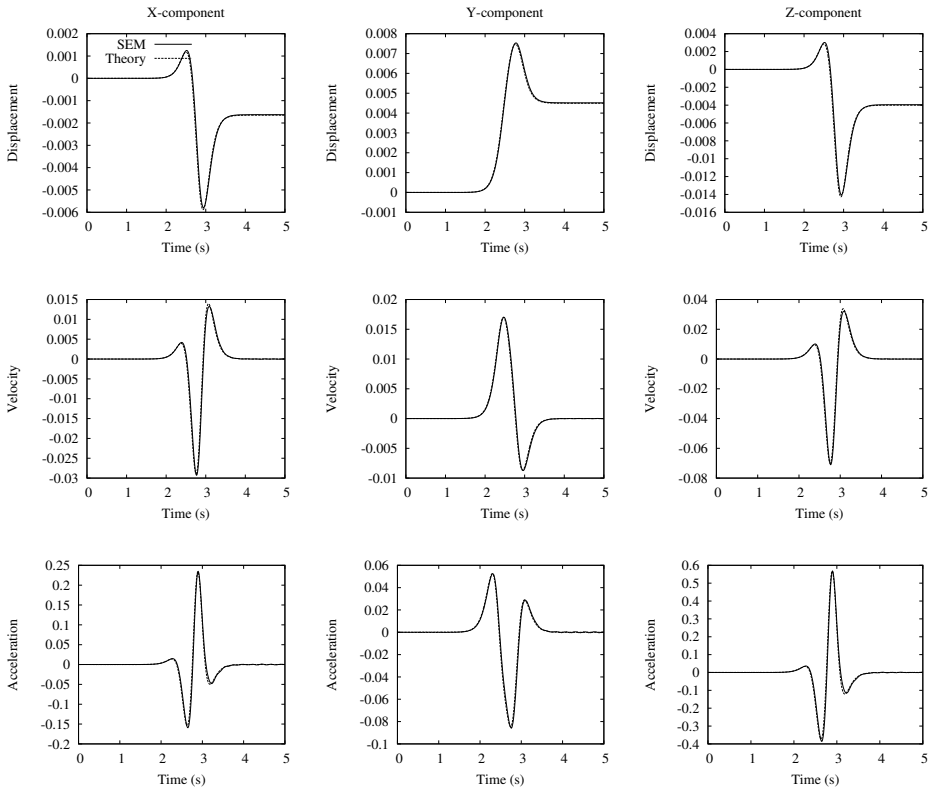

Figure 4.31: Comparison between the theoretical results and the results obtained by the numerical simulation using EFISPEC at the receiver $(x, y, z) = (0{,}2000{,}0)$.

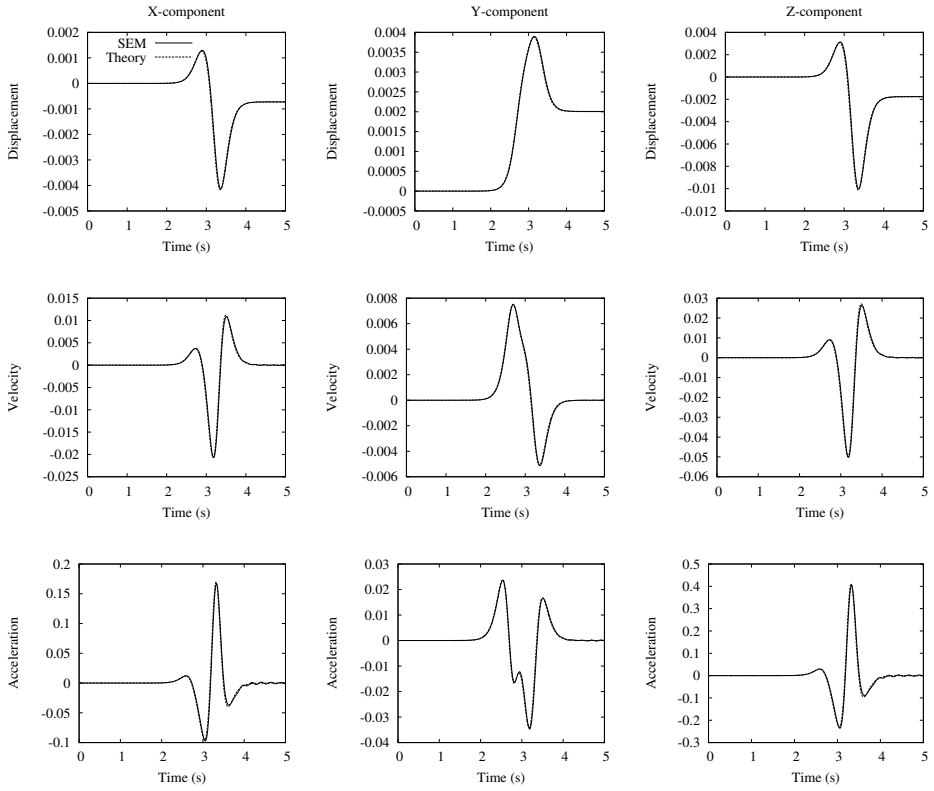

Figure 4.32: Comparison between the theoretical results and the results obtained by the numerical simulation using EFISPEC at the receiver $(x, y, z) = (0,3000,0)$.

4.8.4 Conclusion

We have tested the double-couple point source model in a 2-D and 3-D homogeneous infinite medium using GEFDyn and EFISPEC (3-D only).

As for GEFDyn, the results are mitigated; the order of magnitude, shape and time of arrival of physical quantities are well reproduced, however, a clear numerical dispersion is visible. We should note that the use of equivalent imposed displacements showed sharper results than the use of equivalent body forces. Displacements, velocities and accelerations were well reproduced and very few spurious oscillations were generated.

As for EFISPEC, the numerical results nicely reproduced the theoretical one. We note that the use of paraxial elements is not the best way to absorb wave. More efficient methods have been developped as PML or CPML (e.g., Komatitsch and Martin, 2007).

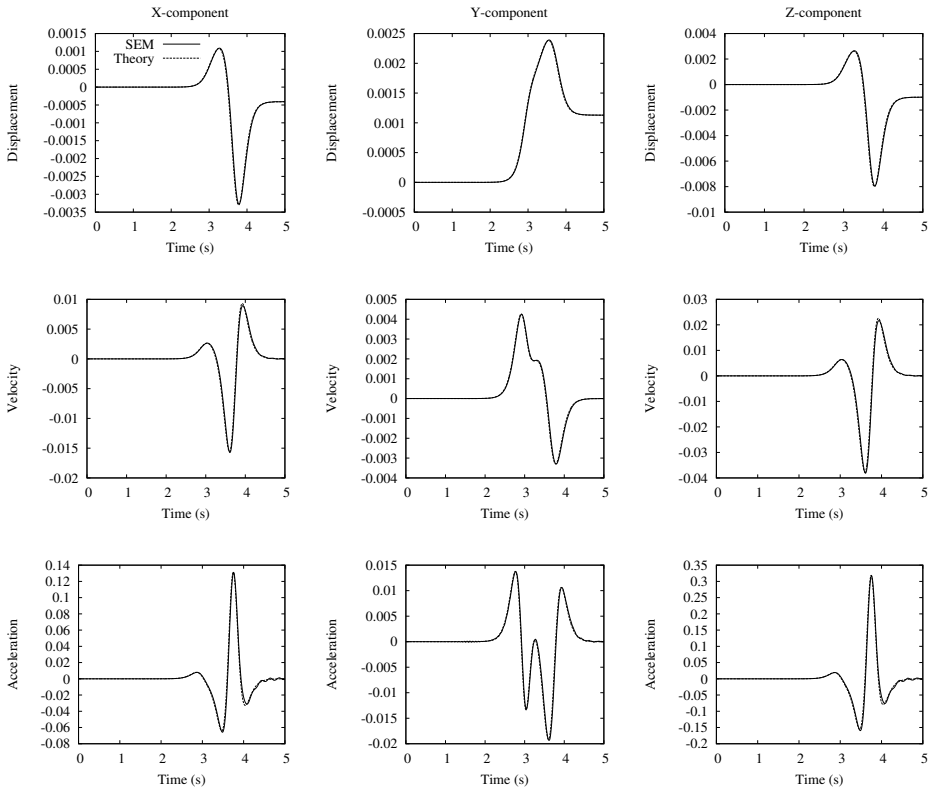

Figure 4.33: Comparison between the theoretical results and the results obtained by the numerical simulation using EFISPEC at the receiver $(x, y, z) = (0,4000,0)$.

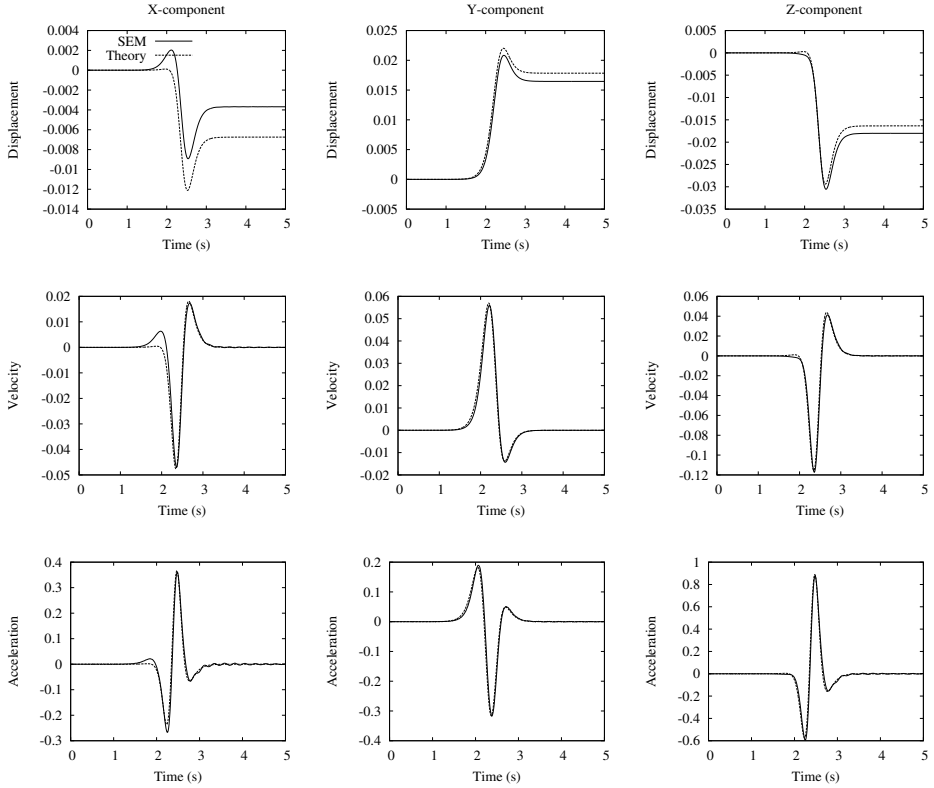

Figure 4.34: Comparison between the theoretical results and the results obtained by the numerical simulation using EFISPEC at the receiver $(x, y, z) = (0,1000,0)$.

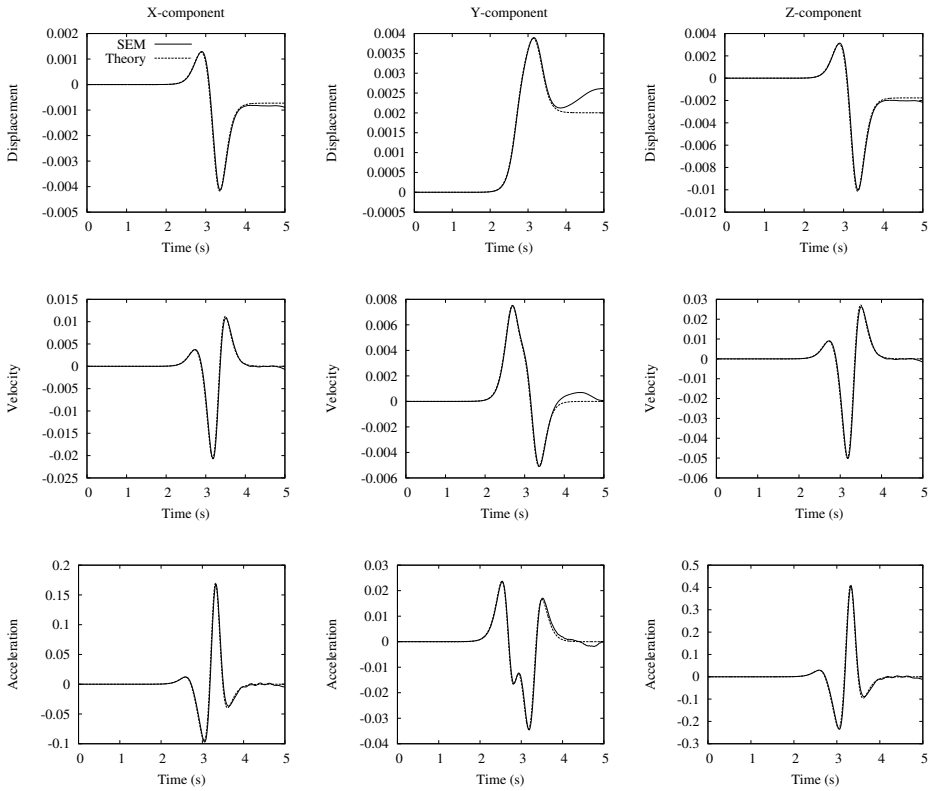

Figure 4.35: Comparison between the theoretical results and the results obtained by the numerical simulation using EFISPEC with paraxial elements attached at the boundaries at the receiver $(x, y, z) = (0,3000,0)$.

4.9 Conclusion

We have developped independent 1-D, 2-D and 3-D spectral elements codes (EFISPEC1D, EFISPEC2D and EFISPEC3D) based on the detailed explanations given by Komatitsch (1997). The verification of the 1-D element code has been performed by comparing the numerical propagation of a Ricker wavelet with the semi-analytical solution given by the Thomson-Haskell propagator matrix method. The accuracy of the SEM is excellent from 4 to 5 GLL points per minimum wavelength. We have also shown that the common rule of thumb used in the classical FEM saying that 10 nodes per minimum wavelength are sufficient to propagate waves correctly is far to be accurate and that 30 nodes per minimum wavelength should be used. We have also noticed that a too large number of nodes per wavelength in the FEM can generate spurious oscillations.

As for the 2-D spectral elements code, it has first been validated by comparing the results of a point source problem with the classical FEM. The agreement is excellent when no numerical dispersion is present in the two numerical methods. Then the code has been compared qualitatively and quantitatively on the effect of a ridge on a vertically incident SV-wave.

The verification of the 3-D spectral elements code has been done by comparing the theoretical and numerical results of a double-couple point source problem.

The implementation of the double-couple point source model in the GEF-Dyn code has shown that the order of magnitude, shape and time of arrival of physical quantities are well reproduced, however, a clear numerical dispersion is visible.

Conclusions and Further Research

The results of this work clearly illustrate the influence of the nonlinear behavior of soft soils on the strong ground motions. However, we note that such a detailed analysis could have been done thanks to an accurate PS logging at the CTI borehole station. In cases where the PS logging is not available, then Cone Penetration Test (CPT) data can be used to obtain the shear-wave velocity via empirical relationship (e.g., Mayne, 2007). The inversion of the S-wave velocity and damping factors (using weak or strong motions) has been done in the frequency domain by finding the closest theoretical spectral ratios to the observed one taken on the S-wave portion of the seismogram. This process gave consistent results, however, a shortcoming remains: the use of a cosine tapered window to smooth to zero both ends of the seismogram in order to compute the Fast Fourier Transform influence the shape of the spectral ratio. One can show that by appling a 15%, 25% or 35% cosine tapared window on the S-wave portion of the signal, the location of the resonant peaks can be slightly moved and the height of these peaks can be greatly affected; this can consequently skew the inversion of the S-wave velocity or the damping factors. Further research should be done to construct efficient time domain objective functions (e.g., Assimaki and Steidl, 2007) to have a better accuracy of the inversion.

As for the nonlinear laws used in Chapter 3, we first investigated the use of a simple elasto-plastic law with a Mohr-Coulomb criterion to simulate strong ground motions. We have shown that such ideal behavior leads to unrealistic velocities or accelerations. In order to obtain a smoother stress-strain relationship, we have used the advanced constitutive law of the Cyberquake software. Even if smoother results have been found in the stress-strain plane, the simulated acceleration remained far from the observation and far from the results obtained by the inversion. A fine tuning of the parameters of the law could certainly help to obtain better results; but are the laboratory tests results conducted at low frequency (i.e., low loading rate) that we try to mimic with advanced mathematical models appropriate for any range of frequency? Results are actually mitigated since

Hardin (1965) found virtrually no significant effect of the loading rate on the dynamic properties of sands; however, more recent experiments conducted by Lin et al. (1996) have clearly shown a dependence of the damping with respect to the frequency.

Besides, we note that this thesis only tackles the subject of site effects within dry soils; however, when cohensionless soils are saturated, rapid loadings under undrained conditions result in a change of pore pressure and consequently in effective stress. Liquefaction phenomenon that results from this process can be either flow liquefaction or cyclic mobility that can cause spectacular damages. Cyclic mobility may occur in contractant sands while sharp acceleration peaks can be generated in dilatant soil.

Finally, this thesis has been the occasion to give birth to four major codes (all programmed in FORTRAN 90):

- The first one has been developed to inverse borehole station data. It is based on the Thomson-Haskell propagator matrix method and on the genetic algorithm optimization method. The code has been developped to invert:
  - the S-wave velocity α;
  - the P-wave velocity β;
  - the compressional damping factor ξ_α;
  - the shear damping factor ξ_β;
  - and the incidence angle of the incoming wave.
- The second one, third one and fourth one are 1D, 2D and 3D spectral elements codes, respectively, used to solve the elastodynamic wave equation. Further research will be done to develop a nonlinear version of the 1D spectral elements code and a parallel version of the 3D spectral elements code.

Appendices

Appendix A

Deconvolution Formulae Via The Thomson-Haskell Method

This appendix exposes the deconvolution formulae in a stack of welded homogeneous horizontal layers subjected to SH wave (The P-SV case follows the same logic but is slightly more complicated). This deconvolution process in seismology consists in computing the incoming wave knowing the linear elastic parameters of the medium and the displacement, velocity or acceleration at one point of the soil column. In general, the free surface acceleration is used but in the case of a vertical array (i.e., a borehole station), the downhole or intermediate records can be used as well. The reader is referred to van Vossen et al. (2006) for more complex deconvolution on real data using surface records.

A.1 Theory

Following the Figure 1.1 and using the notation of the Subsection 1.2.2, the objective of this problem is to use the free surface displacement to find the amount of upgoing wave in the half space (noted layer $n+1$ in the following), that is to say, find w_2^{n+1} of Equation (1.20) (the superscript $n+1$ denoting the layer number). In order to do so, we write the Equation (1.21) as

$$\mathbf{w}^{n+1} = (\mathbf{F}^{n+1}(z))^{-1}\mathbf{P}(z, z_0)\mathbf{F}^1(z_0)\mathbf{w}^1,$$

that we simplify as

$$\mathbf{w}^{n+1} = \mathbf{B}\mathbf{w}^1 \Leftrightarrow \begin{pmatrix} \mathrm{w}_1^{n+1} \\ \mathrm{w}_2^{n+1} \end{pmatrix} = \begin{pmatrix} \mathrm{B}_{11} & \mathrm{B}_{12} \\ \mathrm{B}_{21} & \mathrm{B}_{22} \end{pmatrix} \begin{pmatrix} \mathrm{w}_1^1 \\ \mathrm{w}_2^1 \end{pmatrix} \tag{A.1}$$

with the matrix $\mathbf{B}$ equal to $(\mathbf{F}^{n+1}(z))^{-1}\mathbf{P}(z, z_0)\mathbf{F}^1(z_0)$. Supossing $z_{ref} = z_0$ in Equation (1.15), the free surface condition $\tau_{yz}(z_0) = 0$ combined with the

Equation (1.20) leads to

$$i\omega\mu\eta \mathrm{w}_1^1 - i\omega\mu\eta \mathrm{w}_2^1 = 0 \Leftrightarrow \mathrm{w}_1^1 = \mathrm{w}_2^1$$

at z_0. Consequently,

$$u_y(z_0) = 2\mathrm{w}_1^1$$

or

$$\mathrm{w}_1^1 = \mathrm{w}_2^1 = \frac{1}{2} u_y(z_0).$$

Using Equation (A.1), the downgoing and upgoing quantity can be found as

$$\mathrm{w}_1^{n+1} = \frac{1}{2} u_y(z_0)(\mathrm{B}_{11} + \mathrm{B}_{12})$$

and

$$\mathrm{w}_2^{n+1} = \frac{1}{2} u_y(z_0)(\mathrm{B}_{21} + \mathrm{B}_{22}).$$

The incoming wave is found by multiplying the upgoing quantity by its respective phase as

$$u_y(z)_{upgoing}^{n+1} = \mathrm{F}_{12}^{n+1}(z)\mathrm{w}_2^{n+1}.$$

A.2 Example of deconvolution

In order to test the deconvolution formula in the frequency domain, we use the soil column presented in Table 1.2. As for the direct simulation, a Ricker of order 2 and pseudo-frequency of 5 Hz is used as the incident wave. The free surface motion is used for the deconvolution. Figure A.1 shows the input wave, the free surface motion and the deconvolved wave. The deconvolved wave matches perfectly with the input wave.

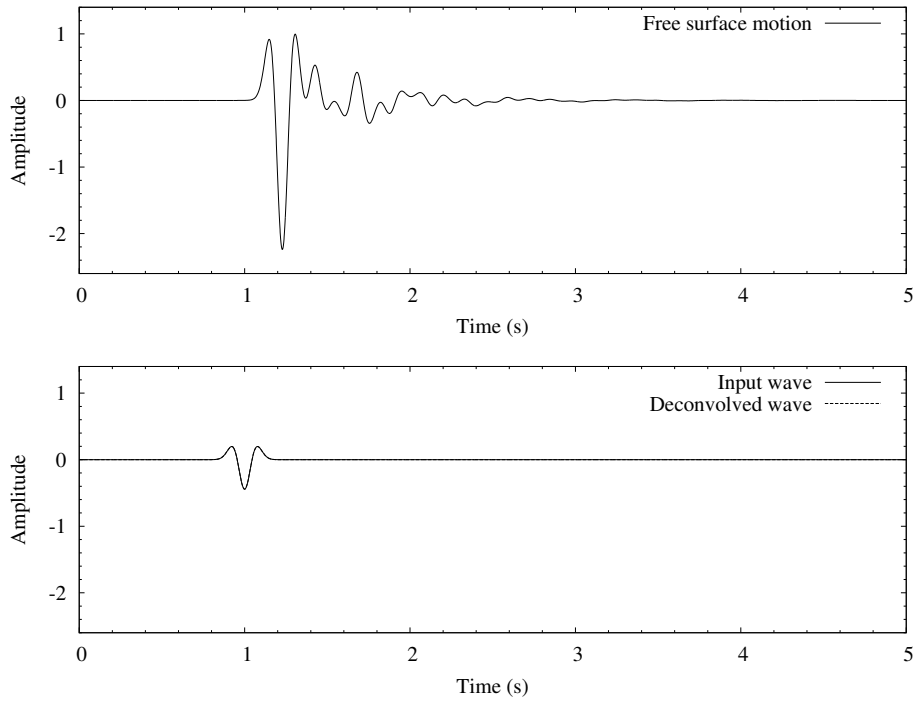

Figure A.1: Example of deconvolution. The input wave and deconvolved wave are shown on the bottom panel. The free surface motion shown on the top panel is used to compute the deconvolved wave.

Appendix B

Possible Presence of Trapped Waves within the Kego Fault

In order to follow the possible presence of trapped waves propagating within the fault gouge (trapped waves could explain the rotation of energy distribution at stations CTI, FKOS01 and FKO006), we first align the onset of the S-wave of each velocity seismogram on the onset of S-wave of CTID01. Then, we will try to validate the four essential characteristics of waves trapped within a low-velocity zone enonced by Li and Leary (1990):

1. they are excited only by sources acting within a low-velocity layer;

2. their amplitudes decay exponentially with receiver offset from the low-velocity zone;

3. they appear as extended and/or dispersive wave trains rather than as compact pulses and their dispersion can be seen by filtering seismograms in the frequency range of interest;

4. and they arrive later in time than the shear body waves traveling the high-speed rock surrounding the low-velocity zone.

As for the first point, the focal depth of the 2005 West-Off Fukuoka Prefecture earthquake has been evaluated to 9.2 km (JMA, 2005). The source has therefore a good probability to be within a low-velocicty structure zone because of its shallowness.

According to the point two, trapped waves should not be visible or slightly visible at stations which are offset from the low-velocity zone like stations FKOS02 or FKOS06. However, they should appear in the vicinity of stations CTI or FKOS05. If we look closely at the plane $f \perp$ - $f \parallel$ (i.e., fault perpendicular and fault parallel, respectively) in the frequency range [0.2-0.5] Hz and [0.5-1.0] Hz:

- For the stations CTI, which are located along the fault gouge, we can clearly see in FigureB.1-(a) an arrival of unexpected waves in the frequency range [0.2-0.5] Hz from 24 to 30 seconds and from 38 to 44 seconds. The same observation can be made in the frequency range [0.5-1.0] Hz from 26 to 34 seconds.

- For the station FKOS05, we can see in FigureB.1-(b) that in the frequency range [0.2-0.5] Hz the unexpected waves arrive around 26 seconds until 34 seconds. This waves train lags the waves train of CTI stations of 2 seconds. In the frequency range [0.5-1.0] Hz, we can also see the supposed trapped waves arriving at 32 seconds until 40 seconds. One more time, the lag time is around 2 seconds.

- For the station FKOS06, which is offseted from the fault, we cannot see such an unexpected arrival of train wave. A slight modification of behaviour is seen within the time windows [30-34] s in the frequency range [0.2-0.5] Hz. This could confirm the fact that trapped waves decay exponentially when offset from the fault. In the frequency range [0.5-1.0] Hz, the same observation can be done within the time interval [36-40] s.

- For the station FKOS02, which is as FKOS06, offseted from the fault, no change of behaviour can be seen.

The point number two is therefore confirmed as well. To validate the point number three, we plot waves at CTIS01, FKOS05, FKOS06 and FKOS02 filtered in the frequency range [0.2-0.5] Hz and [0.5-1.0] Hz. CTIS01 has been taken as the reference station to aligned the others stations on the onset of the S-wave. Results are shown in Figure B.8 to B.10. The only tangible evidence of trapped waves on these filtered velocity seismograms is the change of behaviour at CTIS01 in the frequency range [0.2-0.5] Hz between 25 and 30 seconds. This change is then followed by a waves train until 38 seconds.

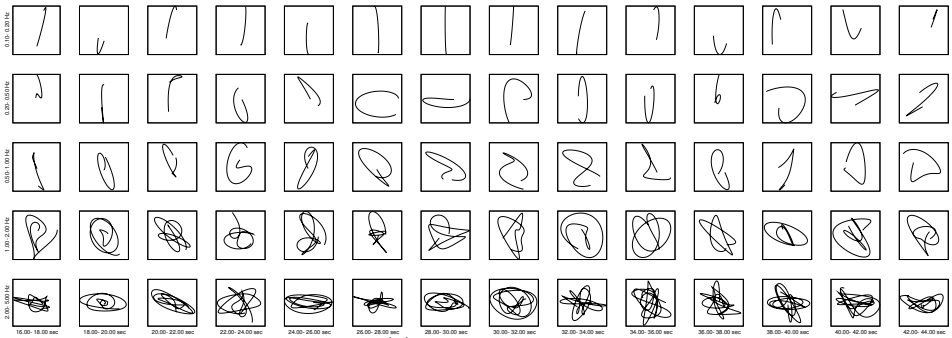

(a) CTI downhole

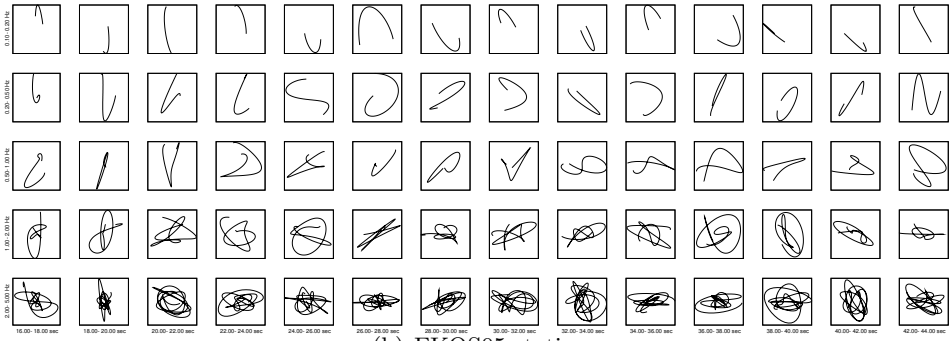

(b) FKOS05 station

Figure B.1: Particle orbits on the horizontal plane at CTI downhole and FKOS05. The particle orbits are plotted in every 2 sec for each band-pass filter velocity seismogram.

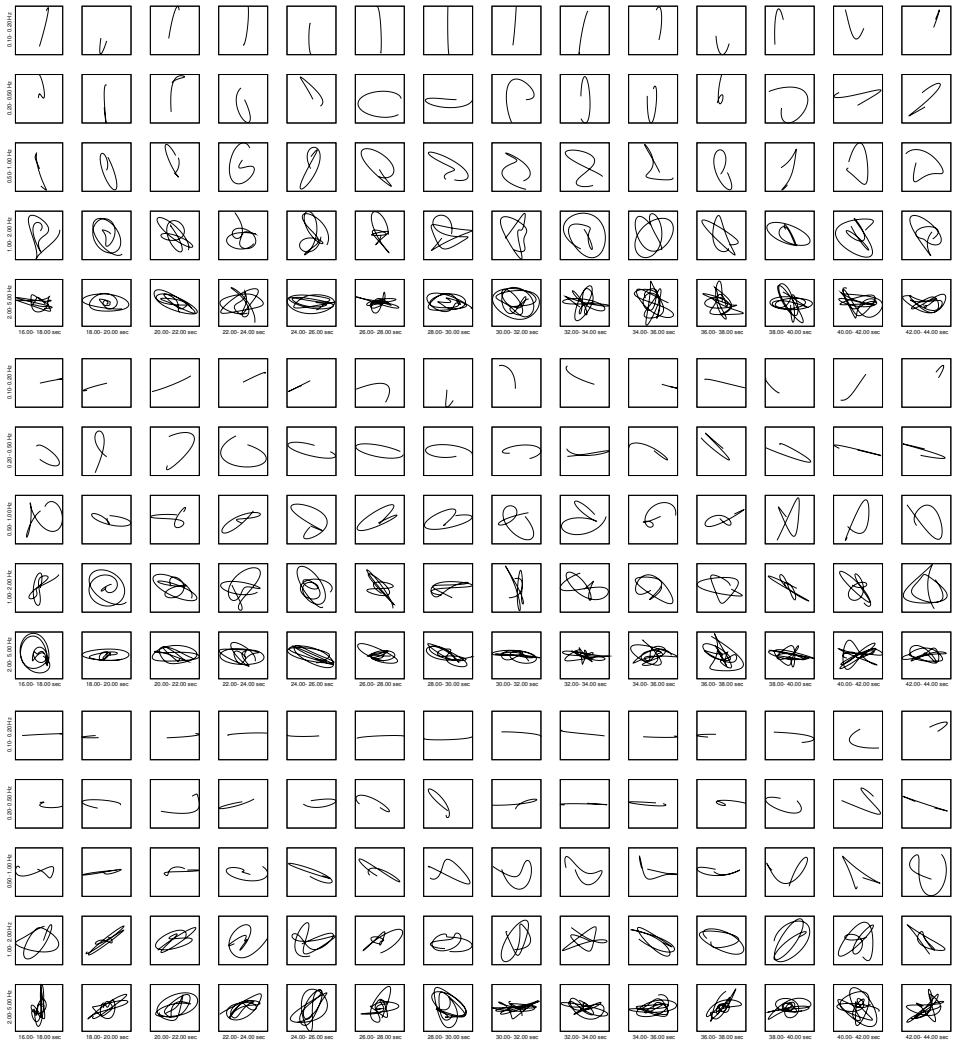

Figure B.2: Downhole particle motion at CTI station in the planes E32S-N32E (top), E32S-Z (middle), N32E-Z (bottom).

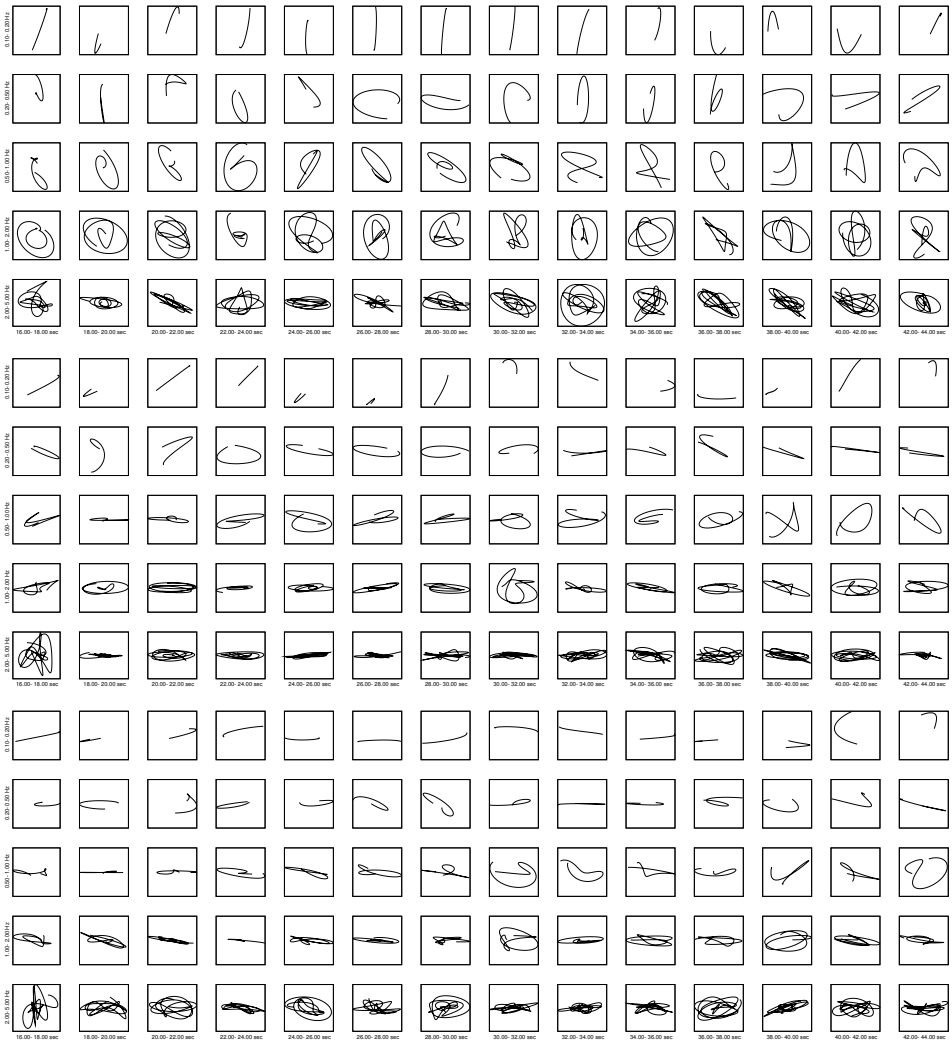

Figure B.3: Free surface particle motion at CTI station in the planes E32S-N32E (top), E32S-Z (middle), N32E-Z (bottom).

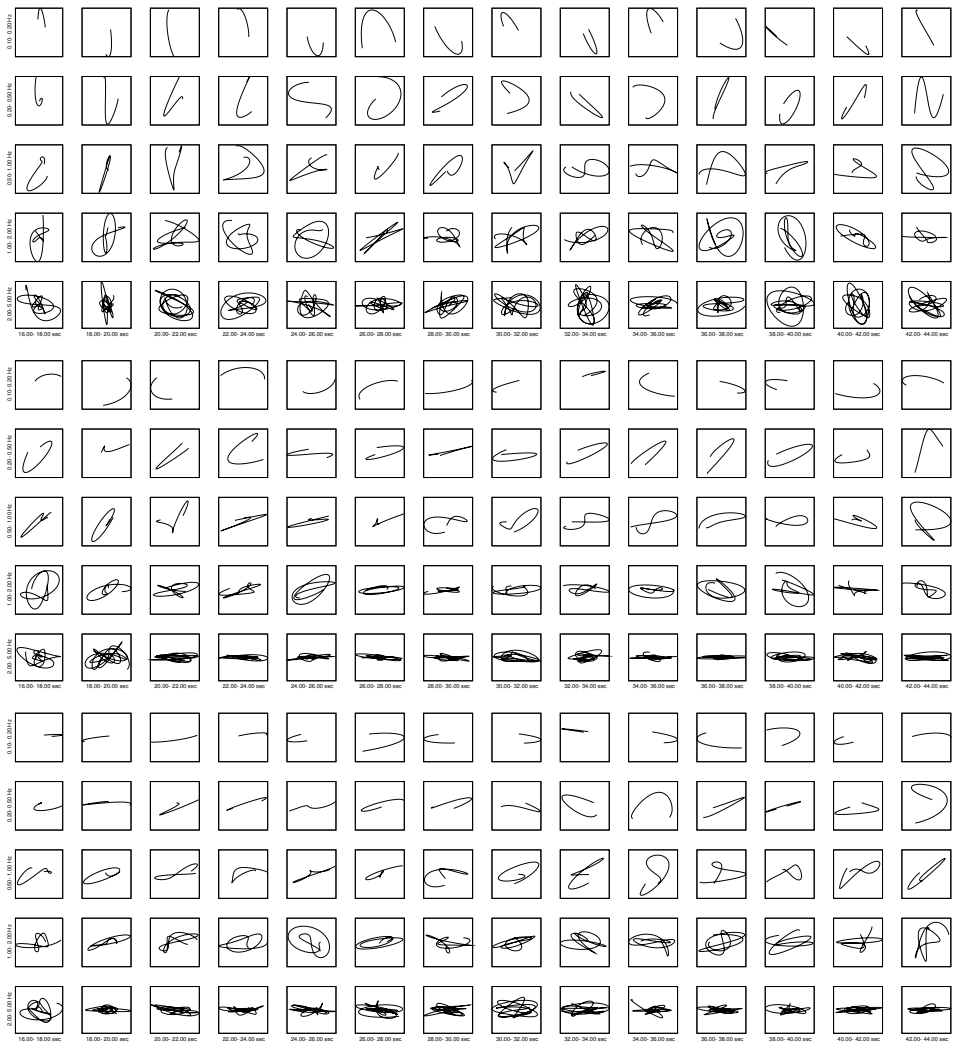

Figure B.4: Free surface particle motion at FKOS05 in the planes E32S-N32E (top), E32S-Z (middle), N32E-Z (bottom).

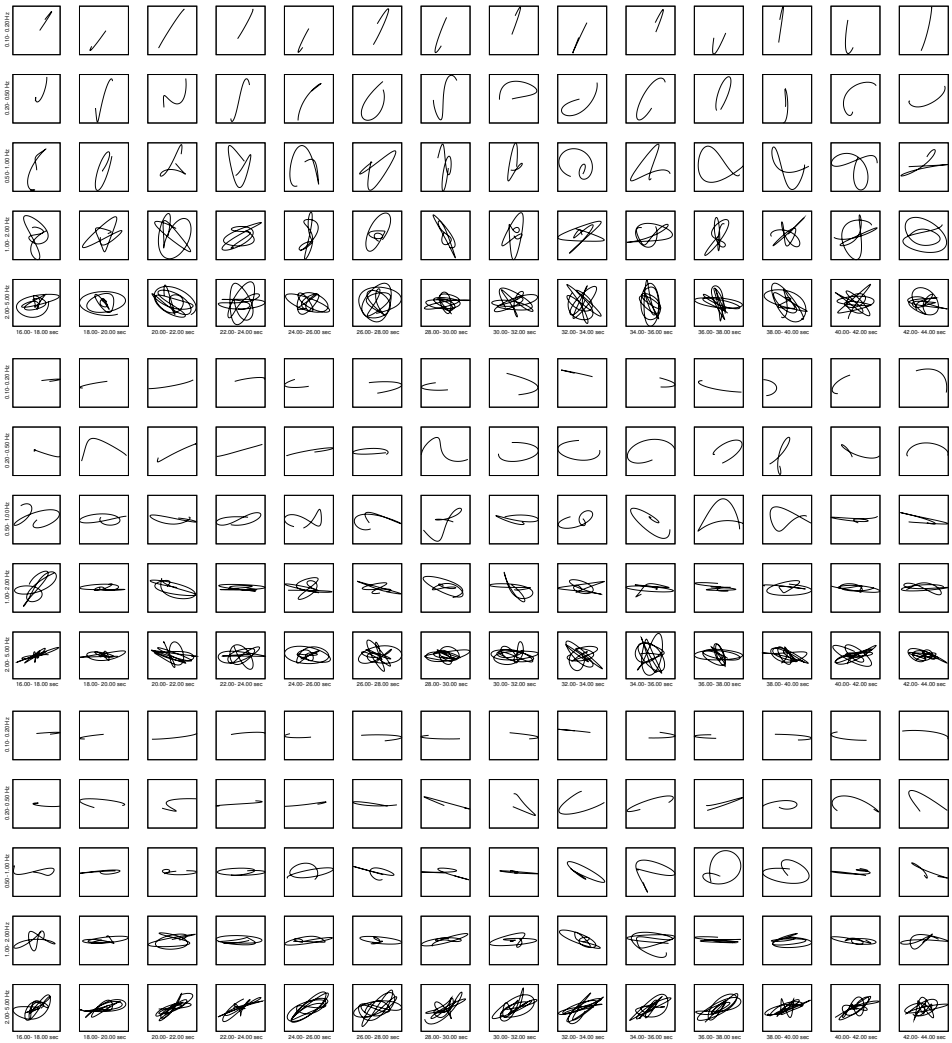

Figure B.5: Free surface particle motion at FKSO06 in the planes E32S-N32E (top), E32S-Z (middle), N32E-Z (bottom).

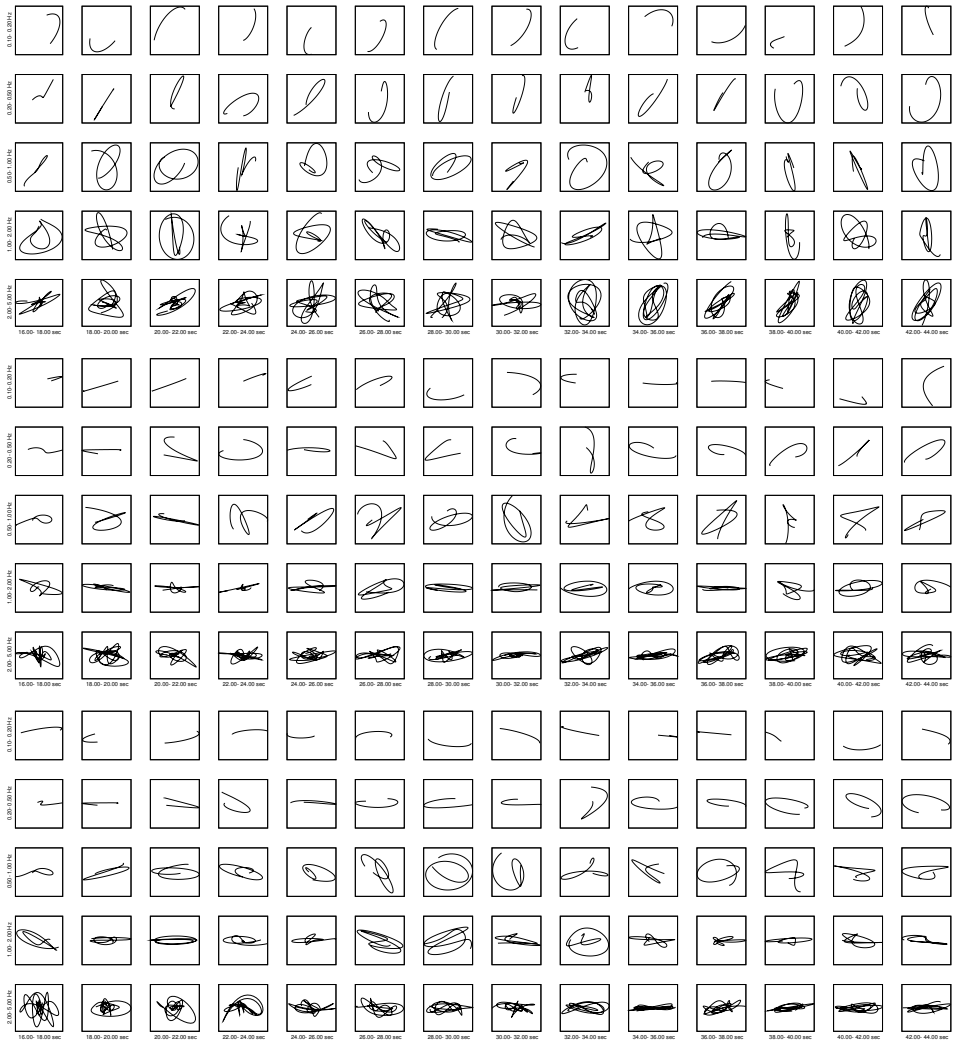

Figure B.6: Free surface particle motion at FKOS02 in the planes E32S-N32E (top), E32S-Z (middle), N32E-Z (bottom).

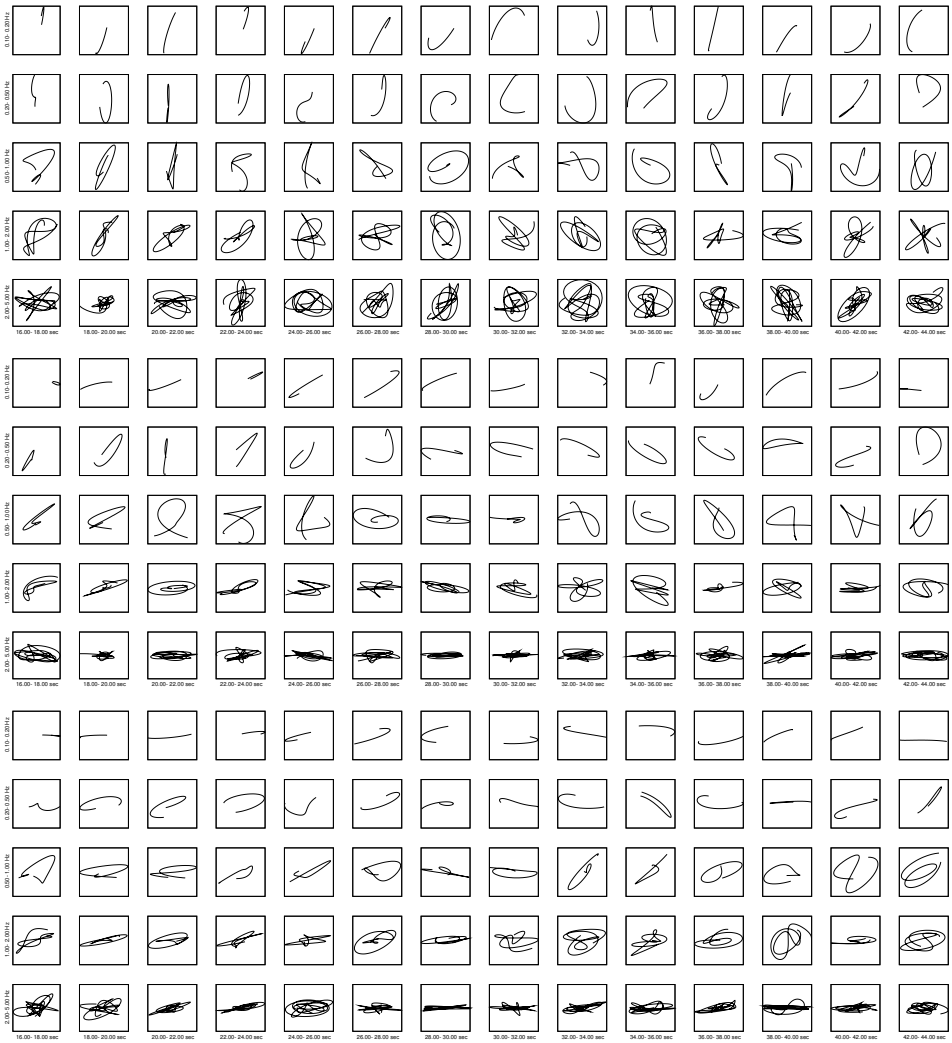

Figure B.7: Free surface particle motion at FKO009 in the planes E32S-N32E (top), E32S-Z (middle), N32E-Z (bottom).

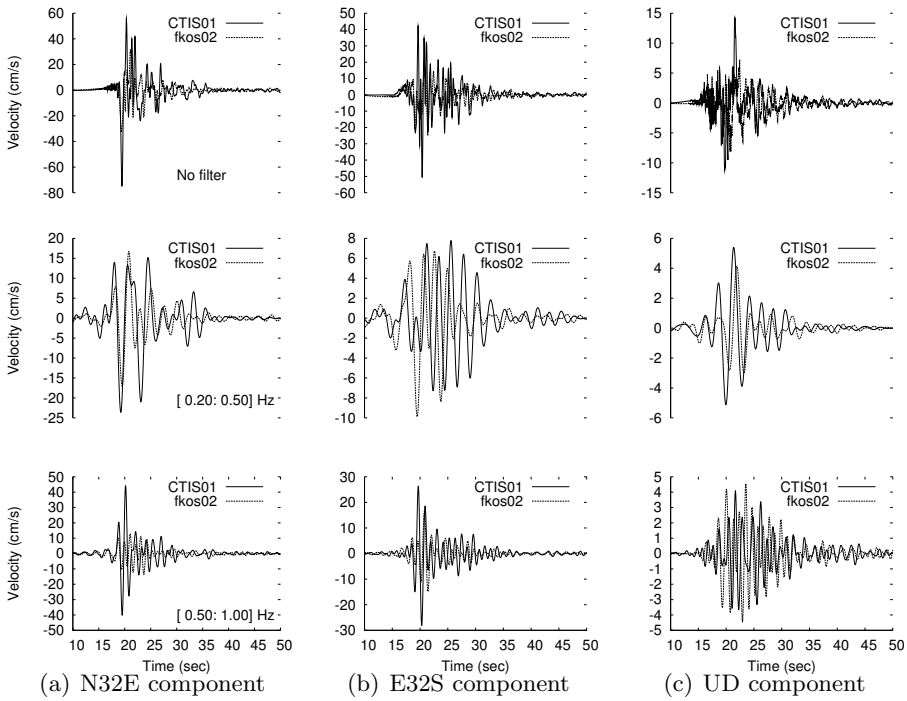

(a) N32E component (b) E32S component (c) UD component

Figure B.8: Band-pass filtered velocity seismograms recorded at CTIS01 and at fkos02. Band-pass frequency range is indicated at the bottom right of the N32E component.

The point number 4 can easily be demonstrated by observing the particle motion for each station as shown in Figure B.1. It is clear that the the shear body waves traveling the high-speed rock, in our case, SH-waves, arrive before the trapped waves.

Except the litigious validation of the point number 3, all the others points strongly reveal the presence of trapped waves within the faut gouge. Futher experiments, like installing a permanent array perpendicular to the fault (Li and Leary, 1990) could enforce the effective presence of a low-velocity profile along the Kego fault.

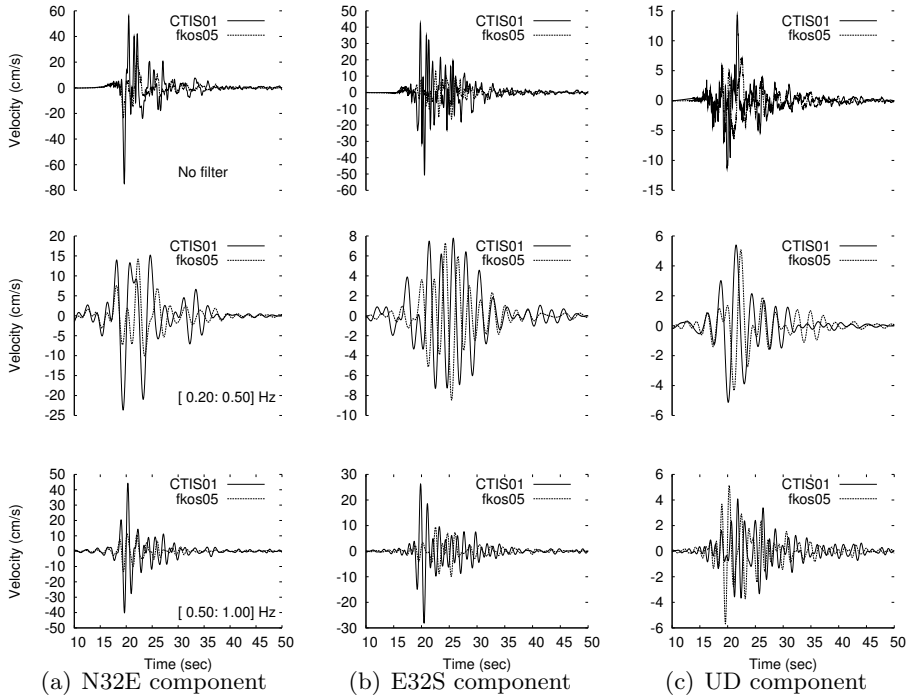

(a) N32E component (b) E32S component (c) UD component

Figure B.9: Band-pass filtered velocity seismograms recorded at CTIS01 and at fkos05. Band-pass frequency range is indicated at the bottom right of the N32E component.

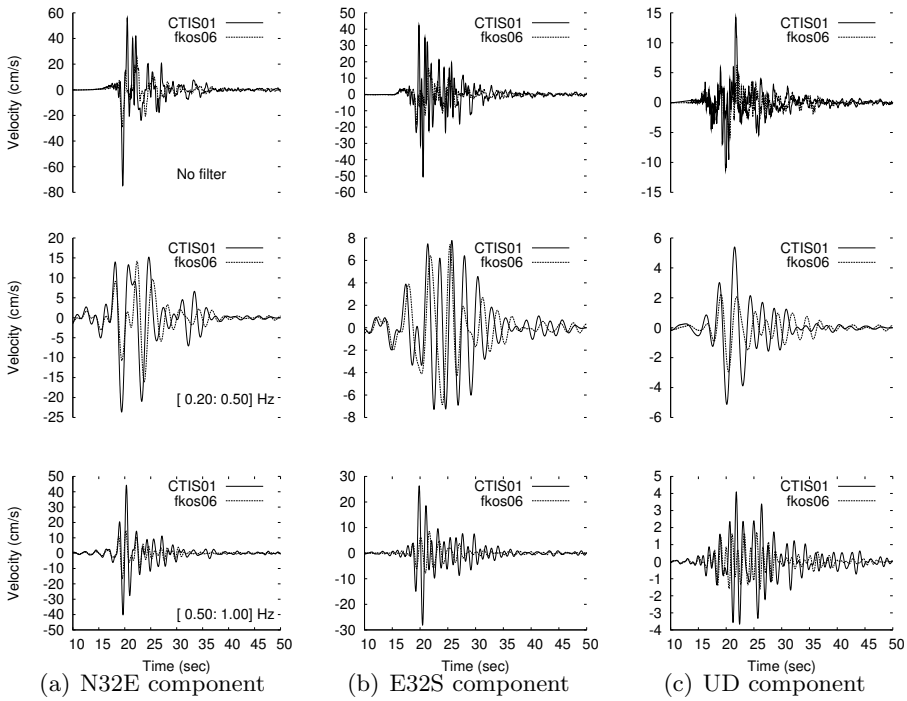

(a) N32E component (b) E32S component (c) UD component

Figure B.10: Band-pass filtered velocity seismograms recorded at CTIS01 and at fkos06. Band-pass frequency range is indicated at the bottom right of the N32E component.

Appendix C

Paraxial Approximation for the Elastic Wave Equation

This appendix develops in detailed the method exposed by Modaressi (1987) which consists in deriving the paraxial approximation in the space-time domain by first expressing the spectral impedance of a wave impigning on an interface Σ in the frequency-waveumber domain.

C.1 Elastodynamic Equations in Local Coordinate System

In order to establish the paraxial approximation along the surface Σ (cf. Figure C.1), the displacement vector $\mathbf{u} = (u, v, w)$ of a general coordinate system is first projected on the plane (x_1, x_2) tangent to the surface Σ and on the x_3-axis shown in Figure C.1 (this local coordinate system can be seen as the local coordinate system of a finite element). We can then write the displacement as

$$\mathbf{u}(\mathbf{x}_\Sigma, x_3) = \mathbf{u}_\Sigma(\mathbf{x}_\Sigma) + u_3\mathbf{e}_3 = u_1\mathbf{e}_1 + u_2\mathbf{e}_2 + u_3\mathbf{e}_3. \tag{C.1}$$

The elastic wave equation

$$\partial_{tt}\mathbf{u} = (\alpha^2 - \beta^2)\nabla(\nabla \cdot \mathbf{u}) + \beta^2\nabla^2\mathbf{u}$$

can therefore be developed in the local coordinate system as

$$\begin{cases} (\alpha^2 - \beta^2)(\partial_{11}u_1 + \partial_{12}u_2 + \partial_{13}u_3) + \beta^2(\partial_{11}u_1 + \partial_{22}u_1 + \partial_{33}u_1) - \partial_{tt}u_1 &= 0 \\ (\alpha^2 - \beta^2)(\partial_{12}u_1 + \partial_{22}u_2 + \partial_{23}u_3) + \beta^2(\partial_{11}u_2 + \partial_{22}u_2 + \partial_{33}u_2) - \partial_{tt}u_2 &= 0 \\ (\alpha^2 - \beta^2)(\partial_{13}u_1 + \partial_{23}u_2 + \partial_{33}u_3) + \beta^2(\partial_{11}u_3 + \partial_{22}u_3 + \partial_{33}u_3) - \partial_{tt}u_3 &= 0. \end{cases}$$

In order to perform a Fourier transformation of these equations with respect to the two space variables lying in the plane tangent to Σ and with

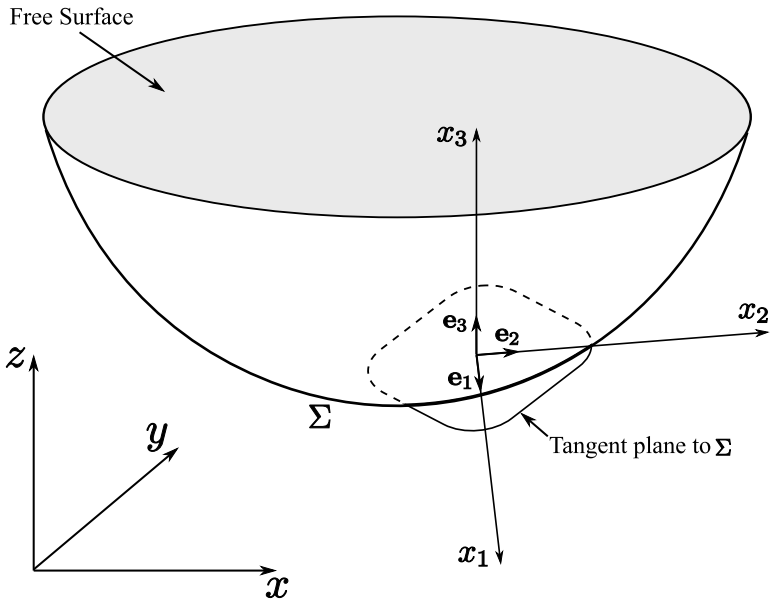

Figure C.1: Definition of local coordinate system used to establish the paraxial approximation on the boundary Σ.

respect to time, we use *Fourier's Differentiation property* exposed in Appendix D.

After multiplying elastodynamic equations by $e^{-ik_1x_1}e^{-ik_2x_2}e^{-i\omega t}$, integrating over dx_1, dx_2 and dt, and using the *Differentiation property* of Fourier transform, we obtain in the space k_1, k_2, x_3 and ω

$$\begin{cases} (\alpha^2-\beta^2)(-k_1^2u_1 - k_1k_2u_2 + ik_1\partial_3u_3) + \beta^2(-k_1^2u_1 - k_2^2u_1 + \partial_{33}u_1) + \omega^2u_1 &= 0 \\ (\alpha^2-\beta^2)(-k_1k_2u_1 - k_2^2u_2 + ik_2\partial_3u_3) + \beta^2(-k_1^2u_2 - k_2^2u_2 + \partial_{33}u_2) + \omega^2u_2 &= 0 \\ (\alpha^2-\beta^2)(ik_1\partial_3u_1 + ik_2\partial_3u_2 + \partial_{33}u_3) + \beta^2(-k_1^2u_3 - k_2^2u_3 + \partial_{33}u_3) + \omega^2u_3 &= 0. \end{cases}$$

Using Equation ((C.1)), we can rewrite them as

$$\begin{cases} (\alpha^2-\beta^2)(-\mathbf{k}_\Sigma\cdot\mathbf{u}_\Sigma + i\partial_3u_3)\mathbf{k}_\Sigma + \beta^2(-|\mathbf{k}_\Sigma|^2 + \partial_{33})\mathbf{u}_\Sigma + \omega^2\mathbf{u}_\Sigma &= \mathbf{0} \\ (\alpha^2-\beta^2)(i\mathbf{k}_\Sigma\cdot\partial_3\mathbf{u}_\Sigma + \partial_{33}u_3) + \beta^2(-|\mathbf{k}_\Sigma|^2 + \partial_{33})u_3 + \omega^2u_3 &= 0 \end{cases} \tag{C.2}$$

where $\mathbf{k}_\Sigma = k_1\mathbf{e}_1 + k_2\mathbf{e}_2$.

C.2 P, SV and SH wave decomposition

The above equations form a system of second order differential equations whose independant variable is x_3. An elegant way to solve it has been

proposed by Modaressi (1987) and consists of decomposing the vector $\mathbf{u}_\Sigma$ along the $\mathbf{k}_\Sigma$-direction and $\mathbf{e}_3 \wedge \frac{\mathbf{k}_\Sigma}{|\mathbf{k}_\Sigma|}$ in order to obtain the P-, SV-, SH-wave decomposition (Figure C.2). Thus, using the direct basis $(\frac{\mathbf{k}_\Sigma}{|\mathbf{k}_\Sigma|}, \mathbf{e}_3 \wedge \frac{\mathbf{k}_\Sigma}{|\mathbf{k}_\Sigma|}, \mathbf{e}_3)$ that we will write for simplification $(\mathbf{e}_k, \mathbf{e}_3 \wedge \mathbf{e}_k, \mathbf{e}_3)$, gives

$$\begin{aligned} \mathbf{u}_\Sigma &= \left(\mathbf{u}_\Sigma \cdot \frac{\mathbf{k}_\Sigma}{|\mathbf{k}_\Sigma|}\right) \frac{\mathbf{k}_\Sigma}{|\mathbf{k}_\Sigma|} + \left(\mathbf{u}_\Sigma \cdot \frac{\mathbf{e}_3 \wedge \mathbf{k}_\Sigma}{|\mathbf{k}_\Sigma|}\right) \frac{\mathbf{e}_3 \wedge \mathbf{k}_\Sigma}{|\mathbf{k}_\Sigma|} \\ &= \quad u_1^{PSV} \mathbf{e}_k \quad + \quad u_2^{SH} \mathbf{e}_3 \wedge \mathbf{e}_k. \end{aligned} \tag{C.3}$$

Total displacement in the basis $(\mathbf{e}_k, \mathbf{e}_3 \wedge \mathbf{e}_k, \mathbf{e}_3)$ will be noted

$$\mathbf{u}(\mathbf{x}_\Sigma, x_3) = \mathbf{u}_\Sigma + u_3^{PSV} \mathbf{e}_3 = u_1^{PSV} \mathbf{e}_k + u_2^{SH} \mathbf{e}_3 \wedge \mathbf{e}_k + u_3^{PSV} \mathbf{e}_3$$

where u_3 remains unchanged but will be noted u_3^{PSV} for convenience. We should also note that

$$\mathbf{k}_\Sigma = |\mathbf{k}_\Sigma| \mathbf{e}_k. \tag{C.4}$$

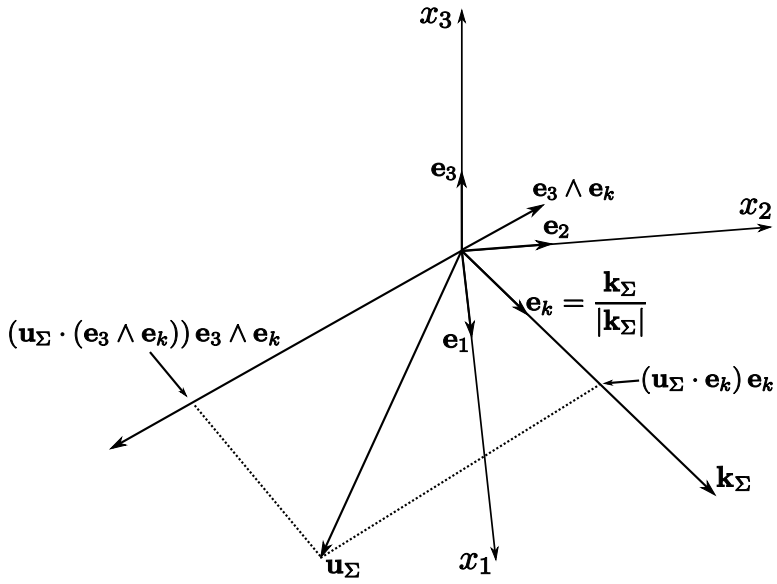

Figure C.2: Definition of local coordinate system used to project $\mathbf{u}_\Sigma$ expressed in the basis $(\mathbf{e}_1, \mathbf{e}_2, \mathbf{e}_3)$ on the basis $(\mathbf{e}_k, \mathbf{e}_3 \wedge \mathbf{e}_k, \mathbf{e}_3)$. This projection allows to decompose the vector $\mathbf{u}$ along P-, SV-, SH-directions.

Injecting the decomposition of $\mathbf{u}_\Sigma$ (Equation (C.3)) into Equations (C.2), we obtain after simplifications

$$\begin{cases} \left[(\omega^2 - \alpha^2|\mathbf{k}_\Sigma|^2 + \beta^2\partial_{33})u_1^{PSV} + i|\mathbf{k}_\Sigma|(\alpha^2 - \beta^2)\partial_3 u_3^{PSV}\right] \mathbf{e}_k + \\ \left[\beta^2(-|\mathbf{k}_\Sigma|^2 + \partial_{33})u_2^{SH} + \omega^2 u_2^{SH}\right] \mathbf{e}_3 \wedge \mathbf{e}_k \qquad = \mathbf{0} \\ \left[(\omega^2 - \beta^2|\mathbf{k}_\Sigma|^2 + \alpha^2\partial_{33})u_3^{PSV} + i|\mathbf{k}_\Sigma|(\alpha^2 - \beta^2)\partial_3 u_1^{PSV}\right] \mathbf{e}_3 \qquad = 0 \end{cases} \tag{C.5}$$

We can see that the equation along $\mathbf{e}_3 \wedge \mathbf{e}_k$ is uncoupled, representing therefore the SH-component. In order to solve this system of second order differential equations whose independent variable is x_3, let us write it in a more conventional way. As for the SH-component, it gives

$$\left\{ \partial_{33} u_2^{SH} = -\left(\frac{\omega^2}{\beta^2} - |\mathbf{k}_\Sigma|^2 \right) u_2^{SH}. \right.$$

The coupled P-, SV-components gives the following system

$$\begin{cases} \partial_{33} u_1^{PSV} = \dfrac{\alpha^2 |\mathbf{k}_\Sigma^2| - \omega^2}{\beta^2} u_1^{PSV} - i|\mathbf{k}_\Sigma|(\alpha^2 - \beta^2)\partial_3 u_3^{PSV} \\ \\ \partial_{33} u_3^{PSV} = \dfrac{\beta^2 |\mathbf{k}_\Sigma^2| - \omega^2}{\alpha^2} u_3^{PSV} - i|\mathbf{k}_\Sigma|(\alpha^2 - \beta^2)\partial_3 u_1^{PSV}. \end{cases}$$

Let $\xi_p^2 = \frac{\omega^2}{\alpha^2} - |\mathbf{k}_\Sigma|^2$ and $\xi_s^2 = \frac{\omega^2}{\beta^2} - |\mathbf{k}_\Sigma|^2$, then above Equations become

$$\left\{ \partial_{33} u_2^{SH} = -\xi_s^2 u_2^{SH} \right. \tag{C.6}$$

and

$$\begin{cases} \partial_{33} u_1^{PSV} = -\dfrac{\alpha^2}{\beta^2} \xi_p^2 u_1^{PSV} - i \dfrac{|\mathbf{k}_\Sigma|(\alpha^2 - \beta^2)}{\beta^2} \partial_3 u_3^{PSV} \\ \partial_{33} u_3^{PSV} = -\dfrac{\beta^2}{\alpha^2} \xi_s^2 u_2^{PSV} - i \dfrac{|\mathbf{k}_\Sigma|(\alpha^2 - \beta^2)}{\alpha^2} \partial_3 u_1^{PSV}. \end{cases} \tag{C.7}$$

C.3 Spectral Impedance

As for system (C.6), solutions are sought of the form $u_2^{SH}(x_3) = e^{\lambda x_3}$. Thus,

$$\lambda^2 = -\xi_s^2$$

and the 2 distinct roots are $\lambda_1 = +i\xi_s$ and $\lambda_1 = -i\xi_s$. The solution of Equation (C.6) is therefore

$$u_2^{SH} = A_{SH}^{+} e^{+i\xi_s x_3} + A_{SH}^{-} e^{-i\xi_s x_3}, \tag{C.8}$$

where $e^{+i\xi_s x_3}$ is an upcoming wave (i.e., propagating along $+x_3$) and $e^{-i\xi_s x_3}$ is a downgoing wave (i.e., propagating along $-x_3$).

To solve the System (C.7), we reduce the system of second order differential equations to a system of first order differential equations as exposed in Appendix E. For the System (C.7), let

$$\begin{pmatrix} w_1 \\ w_2 \\ w_3 \\ w_4 \end{pmatrix} = \begin{pmatrix} u_1^{PSV} \\ u_3^{PSV} \\ \partial_{x_3} u_1^{PSV} \\ \partial_{x_3} u_3^{PSV} \end{pmatrix}, \tag{C.9}$$

such that System (C.7) and Equation (C.9) gives the following new system

$$\begin{pmatrix} w_1' \\ w_2' \\ w_3' \\ w_4' \end{pmatrix} = \begin{pmatrix} 0 & 0 & 1 & 0 \\ 0 & 0 & 0 & 1 \\ -\frac{\alpha^2}{\beta^2}\xi_p^2 & 0 & 0 & -i\frac{|\mathbf{k}_\Sigma|(\alpha^2-\beta^2)}{\beta^2} \\ 0 & -\frac{\beta^2}{\alpha^2}\xi_s^2 & -i\frac{|\mathbf{k}_\Sigma|(\alpha^2-\beta^2)}{\alpha^2} & 0 \end{pmatrix} \begin{pmatrix} w_1 \\ w_2 \\ w_3 \\ w_4 \end{pmatrix}$$

where a prime ($'$) denote the derivative with respect to x_3. This system can be written as

$$\mathbf{W}' = \mathbf{A}\mathbf{W}.$$

Let the solution be

$$\mathbf{W} = \mathbf{Z}e^{\lambda x_3} \Rightarrow \mathbf{W}' = \lambda \mathbf{Z}e^{\lambda x_3}$$

so that the system to resolve is

$$\lambda \mathbf{Z}e^{\lambda x_3} = \mathbf{A}\mathbf{Z}e^{\lambda x_3} \Leftrightarrow (\mathbf{A} - \lambda \mathbf{I})\mathbf{Z} = \mathbf{0}$$

where $\mathbf{I}$ is the identity matrix of the same dimension of $\mathbf{A}$. Eigenvalues of the matrix $\mathbf{A}$ can be found through the characteristic polynomial which is equal to

$$\begin{vmatrix} -\lambda & 0 & 1 & 0 \\ 0 & -\lambda & 0 & 1 \\ -\frac{\alpha^2}{\beta^2}\xi_p^2 & 0 & -\lambda & -i\frac{|\mathbf{k}_\Sigma|(\alpha^2-\beta^2)}{\beta^2} \\ 0 & -\frac{\beta^2}{\alpha^2}\xi_s^2 & -i\frac{|\mathbf{k}_\Sigma|(\alpha^2-\beta^2)}{\alpha^2} & -\lambda \end{vmatrix} = \lambda^4 + (\xi_p^2 + \xi_s^2)\lambda^2 + \xi_p^2\xi_s^2 = 0.$$

Resolution of the biquadratic equation leads to 4 distinct eigenvalues:

$$\begin{cases} \lambda_1 &= +i\xi_p \\ \lambda_2 &= -i\xi_p \\ \lambda_3 &= +i\xi_s \\ \lambda_4 &= -i\xi_p \end{cases}$$

whose associated eigenvectors are

$$\mathbf{Z}_1 = \begin{pmatrix} 1 \\ \xi_p/|\mathbf{k}_\Sigma| \\ i\xi_p \\ i\xi_p^2/|\mathbf{k}_\Sigma| \end{pmatrix}, \ \mathbf{Z}_2 = \begin{pmatrix} 1 \\ -\xi_p/|\mathbf{k}_\Sigma| \\ -i\xi_p \\ i\xi_p^2/|\mathbf{k}_\Sigma| \end{pmatrix}, \ \mathbf{Z}_3 = \begin{pmatrix} 1 \\ -|\mathbf{k}_\Sigma|/\xi_s \\ i\xi_s \\ -i|\mathbf{k}_\Sigma| \end{pmatrix}, \ \mathbf{Z}_4 = \begin{pmatrix} 1 \\ |\mathbf{k}_\Sigma|/\xi_s \\ -i\xi_s \\ -i|\mathbf{k}_\Sigma| \end{pmatrix}.$$

Coming back to the sought quantities, we obtain

$$\begin{cases} u_1^{PSV} &= A_P^+ e^{+i\xi_p x_3} + A_P^- e^{-i\xi_P x_3} + A_{SV}^+ e^{+i\xi_s x_3} + A_{SV}^- e^{-i\xi_s x_3} \\ u_3^{PSV} &= \frac{\xi_p}{|\mathbf{k}_\Sigma|} A_P^+ e^{+i\xi_p x_3} - \frac{\xi_p}{|\mathbf{k}_\Sigma|} A_P^- e^{-i\xi_p x_3} - \frac{|\mathbf{k}_\Sigma|}{\xi_s} A_{SV}^+ e^{+i\xi_s x_3} + \frac{|\mathbf{k}_\Sigma|}{\xi_s} A_{SV}^- e^{-i\xi_s x_3} \end{cases}$$

Since we are interested in outgoing waves for paraxial approximation (i.e., waves propagating in the x_3-direction toward $-\infty$, see Figure C.1), displacements simplify as

$$\begin{cases} u_1^{PSV} &= A_P^- e^{-i\xi_p x_3} + A_{SV}^- e^{-i\xi_s x_3} \\ u_2^{SH} &= A_{SH}^- e^{-i\xi_s x_3} \\ u_3^{PSV} &= -\dfrac{\xi_p}{|\mathbf{k}_\Sigma|} A_P^- e^{-i\xi_p x_3} + \dfrac{|\mathbf{k}_\Sigma|}{\xi_s} A_{SV}^- e^{-i\xi_s x_3} \end{cases} \tag{C.10}$$

In order to determine the constants A_P^-, A_{SV}^- and A_{SH}^-, we suppose that $\mathbf{u}(\mathbf{x}_\Sigma, x_3 = 0, t)$ is known on the boundary Σ. Writing Equations (C.10) in $x_3 = 0$, we obtain for u_2^{SH},

$$u_2^{SH}(\mathbf{k}_\Sigma, x_3 = 0) = u_{20}^{SH} \Rightarrow A_{SH}^- = u_{20}^{SH};$$

and for u_1^{PSV} and u_3^{PSV}

$$\begin{cases} u_1^{PSV}(\mathbf{k}_\Sigma, x_3 = 0) &= u_{10}^{PSV} \Rightarrow A_P^- + A_S^- = u_{10}^{PSV} \\ u_3^{PSV}(\mathbf{k}_\Sigma, x_3 = 0) &= u_{30}^{PSV} \Rightarrow -\dfrac{\xi_p}{|\mathbf{k}_\Sigma|} A_P^- + \dfrac{|\mathbf{k}_\Sigma|}{\xi_s} A_S^- = u_{30}^{PSV} \end{cases}$$

whose solution is given as

$$\begin{cases} A_P^- &= \dfrac{|\mathbf{k}_\Sigma|^2}{\xi_p \xi s + |\mathbf{k}_\Sigma|^2} u_{10}^{PSV} - \dfrac{\xi_s |\mathbf{k}_\Sigma|}{\xi_p \xi_s + |\mathbf{k}_\Sigma|^2} u_{30}^{PSV} \\ A_{SV}^- &= \dfrac{\xi_p \xi s}{\xi_p \xi_s + |\mathbf{k}_\Sigma|^2} u_{10}^{PSV} + \dfrac{\xi_s |\mathbf{k}_\Sigma|}{\xi_p \xi_s + |\mathbf{k}_\Sigma|^2} u_{30}^{PSV} \end{cases}.$$

The final solution expressing displacements on the boundary Σ in the domain $(\mathbf{k}_\Sigma, x_3, \omega)$ is therefore

$$\begin{cases} u_1^{PSV}(\mathbf{k}_\Sigma, x_3, \omega) &= \dfrac{1}{\xi_p \xi_s + |\mathbf{k}_\Sigma|^2} \left[\left(|\mathbf{k}_\Sigma|^2 u_{10}^{PSV} - \xi_s |\mathbf{k}_\Sigma| u_{30}^{PSV} \right) e^{-i\xi_p x_3} \right. \\ & \qquad \left. + \left(\xi_p \xi_s u_{10}^{PSV} + \xi_s |\mathbf{k}_\Sigma| u_{30}^{PSV} \right) e^{-i\xi_s x_3} \right] \\ u_2^{SH}(\mathbf{k}_\Sigma, x_3, \omega) &= u_{20}^{SH} e^{-i\xi_s x_3} \\ u_3^{PSV}(\mathbf{k}_\Sigma, x_3, \omega) &= \dfrac{1}{\xi_p \xi_s + |\mathbf{k}_\Sigma|^2} \left[\left(-\xi_p |\mathbf{k}_\Sigma| u_{10}^{PSV} + \xi_p \xi_s u_{30}^{PSV} \right) e^{-i\xi_p x_3} \right. \\ & \qquad \left. + \left(\xi_p |\mathbf{k}_\Sigma| u_{10}^{PSV} + |\mathbf{k}_\Sigma|^2 u_{30}^{PSV} \right) e^{-i\xi_s x_3} \right] \end{cases} \tag{C.11}$$

This complete solution of displacement allows the derivation of the spectral impedance on the boundary Σ (i.e., the stress vector in the domain $(\mathbf{k}_\Sigma, x_3, \omega)$ on a face perpendicular to the vector $\mathbf{e}_3$). In order to express the spectral impedance, let us calculate the stress vector in the space-time

domain whose basis is $(\mathbf{e}_1, \mathbf{e}_2, \mathbf{e}_3)$ and then perform a Fourier transformation of the stress (as we did for the Elastodynamic equation). Stress vector on a face whose normal is $\mathbf{e}_3$ is equal to

$$\mathbf{T}(\mathbf{x}_\Sigma, x_3, t) = [\lambda tr(\boldsymbol{\varepsilon})\mathbf{I} + 2\mu\boldsymbol{\varepsilon}] \cdot \mathbf{e}_3 = \begin{pmatrix} \mu(\partial_3 u_1 + \partial_1 u_3) \\ \mu(\partial_3 u_2 + \partial_2 u_3) \\ (\lambda + 2\mu)\partial_3 u_3 + \lambda(\partial_1 u_1 + \partial_2 u_2) \end{pmatrix}. \tag{C.12}$$

Using the *Differentiation property* of Fourier transformation exposed in Appendix D and the following formulae: $\lambda = \rho(\alpha^2 - 2\beta^2)$, $\mu = \rho\beta^2$ and $(\lambda + 2\mu) = \rho\alpha^2$; we obtain from Equation (C.12) the spectral impedance in the domain $(\mathbf{k}_\Sigma, x_3, \omega)$ as

$$\mathbf{T}(\mathbf{k}_\Sigma, x_3, \omega) = \begin{pmatrix} \rho\beta^2(\partial_3 u_1 + ik_1 u_3) \\ \rho\beta^2(\partial_3 u_2 + ik_2 u_3) \\ \rho\alpha^2\partial_3 u_3 + \rho(\alpha^2 - 2\beta^2)(ik_1 u_1 + ik_2 u_2) \end{pmatrix}$$

$$= \rho\beta^2(\partial_3 \mathbf{u}_\Sigma + iu_3\mathbf{k}_\Sigma) + \left[i\rho(\alpha^2 - 2\beta^2)\mathbf{k}_\Sigma \cdot \mathbf{u}_\Sigma + \rho\alpha^2\partial_3 u_3\right]\mathbf{e}_3).$$

Thanks to the decomposition of Equations (C.3) and (C.4), the spectral impedance can be rewritten as

$$\begin{aligned} \mathbf{T}(\mathbf{k}_\Sigma, x_3, \omega) = {} & \rho\beta^2(\partial_3 u_1^{PSV} + iu_3^{PSV}|\mathbf{k}_\Sigma|)\mathbf{e}_k + \rho\beta^2\partial_3 u_2^{SH}\mathbf{e}_3 \wedge \mathbf{e}_k \\ & + \left[i\rho(\alpha^2 - 2\beta^2)|\mathbf{k}_\Sigma|u_1^{PSV} + \rho\alpha^2\partial_3 u_3^{PSV}\right]\mathbf{e}_3 \end{aligned}. \tag{C.13}$$

In order to evaluate the spectral impedance on the boundary Σ, we need to calculate the quantities $\partial_3 u_1^{PSV}|_{x_3=0}$, $\partial_3 u_2^{SH}|_{x_3=0}$ and $\partial_3 u_3^{PSV}|_{x_3=0}$. This can be achieved by using Equation (C.11) to obtain

$$\begin{cases} \partial_3 u_1^{PSV}|_{x_3=0} & = \dfrac{i}{\xi_p\xi_s + |\mathbf{k}_\Sigma|^2}\left[-\dfrac{\xi_p\omega^2}{\beta^2}u_{10}^{PSV} + \xi_s|\mathbf{k}_\Sigma|(\xi_p - \xi_s)u_{30}^{PSV}\right] \\ \partial_3 u_2^{SH}|_{x_3=0} & = -i\xi_s u_{20}^{SH} \\ \partial_3 u_1^{PSV}|_{x_3=0} & = \dfrac{i}{\xi_p\xi_s + |\mathbf{k}_\Sigma|^2}\left[\xi_p|\mathbf{k}_\Sigma|(\xi_p - \xi_s)u_{10}^{PSV} - \dfrac{\xi_s\omega^2}{\alpha^2}u_{30}^{PSV}\right] \end{cases}. \tag{C.14}$$

Finally, using Equations (C.13) and (C.14), the spectral impedance on the

boundary Σ (i.e., $x_3 = 0$) can be expressed as

$$\mathbf{T}(\mathbf{k}_\Sigma, x_3 = 0, \omega) = \frac{i\rho}{\xi_p\xi_s + |\mathbf{k}_\Sigma|^2}\left[-\xi_p\omega^2 u_{10}^{PSV} + \beta^2|\mathbf{k}_\Sigma|(|\mathbf{k}_\Sigma|^2 + 2\xi_p\xi_s - \xi_s^2)u_{30}^{PSV}\right]\mathbf{e}_k$$

$$- i\rho\beta^2\xi_s u_{20}^{SH}\mathbf{e}_3 \wedge \mathbf{e}_k$$

$$+ \frac{i\rho}{\xi_p\xi_s + |\mathbf{k}_\Sigma|^2}\left[|\mathbf{k}_\Sigma|(\omega^2 - 2\beta^2(\xi_p\xi_s + |\mathbf{k}_\Sigma|^2))u_{10}^{PSV} - \xi_s\omega^2 u_{30}^{PSV}\right]\mathbf{e}_3 \tag{C.15}$$

In order to return in the space-time domain, we need to take the inverse Fourier transformation of the spectral impedance. This gives

$$\mathbf{T}(\mathbf{x}_\Sigma, x_3 = 0, t) = \frac{1}{8\pi^3}\int_{-\infty}^{\infty} d\omega \int_{-\infty}^{\infty} dk_1 \int_{-\infty}^{\infty} dk_2 \mathbf{T}(\mathbf{k}_\Sigma, x_3 = 0, \omega)e^{i(k_1x_1 + k_2x_2 - \omega t)} \tag{C.16}$$

Equation (C.16) represents the spectral action imposed by waves propagating along $-x_3$. This action is nonlocal since displacements depend on $(\mathbf{k}_\Sigma, \omega)$, Fourier transformation of $(\mathbf{x}_\Sigma, t)$ for every $\mathbf{x}_\Sigma$ and t.

In order to obtain a local impedance, Engquist and Majda (1977) proposed to develop

$$\xi_p = \frac{\omega}{\alpha}\sqrt{1 - \alpha^2\frac{|\mathbf{k}_\Sigma|^2}{\omega^2}} \quad and \quad \xi_s = \frac{\omega}{\beta}\sqrt{1 - \beta^2\frac{|\mathbf{k}_\Sigma|^2}{\omega^2}}$$

as a rational approximation about small $|\mathbf{k}_\Sigma|^2/\omega^2$. We should note that either Taylor series or Padé series can be used. Zero and first order of Taylor or Padé approximations are identical, giving for example for ξ_p

$$\begin{aligned} Zero\ order: \quad & \xi_p = \frac{\omega}{\alpha}\sqrt{1 - \alpha^2\frac{|\mathbf{k}_\Sigma|^2}{\omega^2}} \approx \frac{\omega}{\alpha} + O\left(\alpha^2\frac{|\mathbf{k}_\Sigma|^2}{\omega^2}\right) \\ First\ order: \quad & \xi_p = \frac{\omega}{\alpha}\sqrt{1 - \alpha^2\frac{|\mathbf{k}_\Sigma|^2}{\omega^2}} \approx \frac{\omega}{\alpha}\left[1 - \alpha^2\frac{|\mathbf{k}_\Sigma|^2}{\omega^2}\right] + O\left(\alpha^4\frac{|\mathbf{k}_\Sigma|^4}{\omega^4}\right) \end{aligned} \tag{C.17}$$

In literature, the zero order is called $1st$ approximation and the first order is called $2nd$ approximation. The $1st$ approximation is very accurate for high frequency waves and for waves impinging the boundary with low inclinaison with respect to $\mathbf{e}_3$ (i.e., small $|\mathbf{k}_\Sigma|$). The $2nd$ approximation is a parabola which fits the Elastodynamic equation as shown in Figure C.3.

As for the second order wave equations, Engquist and Majda (1977) claim that from the second order approximation (i.e., $3rd$ approximation), Taylor series expansion of the square root lead to instable differencing schemes.

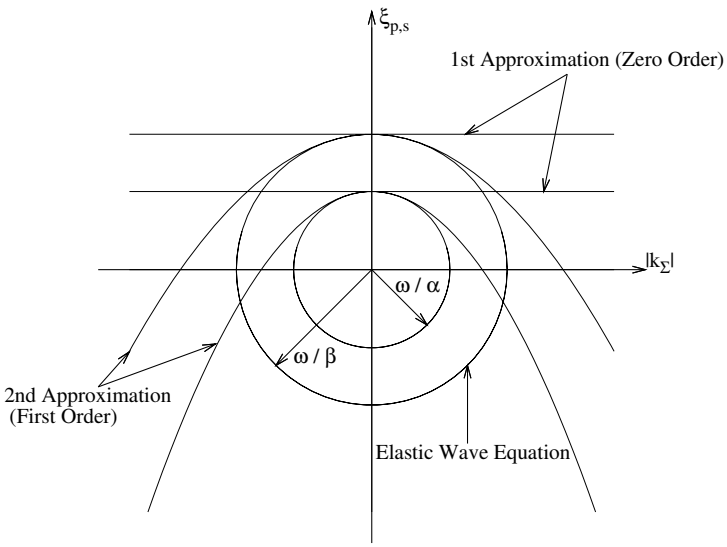

Figure C.3: Dispersion relation for elastic case. The curves 1*st* approximation and 2*nd* approximation are the dispersion relation of the paraxial approximations of the elastic wave equation (circles). For each approximation, there are two curves: that approximating the larger circle is for shear waves while the other is for compressional waves. Figure is plotted with $\alpha/\beta = \sqrt{3}$.

On the contrary, *highly absorbing boundary condition* derived from the 2*nd* order Padé approximation is well posed.

In the following Section, we will expose the 1*st* and 2*nd* approximation of the spectral impedance on the boundary Σ (Equation (C.15)).

C.4 $1st$ paraxial approximation

In order to derive the $1st$ approximation, we substitute the zero order development of ξ_p and ξ_s (Equation (C.17)) into Equation (C.15). After simplification, we obtain

$$\begin{aligned}\mathbf{T}(\mathbf{k}_\Sigma, x_3 = 0, \omega) = &- i\rho\beta\omega(u_{10}^{PSV}\mathbf{e}_k + u_{20}^{SH}\mathbf{e}_3 \wedge \mathbf{e}_k) - i\rho\alpha\omega u_{30}^{PSV}\mathbf{e}_3 \\ &+ i\rho\beta|\mathbf{k}_\Sigma|(2\beta - \alpha)(u_{30}^{PSV}\mathbf{e}_k - u_{10}^{PSV}\mathbf{e}_3)\end{aligned}.$$

And finally, to come back in the basis $(\mathbf{e}_1, \mathbf{e}_2, \mathbf{e}_3)$ (basis of a finite element), we use Equation (C.3) and obtain

$$\begin{aligned}\mathbf{T}(\mathbf{k}_\Sigma, x_3 = 0, \omega) &= -i\rho\beta\omega\mathbf{u}_{\Sigma 0} - i\rho\alpha\omega u_{30}\mathbf{e}_3 + i\rho\beta|\mathbf{k}_\Sigma|(2\beta - \alpha)(u_{30}\mathbf{k}_\Sigma - \mathbf{u}_{\Sigma 0} \cdot \mathbf{k}_\Sigma\mathbf{e}_3) \\ &= \begin{pmatrix} -i\rho\beta\omega u_{10} + i\rho\beta(2\beta - \alpha)u_{30}k_1 \\ -i\rho\beta\omega u_{20} + i\rho\beta(2\beta - \alpha)u_{30}k_2 \\ -i\rho\alpha\omega u_{30} - i\rho\beta(2\beta - \alpha)(u_{10}k_1 + u_{20}k_2) \end{pmatrix}.\end{aligned}$$

Using the correspondance $i\omega \leftrightarrow \partial_t$, $ik_1 \leftrightarrow \partial_1$ and $ik_2 \leftrightarrow \partial_2$, we find in the domain $(x_1, x_2, x_3 = 0, t)$

$$\mathbf{T}(x_1, x_2, x_3 = 0, t) = \begin{pmatrix} -\rho\beta\partial_t u_{10} + \rho\beta(2\beta - \alpha)\partial_1 u_{30} \\ -\rho\beta\partial_t u_{20} + \rho\beta(2\beta - \alpha)\partial_2 u_{30} \\ -\rho\alpha\partial_t u_{30} - \rho\beta(2\beta - \alpha)(\partial_1 u_{10} + \partial_2 u_{20}) \end{pmatrix}.$$

Appendix D

Property of Fourier Transformation

The *Differentiation property* shows that Fourier transformation of $\frac{\partial}{\partial x_1} f(x_1)$ is equal to i times the dual variable (i.e., k_1) times the Fourier transfomation of the function itself, such that:

$$f'(x_1) \longrightarrow h(k_1) = \int_{-\infty}^{\infty} f'(x_1) e^{-ik_1 x_1} dx_1 = ik_1 \int_{-\infty}^{\infty} f(x_1) e^{-ik_1 x_1} dx = ik_1 f(k_1),$$

where k_1 is the dual variable of x_1. The key of the demonstration of this formula lies in the integration by parts. Let $u = e^{-ik_1 x_1}$ and $v' = f'(x_1)$, then

$$h(k_1) = \int_{-\infty}^{\infty} f'(x_1) e^{-ik_1 x_1} dx_1 = [f(x_1) e^{-ik_1 x_1}]_{-\infty}^{+\infty} - \int_{-\infty}^{\infty} -ik_1 f(x_1) e^{-ik_1 x_1} dx_1.$$

Assuming that $f(x_1) \to 0$ as $x_1 \to \infty$ (which is the case for accelerograms), then

$$h(k_1) = ik_1 f(k_1).$$

This property can be used recursively so that Fourier transformation of the n-th derivative of a function $f(x_1)$ is $(ik_1)^n f(k_1)$.

Moreover, the computation of Fourier transformation of $\partial_{x_2} f(x_1, x_2)$ with respect to x_1 leads to:

$$\int_{-\infty}^{\infty} \partial_{x_2} f(x_1, x_2) e^{-k_1 x_1} dx_1 = \partial_{x_2} f(k_1, x_2).$$

The demonstration of this property is as easy as the first demonstration:

$$\begin{aligned}
\int_{-\infty}^{\infty} \partial_{x_2} f(x_1, x_2) e^{-k_1 x_1} dx_1 &= \int_{-\infty}^{\infty} \lim_{h \to 0} \frac{f(x_1, x_2 + h) - f(x_1, x_2)}{h} e^{-k_1 x_1} dx_1 \\
&= \lim_{h \to 0} \frac{1}{h} \left[\int_{-\infty}^{\infty} f(x_1, x_2 + h) e^{-k_1 x_1} dx_1 \right. \\
&\qquad \left. - \int_{-\infty}^{\infty} f(x_1, x_2) e^{-k_1 x_1} dx_1 \right] \\
&= \lim_{h \to 0} \frac{1}{h} \left[f(k_1, x_2 + h) - f(k_1, x_2) \right] \\
&= \frac{\partial}{\partial x_2} f(k_1, x_2).
\end{aligned}$$

Appendix E

Solving System of 2nd Order Ordinary Differential Equations

This appendix presents the resolution of a system of second order ordinary differential equations. Let

$$\partial_{xx}\mathbf{V} = \mathbf{F}(v_1(x), ..., v_n(x), \partial_x v_1(x), ..., \partial_x v_n(x))$$
$$\mathbf{V}(x) = (v_1(x), ..., v_n(x))$$

and

$$\mathbf{W}(x) = (w_1(x), ..., w_n(x), ..., w_{2n}(x))$$

with

$$w_i = v_i, w_{n+i} = \partial_x v_i = \partial_x w_i, 1 \leq i \leq n.$$

Thus, we may form the first order differential system of $2n$ equations:

$$\partial_x \mathbf{W} = \mathbf{G}(\mathbf{W}, x)$$

where

$$G_i(\mathbf{W}, t) = w_{n+i}, 1 \leq i \leq n$$
$$G_i(\mathbf{W}, t) = F_{i-n}(\mathbf{W}, t), n \leq i \leq 2n.$$

Bibliography

Aguirre, J. and K. Irikura (1997). Nonlinearity, liquefaction, and velocity variation of soft soil layers in Port Island, Kobe, during the Hyogo-ken Nanbu earthquake. *Bull. Seism. Soc. Am.* **87** 1244–1258. 41

Aki, K. (1993). Local site effects on weak and strong ground motion. *Tectonophysics* **218** 93–111. 10, 41

Aki, K. (2003). A perspective on the history of strong motion seismology. *Physics of the Earth and Planetary Interiors* **137** 5–11. 10, 41

Aki, K. and P. G. Richards (2002). *Quantitative Seismology, Second Edition.* University Science Books. 8, 9, 11, 14, 99, 125, 126, 127, 129

Archuleta, R. J., S. H. Seale, P. V. Sangas, L. M. Baker, and S. T. Swain (1992). Garner Valley downhole array of accelerometers: Instrumentation and preliminary data analysis. *Bull. Seism. Soc. Am.* **82** 1592–1621. 41

Archuleta, R. J., S. H. Seale, P. V. Sangas, L. M. Baker, and S. T. Swain (1993). Garner valley downhole array of accelerometers: Instrumentation and preliminary data analysis. *Bull. Seism. Soc. Am.* **83** 2039. 41

Asano, K. and T. Iwata (2006). Source process and near-source ground motions of the 2005 West-Off Fukuoka Prefecture earthquake. *Earth Planets Space* **58** 93–98. 43

Assimaki, D. and J. Steidl (2007). Inverse analysis of weak and strong motion downhole array data from the Mw7.0 Sanriku-Minami earthquake. *Soil Dynamics and Earthquake Engineering* **27** 73 – 92. 41, 151

Aubert, P. (1997). *Méthodes Meshless en Géomécanique.* Ph. D. thesis, École Centrale de Paris. 101

Aubry, D., D. Chouvet, A. Modaressi, and H. Modaressi (1985). GEFDYN 5*, Logiciel d'analyse du comportement statique et dynamique des sols par éléments finis avec prise en compte du couplage sol-eau-air.* 101

Aubry, D., J. C. Hujeux, F. Lassoudire, and Y. Meimon (1982). A double memory model with multiple mechanisms for cyclic soil behaviour. In

Proceedings of the International Symposium "Num. Mod. Geomech (NUMOD)", Balkema, pp. 3–13. 76, 89

Aubry, D. and A. Modaressi (1996). GEFDYN,*Manuel Scientifique*. 101

Bamberger, A., G. Chavent, and P. Lailly (1980). Etude de schémas numérique pour les équations de l'élastodynamique linéaire. Technical Report 41, INRIA. 135

Bao, H., J. Bielak, O. Ghattas, L. F. Kallivokas, D. R. O'Hallaron, J. R. Shewchuk, and J. Xu (1998). Large-scale simulation of elastic wave propagation in heterogeneous media on parallel computers. *Comput. Methods Appl. Mech. Engrg.* **152** 85–102. 100

Bard, P. Y. (1983). *Les effets de site d'origine structurale en sismologie; Modélisation et interpretation, Application au risque sismique*. Ph. D. thesis, Université Scientifique et Médicale et Institut national Polytechnique de Grenoble. 130

Bard, P. Y. and M. Bouchon (1980). The seismic response of sediment-filled valleys. part I: The case of incident SH waves. *Bull. Seism. Soc. Am.* **70** 1263–1286. 130

Bard, P. Y., M. Campillo, F. J. Chavez-Garcia, and F. Sanchez-Sesma (1988). The Mexico earthquake of September 19, 1985 - A theoretical investigation of large- and small-scale amplification effects in the Mexico City Valley. *Earthquake Spectra* **4** 609–633. 42

Bard, P. Y. and J. C. Gariel (1986). The seismic response of two-dimensional sedimentary deposits with large vertical velocity gradients. *Bull. Seism. Soc. Am.* **76** 343–346. 10

Belytschko, T., Y. Krongauz, D. Organ, M. Fleming, and P. Krysl (1996). Meshless methods: An overview and recent developments. *Computer Methods in Applied Mechanics and Engineering* **139** 3 – 47. 101

Beresnev, I. A., K.-L. Wen, and Y. T. Yeh (1995). Seismological evidence for nonlinear elastic ground behavior during large earthquakes. *Soil Dynamics and Earthquake Engineering* **14** 103 – 114. 41

Bhattacharyya, J., A. F. Sheehan, K. Tiampo, and J. Rundle (1999). Using a genetic algorithm to model broadband regional waveforms for crustal structure in the western United States. *Bull. Seism. Soc. Am.* **89** 202–214. 30

Bonilla, F. (2000). *Computation of Linear and Nonlinear Site Response for Near Field Ground Motion*. Ph. D. thesis, University of California, Santa Barbara. 82

Bonilla, L. F., R. J. Archuleta, and D. Lavallee (2005). Hysteretic and Dilatant Behavior of Cohesionless Soils and Their Effects on Nonlinear Site Response: Field Data Observations and Modeling. *Bull. Seism. Soc. Am.* **95** 2373–2395. 10, 41

Bonilla, L. F., J. H. Steidl, J.-C. Gariel, and R. J. Archuleta (2002). Borehole Response Studies at the Garner Valley Downhole Array, Southern California. *Bull. Seism. Soc. Am.* **92** 3165–3179. 41

Bouchon, M. (1985). A simple complete numerical solution to the problem of diffraction of SH waves by an irregular surface. *J. Acoust. Soc. Am.* **44** 1–5. 99

Bouchon, M. and K. Aki (1977). Discrete wavenumber representation of seismic source wave fields. *Bull. Seism. Soc. Am.* **67** 259–277. 99

Bouchon, M. and O. Coutant (1994). Calculation of synthetic seismograms in a laterally varying medium by the boundary element-discrete wavenumber method. *Bull. Seism. Soc. Am.* **84** 1869–1881. 129

Bouchon, M., C. A. Schultz, and M. N. Tokstz (1995). A fast implementation of boundary integral equation methods to calculate the propagation of seismic waves in laterally varying layered media. *Bull. Seism. Soc. Am.* **85** 1679–1687. 100

Bravo, M. A., F. J. Sanchez-Sesma, and F. J. Chavez-Garcia (1988). Ground motion on stratified alluvial deposits for incident SH waves. *Bull. Seism. Soc. Am.* **78** 436–450. 99

Campillo, M. (1987). Lg wave propagation in a laterally varying crust and the distribution of the apparent quality factor in central france. *Journal of Geophys. Res.* **92** 12604–12614. 99

Campillo, M. and M. Bouchon (1985). Synthetic SH seismograms in a laterally varying medium by the discrete wavenumber method. *Geophys. J. R. astr. Soc.* **83** 307–317. 99

Canuto, C., M. Y. Hussaini, A. Quarteroni, and T. A. Tang (1987). *Spectral Methods in Fluid Dynamics*. 103

Carcione, J. M. and P. J. Wang (1993). A Chebyshev collocation method for the wave equation in generalized coordinates. *Comp. Fluid Dyn. J.* **2** 269–290. 100

Castaings, M. and B. Hosten (1994). Delta operator technique to improve the thomson-haskell-method stability for propagation in multilayered anisotropic absorbing plates. *The Journal of the Acoustical Society of America* **95** 1931–1941. 11

Chaljub, E., Y. Capdeville, and J.-P. Vilotte (2003). Solving elastodynamics in a fluid-solid heterogeneous sphere: a parallel spectral element approximation on non-conforming grids. *Journal of Computational Physics* **187** 457 – 491. 100

Chang, C. Y., C. M. Mok, M. S. Power, Y. K. Tang, H. T. Tang, and J. C. Stepp (1991). Development of shear modulus reduction curves based on Lotung downhole ground motion data. In *Proc. of the 2nd Intel. Conf. on Recent Advances in Geotechnical Earthquake Engineering and Soil Dynamics*, St. Louis, Missouri, pp. 111–118. 41

Chang, S.-J., C.-E. Baag, and C. A. Langston (2004). Joint Analysis of Teleseismic Receiver Functions and Surface Wave Dispersion using the Genetic Algorithm. *Bull. Seism. Soc. Am.* **94** 691–704. 30

Chávez-García, F. J. and D. Raptakis (2008). Inversion of soil structure and analysis of the seismic wavefield from a vertical array. In *Proc. of the 14th World Conference on Earthquake Engineering*, Beijing, China. 41

Chen, W. F. and E. Mizuno (1990). *Nonlinear Analysis in Soil Mechanics.* Elsevier Science. 9, 80

Chin, B.-H. and K. Aki (1991). Simultaneous study of the source, path, and site effects on strong ground motion during the 1989 Loma Prieta earthquake: A preliminary result on pervasive nonlinear site effects. *Bull. Seism. Soc. Am.* **81** 1859–1884. 10, 41

Claerbout, J. F. (1976). *Fundamentals of geophysical Data Processing.* McGraw-Hill Inc. 106

Clayton, R. and B. Engquist (1977). Absorbing boundary conditions for acoustic and elastic wave equations. *Bull. Seism. Soc. Am.* **67** 1529–1540. 106, 132

Clouteau, D. and D. Aubry (2003). *Boundary Element Methods for Soil-Structure Interaction*, Chapter Computational Soil-Structure Interaction, pp. 61–126. Kluwer Academic Publishers. 99

Cohen, M. and P. C. Jennings (1983). Silent boundary methods for transient analysis. *In: T. Belytschko and T.J.R. Hughes, Editors, Computational Methods for Transient Analysis* 301–360. 106

Coutant, O. (1989). Numerical study of the diffraction of clastic waves by fluid-filled cracks. *Journal of Geophys. Res.* **94** 17805–17818. 99

Cramer, C. and C. Real (1992). A statistical analysis of submitted site-effects predictions for the weak-motion blind prediction test conducted at the Turkey Flat, USA, site effects test area near Parkfield, California.

In J. ESG, Odawara (Ed.), *Int. Sym. Effects of Surf. Geol. on Seismic Motion*, Volume II, pp. 15–20. 10, 42

Cultrera, G. C., D. M. Boore, W. B. Joyner, and C. M. Dietel (1999). Nonlinear soil response in the vicinity of the Van Norman Complex following the 1994 Northridge, California. *Bull. Seism. Soc. Am.* **89** 1214–1231. 10, 41

Darragh, R. B. and A. F. Shakal (1991). The site response of two rock and soil station pairs to strong and weak ground motion. *Bull. Seism. Soc. Am.* **81** 1885–1899. 10, 41

De Martin, F., H. Kawase, and A. Modaressi (2010). Nonlinear soil response of a borehole station based on one-dimensional inversion during the 2005 West off Fukuoka Prefecture earthquake. *Bull. Seism. Soc. Am.* **100** 151–171. 10

Dikmen, S. U. and J. Ghaboussi (1984). Effective stress analysis of seismic response and liquefaction, theory. *Journal of Geotechnical Engineering* **110** 628–644. 81

Dravinski, M. (1983). Scattering of plane harmonic SH wave by dipping layers of arbitrary shape. *Bull. Seism. Soc. Am.* **73** 1303–1319. 99

Dupros, F., F. De Martin, E. Foerster, D. Komatitsch, and J. Roman (2008). High-performance finite-element simulations of seismic wave propagation in three-dimensional inelastic geological media. Submitted to Parallel Computing. 100

Engquist, B. and A. Majda (1977). Absorbing boundary conditions for numerical simulation of waves. *Mathematics of Computation* **31** 629–651. 106, 132, 178

Faccioli, E., F. Maggio, R. Paolucci, and A. Quarteroni (1997). 2D and 3D elastic wave propagation by a pseudo-spectral domain decomposition method. *Journal of Seismology* **1** 237–251. 100, 101

Field, E. H., P. A. Johnson, I. A. Beresnev, and Y. Zeng (1997). Nonlinear ground-motion ampliïňĄcation by sediments during the 1994 Northridge earthquake. *Nature* **390** 599–602. 10, 41

Finn, W. D. L., K. W. Lee, and G. R. Martin (1977). An effective stress model for liquefaction. *Journal of Geotechnical Engineering Division* **103** 517–533. 82

Fischer, P. F. and E. M. Rønquist (1994). Spectral-element methods for large scale parallel Navier-Stokes calculations. *Comput. Methods Appl. Mech. Engrg.* **116** 69–76. 100

Foerster, E. (2003). *Évaluation des méthodes Meshfree pour les Simulations Géomécaniques en Transformations Finies*. Ph. D. thesis, École Centrale de Paris. 101

Foerster, E. and H. Modaressi (2007). Nonlinear numerical method for earthquake site response analysis II-case studies. *Bull. of Earthq. Eng.* **5(3)** 325–345. 101

Fonseca, C. M. and P. J. Fleming (1993). Genetic algorithms for multiobjective optimization: Formulation, discussion and generalization. 30

Frankel, A. (1994). Dense array recordings in the San Bernardino Valley of landers-big bear aftershocks: Basin surface waves, Moho reflections, and three-dimensional simulations. *Bull. Seism. Soc. Am.* **84** 613–624. 42

Frankel, A. D., D. L. Carver, and R. A. Williams (2002). Nonlinear and linear site response and basin effects in Seattle for the M 6.8 Nisqually, Washington, earthquake. *Bull. Seism. Soc. Am.* **92** 2090–2109. 10, 41

Gaffet, S. and M. Bouchon (1989). Effects of two-dimensional topographies using the discrete wavenumber-boundary integral equation method in P-SV cases. *J. Acoust. Soc. Am.* **85** 2277–2283. 99, 117

Gaffet, S. and M. Bouchon (1991). Source location and valley shape effects on the P-SV displacement field using a boundary integral equation-discrete wavenumber representation method. *Geophys. J. Int.* **106** 341–355. 99

Gantmatcher, R. R. (1959). *Theory of Matrices*. New York: Chelsea Publishing Co. 11

Garvin, W. (1956). Exact transient solution for the buried line source problem. *Proc. Roy. Soc. London* **203** 528–541. 99

Gen, M. and R. Cheng (1999). *Genetic Algorithms and Engineering Optimization (Engineering Design and Automation)*. Wiley-Interscience. 30

Ghayamghamain, M. R. and H. Kawakami (1996). On the characteristics of non-linear soil response and dynamic soil properties using vertical array data in Japan. *Earthquake Engineering and Structural Dynamics* **25** 857–870. 41

Gilbert, F. and G. Backus (1966). Propagator matrices in elastic wave and vibration problems. *Geophysics* **31** 326–332. 11

Gingold, R. A. and J. J. Monaghan (1977). Smoothed particle hydrodynamics: theory and application to non-spherical stars. *Mon. Not. R. Astr. Soc.* **181** 375–389. 101

Goldberg, G. (1989). *Genetic algorithms in search, optimization, and machine learning*. Addison-Wesley. 30, 42

Graves, R. (1993). Modeling three dimensional site response effects in the Marina district basin, San Francisco, California. *Bull. Seism. Soc. Am.* **83** 1042–1063. 42

Graves, R. (1996). Simulating seismic wave propagation in 3D elastic media using staggered-grid finite differences. *Bull. Seism. Soc. Am.* **86** 1091–1106. 100

Hadamard, J. (1902). Sur les problèmes aux dérivée partielles et leur signification physique. *Princeton University Bulletin* **13** 49–52. 7

Hardin, B. O. (1965). The nature of damping in sands. In *Proc. of ASCE*, Volume 91, pp. 63–97. SM 1. 152

Harvey, D. (1981). Seismogram synthesis using normal mode superposition: the locked mode approximation. *Geophysical Journal of the Royal Astronomical Society* **66** 37–69. 11

Haskell, N. A. (1953). The dispersion of surface waves in multilayered media. *Bull. Seism. Soc. Am.* **43** 17–34. 11, 42

Hujeux, J. (1979). *Calcul numérique de problèmes de consolidation élastoplastiques*. Thèse de doctorat, École Centrale Paris, France. 89

Hujeux, J. (1985). Une loi de comportement pour le chargement cyclique des sols. In *Génie Parasismique*, pp. 287–302. Presse ENPC. 89, 93

Ishihara, K. (1996). *Soil behaviour in earthquake geotechnics*. 1, 3

Iwan, W. D. (1967). on a class of models for the yielding behavior of continuous and composite systems. *Journal of Applied Mechanics* **34** 612–617. 82

Jeffreys, H. and B. S. Jeffreys (1972). *Methods of Mathematical Physics* (3rd ed.). Cambridge: Cambridge University Press. 9

Jimenez, A., J. M. Garcia, and M. D. Romacho (2005). Simultaneous Inversion of Source Parameters and Attenuation Factor Using Genetic Algorithms. *Bull. Seism. Soc. Am.* **95** 1401–1411. 30

JMA (2005). http://www.hinet.bosai.go.jp/regs/jma/list/. *Japan Meteorological Agency*. 159

Joyner, W. B. and A. T. M. Chen (1975). Calculation of nonlinear ground response in earthquakes. *Bull. Seism. Soc. Am.* **65** 1315–1336. 80

Kawase, H. (1988). Time-domain response of a semicircular canyon for incident SV, P, and Rayleigh waves calculated by the discrete wave-number boundary element method. *Bull. Seism. Soc. Am.* **78** 1415–1437. 99

Kawase, H. and K. Aki (1989). A study one the response of soft basin for incident S, P and Rayleigh waves with special reference to the long duration observed in Mexico City. *Bull. Seism. Soc. Am.* **79** 1361–1382. 42, 99

Kawase, H. and K. Aki (1990). Topography effect at the critical SV-wave incidence: possible explaination of damage pattern by the Whittier Narrows, California, earthquake of 1 october 1987. *Bull. Seism. Soc. Am.* **80** 1–22. 43

Kawase, H. and S. Matsushima (1998). Strong motion simulation in Kobe during the Hyogo-ken Nanbu earthquake of 1995 based on a three-dimensional basin structure. *J. Struct. Constr. Eng. Trans. Architectural Inst.* **514** 111–118. In Japanese with English abstract. 42

Kawase, H. and T. Sato (1992). Simulation analysis of strong motions in Ashigara valley considering one- and two-dimensional geological structures. *Journal of Physics of the Earth* **40** 27–56. 16, 42

Kawase, H., T. Satoh, and K. Fukutake (1996). Simulation of the borehole records observed at the Port Island in Kobe, Japan, during the Hyogo-ken Nanbu earthquake of 1995. In *Proc. of the 11th World Conference on Earthquake Engineering*, Acapluco, Mexico, pp. 8. CD-ROM Ref. No. 140. 41

Kawase, H., T. Satoh, and N. Umeda (2006). Strong motion characteristics observed during the West off Fukuoka earthquake of 2005 and their simulation. In *Proc. of Third International Symposium on the Effects of Surface Geology on Seismic Motion*, Grenoble, France, pp. 587–597. No. 53. 47

Kokusho, T. (1980). Cyclic triaxial test of dynamic soil properties for wide strain range. *Soils and Fundations* **20**. 80

Kokusho, T. (2004). Nonlinear site response and strain-dependent soil properties. *Current Science* **87** 1363–1369. 41

Komatitsch, D. (1997). *Méthodes spectrales et éléments spectraux pour l'équation de l'élastodynamique 2D et 3D en milieu hétérogène (Spectral and spectral-element methods for the 2D and 3D elastodynamics equations in heterogeneous media)*. Ph. D. thesis, Institut de Physique du Globe, Paris, France. 76, 100, 101, 102, 112, 117, 150

Komatitsch, D., F. Coutel, and P. Mora (1996). Tensorial formulation of the wave equation for modelling curved interfaces. *Geophys. J. Int.* **127** 156. 100

Komatitsch, D. and R. Martin (2007). An unsplit convolutional Perfectly Matched Layer improved at grazing incidence for the seismic wave equation. *Geophysics* **72** SM155–SM167. 100, 106, 146

Komatitsch, D., R. Martin, and J. Tromp (2001). Wave propagation in 2-D elastic media using a spectral element method with triangles and quadrangles. *Journal of Computational Acoustics* **9** 703–718. 102, 112

Komatitsch, D. and J. P. Vilotte (1998). The spectral-element method: an efficient tool to simulate the seismic response of 2D and 3D geological structures. *Bull. Seism. Soc. Am.* **88** 368–392. 100, 101

Komatitsch, D., J. P. Vilotte, R. Vai, J. M. Castillo-Covarrubias, and F. J. Sanchez-Sesma (1999). The spectral element method for elastic wave equations - application to 2-D and 3-D seismic problems. *Int. J. Numer. Meth. Engng.* **45** 1139–1164. 107

Kramer, S. L. (1996). *Geotechnical Earthquake Engineering*. Prentice Hall. 80

Kwok, A. O. L., J. P. Stewart, and Y. M. A. Hashash (2008). Nonlinear Ground-Response Analysis of Turkey Flat Shallow Stiff-Soil Site to Strong Ground Motion. *Bull. Seism. Soc. Am.* **98** 331–343. 41

Lamb, H. (1904). On the propagation of tremors over the surface of an elastic solid. *Philosophical Transactions of the Royal Society of London* **A203** 1–42. 99

Levasseur, S., Y. Malécot, M. Boulon, and E. Flavigny (2007). Soil parameter identification using a genetic algorithm. *International Journal for Numerical and Analytical Methods in Geomechanics* **32** 189–213. 30

Li, Y. and P. Leary (1990). Fault zone trapped seismic waves. *Bull. Seism. Soc. Am.* **80** 1245–2271. 159, 168

Lin, M.-L., T.-H. Huang, and J.-C. You (1996). The effects of frequency on damping properties of sand. *Soil Dynamics and Earthquake Engineering* **15** 269 – 278. 152

Lopez-Caballero, F., Modaressi-Farahmand Razavi, and F. Elmi (2003). Identification of an elastoplastic model parameters using laboratory and in-situ tests. A.A. Balkema, Rotterdam, pp. 1183–1190. 89

Lopez-Caballero, F., A. Modaressi-Farahmand Razavi, and H. Modaressi (2007). Nonlinear numerical method for earthquake site response analysis I - elastoplastic cyclic model and parameter identifification strategy. *Bull. of Earthq. Eng.* **5(3)** 303–323. 89, 93

Lucy, L. (1977). A numerical approach to testing the fission hypothesis. *Astro. J.* **82** 1013–1024. 101

Ma, S. and P. Liu (2006). Modeling of the perfectly matched layer absorbing boundaries and intrinsic attenuation in explicit finite-element methods. *Bull. Seism. Soc. Am.* **96** 1779–1794. 145

Maday, Y. and A. T. Patera (1989). Spectral element methods for the incompressible navier-stokes equations. *State of the art survey in computational mechanics* 71–143. 100

Martin, P. P. and H. B. Seed (1978). MASH - A computer program for the nonlinear analysis of vertically propagating shear wave in horizontally layered soil deposits. Technical Report UCB/EERC-78/23, Earthquake Engineering Research Center, University of California, Berkley, California. 81

Masing, G. (1926). Eigenspannungen und verfertigung beim messing. In *Proc. of the 2nd International Congress on Applied Mechanics*, Zurich. 82

Mayne, P. W. (2007). Cone penetration testing state-of-practice. Technical report, Georgia Institute of Technology. 151

Mazda, T., T. Irie, A. Sumaya, and H. Matsumoto (2005). Damage of building structure and their earthquake response at West off Fukuoka Prefecture earthquake. In *Proc. of 28th JSCE Earthquake Engineering Symposium, JSCE*, Japan. 47

Mirodikawa, S. (1992). A statistical analysis of submitted predictions for the Ashigara valley blind prediction test. In J. ESG, Odawara (Ed.), *Int. Sym. Effects of Surf. Geol. on Seismic Motion*, Volume II, pp. 65–77. 10, 42

Mitchell, M. (1998). *An Introduction to Genetic Algorithms*. The MIT Press. 30

Modaressi, H. (1987). *Modélisation numérique de la propagation des ondes dans les milieux poreux anélastiques*. Ph. D. thesis, École Centrale de Paris. 101, 106, 130, 132, 135, 171, 173

Modaressi, H. and P. Aubert (1998). Element-free galerkin method for deforming multiphase porous media. *Int. J. Num. Meth. Eng.* **42** 313–340. 101

Monaghan, J. J. (1982). Why particle methods work. *SIAM J. Sci. Stat. Comput.* **3** 422–433. 101

Mossessian, T. K. and M. Dravinski (1992). A hybrid approach for scattering of elastic waves by three-dimensional irregularities of arbitrary shape. *Journal of Physics of the Earth* **40** 241–261. 99

Mroz, Z. (1967). On the description of anisotropic work hardening. *Journal of Mechanics and Physics of Solids* **15** 163–175. 89

Newmark, N. M. (1959). A method for computation of structural dynamics. In *Proc. Am. Soc. Civ. Eng.*, pp. 67–94. 105

Niazy, A. (1973). Elastic displacements caused by a propagating crack in an infinite medium: an exact solution. *Bull. Seism. Soc. Am.* **63** 357–379. 99

Oprsal, I. and J. Zahradnk (2002). Three-dimensional finite difference method and hybrid modeling of earthquake ground motion. *Journal of Geophys. Res.* **107** 2161–2177. 100

Papageorgiou, A. S. and J. Kim (1991). Study of the propagation and amplification of seismic waves in Caracas Valley with reference to the 29 July 1967 earthquake: SH waves. *Bull. Seism. Soc. Am.* **81** 2214–2233. 99

Parzen, E. (1962). On the estimation of a probability density function and the mode. *Annals of Math. Stats.* **33** 1065–1076. 55

Patera, A. T. (1984). A spectral element method for fluid dynamics: laminar flow in a channel expansion. *J. Comput. Phys.* **54** 468–488. 100

Pavlenko, O. V. and K. Irikura (2003). Estimation of nonlinear time-dependent soil behavior in strong ground motion based on vertical array data. *Pure and Applied Geophysics* **160** 2365–2379. 41

Pavlenko, O. V. and K. Irikura (2005). Identification of the non-linear behaviour of liquefied and non-liquefied soils during the 1995 Kobe earthquake. *Geophys. J. Int.* **160** 539–553. 41

Pavlenko, O. V. and K. Irikura (2006). Nonlinear Behavior of Soils Revealed from the Records of the 2000 Tottori, Japan, Earthquake at Stations of the Digital Strong-Motion Network Kik-Net. *Bull. Seism. Soc. Am.* **96** 2131–2145. 41

Pezeshk, S. and M. Zarrabi (2005). A New Inversion Procedure for Spectral Analysis of Surface Waves Using a Genetic Algorithm. *Bull. Seism. Soc. Am.* **95** 1801–1808. 30

Potts, D. M. and L. Zdravkovic (1999). *Finite element analysis in geotechnical engineering*. Thomas Telford. 80

Prevost, J. H. (1977). Mathematical modelling of monotonic and cyclic undrained clay behaviour. *Int. J. in Num. and Ana. Meth. in Geomech.* **1** 195–216. 89

Prevost, J. H. (1985). A simple plasticity theory for frictional cohesionless soils. *International Journal of Soils Dynamics and Earthquake Engineering* **4** 9–17. 89

Priolo, E., J. M. Carcione, and G. Seriani (1994). Numerical simulation of interface waves by high-order spectral modeling techniques. *The Journal of the Acoustical Society of America* **95** 681–693. 100

Pyke, R. M. (1979). Nonlinear soil models for irregular cyclic loadings. *Journal of Geotechnical Engineering Division* **105** 715–726. 82

Ramberg, W. and W. R. Osgood (1943). Description of stress-strain curves by three parameters. Technical Report Technical Note 902, National Advisory Committee for Aeronautics, Washington, D.C. 82

Randles, P. W. and L. D. Libersky (1996). Smoothed particle hydrodynamics: Some recent improvements and applications. *Computer Methods in Applied Mechanics and Engineering* **139** 375 – 408. 101

Samarajiva, P., E. J. Macari, and W. Wathugala (2005). Genetic algorithms for the calibration of constitutive models for soils. *International Journal of Geomechanics* **5**. 30

Sanchez-Sesma, F. J. and M. Campillo (1991). Diffraction of P, SV, and Rayleigh waves by topographic features: a boundary integral formulation. *Bull. Seism. Soc. Am.* **81** 2234–2253. 99

Sanchez-Sesma, F. J. and J. Esquivel (1979). Ground motion on alluvial valleys under incident plane SH waves. *Bull. Seism. Soc. Am.* **69** 1107–1120. 99

Satoh, T. (2006). Inversion of Qs of deep sediments from surface-to-borehole spectral ratio considering obliquely incident SH and SV-waves. *Bull. Seism. Soc. Am.* **96** 943–956. 15

Satoh, T., M. Fushimi, and Y. Tatsumi (2001). Inversion of strain-depend nonlinear characteristics of soils using weak and strong motions observed by borehole sites in Japan. *Bull. Seism. Soc. Am.* **91** 365–380. 41, 61, 73

Satoh, T., M. Horike, Y. Takeuchi, T. Uetake, and H. Suzuki (1997). Nonlinear behavior of scoria evaluated from borehole records in eastern Shizuoka

prefecture, Japan. *Earthquake Engineering and Structural Dynamics* **26** 781–795. 41

Satoh, T. and H. Kawase (2005). Simulation of strong motions in Fukuoka City during the 2005 West off Fukuoka Prefecture earthquake with special reference to thick Quaternary sediments around the Kego fault. *Earth Planets Space* **58** 105–110. 47

Satoh, T., H. Kawase, and T. Sato (1995a). Evaluation of local site effects and their removal from borehole records observed in the Sendai region, Japan. *Bull. Seism. Soc. Am.* **85** 1770–1789. 33, 41, 63, 69, 71

Seed, H. B. and I. M. Idriss (1970a). Analyses of ground motions at Union Bay, Seattle during earthquakes and distant nuclear blasts. *Bull. Seism. Soc. Am.* **60** 125–136. 41

Seed, H. B. and I. M. Idriss (1970b). Soil moduli and damping factors for dynamic response analyses. Technical report, University of California, Berkeley. Report No. EERC 70-10. 10, 73, 75, 80, 81

Seed, H. B., R. T. Wong, I. M. Idriss, and K. Tokimatsu (1986). Moduli and damping factors for dynamic analyses of cohesionless soils. *Journal of Geotechnical Engineering* **112**. 10, 80, 83, 84, 85, 86, 88

Seriani, G. and E. Priolo (1994). Spectral element method for acoustic wave simulation in heterogeneous media. *Finite Elements in Analysis and Design* **16** 337–348. 107

Shibuya, T., H. Kawase, and T. Seike (2009). Research on presumption of lying active behind fault that uses H/V spectrum ratio by microtremor measurement -the Kego fault as an example-. *Bulletin of the Geological Survey of Japan*. In Japanese. 43

Sills, L. B. (1978). Scattering of horizontally polarized shear waves by surface irregularities. *Geophys. J. R. astr. Soc.* 319–348. 117

Srivinas, M. and L. M. Patnaik (1994). Genetic algorithms: a survey. *Computer* **27** 17–26. 33

Stupazzini, M. and R. Paolucci (2009). Near-fault earthquake ground-motion simulation in the Grenoble valley by high-performance spectral element code. *Bull. Seism. Soc. Am.* **99** 286–301. 100

Su, F., J. G. Anderson, and Y. Zeng (1998). Study of weak and strong ground motion including nonlinearity from the Northridge, California, earthquake. *Bull. Seism. Soc. Am.* **88** 1411–1425. 10, 41

Swegle, J. W., D. L. Hicks, and S. W. Attaway (1995). Smoothed particle hydrodynamics stability analysis. *J. Comput. Phys.* **116** 123–134. 101

Takizawa, H. (1982). Work done by earthquake ground shacking upon various types of dynamics systems. In *Proc. of 6th Japan Earthquake Engineering Symposium*, Tokyo, Japan, pp. 1065–1072. 43

Tessmer, E. and D. Kosloff (1994). 3-D elastic modeling with surface topography by a Chebyshev spectral method. *Geophysics* **59** 464–473. 100

Thomson, W. (1950). Transmission of elastic waves through a stratified solid. *Journal of Applied Physics* **21** 89–93. 11, 42

van Vossen, R., A. Curtis, A. Laake, and J. Trampert (2006). Surface-consistent deconvolution using reciprocity and waveform inversion. *Geophysics* **71** 19–30. 155

Virieux, J. (1986). P-SV wave propagation in heterogeneous media velocity-stress finite-difference method. *Geophysics* **51** 889–901. 100

Vucetic, M. (1990). Normalized behavior of clay under irregular cyclic loading. *Canadian Geotechnical Journal* **27** 29–46. 82

Vucetic, M. and R. Dobry (1991). Effect of soil plasticity on cyclic response. *Journal of Geotechnical Engineering* **117** 89–107. 73, 75

Wen, K. L. (1994). Non-linear soil response in ground motions. *Earthquake Engineering and Structural Dynamics* **23** 599–608. 41

Yamanaka, H. and H. Ishida (1996). Application of genetic algorithms to an inversion of surface-wave dispersion data. *Bull. Seism. Soc. Am.* **86** 436–444. 30, 42

Zeghal, M., A.-W. Elgamal, H. T. Tang, and J. C. Stepp (1995). Lotung downhole array. II: Evaluation of soil nonlinear properties. *Journal of Geotechnical Engineering* **121** 363–378. 41

Zhou, R., F. Tajima, and P. L. Stoffa (1995). Application of genetic algorithms to constrain near-source velocity structure for the 1989 Sichuan earthquakes. *Bull. Seism. Soc. Am.* **85** 590–605. 30

Zienkiewicz, O. Z. (2005). *The Finite Element Method For Solid And Structural Mechanics*. Elsevier Butterworth-Heinemann. 100, 101

Zienkiewicz, O. Z. and R. L. Taylor (1989a). *The Finite Element Method, Fourth Edition, Volume 1: Basic Formulation and Linear Problems*. McGraw-Hill Book Company. 102

Zienkiewicz, O. Z. and R. L. Taylor (1989b). *The Finite Element Method, Fourth Edition, Volume 2: Solid and Fluid Mechanics Dynamics and Non-Linearity*. McGraw-Hill Book Company. 90